TECHNISCHE UNIVERSITÄT MÜNCHEN

Lehrstuhl für Energiewirtschaft und Anwendungstechnik

Development of a Modular Systems Code to Analyse the Implications of Physics Assumptions on the Design of a Demonstration Fusion Power Plant

Tobias Hartmann

Vollständiger Abdruck der von der Fakultät für Elektrotechnik und Informationstechnik der Technischen Universität München zur Erlangung des akademischen Grades eines

Doktors der Naturwissenschaften (Dr. rer. nat.)

genehmigten Dissertation.

Vorsitzender:		Univ.-Prof. Dr.-Ing. Erwin Biebl
Prüfer der Dissertation:	1.	Univ.-Prof. Dr. rer. nat. Thomas Hamacher
	2.	Hon.-Prof. Dr. rer. nat. Hartmut Zohm, Ludwig-Maximilians-Universität München
	3.	Hon.-Prof. Dr. rer. nat. Sibylle Günter

Die Dissertation wurde am 04.04.2013 bei der Technischen Universität München eingereicht und durch die Fakultät für Elektrotechnik und Informationstechnik am 03.07.2013 angenommen.

Abstract

The successful development and operation of a demonstration power plant (DEMO) is the next important step on roadmaps for fusion energy after ITER that is currently constructed in France. In the first phase of the development process for such devices, the conceptual design phase, the primary aim is to identify coherent designs that are composed of self-consistent sets of values for all key parameters like machine size, plasma current or magnetic field strength. This multi-dimensional parameter space can be explored with systems codes in order to identify areas that seem to be suited for more detailed investigation. Systems codes are composed of simplified models for all crucial systems of fusion devices that take into account all requirements and constraints of each component.

This thesis is about the development of a new systems code called TREND (Tokamak Reactor code for the Evaluation of Next-step Devices). TREND is implemented with modular code architecture and consists of modules for geometry, core plasma physics, divertor, power flow, technology and costing. The main focus has been on the core physics module, since the development of TREND was done in parallel to work on physics design guidelines for DEMO. Moreover, the validation of TREND in terms of benchmarks with other European and Japanese systems codes is discussed. For these benchmarks, specific parameter sets were selected and the observed deviations were traced back to differences concerning the individual modellings. One of these parameter sets constitutes also the basis for parameter studies that were conducted with TREND. The general idea behind these studies is the analysis of implications that arise from specific assumptions on selected key parameters. Besides constant fusion power and constant additional heating power, the plasma density is fixed with respect to the Greenwald limit.

The benchmarks helped particularly to detect shortages in the modellings of all involved systems codes. Significant improvement needs could be identified concerning the applied modellings of the divertor, the dynamical phases, the line radiation in different plasma regions, the contribution of fast plasma particles, as well as the plasma current profile. Some proposals for improved modellings are already discussed within this thesis. Furthermore, the conducted parameter studies show that due to the various boundary conditions characterising the tokamak operational space, the observed trends can be surprising when compared to simple models. In particular, it is observed that the plasma temperature plays a key role in case of fixed plasma densities. The feasible operation range for the plasma temperature is clearly restricted by the H-mode threshold power on the one side and the limits for the power exhaust on the other side.

Table of Contents

1. Introduction

One of the challenges for mankind of this century is certainly the sustainable supply of a growing world population with energy. The boundary conditions for this project are manifold. The UN Department of Economic and Social Affairs predicts that about 10 billion people will live on earth in 2100 [1]. This development in conjunction with an increasing prosperity and economic growth is the key driver of an increasing demand for energy [2]. At present, about 80 % of the world primary energy demand is produced with fossil fuels including coal, gas and oil [2]. Considering the limitations of fossil resources and their reinforcing effect on the global climate change, efforts to modify the energy supply system in the next decades seem to be worthwhile. In this context, scenario analysis is an auspicious and wide-spread method to deduce operation guidelines in order to achieve defined objectives [2]. A wide range of scenarios can be analysed with energy system models like the EFDA Times Model (ETM) [3, 4]. The latter is a process-oriented, partial-equilibrium model that is applied to describe the global energy system with the aim to identify future potentials of different energy technologies based on economic optimization.

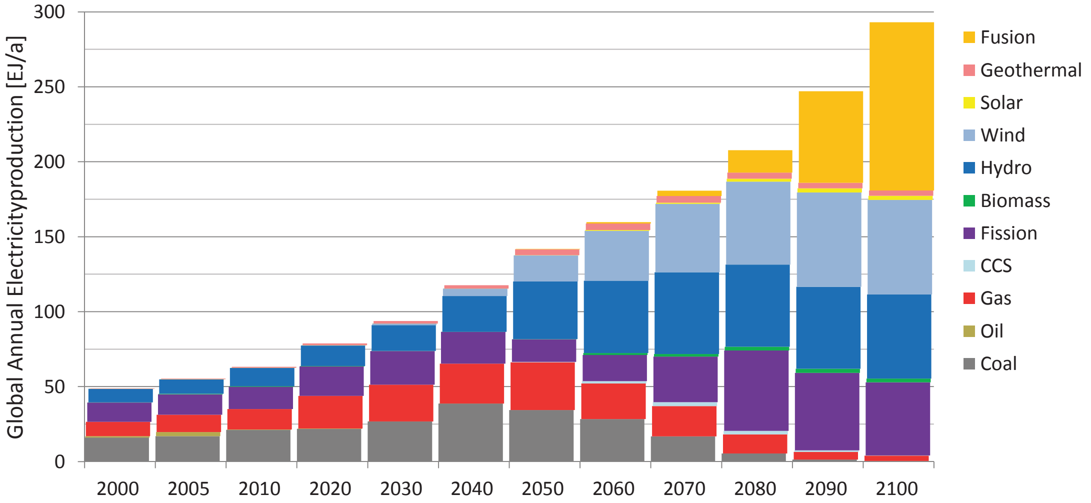

Figure 1.1.: Results of the EFDA Times Model (ETM) for a scenario with explicit climate protection limiting the global warming to 3 °C. Ref: [5]

Figure 1.1 shows the results for a scenario including explicit measures for climate protection in order to limit the global warming to 3 °C. These boundary conditions require a massive change of the energy system including the renunciation from fossil fuels. These developments establish the conditions for the entry of climate-neutral and resource-sensitive technologies like thermonuclear fusion into the energy market beginning in the second half of the century leading to a significant contribution in 2100 [5].

Thermonuclear Fusion

In principle, nuclear fusion is a comparable mature process. The energy of the sun is generated already for a long time by fusion reactions. Hence, the so-called renewable energy sources like solar, wind, biomass or hydro owe their existence strictly speaking also to nuclear fusion. It is basically a nuclear reaction where two or more atomic nuclei combine after a collision. On earth, the most promising reaction involves two hydrogen isotopes, deuterium (D) and tritium (T) [6],

$$ {}^{2}_{1}\mathrm{D} + {}^{3}_{1}\mathrm{T} \quad \rightarrow \quad {}^{4}_{2}\mathrm{He} + \mathrm{n} + 17.6\,\mathrm{MeV} \tag{1.1} $$

That is based on the largest cross-sections at the lowest temperatures (see Figure A.1). But even more important for thermonuclear fusion is the fusion reactivity $\langle \sigma v \rangle$ that also shows clear advantages regarding the above reaction (see Figure A.2). In addition, the amount of energy released per fusion reaction is comparable high. This energy originates from a difference in the binding energy per nucleon for the reactants and the products that manifests also in the corresponding masses of the atomic nuclei. The released energy is distributed on the products with respect to energy and momentum conservation. Since the atomic nuclei of both reactants are positively charged, certain conditions are required to overcome the Coulomb-barrier. That includes high temperatures of the order of several 10^8 °C or 10s of keV, respectively. By convention, temperatures are predominantly given in keV in fusion research. At these temperatures, the hydrogen isotopes are fully ionized and form a conductive gas, the plasma. Since just a small percentage of the collisions leads essentially to fusion reactions, the collision rate has to be high. Therefore, the required conditions include in addition a certain density of the plasma.

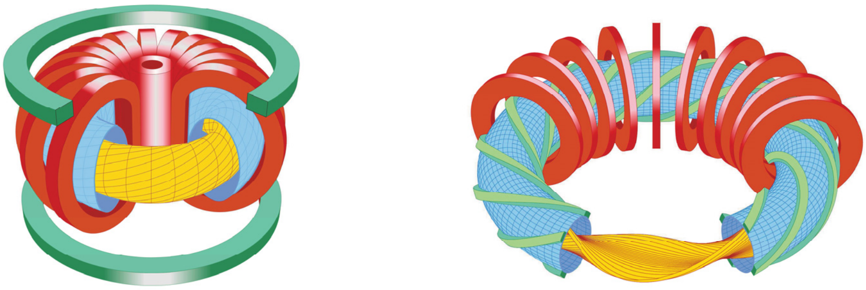

(a) Tokamak

(b) Stellarator

Figure 1.2.: Scheme of tokamak and stellarator configuration for fusion power plants. Ref: [7]

In order to achieve these conditions and to maintain them for characteristic time-scales, different concepts are developed. For some of them, the confinement of the hot plasma is realized by magnetic fields, since the movement of the charged particles is then influenced by the Lorentz force leading to gyro motions along the magnetic field lines. A configuration that has proven in the past to be reliable in this context is the so-called tokamak (see Figure 1.2(a)). It is basically a toroidal device with a helical structure of the magnetic field that is produced by toroidal magnetic field coils and a current flowing in the plasma. Whereas for an alternative concept, the stellarator (see Figure 1.2(b)), the magnetic field configuration is produced exclusively by external magnetic field coils with a complex 3-D geometry. In the following, this thesis is strongly focused on fusion devices that base on the tokamak concept. Nevertheless, some ideas, modellings and concepts presented within this thesis can also be transferred to stellarators.

Components of Fusion Power Plants

Besides the plasma and the magnetic field coils, a fusion power plant consists of several other components. Some of them are illustrated in Figure 1.3. The plasma is heated up to the required temperatures by different heating processes including self-heating by fusion reactions, ohmic heating due to the plasma current and external heating systems like neutral beam injection (NBI), electron-cyclotron resonance heating (ECRH), ion-cyclotron resonance heating (ICRH) and lower hybrid current-drive (LHCD). These can also be applied to drive current in the plasma (see Chapter 2.3.2).

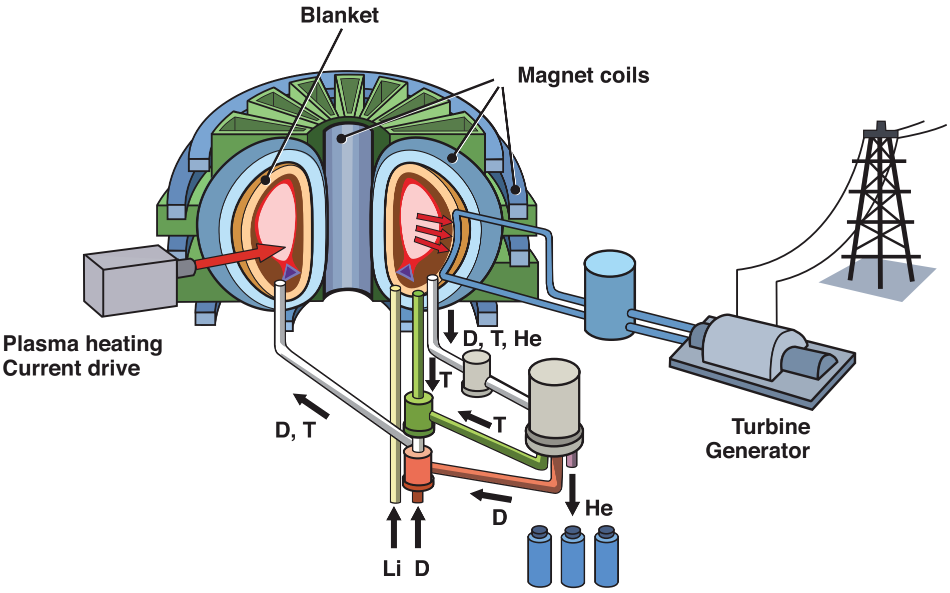

Figure 1.3.: Scheme of a fusion power plant including important systems. Ref: [7]

The generated fusion power as well as the external plasma heating power is transferred via different mechanisms from the plasma to the surrounding structures including the so-called blanket. For instance, neutrons that are produced by fusion reactions are not confined by the magnetic field, leave the plasma and deposit their energy in the blanket. Consequently, the blanket is heated up. This heat can be transported by cooling fluids like water or helium to conventional steam cycles that consist of heat exchangers, turbines and generators. These convert heat into electrical energy. But the blanket is also responsible for another important task. Tritium is radioactive and the amount of naturally occurring tritium is quite limited due to a half-life of about 12.3 years. Hence, the required tritium must be generated in the blanket by breeding out of lithium (Li):

$$ {}^{7}_{3}\mathrm{Li} + \mathrm{n} \rightarrow {}^{4}_{2}\mathrm{He} + {}^{3}_{1}\mathrm{T} + \mathrm{n} - 2.5\,\mathrm{MeV} \tag{1.2} $$

$$ {}^{6}_{3}\mathrm{Li} + \mathrm{n} \rightarrow {}^{4}_{2}\mathrm{He} + {}^{3}_{1}\mathrm{T} + 4.8\,\mathrm{MeV} \tag{1.3} $$

In order to increase the so-called tritium breeding ratio (TBR) of fusion neutrons, beryllium (Be) or lead (Pb) is added in the blanket for neutron multiplication. Another crucial component is the so-called divertor. Additional poloidal magnetic field coils produce a specific magnetic configuration including an X-point where the poloidal magnetic field vanishes. Consequently, regions with closed and open magnetic field lines are created. Particles that leave the core plasma and enter the region with open magnetic field lines are directly guided to specific plates and can efficiently be pumped out of the plasma vessel. Separation systems isolate unused fuel from fusion ash and other impurities. After reprocessing, these can then be recycled in fuelling systems.

On the Roadmap for Fusion: DEMO

Existing devices like ASDEX Upgrade (Axially Symmetric Divertor EXperiment) in Garching (D) or JET (Joint European Torus) in Culham (GB) do not consist of all required components of fusion power plants. These are experiments to explore the fundamentals of plasma physics for next-step devices. In addition, the dominant heating processes in these machines still base on external heating systems. But reliable self-heating of the plasma by alpha particles is an essential requirement for power plants. It is one of the main objectives of ITER that is currently constructed in France to prove this principle. Hence, ITER is the next crucial step for fusion research. But ITER will be equipped with many diagnostic systems that will occupy a significant part of the first wall area. Moreover, just test blanket modules will be installed that cover only a small fraction of the first wall area. Thus, reliable electricity production in combination with tritium self-sufficiency cannot be shown. That is the aim of next steps beyond ITER on roadmaps for fusion. At present, there is no clear agreement of the international fusion community how to bridge the gap between ITER and fusion power plants that are ready for the market [8]. The European Union pursues the strategy in the so-called fast track approach to build a single step between ITER and commercial fusion reactors, a demonstration fusion power plant, called DEMO [9, 10, 11]. According to Zohm [12], a potential set of objectives for such a device comprises the following aspects:

1. “Demonstrate a workable solution for all physics and technology questions.”

2. “Demonstrate large scale net electricity production with self-sufficient fuel supply” (i.e. at least several 100s of MW).

3. “Demonstrate high availability and reliability operation over a reasonable time span” (steady state or long pulse, e.g. 8 h operation with 30 min downtime).

4. “Allow to access the economic prospects of a power plant” (run at reasonable recirculating power fractions, maybe < 30 %).

Hence, there is a clear emphasis on the demonstration of the technological reliability of fusion. The requirements on pulse length for pulsed operation result from fatigue life considerations where a total lifetime of about 30 years and a total number of about 30 000 pulses similar to ITER are assumed [13]. The economic competitiveness is only a minor consideration at this stage. The development of the EU DEMO is coordinated by the Power Plant Physics and Technology (PPPT) department of the European Fusion Development Agreement (EFDA) involving different

European research institutes. Figure 1.4 shows an idealized illustration of the basic steps for the general design process of fusion devices. The decision to develop and build such machines is combined with the specification of particular objectives. Subsequently, the values for key parameters are evaluated targeting one or more conceptual design points. Before the start of construction, detailed designs for each component based on the conceptual design work are elaborated during the engineering design phase.

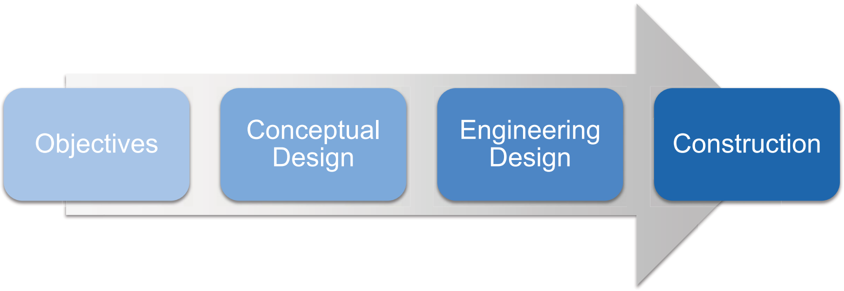

Figure 1.4.: Basic steps of the design process for fusion devices.

At present, the EU DEMO project is in the conceptual design phase. The pursued strategy in order to develop a mature conceptual design for DEMO is based on two concepts, DEMO 1 and DEMO 2. These are located at the lower and the upper end of the potential range of technological and physical assumptions, from conservative to optimistic. The top level objectives guiding the development of these concepts are summarized in Table 1.1.

Parameter	Unit	DEMO 1	DEMO 2
P_{elNet}	[MW]	500	500
P_{CD}	[MW]	–	~ 200
η_{th}		0.33	0.40
β_N	[%]	≤ 3.0	≤ 3.5
H		≤ 1.0	≤ 1.3
τ_{pulse}	[h]	≥ 2	n/a*

Table 1.1.: Top level assumptions for the EU concepts DEMO 1 and DEMO 2. *due to steady-state operation. Ref: [14]

Hence, DEMO 1 is a pulsed device with conservative assumptions about plasma physics and technology. DEMO 2 relies on more advanced assumptions including steady state operation. Most of the work for this thesis is based on a specific reference design of DEMO 1. This set of parameters is the result of the systems code PROCESS from Culham Centre for Fusion Energy (CCFE) (see next section). It is obtained during the EFDA workprogramme for 2011 [15, 16]. More detailed information about the parameters describing this operation point is given in Chapter 3.1. In the following, “DEMO 1” without further specifications refers to this particular parameter set.

Systems Codes

There are several tools, methods and approaches in order to advance projects in the conceptual design phase. That includes the so-called systems codes. Without claiming for completeness, I will try to set up a definition for these tools consisting of a few points that are discussed in more detail in the following. It is based on other definitions by Ward [17, 18], Johner [19], Dragojlovic et al. [20, 21], Nakamura et al. [22] and Federici et al. [23]:

> Systems codes are computational tools with appropriate computational times used for the conceptual design of fusion devices, consisting of simplified models for all crucial systems (often 0-dimensional) taking into account all requirements and constraints of each component with the ultimate ambition of self-consistency of the solution and the ability to identify and explore promising areas in the multi-dimensional parameter space.

After the decision to build ITER in 1985, several systems codes have been developed. Some examples are listed in Table 1.2, more examples can be found in Franza et al. [24] and references therein. Additional information on a few selected systems codes is given in Chapter 3. Based on history and maybe on the preferences and the scientific background of the developers, FORTRAN is widely used as programming language. Just recently, ASC, the systems code developed and used in the US Advanced Reactor Innovation and Evaluation Study (ARIES) program, was re-implemented in C++ reflecting the advantages of an object-oriented programming language in this context [21]. For the same reason, TREND is implemented in JAVA, but there are plans to transfer it to more efficient computational languages in the future.

Name	Host	Reference(s)
PROCESS	CCFE, United Kingdom	[25, 26]
HELIOS	CEA, France	[19, 27]
SYCOMORE	CEA, France	[24]
TPC / TOPPER	JAEA, Japan	[22, 28, 29]
ASC	ARIES Program, USA	[20, 21]
TREND	IPP, Germany	

Table 1.2.: Examples for existing systems codes.

In general, systems codes differ concerning their objectives, the implicit assumptions and the level of sophistication. In addition, they can be assigned with respect to the available mode(s) of operation. As shown later in more detail, a systems code is essentially a set of non-linear equations coupled to inequalities. One possibility to calculate a solution, a so-called design point (DP) or operation point (OP), is to apply algorithms that optimize a selected parameter like the plant size or the levelized costs of electricity (COE) [20]. But the result of such a procedure, the "optimizing mode", is possibly just a local optimum depending on the starting point and the optimization algorithm. A further disadvantage of this approach is that the analysis of the surrounding region and of other attractive near-optimal design points is limited, but could potentially provide profound insight [21]. Therefore, another possibility is to use a "scan mode" that iterates selected parameters in defined ranges including the application of filters for constraints. The result of this approach is a collection of design points that satisfy the requirements of all components as implemented in the systems code. These can subsequently be analysed with different tools. For that reason, this mode of operation is implemented in TREND. However, a comprehensive systems code should allow both modes of operation, since each has its legitimate advantages. In the following, no specific distinction is considered between the definition of operation and design points. Both represent a parameter set that characterizes the outline of a power plant concept.

Systems codes are no "pure" physics or technology codes that try to model the characteristics of one component of a fusion device as accurate as possible. First priority for systems codes is the comprehensive modelling of the whole power plant. Therefore, systems codes are ideally modular structured with modules for each crucial system. A proposal for a comprehensive set of modules is given in Tables 2.1 and 2.2. A modular structure also allows simple implementations of improved modules without major challenges. However, the modellings of all modules should be at a similar level of sophistication reflecting a good balance between complexity and computational times. That is important, since thousands of iterations may have to be carried out during one run [13]. Moreover, the applied modellings should incorporate all requirements and constraints of each component to guarantee that the results are self-consistent. This point is of high importance to assure that problems are not simply passed to other systems during the design process. Considering these general requirements of systems codes, the modellings are often based on a 0-dimensional structure.

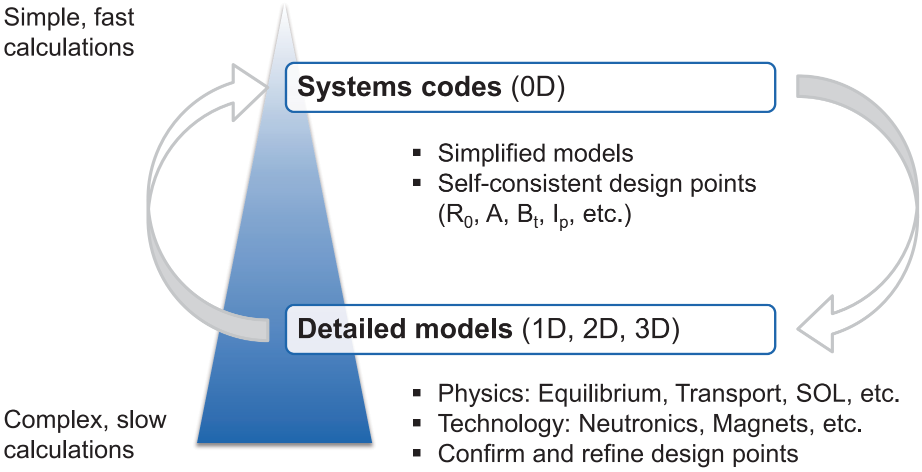

Figure 1.5.: General flow chart for the conceptual design of fusion reactors (based on Nakamura [30]).

There are already models for some systems that describe the corresponding characteristics with a significantly higher accuracy. For instance, that includes the equilibrium or transport codes for the plasma core. However, it seems to be not infeasible to include these tools in systems codes in the future. But another approach is proposed at present, since systems codes should be able to scan large areas in the multidimensional parameter space within reasonable time-scales.

Moreover, the level of sophistication should be increased similarly for all the other systems. For instance, there seems to be no evidence to favour the plasma core compared to detailed neutronic analysis of surrounding structures. The proposed procedure is shown in Figure 1.5. Systems codes with simplified models are used to identify and explore promising regions in the multidimensional parameter space leading to distinguished and self-consistent design points. These compose the starting points for more detailed models like the mentioned transport or neutronic codes. Their application helps to confirm and refine the design points. The results of these detailed analyses can subsequently be feed back into the systems codes to improve the modellings. This procedure represents a circular workflow that can be used to develop mature conceptual designs. But there is also work in progress to merge the more detailed models into new tools for fusion fostered by the development of computational power in the future.

General Outline

This thesis is basically structured in three main chapters as follows. In Chapter 2, detailed information about the systems code TREND is given. Besides the general structure, the modellings and assumptions of all implemented modules are presented. That includes the geometry, the core physics, the divertor, the power flow, the technology and the costing module. For the geometry module, two different versions exist. Hence, it is possible to show one of the ideas of modular systems codes by simply exchanging both modules at the corresponding interface of TREND. Most of the space of this chapter is taken up by the documentation of the physics module. That is due to the fact that a major part of the total development time was dedicated to the development of this module. In addition, its development was done in conjunction with work on so-called “Physics Design Guidelines for a DEMO Tokamak” [31, 32]. This document is set up as continuation of the “ITER Physics Design Guidelines: 1989” [33] including updates with respect to the progress in physics of the last two decades. These guidelines in combination with these for technology [24] are foreseen as the fundamental framework for the conceptual design phase of the EU DEMO project.

All existing fusion devices are still experiments without the full set of required power plant systems like breeding blankets, for instance. Hence, it is not possible to validate the results of TREND in total against the properties of existing systems. Therefore, I decided to compare the results of TREND with those of existing systems codes. These benchmarks are reported in Chapter 3 by means of one characteristic design point for each of the selected systems codes. This activity appeared to be helpful for the identification of programming errors and modelling weaknesses of all involved systems codes. Hence, the reliability of calculations in TREND and the modellings of all involved systems codes could be improved significantly.

The application of TREND is presented in Chapter 4 by means of four parameter studies. The general idea behind these studies is the analysis of implications of physics assumptions on a reference design point for DEMO 1. For each study, the chosen approach is basically as follows. One key parameter is scanned within a reasonable range. That includes the aspect ratio, the safety factor, the energy confinement in terms of the H-factor and the plasma density with respect to the Greenwald limit. In order to achieve the design targets for DEMO 1 as given in Table 1.1 and to satisfy all imposed constraints, it is necessary to vary also other parameters like the temperature and the impurity concentrations.

Finally, I tried to condense the information on the physical and technological background of each modelling to keep this thesis at reasonable length. For more detailed information, the reader is referred to the given references. The description of well-known and comprehensive physics elements is oriented on the following physics and plasma physics text books, as well as lecture notes without further referencing: Demtröder [34, 35, 36, 37], Wesson [38], Freidberg [39], Kaufmann [40], Dinklage et al. [41], Stangeby [42], Raeder [43], Kleiber and Bilato [6], Zohm [44, 45]. A comprehensive list of symbols is given at the end of this thesis. Therefore, not all applied symbols in the individual equations are explained in the surrounding paragraph. The same holds for the individual units. But in case that units differ from the standard ones given in the list of symbols, the particular unit is specified explicitly. For reasons of clarity and readability, values are often rounded to a reasonable number of digits throughout this thesis. But the calculations are always done with higher precision. Therefore, small inconsistencies can exist in the presented values due to rounding effects.

2. Methodology: The Systems Code TREND

This chapter is dedicated to present the systems code TREND including the general structure and the implemented modules. The name TREND has a twofold meaning. First, it is an acronym for “Tokamak Reactor code for the Evaluation of Next-step Devices”. This implies that only equations, constraints and requirements for fusion devices that rely on the tokamak principle are considered. But an extension to stellarators is not prohibited due to its modular structure. Second, a purpose of TREND is to conduct trend analyses on next-step fusion devices. Some examples of such trend analyses or parameter studies are presented in Chapter 4. The origin of TREND is a set of equations derived and applied by Zohm [9] to estimate the minimum size of DEMO. The further improvement of these equations with the objective to enhance self-consistency finally led to the development of TREND. The focus of the implemented modellings is particularly on physics for DEMO and beyond. These are extrapolated from and different from current machine physics.

2.1. General Structure

As mentioned, systems codes benefit from a modular structure that implies a higher flexibility. In case that new modellings for individual modules are available, the outdated ones can simply be replaced. Moreover, it is possible to implement different versions with varying levels of sophistication or objectives. Therefore, TREND is designed with a modular structure that is shown in Figure 2.1. The main class is `Control.java`. It basically reads the input file, loads the modules, iterates the parameters in the specified ranges, coordinates the application of the loaded modules and writes the outputs either on the console or in a file.

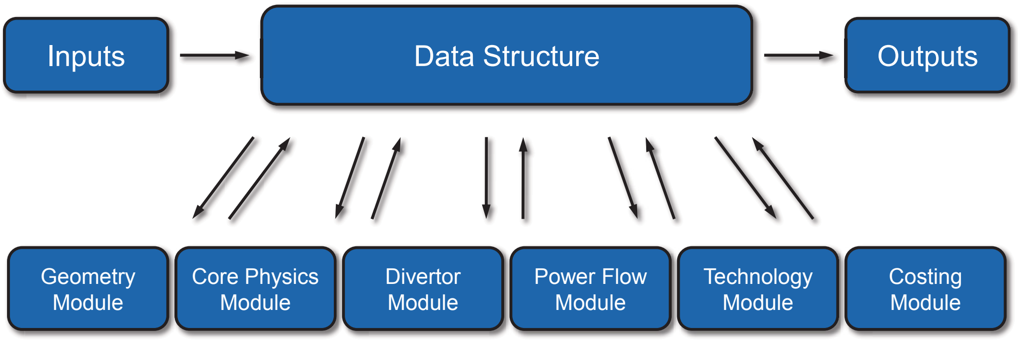

Figure 2.1.: Modular structure of TREND.

Each input parameter can be defined in a text file either as a constant value or as a range. For the latter case, minimum and maximum values as well as an increment must be specified. Then TREND integrates this parameter into the iteration procedure. For example, the command, `R0 = 7:0.1:12`, means that the major radius should be iterated in the range from 7 to 12 m with an increment of 0.1 m. The required and optional input parameters are marked as such in the list of symbols starting on page XLVII. If not defined in the input file, the optional input parameters are either set with default values or calculated by TREND using implemented modellings. Basically each possible input parameter and also arbitrary combinations can be iterated. With this approach a large multi-dimensional database can be populated in one run. In case that variations of parameters are intended that cannot be specified directly in the input file, appropriate inputs should be selected instead. For instance, the pressure can be varied by iterations either of the temperature, the density or both.

The class `DesignPoint.java` comprises the data structure of TREND (see ASC systems code [21]). For each iteration, the full set of all parameters is stored in this class. The different modules when executed have access and can operate on it. At present, interfaces for the following modules are implemented in TREND: Geometry, Core Physics, Divertor, Power Flow, Technology and Costing (see Figure 2.1). The order of this list is also the execution order, since TREND operates sequentially. Cross-links between different modules are represented by filters as explained below. TREND originates from equations derived and used by Zohm [9] to assess the size of DEMO. This set of equations has been improved and extended to enhance self-consistency leading to the present version of the core physics module of TREND. Surrounded by the before mentioned classes, interfaces and modules, the core physics module constitutes also the core of TREND. There are plans to implement more interfaces and modules in the future. An overview of basic and additional modules for comprehensive systems codes is shown in Tables 2.1 and 2.2 based on discussions with Franza et al. [46]. The existing modules of TREND are described in the following sections in more detail.

Module	TREND	Description
Geometry	✓	Design of radial build and reactor cross-section
Core Physics	✓	Plasma physics (power, pressure, particles, current and flux balance)
Divertor	(✓)	Power exhaust, material erosion and divertor plasma conditions
Heating & CD	(✓)	Physics and technology for heating and current-drive systems
Power Flow	✓	Power flow through the plant for different operation phases
Costing	(✓)	Calculation of direct and indirect costs, as well as the COE

Table 2.1.: Overview of basic modules for systems codes and the status of implementation in TREND. A checkmark in brackets signalizes a rudimentary status. For heating and current-drive, no independent module and interface is implemented in TREND, the modellings are included in the core physics and the power flow module. Ref: [46]

Module	Description
Blanket	Design and neutronic analysis including TBR approximation
TF Magnets	Design, materials, field, current and stresses of the TF coils
PF Magnets	Design, materials, control and flux supply of the PF coils
Maintenance	Availability and design issues due to O&M scheme
Tritium Cycle	Complete tritium cycle including inventories and losses
Waste	Estimation of waste qualities and quantities / management
Vacuum Vessel	Design of the vacuum vessel
Buildings	Design of the plant site

Table 2.2.: Overview of additional modules for comprehensive systems codes. Ref: [46]

At the end of the execution of each module, arbitrary filters can be applied. Those have the possibility to change a flag in the class `DesignPoint.java` deciding whether the current design point is considered as reasonable. This procedure can help to represent cross-links of different modules. The application is explained exemplary at one specific relation. The thickness of the blanket including the neutron shielding is an important driver for the radial build in terms of d_{int}, the distance of the inboard toroidal field coil to the separatrix (see Figure 2.5). This parameter is also of high importance for the core physics module, since it determines the toroidal magnetic field at the plasma centre (see Equation 2.56). But an approximation of the blanket thickness for a specific concept is the result of simplified modellings that can be included in blanket modules. These, in turn, rely on the total neutron yield calculated by the core physics module to evaluate the tritium breeding ratio (TBR). One possible solution of sequential code structures is then to consider d_{int} as input, to iterate it within reasonable ranges and to execute the core physics and the blanket module. Afterwards appropriate filters can be used to check if the TBR is within its desired limits.

2.2. Geometry Module

The first module that is executed for each iteration is the geometry module that is loaded at the corresponding interface. It completes the plasma geometry and the radial build of the machine based on given input parameters. At present, two different geometry modules are available in TREND, the “Standard” and the “Advanced”. The specific details of each are given in Chapters 2.2.1 and 2.2.2. Since both rely on a similar description of the plasma geometry, the basics for both modules are presented in the following, as well as a comparison of both. The geometry interface is the only one where two options are implemented. The selection of the particular module is simply done in one line of TREND showing the flexibility of modular structures. That can be part of the input file or a graphical user interface.

Figure 2.2 shows the coordinate system that is commonly used in fusion research for axisymmetric toroidal objects like tokamaks. It is a combination of a cylindrical and a polar coordinate system [47]. The former is defined by a radial coordinate R, a vertical coordinate z and a toroidal angle ϕ. Considering the R-z-plane for one specific toroidal angle ϕ_0, a distinguished point is the location of the plasma centre given by the major radius R_0 and z_0. Due to axisymmetry, the choice of ϕ_0 is arbitrary. Points in the R-z-plane can then be described by a radial coordinate r and a poloidal angle θ constituting a polar coordinate system. The radius of the plasma is given by the minor radius a.

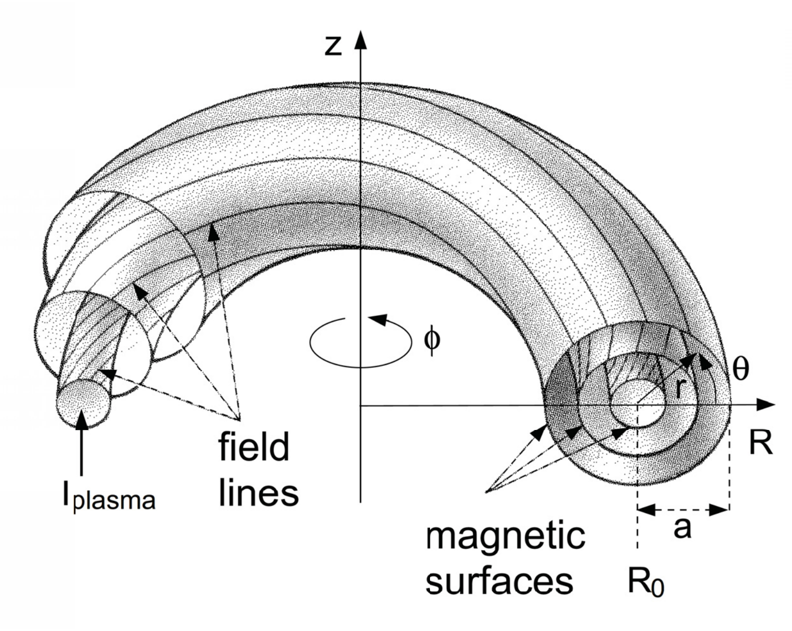

Figure 2.2.: Coordinate system of tokamaks. Ref: [6]

Different shapes of the plasma poloidal cross-section can be modelled with the following geometry parameters and the corresponding parametrization (see Figure 2.3 and Johner [19]). First, the poloidal cross-section is divided by the midplane into an upper and a lower part, (1) and (2), respectively. Then, the deformation of both parts compared to a semi-circle is described by elongation, triangularity and two intersection angles. The elongations $\kappa_X^{(i)}$ are measures for the deformation of the semi-circles to semi-ellipses that are divided at the minor axis or conjugate diameter. Precisely, the elongation is the ratio of the major to the minor axis of the specific ellipse. The index "X" refers to the specific values at the X-point, since also other definitions are commonly used (see Chapter 2.3.1). The triangularities $\delta_X^{(i)}$ describe the deformation of the semi-ellipses to D-shaped curves by shifting the vertical axis of the ellipses. Finally, if one or two X-points are considered, this configuration can be described by the intersection angels $\psi^{-(i)}$ and $\psi^{+(i)}$ of the elongated and D-shaped curves with a horizontal line at the top or the bottom of the cross-section. Based on the magnetic field configuration leading to an X-point, the values of the intersection angles should in principle sum up to 90°. These parameters in combination with the major radius R_0 and the minor radius a represent the backbone of the plasma geometry for both modules. The mean elongation and triangularity as used in subsequent modules are defined by

$$\kappa_X = \frac{\kappa_X^{(1)} + \kappa_X^{(2)}}{2} \tag{2.1}$$

$$\delta_X = \frac{\delta_X^{(1)} + \delta_X^{(2)}}{2} \tag{2.2}$$

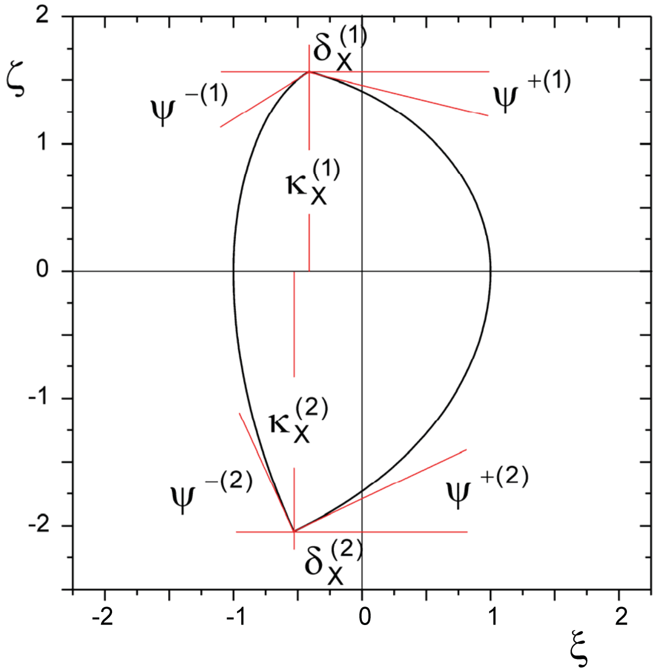

Figure 2.3.: Description of the poloidal cross-section of the plasma with elongation $\kappa_X^{(i)}$, triangularity $\delta_X^{(i)}$ and two intersection angles $\psi^{-(i)}$, $\psi^{+(i)}$ for the upper (1) and the lower (2) part. Ref: [19]

The “Standard” geometry module is based on the PROCESS code [26] and the “Advanced” on the HELIOS code [19]. It was shown analytically by Johner [48] during a benchmark exercise of European systems codes that the description of the plasma cross-section used in the “Standard” module is a special case of the “Advanced”. For the former, up-down-symmetry of the poloidal cross-section is assumed and the intersection angles have fixed values, i.e.

$$\kappa_X = \kappa_X^{(1)} = \kappa_X^{(2)}, \qquad \delta_X = \delta_X^{(1)} = \delta_X^{(2)} \tag{2.3}$$

$$\psi^{+} = \psi^{+(1)} = \psi^{+(2)} = \arctan \frac{\kappa_X^2 - 1 - \delta_X\left(2+\delta_X\right)}{2\kappa_X\left(1+\delta_X\right)} \tag{2.4}$$

$$\psi^{-} = \psi^{-(1)} = \psi^{-(2)} = \arctan \frac{\kappa_X^2 - 1 + \delta_X\left(2-\delta_X\right)}{2\kappa_X\left(1-\delta_X\right)} \tag{2.5}$$

In the following, a comparison of both modules is presented for the DEMO 1 reference design to get an idea of the differences. Furthermore, the comparison to a simple ellipse is added. The required parameters for the “Standard” module and the reference ellipse are given in Table 2.3. The additional parameters for the “Advanced” module are listed in Table 2.4.

Figure 2.4 shows the corresponding poloidal cross-sections of the plasma for the “Standard” in green and the “Advanced” in yellow, as well as for the reference ellipse in red. The shapes of both implemented modules look quite similar. The curve of the “Advanced” module is slightly shifted downwards and consists of only one X-point. Therefore, a more accurate modelling of the plasma cross-section is possible considering the additional options of the “Advanced”

Parameter	Symbol	Unit	Value
Major Radius	R_0	[m]	9.0
Minor Radius	a	[m]	2.25
Aspect Ratio	A		4.0
Elongation	κ_X		1.85
Triangularity	δ_X		0.50
Left Intersection Angle	ψ^-	[°]	59.8
Right Intersection Angle	ψ^+	[°]	12.0

Table 2.3.: Basic parameters and values of the plasma geometry used by the “Standard” module and the reference ellipse for the comparison of the different geometry modules of TREND.

Parameter	Symbol	Unit	Value
Upper Elongation	κ_X^1		1.70
Lower Elongation	κ_X^2		2.01
Upper Triangularity	δ_X^1		0.45
Lower Triangularity	δ_X^2		0.55
Upper Left Intersection Angle	$\psi^{-(1)}$	[°]	0
Upper Right Intersection Angle	$\psi^{+(1)}$	[°]	0
Lower Left Intersection Angle	$\psi^{-(2)}$	[°]	67.9
Lower Right Intersection Angle	$\psi^{+(2)}$	[°]	22.5

Table 2.4.: Basic parameters and values of the plasma geometry used by the “Advanced” module for the comparison of the different geometry modules of TREND. Since no parameters are available for DEMO 1 that reflect the asymmetry of the poloidal cross-section, the values of the ITER cross-section as used by Johner [19] were scaled linearly. The values for major radius, minor radius and aspect ratio are the same as given in Table 2.3.

geometry module. But the expected effects seem to be small for this configuration. In fact, the differences on the calculated values for the plasma volume V, the plasma surface area S and the area S_p, as well as the perimeter L of the poloidal cross-section are not significant (see Table 2.5). The relative deviation is less than 1 % for this specific case. Therefore, the application of the “Advanced” module seems not to be obligatory for conventional plasmas. But in case of more strongly deformed plasma shapes, the use of the “Advanced” module could be advised for higher accuracy. Comparing both geometry modules to the reference ellipse, considerably higher differences can be discovered (see Table 2.5). There are clearly more elements located at higher distances to the torus axis for the reference ellipse compared to the other cross sections as can be seen in Figure 2.4. Only the perimeter is quite similar for all parametrizations. Hence, the perimeter of the ellipse is only deformed and not stretched or compressed. Nevertheless, this analysis indicates that the use of pure elliptic shapes for the plasma cross-section leads to deviations of the order a few percent for the plasma volume. That implies subsequent effects on volume-dependent quantities like the fusion power, for instance. Therefore, the application of more sophisticated parametrizations as given in the “Standard” or “Advanced” geometry module of TREND are recommended.

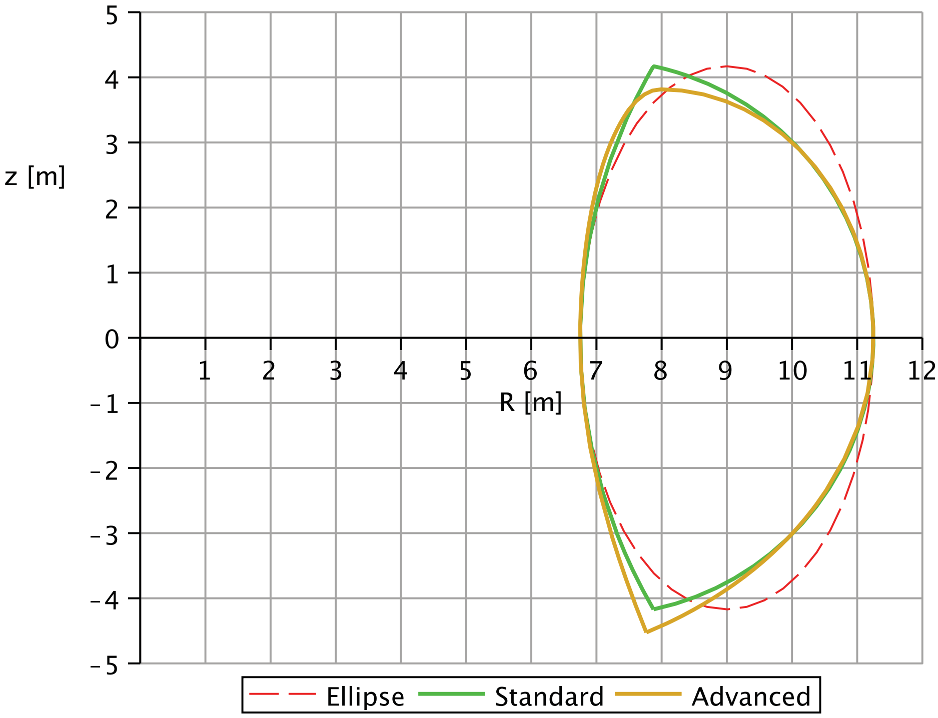

Figure 2.4.: Plasma poloidal cross-sections of DEMO 1 corresponding to the “Standard” and the “Advanced” geometry module. The parameters of the specific shapes are shown in Tables 2.3 and 2.4. A reference ellipse with the same values for elongation, major and minor radius as used for the “Standard” module is included for comparison.

Parameter	Symbol	Unit	Standard	Advanced	Ellipse
Plasma volume	V	[m^3]	1523	1538	1667
Plasma surface area	S	[m^2]	1124	1130	1166
Cross-sectional area	S_p	[m^2]	27.4	27.7	29.5
Plasma perimeter	L	[m]	20.3	20.5	20.6

Table 2.5.: Comparison of the main results of the different geometry modules for the given plasma shape of DEMO 1 (see Tables 2.3, 2.4 and Figure 2.4). An elliptic approximation with the same dimensions and elongation as used in the “Standard” module is included for comparison.

2.2.1. Standard

The “Standard” geometry module is one of two geometry modules that are currently implemented in TREND. If not stated explicitly throughout this thesis, the “Standard” module is selected at the geometry interface of TREND. For conventional tokamak configurations, the differences of both modules seem to be marginal (see Table 2.5). Since most of the work for this thesis is based on a reference design for DEMO 1 and this configuration is more or less conventional, the errors due to this selection are expected to be small. Moreover, the "Standard" module originates from the modelling of the PROCESS code and the parameter set of DEMO 1 was obtained by PROCESS runs. Hence, the reference parameters for the trend analysis in Chapter 4 are still quite close to the results of PROCESS.

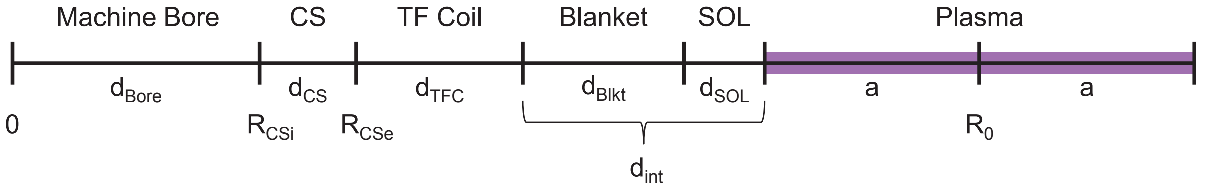

Figure 2.5.: Scheme of a simplified radial build at the midplane from the centre of the machine to the plasma. Note: the illustration is not in the correct scale and the "blanket" region includes breeding and shielding zones, as well as support structures and the vacuum vessel.

First of all, a geometry module should provide information on the radial build of the device. Figure 2.5 schematically shows important elements of the radial build. The individual role of each component is explained in the following sections. Since the systems outside the plasma are modelled rather rudimentary in TREND, only the inboard side of the plasma is illustrated. Starting at the torus axis in the middle of the machine, the first component is the central solenoid (CS) with the machine bore inside. Its thickness is simply defined as the difference of the outer and inner radial position of the CS, i.e.

$$d_{CS} = R_{CSe} - R_{CSi} \tag{2.6}$$

Thereafter, the inboard leg of the toroidal field coils (TFCs) is located with a thickness of d_{TFC}. Then there is space for the blanket. At present, no distinction is made in TREND between so-called breeding zones and shielding zones. The former are often called "blanket" and the latter "shielding". Due to the absence of a comprehensive blanket module that estimates the requirements on the breeding zone based on the target for the TBR and those for the shielding zone with respect to the limit for the neutron irradiation on the TFCs, both regions are summarized by d_{Blkt}. Between the blanket and the magnetically confined plasma inside the closed flux surfaces, there is a region called scrape-off layer (SOL) with a thickness of d_{SOL}. That region is also called the clearance. Based upon its definition, this layer consists of open magnetic field lines. The sum of the SOL, the breeding and the shielding zone is characterized by d_{int} that represents the radial distance of the inboard separatrix position to the radial location with the highest toroidal magnetic field. From a physics point of view, d_{int} should be as low as possible for high toroidal magnetic fields on axis (see Equation 2.56). But the breeding and shielding capabilities of the blanket region impose some lower engineering limits. Therefore, an optimization of d_{int} seems to be necessary for a certain maturity of the conceptual design. The radial extent of the plasma is given by two times the minor radius a. Hence,

$$R_0 = R_{CSi} + d_{CS} + d_{TFC} + d_{int} + a \tag{2.7}$$

For the sake of simplicity, the requirements on radial space for structural materials, manifolds, casings, gaps or thin layers like the first wall (FW) are assigned in the radial build modelling of TREND to the major components as described above. The ratio of major and minor radius for toroidal fusion devices is characterized by the aspect ratio,

$$A = \frac{R_0}{a} \tag{2.8}$$

or the inverse counterpart $\varepsilon = 1/A$, respectively. As a key parameter for the configuration of the machine, its value is often predefined and consequently considered as an input in TREND. A more detailed discussion on the aspect ratio is given in Chapter 4.1 in combination with the analysis of its impact on a reference design for DEMO 1.

In addition to the characterization of the radial build, a fundamental task of geometry modules is the accurate calculation of "plasma size" quantities including the plasma volume V, the plasma surface area S, the area of the poloidal cross-section S_p and the poloidal perimeter L. For each of those parameters, Johner [19] analytically derived an equation that consists of an elliptic part multiplied by a correction factor Θ. The former essentially estimates the specific parameter based on the poloidal cross-section of a reference ellipse. Hence, the correction factor is equal to unity for elliptical plasma cross-sections. Otherwise, it can be calculated with respect to the particular parametrization, i.e.

Plasma volume

$$V = 2\pi^2 R_0 a^2 \kappa_X \Theta_V \tag{2.9}$$

Plasma surface area

$$S = 2\pi R_0 \frac{L}{\theta_L} \Theta_S \tag{2.10}$$

Area of the plasma poloidal cross-section

$$S_p = \pi a^2 \kappa_X \Theta_{S_p} \tag{2.11}$$

Perimeter of the plasma poloidal cross-section

$$L = 2\pi a \mathrm{E}_1\left(\kappa_X\right) \Theta_L \tag{2.12}$$

where $\mathrm{E}_1\left(\kappa\right)$ is defined by

$$\mathrm{E}_1\left(\kappa\right) = \begin{cases} \frac{2}{\pi}\kappa \mathrm{E}\left(\sqrt{1-\frac{1}{\kappa^2}}\right) & \text{for } \kappa \geq 1 \\ 1 & \text{for } \kappa = 1 \end{cases} \tag{2.13}$$

and

$$\mathrm{E}\left(\kappa\right)=\int\limits_{0}^{\pi/2}\sqrt{1-\kappa^2\sin^2\theta}\,\mathrm{d}\theta \tag{2.14}$$

is the complete elliptic integral of the second kind. For the correction factors Θ_V, Θ_S, Θ_{S_p} and Θ_L, Johner [48] derived the following analytical formulas corresponding to the characteristics of the “Standard” geometry module:

$$\Theta_V=\frac{1}{\pi R_0 a^2\kappa_X}\left[c_1R_1^2\left(\frac{\pi}{2}-\psi^+\right)+c_2R_2^2\left(\frac{\pi}{2}-\psi^-\right)-a^2\kappa_X\frac{\kappa_X^2+\delta_X^2-1}{1-\delta_X^2}\left(R_0+\frac{\delta_X\kappa_X^2a}{1-\delta_X^2}\right)\right] \tag{2.15}$$

$$\Theta_S=\frac{2\theta_L}{R_0L}\left[c_1R_1\left(\frac{\pi}{2}-\psi^+\right)+c_2R_2\left(\frac{\pi}{2}-\psi^-\right)-a^2\kappa_X\delta_X\frac{\kappa_X^2+\delta_X^2-1}{1-\delta_X^2}\right] \tag{2.16}$$

$$\Theta_{S_p}=\frac{1}{\pi a^2\kappa_X}\left[R_1^2\left(\frac{\pi}{2}-\psi^+\right)+R_2^2\left(\frac{\pi}{2}-\psi^-\right)-a^2\kappa_X\frac{\kappa_X^2+\delta_X^2-1}{1-\delta_X^2}\right] \tag{2.17}$$

$$\Theta_L=\frac{1}{2\pi a\,\mathrm{E}_1\left(\kappa_X\right)}\left[2R_1\left(\frac{\pi}{2}-\psi^+\right)+2R_2\left(\frac{\pi}{2}-\psi^-\right)\right] \tag{2.18}$$

where

$$R_1=a\frac{\kappa_X^2+1+\delta_X\left(2+\delta_X\right)}{2\left(1+\delta_X\right)} \tag{2.19}$$

$$R_2=a\frac{\kappa_X^2+1-\delta_X\left(2-\delta_X\right)}{2\left(1-\delta_X\right)} \tag{2.20}$$

and

$$c_1=R_0-a\frac{\kappa_X^2+\delta_X^2-1}{2\left(1+\delta_X\right)} \tag{2.21}$$

$$c_2=R_0+a\frac{\kappa_X^2+\delta_X^2-1}{2\left(1-\delta_X\right)} \tag{2.22}$$

Finally, the geometry module not only provides the surface area of the plasma, it also estimates the surface area of the first wall (FW) excluding the divertor. This parameter is important for the evaluation of the neutron and heat loads on the FW (see Equations 2.216 and 2.217). Assuming a linear dependence of the surface area on the minor radius, the FW area is simply obtained by taking into account the radial width of the SOL, i.e.

$$S_{FW}=\left(\frac{a+\delta_{SOL}}{a}\right)S \tag{2.23}$$

This assumption neglects that the correction factor for the surface area Θ_S also depends on the minor radius. But considering the rough evaluation of the neutron and heat loads on the FW due to the assumption of isotropic sources and the fact that typically $\delta_{SOL}/a \approx 5\,\%$, the above approximation seems to be acceptable.

No magnetic equilibrium including the individual shapes of the magnetic flux surfaces as a solution of the Grad-Shafranov equation is calculated by TREND. Magnetic flux surfaces are formed by magnetic field lines such that the magnetic field is always perpendicular to the surface normal (see Figure 2.2). Based on a balance for the magnetic force and a force due to the plasma pressure, no pressure gradient exists along the magnetic field lines. Thus, the plasma pressure is constant on individual magnetic flux surfaces [38]. In order to consider the effects of the spatial dependency of different plasma parameters, the following assumptions are used: (i) the magnetic flux surfaces are similar to the shape of the last closed magnetic surface (LCMS) and (ii) the Shafranov shift is negligible. The second assumption implies that the magnetic axis is located approximately at the geometrical centre of the torus, i.e. $R_m \approx R_0$. Hence, a similarity factor ρ can be defined and used to label the magnetic flux surfaces. It is $\rho = 0$ on axis and $\rho = 1$ at the LCMS (see Johner [19]). The similarity factor ρ is also called the normalized radial coordinate. Consequently, the following calculations can be applied for poloidal surface or volume averages of arbitrary quantities $F(\rho)$ that observe a dependency on the normalized radial coordinate [19],

$$\langle F \rangle_{S_p} = \int\limits_{S_p} F(\rho)\,\mathrm{d}S_p \Big/ \int\limits_{S_p} \mathrm{d}S_p = \int\limits_0^1 F(\rho)\, 2\rho\,\mathrm{d}\rho \tag{2.24}$$

$$\langle F \rangle = \int\limits_{V} F(\rho)\,\mathrm{d}V \Big/ \int\limits_{V} \mathrm{d}V = \frac{1}{1-\frac{\Theta_1}{A}} \int\limits_0^1 F(\rho) \left(1 - \frac{3}{2}\frac{\Theta_1}{A}\rho\right) 2\rho\,\mathrm{d}\rho \tag{2.25}$$

where

$$\frac{\Theta_1}{A} = 1 - \frac{\Theta_V}{\Theta_{S_p}} \tag{2.26}$$

The upper and lower limits of the integrations can be adjusted with respect to the considered plasma region.

2.2.2. Advanced

The second geometry module that is implemented in TREND is named “Advanced”. It is based on the modelling of the HELIOS code. This module is an improved version of the “Standard” module, since the basic set of equations is identical (see Equations 2.7 to 2.14 and 2.23). The improvement consists mainly in the breakup of the up-down symmetry and the possibility to describe advanced deformations of the plasma. As mentioned in the introduction of this chapter, this allows a more detailed and realistic modelling of the plasma poloidal cross-section leading to higher accuracy. This advantage can be of importance especially for the modelling of advanced plasma scenarios that often include extremely deformed plasma shapes, i.e. strongly elongated and D-shaped. The improvement compared to the "Standard" module becomes manifest in the correction factors for the plasma size parameters, Θ_V, Θ_S, Θ_{S_p} and Θ_L. For these, analytic formulas have been derived by Johner [19] and are implemented in TREND in their original form. Due to their complexity, the reader is referred to the original paper where the corresponding equations can be found in the appendix beginning on page 337 [19].

2.3. Core Physics Module

The core physics or plasma core module comprises essentially the processes inside the separatrix, i.e. the region where fusion reactions are generated. Hence, it is of high importance for systems codes, since it specifies the energy source of fusion devices. Moreover, this module is also distinguished in the special case of TREND, since most of the previous efforts were dedicated to its development. That is based on two reasons. The first is due to history, since TREND originated from a set of mainly physics equations derived and applied by Zohm [9]. The second reason is the fact that I was part of a team that successfully applied for an EFDA task to review the physics modelling of the European systems codes considering the recent scientific progress and achievements. This work was decided to result in so-called "Physics Design Guidelines for a DEMO Tokamak" (see [31, 32]). These guidelines can finally build a common basis for future design studies and help to improve the existing systems codes. The predecessor of this document, the "ITER Physics Design Guidelines: 1989" [33], is still the fundamental framework for the physics modules of several systems codes. During the development process, I tried to keep the physics module of TREND updated as far as possible with respect to the achievements for the new guidelines. The flexibility of TREND was quite helpful to assess the possibilities for implementing specific items into systems codes. The present version of the core physics module of TREND is consequently a trade-off between a well-established framework and a basis that tries to incorporate the most recent physics progress.

The main ingredients of core physics modules are basically balance equations for plasma current, magnetic flux, power, pressure and particles with vanishing time derivatives, since only steady state operation points are considered. Therefore, it seems to be convenient to structure the description of the core physics module along with these balance equations. For completeness, there are two additional sections, one at the beginning describing general plasma equilibrium properties and one at the end summarizing operational limits due to plasma physics.

In the following, it is sometimes referred to a workshop with experts [49]. This workshop was about physics assumptions for a tokamak DEMO. It was organized by H. Zohm and me in March 2012 at the Max-Planck-Institute for Plasma Physics (IPP) in Garching (D). The participants were L. Aho-Mantila, C. Angioni, W. Biel, R. Dux, E. Fable, A. Kallenbach, R. Kemp, E. Poli, F. Ryter, O. Sauter, G. Tardini, M. Wischmeier and others. The results of this workshop were included later on in Hartmann et al. [31] and Zohm et al. [32].

2.3.1. Equilibrium Properties

Since no magnetic equilibrium is calculated in TREND, some important parameters describing the plasma equilibrium should at least be defined and estimated. That includes values for the safety factor at the centre and at the edge, the plasma current and an approximation of its profile, as well as for the internal inductance and the magnetic fields.

Safety Factor

In fusion devices with toroidal structures, the magnetic field lines should be of helical geometry to guarantee stability of the plasma and to attenuate particle and energy losses. In a purely toroidal magnetic field, the positive and negative charged plasma particles separate due to the $\vec{B} \times \nabla \vec{B}$ drift. This leads to an electric field that causes an outward transport for all charged particles based on the $\vec{E} \times \vec{B}$ drift. Therefore, an additional poloidal field is necessary to balance the potential differences, since the charged particles follow the resulting helical structure of the magnetic field lines. This geometrical structure can be described by the safety factor named with respect to its role for stability (see Chapters 2.3.7 and 4.2). The safety factor q is generally defined by the ratio of the number of toroidal to the number of poloidal turns of one field line until it joins up on itself again. Hence, higher values for the q-factor imply usually higher stability caused by lower twisting of the field lines. Moreover, the safety factor is a flux surface quantity, i.e. its value is the same for all field lines of one specific flux surface. That is similar to the plasma pressure as mentioned before in Chapter 2.2.1. Thus, distinguished flux surfaces are commonly labelled with respect to their q-value, the $q = 3/2$ flux surface, for instance. With the assumption of constant magnetic fields and a circular cross-section, the following equation for the safety factor can be derived,

$$q(r) = \frac{rB_\phi}{R_0 B_\theta} \tag{2.27}$$

where B_ϕ and B_θ are magnetic fields in toroidal and poloidal direction, r is a radial coordinate of the coordinate system for tokamaks (see Figure 2.2). In a strict sense, the assumption of constant magnetic fields is only valid in the limit of high aspect ratios where the torus can be approximated by a long cylinder with a homogeneous toroidal magnetic field. The following scaling relates this so-called “cylindrical” edge safety factor q_{cyl} to the edge safety factor of a torus with the inverse aspect ratio ε [33],

$$q_{95} = q_{cyl} \frac{1.17 - 0.65\varepsilon}{\left(1 - \varepsilon^2\right)^2} \tag{2.28}$$

In case of a divertor configuration, one or more magnetic X-points exist. There, the poloidal component of the magnetic field vanishes (compare “Single-Null” or “Double-Null” divertor configuration, for instance). Consequently, the safety factor diverges, since the poloidal rotation of one field line close to one X-point is impeded due to the smallness of the poloidal field. These field lines stay close to the X-point. Since comparison is only reasonable for finite values, it is decided to consider the edge safety factor somewhat inside the separatrix. By definition, the particular value of that flux surface is selected where 95 % of the poloidal flux lies within. The corresponding safety factor is then called q_{95} (see Equation 2.28). A well-established method in the development of scaling laws is the use of this 95 % flux surface as a reference point, even if other parameters would be well-defined at the separatrix. That includes elongation and triangularity, for instance. The ITER Physics Design Guidelines [33] specify the following equations relating the values corresponding to both positions,

$$\kappa_X = 1.12\kappa_{95} \tag{2.29}$$

$$\delta_X = 1.5\delta_{95} \tag{2.30}$$

Since these relations base on specific magnetic equilibria, their portability to equilibria for DEMO and fusion reactors should be assessed as soon as reference equilibria are available. Besides the above definitions for the elongation, there are also others, such as κ_a that is used in Equation 2.113, for instance.

Plasma Current

As mentioned before, the magnetic field of toroidal fusion devices should have a poloidal component in order to improve the confinement of particles and energy. For tokamaks, this poloidal magnetic field is generated by currents flowing in the plasma based on

$$\nabla \times \vec{B} = \mu_0 \vec{j} \quad \Leftrightarrow \quad \int\limits_{S_\rho} \nabla \times \vec{B}\, \mathrm{d}\vec{S}_\rho = \mu_0 \int\limits_{S_\rho} \vec{j}\, \mathrm{d}\vec{S}_\rho \quad \Leftrightarrow \quad \oint\limits_{\partial S_\rho} \vec{B}\, \mathrm{d}\vec{s} = \mu_0 I(\rho) \tag{2.31}$$

where Ampère's law in combination with Stokes' theorem is applied. The plasma current $I_p(\rho)$ flowing through the cross-section of a specific flux surface S_ρ is defined by the integral on the profile of the current density $j(\rho)$, i.e.

$$I_p(\rho) = \int\limits_{S_\rho} j(\rho)\, \mathrm{d}S_\rho \tag{2.32}$$

The normalized radial coordinate ρ is defined in Chapter 2.2.1. In most cases, only the total plasma current $I_p \equiv I_p(\rho = 1)$ is considered based on the 0-dimensional structure of TREND. As far as radial dependencies are of importance, these are marked explicitly. The line integral on the poloidal magnetic field in Equation 2.31 can be simplified further by defining a surface-line-averaged poloidal magnetic field as follows [33],

$$\left\langle B_p(\rho)\right\rangle_l = \oint\limits_{\partial S_\rho} B_p(\rho)\, \mathrm{d}l \Big/ \oint\limits_{\partial S_\rho} \mathrm{d}l = \oint\limits_{\partial S_\rho} B_p(\rho)\, \mathrm{d}l \Big/ L(\rho) \tag{2.33}$$

where $L(\rho)$ is the perimeter of the particular poloidal flux surface cross-section. Thus,

$$\left\langle B_p(\rho)\right\rangle_l = \frac{1}{L(\rho)} \mu_0 I_p(\rho) \tag{2.34}$$

and

$$\left\langle B_p \right\rangle_l \equiv \left\langle B_p\left(\rho=1\right)\right\rangle_l = \frac{1}{L}\mu_0 I_p \tag{2.35}$$

Hence, the following radial profile for the cylindrical safety factor can be deduced,

$$q_{cyl}\left(\rho\right) = \frac{\rho a B_t L\left(\rho\right)}{R_0 \mu_0 I_p\left(\rho\right)} \tag{2.36}$$

For the definition of the safety factor on axis q_0, it is noted that the current density in the vicinity of the axis has no radial dependency. Moreover, it is assumed that the flux surfaces in this region have circular cross-sections, i.e.

$$j\left(\rho \mapsto 0\right) \approx j\left(0\right) \equiv j_0 \tag{2.37}$$

$$I_p\left(\rho \mapsto 0\right) \approx j_0 S_\rho\left(\rho \mapsto 0\right) \tag{2.38}$$

and

$$S_\rho\left(\rho \mapsto 0\right) \approx \pi\left(\rho a\right)^2 \tag{2.39}$$

$$L\left(\rho \mapsto 0\right) \approx 2\pi\rho a \tag{2.40}$$

Hence,

$$q_0 \equiv q_{cyl}\left(\rho=0\right) = \frac{2B_t}{R_0 \mu_0 j_0} \tag{2.41}$$

where it is assumed that the Shafranov shift is small so that the radial position of the magnetic axis is approximately at the centre of the torus, i.e. $R_m \approx R_0$. Using Equation 2.36, the following equation for the total plasma current can be derived,

$$I_p = 5\frac{a^2 B_t}{R_0 q_{cyl}}\frac{L}{2\pi a} \tag{2.42}$$

where I_p is now given in [MA] based on an equivalence that is commonly used in plasma physics,

$$\mu_0 I_p\left[\mathrm{A}\right] = \frac{2\pi}{5} I_p\left[\mathrm{MA}\right] \tag{2.43}$$

In the following, the total plasma current is always given in [MA], if not stated explicitly. Instead of applying Equation 2.42 combined with an approximation for L to relate plasma current and safety factor for a given configuration including plasma size and toroidal magnetic field, a scaling law obtained for ITER [33] is usually implemented in most systems codes,

$$I_p = 5\frac{a^2 B_t}{R_0 q_{cyl}}\frac{1+\kappa_{95}^2\left(1+2\delta_{95}^2-1.2\delta_{95}^3\right)}{2} \tag{2.44}$$

With respect to Equation 2.42, this scaling corresponds to a simple approximation for L as the perimeter of an ellipse taking into account some effects based on triangularity,

$$L = \pi a\left(1+\kappa_{95}^2\left(1+2\delta_{95}^2-1.2\delta_{95}^3\right)\right) \tag{2.45}$$

An assessment of the applicability of Equation 2.44 for DEMO studies in combination with the "torus" factor for q_{95} according to Equation 2.28 is recommended. Until then, TREND uses both equations for coherence with other systems codes.

The profile of the current density $j(\rho)$ can be modelled for conventional plasma scenarios with a simple parabolic type profile,

$$j(\rho) = j_0(1-\rho^2)^{\alpha_j} \tag{2.46}$$

with the current density on axis j_0 and the profile coefficient α_j. Using this profile shape, the current peaking factor c_j can analytically be calculated,

$$c_j = \frac{j_0}{\langle j\rangle_{S_p}} = 1+\alpha_j \tag{2.47}$$

with the surface-averaged current density that is defined by

$$\langle j\rangle_{S_p} = \frac{1}{S_p}\int\limits_{S_p} j(\rho)\,\mathrm{d}S_p = \frac{I_p}{S_p} \tag{2.48}$$

where I_p is given in [A]. Since the profile of the current density influences the q-profile based on Equations 2.32 and 2.36, the definition of the current peaking factor can be used to derive a simple relation combining the safety factors at the edge and on axis,

$$\frac{q_{cyl}}{q_0} = c_j \cdot \frac{aL}{2S_p} \tag{2.49}$$

That simplifies further for circular poloidal cross-sections, i.e. $aL = 2S_p$.

Internal Inductance

Another parameter that is directly affected by the shape of the current density profile is the (normalized) internal inductance l_i being the normalized internal part of the total plasma inductance L_p (see Chapter 2.3.3). In general, it is defined by

$$l_i = \frac{\left\langle \langle B_p(\rho)\rangle_l^2 \right\rangle}{\langle B_p\rangle_l^2} \tag{2.50}$$

where

$$\left\langle \langle B_p(\rho)\rangle_l^2 \right\rangle = \frac{1}{V}\int \langle B_p(\rho)\rangle_l^2\,\mathrm{d}V \tag{2.51}$$

That illustrates the impact of the current density profile on l_i, since the shape of the poloidal magnetic field $\langle B_p(\rho)\rangle_l$ is based on $j(\rho)$ (see Equations 2.32 and 2.34). Hence, a broad current density profile leads to small values for the internal inductance. Unfortunately, different definitions for l_i exist based on different assumptions. TREND uses the following definition that is proposed by the ITER Physics Design Guidelines [33],

$$l_i \equiv l_i(3) = \frac{2V}{R_0 \mu_0^2 I_p^2} \left\langle \left\langle B_p(\rho) \right\rangle_l^2 \right\rangle \tag{2.52}$$

where the unit of the plasma current is [A]. Again, the Shafranov shift is assumed to be small. For parabolic type current density profiles (see Equation 2.46), Pomphrey [50] derived the following Pade approximation for the internal inductance using a Taylor expansion,

$$l_i = \frac{1}{2} \left[\frac{1 + 1.1918\alpha_j}{1 + 0.1918\alpha_j} \right] \tag{2.53}$$

Wesson [38] also describes a scaling for the internal inductance based on an empirical fit,

$$l_i = \log\left(0.89\alpha_j + 1.65\right) \tag{2.54}$$

Since both scalings are in reasonable good agreement for potential values of α_j, Equation 2.54 is implemented in TREND. For the ITER 15 MA ELMy H-mode scenario, the edge safety factor is given by $q_{95} = 3.0$. For an aspect ratio of $A = 3.1$, that leads to a cylindrical equivalent of about $q_{cyl} \approx 2.5$. Assuming that the safety factor on axis is about $q_0 \approx 1.0$ based on a periodic plasma instability (sawtooth oscillations), the value for the internal inductance should be about $l_i \approx 1.1$ according to the above scaling laws. But recent analysis of this scenario suggests that the internal inductance in the current flat-top phase is lower at about $l_i \approx 0.8 - 0.85$ [51, 52]. High values for l_i not only complicate the controllability of the vertical position of the plasma, also the available flux swing for the current flat-top phase is reduced (see Chapter 2.3.3). Based on Equation 2.52, more detailed calculations yielded that both scalings are quite properly in line with the assumption of circular plasma cross-sections and deviate for more realistic plasma shapes.

Unfortunately, this context is not treated coherently in most systems codes. Often the values for the current peaking, the safety factor and the internal inductance can be chosen independently. Therefore, the users of these systems codes have to act with caution based on detailed knowledge and experience. The presented relations given by Equations 2.49 and 2.54, could be a starting point to enhance self-consistency inside the systems codes. However, more accurate parametrizations of the internal inductance on the current profile would be beneficial. In addition, some insight could emerge from the analysis of characteristic magnetic equilibria and the evolution of l_i in transport code simulations.

Magnetic Fields

As mentioned before, the helical structure of the magnetic field in tokamaks results from two different components, the toroidal B_t and the poloidal magnetic field B_p. From a physics point of view, a high B_t comes along with several advantages for the performance of the plasma. Unfortunately, the toroidal magnetic field decays in the plasma with $1/R$ due to the following consideration. Imagine two closed loops in the midplane of the torus, one at the centre of the plasma at R_0 and one at R, an arbitrary radius between the plasma facing radial positions of the inboard and outboard legs of the TFCs. Based on Ampère's law, the integrals of the magnetic field along these loops are equal, since the current passing through both is identical (see Equation 2.31), i.e.

$$\oint_{R_0} B_t\left(R_0\right)\,\mathrm{d}l = \oint_{R} B_t\left(r\right)\,\mathrm{d}l \qquad \Leftrightarrow \qquad B_t\left(R\right) = \frac{R_0}{R} B_t\left(R_0\right) \tag{2.55}$$

Hence, the position with maximum toroidal field B_{tMax} is at the plasma facing side of the inboard leg of the TFCs. Considering the radial build of the machine as shown in Figure 2.5, the following equation can be derived for the toroidal magnetic field on axis [19, 31],

$$B_t \equiv B_t\left(R_0\right) = \left(1 - \frac{a}{R_0} - \frac{d_{int}}{R_0}\right) B_{tMax} \tag{2.56}$$

Thus, in order to have high toroidal magnetic fields on axis, the magnetic field at the inboard leg of the TFCs, B_{tMax}, should be as high and d_{int}, the distance between the separatrix and the inboard TFCs, should be as small as possible. Unfortunately, both are constrained due to technical reasons (see Chapters 2.2.1 and 2.6). Considering the poloidal magnetic field as defined by Equation 2.35, the total magnetic field B_{tot} can be evaluated with respect to vector geometrics,

$$B_{tot} = \sqrt{B_t^2 + \left\langle B_p \right\rangle_l^2} \tag{2.57}$$

In addition, a vertical magnetic field B_V has to be applied externally by the poloidal field coils (PFCs) to maintain the plasma in equilibrium. Due to the plasma kinetic pressure and the toroidal plasma current in combination with Ampère's force law, an outward hoop force exists that tries to expand the plasma ring. This force can be balanced by a Lorentz force that is based on the interaction of the toroidal plasma current with a vertical magnetic field. In equilibrium,

$$B_V = \frac{\mu_0 I_p}{4\pi R_0}\left(\beta_p + \frac{l_i}{2} - \frac{3}{2} + \ln\left(8A\right)\right) \tag{2.58}$$

where I_p is given in [A] and β_p in [–]. Expansion forces due to the plasma kinetic pressure are taken into account in terms of the total poloidal plasma beta β_p including explicitly fast particle contributions (see Chapter 2.3.5).

2.3.2. Current Balance

The toroidal plasma current consists of various contributions that base on different processes, inductive and additional external current-drive, as well as internal effects due to the bootstrap current. Each can be defined with respect to its fraction of the total plasma current, i.e. $f_{BS} = I_{BS}/I_p$ for the bootstrap current fraction, $f_{CD} = I_{CD}/I_p$ for the additional current-drive fraction and $f_{ind} = I_{ind}/I_p$ for the inductive current-drive fraction. Hence, the 0-dimensional current balance reads,

$$I_p = I_{BS} + I_{CD} + I_{ind} \qquad \Leftrightarrow \qquad 1 = f_{BS} + f_{CD} + f_{ind} \tag{2.59}$$

Both equations represent only a global balance for the plasma current. But the various components can differ essentially in their radial distribution. Moreover, the profile shape for the plasma current density is of high importance, especially for advanced tokamak scenarios. The alignment of the total current density profile with the bootstrap current density profile is obligatory for plasma configurations with high bootstrap current contributions as foreseen in steady state scenarios (see $f_{BS} = 89\,\%$ of the ARIES AT concept [53], for instance). Thus, the implementation of local current density balances would be advantageous for systems codes. There is work in progress on this topic considering work by Sauter et al. [31, 54, 55]. In the following, the different components of the total plasma current are described in more detail.

Inductive Current-Drive

The central solenoid (CS) coils of a tokamak and the conductive plasma can be seen as the primary and the secondary winding of a transformer. In analogy, a change of the current in the CS coils leads to a variation of the corresponding magnetic field $\vec{B}$. That, in turn, results in a modification of the poloidal magnetic flux $\Phi = \int_A \vec{B}\,\mathrm{d}\vec{A}$. Based on Faraday's law of induction described in its differential form by the Maxwell-Faraday equation, $\nabla \times \vec{E} = -\partial \vec{B}/\partial t$, that causes an electric field $\vec{E}$ in the plasma embodied in terms of an inductive loop voltage,

$$U_{loop} = \frac{\mathrm{d}\Phi}{\mathrm{d}t} \tag{2.60}$$

Thus, the inductively driven current can be evaluated with respect to Ohm's law by

$$I_{ind} = \frac{U_{loop}}{R_p} \tag{2.61}$$

where I_{ind} is given in [A] and the plasma resistance R_p depends on the length and cross-sectional area of the plasma loop, as well as the conductivity of the plasma, i.e.

$$R_p = \frac{1}{\langle\sigma\rangle_{S_p}} \left(\frac{2\pi R_0}{S_p}\right) \tag{2.62}$$

The surface-averaged plasma conductivity relies basically on the following structure,

$$\langle\sigma\rangle_{S_p} = \frac{\sigma_{Sp}}{\gamma_{NC}} \tag{2.63}$$

where σ_{Sp} refers to an expression for the conductivity of a cylindrical plasma without considering neoclassical effects (Spitzer conductivity). These are taken into account by γ_{NC}, the so-called neoclassical resistivity enhancement factor. In tokamaks, trapped and passing particles exist due to the radial variation of the toroidal magnetic field (see Equation 2.55). The passing particles have a sufficiently large velocity parallel to the magnetic field and can move freely along the magnetic field lines. Based on magnetic mirrors that are formed due to the non-uniformity of the magnetic field, the trapped particles are locked in so-called banana orbits on the outer side of the torus [38]. These are consequently unable to respond freely to an applied electric field with a movement along the field lines. Hence, their presence imposes an increase of resistivity and leads to a reduction of the current. At present, an established scaling that was derived for ITER [33] is implemented in TREND,

$$\sigma_{Sp} = 4.65 \times 10^{8} \frac{\left(\langle T \rangle_n / 10\right)^{3/2}}{Z_{\mathrm{eff}}} \left(\frac{2\pi\kappa_{95} a^2}{S_p} \right) \tag{2.64}$$

and

$$\gamma_{NC} = 4.3 - 0.6A \tag{2.65}$$

Thus, the plasma temperature, here in terms of the density-normalized volume-average, has a high influence on the conductivity of the plasma. Since the spatial variation of the temperature from plasma core to the edge can be significant, the accuracy of the calculation with averaged values should be assessed, at least for temperature profiles with high gradients. Furthermore, improved scaling laws for σ_{Sp} and γ_{NC} with spatial resolutions have been developed and are successfully applied in several plasma physics codes [54, 55]. Both are in favour for a local current balance in addition to the mentioned alignment of the different plasma current contributions. Moreover, the ITER scaling assumes a constant value for the Coulomb logarithm $\ln\Lambda$. A more detailed value can be calculated based on the following equation [54, 55],

$$\ln\Lambda = 31.3 - 0.5 \ln(n_e) + \ln(T) \tag{2.66}$$

that depends on the temperature T in [eV] and the electron density n_e in [m^{-3}]. Collisions of plasma particles are Rutherford scattering interactions that rely on the Coulomb force, rather than classical “pool ball” collisions. The Coulomb logarithm is defined as the logarithm of the Debye length compared to the collision impact parameter for a 90° scatter. It is typically about 17 in tokamak plasmas [38]. The Debye length is a characteristic length-scale that characterizes the shielding of the electrostatic potential of individual plasma particles by the surrounding plasma. Thus, the Coulomb logarithm is a measure for the dominance of small-angle compared to large-angle collisions. Consequently, 90° scatterings are more likely the result of many small-angle collisions.

Bootstrap Current

For fusion devices that base on the tokamak principle, the bootstrap current can be advantageous, since it is generated automatically in confined high-pressure plasmas [56, 57, 58]. In optimized configurations, a large fraction of the plasma current required for confinement can be driven by the bootstrap effect “for free”. That is beneficial for pulsed as well as steady state machines, since the requirements on external current-drive means are lowered having a considerable impact on the performance of the power plant. The bootstrap current is a neoclassical effect that produces a current parallel to the magnetic field in the presence of a pressure gradient. Trapped particles on the same magnetic flux surface move on banana orbits either inwards or outwards with respect to the direction of their parallel velocity (parallel with respect to the magnetic field). Hence, in case of existing density gradients, more particles move in one than in the other direction. This leads to an asymmetry in the parallel velocity distribution for the trapped electrons and ions that differs in the individual direction due to the opposite charge. Based on coupling by collisions, the velocity distribution of passing particles is also shifted. Keeping in mind that ions collide predominantly among each other and electrons predominantly with ions, a distribution function as shown schematically in Figure 2.6 results. The fact that more ions move in one and more electrons in the opposite direction leads to a net current, the bootstrap current, that is sustained mainly by passing particles.

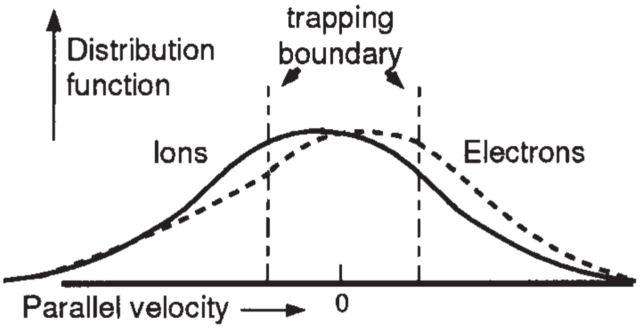

Figure 2.6.: Velocity distribution of electrons and ions in the presence of density gradients in tokamaks. Ref: [58]

Thus, the main drivers of the bootstrap current are density and temperature gradients, as well as the toroidal magnetic field geometry. A comprehensive formula for the bootstrap current fraction was derived by Sauter et al. [54, 55]. In systems codes, more simplified scalings are commonly used. Most of them are of the following general form,

$$f_{BS} = c_{BS} \beta_p \varepsilon^{1/2} \tag{2.67}$$

The bootstrap coefficient c_{BS} can depend on the peaking of the temperature, density and current profile, i.e. c_T, c_n and c_j, as well as the effective ion charge number Z_{eff} and the inverse aspect ratio ε. Table 2.6 lists different scalings for the bootstrap current fraction that are implemented in TREND. Special attention has to be paid, whether the total or only the thermal poloidal plasma beta, β_p or $\beta_{p,th}$, is applied in the specific scaling considering additional contributions of fast particles or not. In the following, some scalings are presented that are used predominantly in studies with TREND. For the others, the reader is referred to the original references given in Table 2.6.

Name / Author(s)	Ref.
Nevins 1988	[59]
Uckan et al. 1990	[33]
Wilson 1992	[60]
Hoang et al. 1997 (1)	[61]
Hoang et al. 1997 (2)	[61]
Andrade and Ludwig 2008 (1)	[62]
Andrade and Ludwig 2008 (2)	[62]
ASC (US systems code)	[21]
TOPPER (JAEA systems code)	[63]

Table 2.6.: Scalings for the bootstrap current fraction implemented in TREND.

Uckan et al. 1990 [33] The following scaling was derived for ITER where the bootstrap coefficient c_{BS} depends only on the current peaking. In addition, an average poloidal beta is calculated with respect to a circular poloidal cross-section and an “effective” plasma radius $\langle a \rangle$,

$$f_{BS} = c_{BS} \left(\beta_{pa} \varepsilon^{1/2} \right)^{1.3} \tag{2.68}$$

where

$$c_{BS} = 1.32 - 0.235 \frac{q_{95}}{q_0} + 0.0185 \left(\frac{q_{95}}{q_0} \right)^2 \tag{2.69}$$

and

$$\beta_{pa} = \beta_t \left(\frac{B_t}{B_{pa}} \right)^2 = \beta_t \left(\frac{B_t}{I_p/5 \langle a \rangle} \right)^2 = \beta_t \left(\frac{B_t}{I_p/5 \sqrt{\frac{V}{2\pi^2 R_0}}} \right)^2 \tag{2.70}$$

Wilson 1992 [60] Based on analytical expressions for the bootstrap current density, Wilson derived a scaling by fitting to different numerical calculations. The general form of the scaling is similar to Equation 2.67. Moreover, it considers explicitly the total poloidal plasma. The bootstrap coefficient is given by

$$c_{BS} = \sum_{i=1}^{12} a_i \left(\alpha_{jW}, Z_{\text{eff}} \right) b_i \left(\alpha_{TW}, \alpha_{pW}, \varepsilon \right) \tag{2.71}$$

where the definition of the coefficients a_i and b_i can be found in the appendix (see Table A.1). Even if this scaling was developed with the assumption of simple parabolic type profiles, an extension to other profile shapes seems to be possible by defining the profile coefficients as $\alpha_{xW} = c_x - 1$, where “x” is a wild-card for temperature, pressure and current density. Wilson also compared his result with the ITER scaling and discovered significant differences. Since the agreement of the Wilson scaling with analytic calculations in the large aspect ratio limit is more accurate than the ITER scaling and includes additional dependencies on the pressure and the temperature profile, it is considered as the default scaling in TREND. But work on new scalings for systems codes is in progress based on work by Sauter et al. [54, 55].

Hoang et al. 1997 [61] Analysing discharges of three circular cross-section experiments, TFTR, Tore Supra and TEXTOR, Hoang et al. derived the following bootstrap coefficients,

$$c_{BS} = 0.5 \sqrt{\frac{c_p}{c_j}} \tag{2.72}$$

$$c_{BS} = 0.45 c_p^{0.47} c_j^{-0.45} \beta_{p,th}^{-0.08} \tag{2.73}$$

where Equation 2.67 is kept as framework and additional effects are included in the bootstrap coefficient. The second scaling is obtained without the constraint of a linear dependence on the poloidal beta. Both scalings consider only the thermal poloidal plasma beta, i.e. both neglect effects due to fast particles.

Additional Heating and Current-Drive

The generation of additional heating and current-drive (H&CD) power can be one of the key drivers for the recirculating electrical power of fusion power plants (see Chapter 2.5). Moreover, the responsible systems include plasma physics as well as technology issues. At present, the former are modelled in the core physics module and the latter in the power flow module of TREND. But for the future, a comprehensive modelling of the H&CD systems in independent modules is proposed (see Table 2.1). Besides the advantage to combine all aspects in one module, systems with different characteristics and arbitrary combinations can simply be selected and analysed at the corresponding interface. Depending on the technical specifications, a heating system can also be used to drive current in addition to its task to heat the plasma. Hence, the total additional heating power injected in the plasma is given by the sum of the power applied also for current-drive P_{CD} and "pure" heating power P_{nCD} that is not explicitly used for drive current, i.e.

$$P_{add} = P_{CD} + P_{nCD} \tag{2.74}$$

Considering the total performance of a fusion device, it is desirable that the amount of power installed and used exclusively for plasma heating is as small as possible. The amount of externally driven plasma current I_{CD} is related to the injected power by the global normalized current-drive efficiency $\langle\gamma_{CD}\rangle$ where the leading dependencies on electron density $\langle n_e\rangle$ and the plasma size in terms of R_0 are already extracted, i.e.

$$I_{CD} = \frac{\langle\gamma_{CD}\rangle}{R_0\,\langle n_e\rangle} P_{CD} \tag{2.75}$$

The amount of electricity that is needed to supply the H&CD systems is determined by the wall plug efficiency η_{add} (see Equation 2.200 and Figure 2.14). It describes the conversion of electricity into H&CD power. Whereas $\langle\gamma_{CD}\rangle$ describes the conversion of H&CD power into driven plasma current. Hence, H&CD systems are essentially characterized by two parameters, the normalized current-drive efficiency $\langle\gamma_{CD}\rangle$ and the wall plug efficiency η_{add}. In general, there are significant differences on both parameters for all heating systems including neutral beam injection (NBI), electron-cyclotron resonance heating (ECRH), ion-cyclotron resonance heating (ICRH) and lower hybrid current-drive (LHCD). Typical values for the current-drive efficiency are $\langle\gamma_{CD}\rangle = 0.3 - 0.4$ and for the wall plug efficiency $\eta_{add} = 0.3 - 0.5$ depending on the particular technology [64, 65, 66]. NBI heating is based on the injection of accelerated and neutralized particles. The others rely on the absorption of electro-magnetic waves launched into the plasma at specific frequencies. These correspond to the circular motion of electrons and ions along the magnetic field lines due to the Lorentz force. These systems differ not only concerning the particular frequencies and the coupling to the plasma, but also technologically in terms of wave generation, wave transmission and antennas. LHCD is just reported for completeness, but it is not foreseen in DEMO or power plants due to the fact that the injected power is likely absorbed at the very edge of the plasma [64]. At present, it is assumed that DEMO and power plants do not require the application of more than one technology for H&CD. But in case that combinations of different systems should be taken into account, that can simply be done by defining additional pairs of ($\langle\gamma_{CD}\rangle$, η_{add}) and summing up the contributions. Considering the power flow of TREND (Figure 2.14), it is obvious that the product of both key parameters is of high importance for the selection of the particular heating system(s), since it matches the amount of driven current to the corresponding requirements on electricity. A development target for this product is $\langle \gamma_{CD} \rangle \cdot \eta_{add} \approx 0.25$ [65]. Moreover, attention should also be paid in the selection process to the possible plasma regions where the power could be absorbed or is reflected matching the spatial requirements on current-drive.

Finally, it is observed that the normalized current-drive efficiency of the considered H&CD systems scales approximately linear in temperature. Therefore, a simple scaling is implemented in TREND that was derived by Johner [19] for negative NBI current-drive,

$$\langle \gamma_{CD} \rangle = 0.035 \cdot \langle T \rangle \tag{2.76}$$

This scaling is applied, in case that $\langle \gamma_{CD} \rangle$ is not set in the input file of TREND. The value for the proportionality constant will soon be updated due to recent work on the different H&CD systems [66].

2.3.3. Magnetic Flux Balance

Generally speaking, the magnetic field $\vec{B}$, also known as the magnetic flux density, is characterized by the magnetic flux Φ through a perpendicular reference area $\vec{A}$, i.e.

$$\Phi = \int_A \vec{B} \, \mathrm{d}\vec{A} \tag{2.77}$$

Even if the name, magnetic flux, suggests a certain flow or movement similar to the electrical pendant, the electric current in terms of charged particles, the magnetic flux does not rely on a specific medium. With respect to the Maxwell-Faraday equation, a temporal change of the magnetic flux is related to an induced voltage (see Equation 2.60). That is the precondition for inductive current-drive as described in Chapter 2.3.2. Focusing on the so-called current flat-top phase of pulsed machines (see dynamical phases in Chapter 2.6), a constant change in time of the magnetic flux implies a constant value for the induced voltage. Hence, the duration of this phase can be calculated by an integral over time that simplifies to

$$\tau_{flat} = \frac{\Phi_{flat}}{U_{loop}} \tag{2.78}$$

where U_{loop} is the induced voltage in the plasma loop and Φ_{flat} is the available flux swing of this phase. The latter is the reminder of the total flux swing Φ_{tot} reduced by other flux requirements. That quantifies in the magnetic flux balance,

$$\Phi_{tot} = \Phi_{CS} + \Phi_{PF} = \Phi_{RU} + \Phi_{PI} + \Phi_{flat} \tag{2.79}$$

where Φ_{CS} and Φ_{PF} characterize the magnetic flux provided by the CS and other PFCs. Φ_{RU} summarizes flux requirements during the current ramp-up phase. Specific requirements for plasma initiation (PI) can be taken into account by specifying Φ_{PI} in the input file.

Sources for Magnetic Flux

The coils of the central solenoid (CS) are often included in the set of the poloidal field coils (PFCs). In TREND, these are considered independently, since their main task is the supply of magnetic flux for inductive current-drive in contrary to the responsibilities of the other PFCs as discussed below. In general, the CS is a long circular hollow cylinder with an overall height h_{CS}, as well as an inner and outer radius, R_{CSi} and R_{CSe}. Its thickness d_{CS} is simply the difference of both (see Equation 2.6). The magnetic field due to the surface-averaged current density j_{CS} flowing in the coils can be calculated according to Ampère's law in combination with Stokes' theorem (see Equation 2.31). This evaluation is based on a simple rectangular reference area with one leg at the centre and the parallel leg at infinity where the magnetic field vanishes, i.e.

$$\oint_{\partial S} \vec{B_{CS}}\,\mathrm{d}\vec{s} = \mu_0 \int_S \vec{j_{CS}}\,\mathrm{d}\vec{S} \qquad \Leftrightarrow \qquad B_{CSmax} = \mu_0 j_{CS} d_{CS} \tag{2.80}$$

In the limit of infinitely thin coils, the magnetic flux swing provided by the CS can be estimated according to Equation 2.77 by $\Phi_{CS} = 2 \cdot B_{CSmax} \cdot \pi R_{CSe}^2$. The doubling is caused by the fact that j_{CS} may be reversed during the process. Allowing for a finite thickness of the CS coils, a proper calculation yields [19],

$$\Phi_{CS} = \frac{2}{3}\pi B_{CSmax}\left(R_{CSe}^2 + R_{CSe}R_{CSi} + R_{CSi}^2\right) \tag{2.81}$$

The other PFCs have general duties like plasma shaping, formation of the divertor configuration, stability control and the generation of a vertical magnetic field. But in addition, they can also supply magnetic flux swing in the current ramp-up phase. Their contribution to the magnetic flux balance can be evaluated considering the effective area and the generated magnetic field [19],

$$\Phi_{PF} = \pi\left(R_0^2 - R_{CSe}^2\right)B_V \tag{2.82}$$

Requirements during Current Ramp-Up

As shown later in more detail, the requirements on flux swing in the current ramp-up phase consist of two parts, a resistive (dissipative) and an inductive (non-dissipative) component, i.e.

$$\Phi_{RU} = \Phi_{res} + \Phi_{ind} \tag{2.83}$$

The resistive flux consumption Φ_{res} is characterised by the definition of the Ejima coefficient [67],

$$c_{Ejima} = \frac{\Phi_{res}}{\mu_0 R_0 I_p} \tag{2.84}$$

where I_p is given in [A]. Similar to the approach of other systems codes, the value for c_{Ejima} can be set as an input in TREND. Just recently, Fable [68] derived a simple modelling that allows an estimation of the Ejima coefficient inside the systems codes to enhance self-consistency. As starting point, it is assumed that the current in the plasma is ramped up linearly from zero to the flat-top value, i.e.

$$I_p(t) = c_{RU\,rate} \cdot t \tag{2.85}$$

with the constant ramp rate $c_{RU\,rate} = I_p/\tau_{RU}$ that depends on the characteristic time-scale τ_{RU} of this period. For simple approximations, the ramp rates for DEMO and beyond can be expected to be at least in the same range as ITER values. For instance, the current flat-top value for the ITER 15 MA ELMy H-mode scenario is assumed to be reached in about 100 s, i.e. $c_{RU\,rate} \approx 0.15\,\mathrm{MA/s}$ [69, 70]. More precise values result from the analysis of the corresponding limits. A lower limit for the duration of the ramp-up phase τ_{RU} can be derived by defining a fundamental resistive time-scale,

$$\tau_{res} = \mu_0 a^2 \langle\sigma\rangle_{S_p} \left(\frac{\langle T_{RU}\rangle}{\langle T\rangle}\right)^{1.5} \tag{2.86}$$

where the plasma minor radius is taken as a typical length scale [68]. Based on Equation 2.63, the plasma conductivity scales with temperature like $\sigma \propto T^{1.5}$. Hence, the ratio of the average temperature of the ramp-up phase $\langle T_{RU}\rangle$ to the average temperature of the burn phase $\langle T\rangle$ intends to account in first order for lower temperatures in that period. A more sophisticated calculation should consider the temporal evolution of the temperatures. As a starting point, $\langle T_{RU}\rangle \approx 0.6\,\mathrm{keV}$ can be assumed for DEMO based on values of ASDEX Upgrade and calculations with the transport code ASTRA [71]. Generally, the resistive time scale determines the impact of the ramp rate on the current profile. If the time-scale of the ramp-up phase is similar to the resistive time-scale, the current profile is flat or even hollow. This can be seen as a limit for fast ramp-rates. Hence, τ_{RU} should be at least some numbers of τ_{res} [68], i.e.

$$\tau_{RU} \geq c_{RU} \cdot \tau_{res} \qquad \text{with } c_{RU} = 3 - 10 \tag{2.87}$$

Essentially, τ_{RU} is not limited on the upper end. But the resistive flux consumption scales to zero order linear in time as shown below [68]. Thus, slow current ramps come along with the penalty of higher requirements on magnetic flux. The flux consumption in the current ramp-up phase is generally given by the time integral over the loop voltage (see Equation 2.60), i.e.

$$\Phi_{RU} = \int\limits_{\tau_{RU}} U_{loop,RU}(t)\,\mathrm{d}t \tag{2.88}$$

With respect to Ohm's law in 0-dimensions, the loop voltage consists of resistive and inductive components [68],

$$U_{loop,RU}(t) = R_{p,RU} I_p(t) + L_p \frac{\mathrm{d}I_p(t)}{\mathrm{d}t} \tag{2.89}$$

where the plasma current I_p is given in [A]. Hence, in case of constant current ramp rates in line with the discussion above, Φ_{RU} is the sum of a resistive and an inductive part,

$$\Phi_{RU} = \frac{1}{2} R_{p,RU} \tau_{RU} I_p + L_p I_p \tag{2.90}$$

The plasma resistance of the ramp-up phase $R_{p,RU}$ can be related to the plasma resistance of the burn phase R_p by

$$\frac{R_{p,RU}}{R_p} = \left(\frac{d_{RU}}{a}\right)^2 \left(\frac{\langle T_{RU}\rangle}{\langle T\rangle}\right)^{-1.5} \tag{2.91}$$

Again, the ratio of $\langle T_{RU} \rangle / \langle T \rangle$ considers lower plasma temperatures during the ramp-up phase. The parameter d_{RU} allows for the fact that the resistive consumption accumulates predominantly in the outer plasma regions. Values of $d_{RU} \approx 0.25a$ fit reasonably well for ASDEX Upgrade and are recommended also for next-step devices [68]. Considering the definition of the Ejima coefficient in Equation 2.84, the following relation can be derived,

$$c_{Ejima} = \frac{R_{p,RU}}{2\mu_0 R_0} \tau_{RU} = 0.0625 \left(\frac{\pi a^2}{S_p} \right) \frac{\tau_{RU}}{\tau_{res}} = 0.0625 \left(\frac{\pi a^2}{S_p} \right) c_{RU} \tag{2.92}$$

Based on Equation 2.90, the inductive part of Φ_{RU} is proportional to the flat-top value of the plasma current given in [A], i.e.

$$\Phi_{ind} = L_p I_p \tag{2.93}$$

The proportionality constant L_p is the self-inductance of the plasma loop. It describes the character of the plasma loop to react on a variation of the plasma current by inducing a voltage in the opposite direction in order to retard the evolution. Moreover, the plasma inductance also relates the poloidal magnetic energy W_{mag} to the plasma current. But W_{mag} is also equal to the volume integration over the energy density of the magnetic field. This integration can be divided in two spatial parts, inside the plasma and outside the plasma [62], i.e.

$$W_{mag} = \frac{1}{2} L_p I_p^2 = \frac{1}{2\mu_0} \int_0^\infty B_p^2 \, dV = \frac{1}{2\mu_0} \left[\int_0^a B_p^2 \, dV + \int_a^\infty B_p^2 \, dV \right] \tag{2.94}$$

Hence, the self-inductance of the plasma loop can be separated into an internal and an external part, i.e.

$$L_p = L_{p,int} + L_{p,ext} \tag{2.95}$$

Normalization of the internal part leads to the definition of l_i, the normalized internal inductance of the plasma loop [62],

$$l_i = \frac{L_{p,int}}{\frac{1}{2} \mu_0 R_m} = \frac{2}{\mu_0^2 I_p^2 R_m} \int_0^a B_p^2 \, dV \tag{2.96}$$

where R_m is the radial coordinate of the plasma magnetic axis. As discussed in Chapter 2.3.1, the internal inductance comprises also a measure for the peakedness of the current profile. For the external plasma inductance, Hirshman et al. [72] obtained the following expression that is also used in TREND,

$$L_{p,ext} = \mu_0 R_0 \frac{a(\varepsilon)(1-\varepsilon)}{1 - \varepsilon + b(\varepsilon)\kappa_{95}} \tag{2.97}$$

with

$$a(\varepsilon) = \left(1 + 1.81\sqrt{\varepsilon} + 2.05\varepsilon\right) \ln\left(\frac{8}{\varepsilon}\right) - \left(2.0 + 9.25\sqrt{\varepsilon} - 1.21\varepsilon\right) \tag{2.98}$$

$$b(\varepsilon) = 0.73\sqrt{\varepsilon}\left(1 + 2\varepsilon^4 - 6\varepsilon^5 + 3.7\varepsilon^6\right) \tag{2.99}$$

2.3.4. Power Balance

The power balance of the plasma contains the gains and losses inside the confined plasma regions. Besides classical processes like conduction and convection, the losses in the plasma centre are mainly determined by neoclassical and anomalous transport, i.e. turbulence, trapped particles losses or various instabilities. Since these physical processes are not yet understood comprehensively, the transport losses are quantified by defining a 0-dimensional energy confinement time τ_E (see Equations 2.110 and 2.112). Therefore, the other quantities affecting the power balance and the balance itself are also described in zero dimensions. The dependencies on the specific shapes of temperature and density profiles are taken into account by introducing shaping functions that reflect these profile effects. The modelling of the temperature and density profiles itself is illustrated in the last subsection.

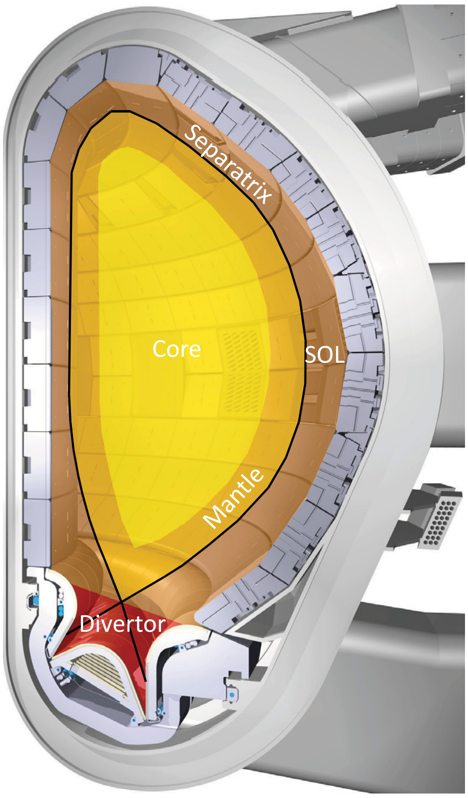

Figure 2.7.: Different plasma regions implemented in TREND. Reference of the original image: [73]

As mentioned, transport losses are of high importance especially in the plasma centre. But in the edge regions, radiation losses, particularly line radiation, become more and more important. Moreover, the edge radiation has a reduced impact on the power balance in the plasma core. These facts can be covered by a classification of the confined plasma inside the separatrix into different regions. Hence, TREND distinguishes the following plasma regions also shown in Figure 2.7, plasma core ($0 \leq \rho \leq \rho_{core}$), plasma mantle ($\rho_{core} < \rho \leq 1$), scrape-off layer (SOL) and divertor (see HELIOS code [19]). The normalized radial coordinate ρ is defined in Chapter 2.2.1. The boundary of plasma core and mantle is marked by $\rho_{core} \approx 0.90 - 0.95$ [19]. The specific value depends on the profile shapes for temperature and density, especially the modelling of the plasma pedestal, as well as on the assumptions about the influence of edge radiation on the power balance of the core plasma. The approach of two regions inside the separatrix also offers the possibility for a more realistic modelling of the impurity concentrations as explained later in Chapter 2.3.6.

For steady state operation, the energy content of the plasma has to be constant, i.e. the energy sources and sinks must balance. Thus, the 0-dimensional power balance for the plasma core region reads,

$$\frac{\mathrm{d}W_{th}}{\mathrm{d}t} = 0 = P_{heat} - P_{loss} \tag{2.100}$$

i.e.

$$P_{\alpha} + P_{add} + P_{OH} = P_{con} + P_{radCore} \tag{2.101}$$

The heat sources summarized in P_{heat} are discussed in the next paragraph. The losses are based on transport processes P_{con} and on core radiation $P_{radCore}$. Accordingly, the power balance in the mantle region is given by

$$P_{sep} = P_{con} - P_{radMantle} \tag{2.102}$$

describing the reduction of the core transport losses by radiation in the mantle. The remainder is P_{sep}, the power that is transported across the separatrix.

Heating Power

The total plasma heating power P_{heat} consists of internal sources, the fast alpha particles produced by fusion reactions, and external sources including power injected by external heating systems, as well as ohmic heating based on the plasma current. Therefore,

$$P_{heat} = P_{\alpha} + P_{add} + P_{OH} \tag{2.103}$$

The alpha heating power P_{alpha} is described in the next paragraph. The additional heating power P_{add} applied by external heating systems is given by the sum of “pure” heating power and power that is also used to drive plasma current (see Equation 2.74). A commonly implemented approach to solve the power balance in systems codes is the use of the “H-factor” as a free parameter. The H-factor characterizes the quality of the energy confinement compared to scaling laws. Since the transport losses are generally determined by the specific configuration of the plasma, a different approach is considered in TREND. In order to match the requirements on H&CD power of the current balance and the core power balance, the “pure” heating power P_{nCD} is adjusted accordingly. Negative values represent non-physical operation points. These can be filtered or even analysed. A simple procedure to transform non-physical into reasonable operation points is the enhancement of radiative losses by increasing the seeded impurity concentrations. Large values of P_{nCD} indicate an inefficient use of the H&CD systems, at least in terms of operation performance as mentioned in Chapter 2.3.2.

The ohmic heating power is defined with respect to Joule's first law as the heat produced in the plasma due to the plasma current, i.e.

$$P_{OH} = U_{loop} I_p \tag{2.104}$$

The absolute value of P_{OH} is comparably small in most cases. Hence, it could be neglected, since it is often smaller than the uncertainties of the other quantities contributing to the power balance.

A parameter that quantifies the relation of internal to external heat sources in the plasma is the fusion gain Q. In general, it is defined as the ratio of the fusion power to the external heating power including ohmic heating, i.e.

$$Q = \frac{P_{fus}}{P_{add} + P_{OH}} \tag{2.105}$$

Since the energy of the alpha particles is about $1/5$ of the energy released per fusion reaction (see Equation 2.108), $Q = 10$ as foreseen in the standard ITER scenario implies that plasma heating is dominated by internal heating processes due to fusion reactions by a factor of two. Infinite values for the fusion gain represent conditions corresponding to ignition, i.e. no external heating is needed to maintain the plasma in steady state, the plasma heats itself. In general, that is not a fundamental requirement for fusion reactors considering the advantages of current-drive power with respect to the current balance and stability control, for instance. But for reasonable performances in terms of the recirculating power fraction (defined in Equation 2.194), the fusion gain should at least be somewhat above the ITER value [74]. Promising values for Q depend amongst others on the efficiencies of the power conversion and the H&CD systems. The condition for the so-called break-even, $Q = 1$, characterizes just that the same amount of fusion power is produced as power is injected externally. That may be of relevance for the power balance of the plasma, but not for the balance of the whole device.

Fusion Power

At present, only the reaction of deuterium and tritium as described by Equation 1.1 is considered in TREND for the generation of fusion power. Moreover, effects based on fast particles are assumed to be less than a few percent and are neglected up to now. Therefore, the total fusion power generated by thermal particles in the plasma can be evaluated with

$$P_{fus} = \int n_D n_T \langle \sigma v \rangle E_{fus} \, \mathrm{d}V = \frac{1}{4} f_{DT}^2 \langle n_e \rangle^2 \langle \sigma v \rangle^* E_{fus} V \tag{2.106}$$

where densities are given in [m^{-3}], f_{DT} is the fuel concentration with equal parts for deuterium and tritium (see Equations 2.161 and 2.162) and $\langle \sigma v \rangle^*$ is the profile averaged thermonuclear reaction rate [19],

$$\langle \sigma v \rangle^* = \frac{1}{\langle n_e \rangle^2 V} \int n_e^2 (\rho) \langle \sigma v \rangle (T(\rho)) \, \mathrm{d}V \tag{2.107}$$

covering the profile effects of the electron density and the fusion reactivity $\langle\sigma v\rangle$ that depends on the specific temperature profile (see Figure A.2). The latter is often assumed to scale like $\langle\sigma v\rangle \propto T^2$. But Ward [75] recently showed that this assumption is only valid for temperatures below 20 keV. Above, a linear scaling on temperature seems to be more reasonable. For accurate estimations of the fusion reactivity, the Bosch / Hale fit [76, 77] is implemented in TREND. The energy released per fusion reaction, $E_{fus} = 17.6\,\mathrm{MeV}$, is distributed on the reaction products, an alpha particle and a neutron, with respect to their inverse mass ratio based on energy and momentum conservation [19, 31], i.e.

$$P_\alpha = 0.202 \cdot P_{fus} \tag{2.108}$$

$$P_{neutron} = 0.798 \cdot P_{fus} \tag{2.109}$$

Transport Losses

Energy losses that are based on diffusive processes can locally be described by the divergence of a heat flux $\nabla\vec{q}$ summing up flows from and into the vicinity of a specific point [39]. Hence, volume integration leads to the total energy loss rate of the plasma. In combination with Gauss's law, it can be shown that the total energy loss rate is determined by the heat flux through the surface surrounding the volume. For plasmas confined in a toroidal magnetic configuration, heat conduction is a major diffusive process. The corresponding heat flux is given by Fourier's law, $\vec{q} = -\kappa\nabla T$. Unfortunately, the physical processes determining the thermal conductivity κ of the plasma still lack a detailed understanding. In order to circumvent this problem, a 0-dimensional energy confinement time τ_E can be defined that characterizes the total energy loss rate, i.e.

$$P_{con} = \int_V \nabla\vec{q}\,\mathrm{d}V = \int_S \vec{q}\,\mathrm{d}S \equiv \frac{W_{th}}{\tau_E} \tag{2.110}$$

where W_{th} is the thermal energy of the plasma given with respect to the equipartition theorem and the ideal gas law by

$$W_{th} = \int_V \left(\frac{3}{2}n_e T_e + \sum \frac{3}{2}n_j T_j\right)\mathrm{d}V = \frac{3}{2}(1+f_i)\langle n_e\rangle\langle T\rangle_n V = \frac{3}{2}\langle p_{th}\rangle V \tag{2.111}$$

where f_i is the total ion concentration including deuterium, tritium, helium and the impurities as defined by Equation 2.159. In general, the global energy confinement time is defined considering the non-stationary power balance,

$$\frac{\mathrm{d}W_{th}}{\mathrm{d}t} = P_{net} - \frac{W_{th}}{\tau_E} \tag{2.112}$$

where P_{net} is the difference of all sources and sinks without transport losses. Hence, the solution of this differential equation with vanishing P_{net} suggests that τ_E represents a characteristic time-scale for the relaxation of the plasma energy due to transport losses. After τ_E, only $1/e$ of the initial energy is remaining. Since transport in plasmas is still an active research topic as mentioned before, different scaling laws for τ_E have been developed to assess the confinement of future devices. These are results of regression analysis on plasma discharges in various existing devices. Since core radiation did not play an important role in these experiments, P_{net} was measured in terms of the total absorbed heating power. This implies that radiation is implicitly included in the scalings of τ_E. During the design process of ITER, it was decided that P_{net} is just the power leaving the plasma by transport processes leading to a more conservative prediction of the thermal plasma energy [78]. Hence, TREND uses P_{con} as reference for the energy confinement. At present, the IPB98(y,2) scaling [79, 80] is predominantly used to estimate the energy confinement time of future devices, since it has been recommended by an expert group [80] for the conceptual design of ITER. It is

$$\tau_{E,th}^{IPB98(y,2)} = 0.1445 H I_p^{0.93} B_t^{0.15} P_{con}^{-0.69} \overline{n}_e^{0.41} M^{0.19} R^{1.97} \varepsilon^{0.58} \kappa_a^{0.78} \tag{2.113}$$

where the units are [s, MA, T, MW, $10^{20}\,\mathrm{m}^{-3}$, AMU, m] and $\kappa_a = S_p/\pi a^2$. The RMSE of this scaling is specified by 15.6 %. Compared to the original scaling, the so-called H-factor is already included in the above equation in order to consider enhancements or degradations of the confinement. Figure A.3 shows the comparison of the IPB98(y,2) scaling with measured energy confinement times of ELMy H-mode discharges in different devices and the prediction of τ_E for an ITER-FEAT discharge with $Q = 10$. As explained in more detail in Chapter 4.3, the adaptability of the IPB98(y,2) scaling for DEMO design studies seems to be questionable. The doubts are mainly based on the fact that the database corresponding to the IPB98(y,2) scaling was optimized for ITER operation points. But those foreseen for DEMO and beyond seem to differ significantly with respect to radiation, plasma density and plasma beta [32, 81].

Radiation Losses

The total radiation losses of the confined plasma inside the separatrix is the sum of contributions from the plasma core and the mantle region, i.e.

$$P_{rad} = P_{radCore} + P_{radMantle} \tag{2.114}$$

Hence, the total radiation fraction indicating the amount of the total heating power that is lost by radiation in core and mantle is given by

$$f_{rad} = \frac{P_{rad}}{P_{heat}} \tag{2.115}$$

Since synchrotron and bremsstrahlung radiation occur predominantly in the plasma core due to essentially higher temperatures, both are assigned exclusively to $P_{radCore}$. Thus, the dominant radiation process in the mantle is assumed to be line radiation, i.e.

$$P_{radCore} = P_{syn} + P_{brem} + P_{lineCore} \tag{2.116}$$

$$P_{radMantle} = P_{lineMantle} \tag{2.117}$$

Synchrotron Radiation Charged particles in the plasma gyrate on circular orbits around the magnetic field lines due to the Lorentz force. Based on this permanent radial acceleration, electromagnetic radiation is emitted, the synchrotron or cyclotron radiation. In a wider sense, that can be seen as a special type of bremsstrahlung as discussed below. Since the gyration of the charged particles depends strongly on their thermal energy, synchrotron radiation is only important at high temperatures. The corresponding loss power can be calculated by [19, 82, 83],

$$P_{syn} = C_{syn} \frac{(1-r_{syn})^{0.62} T_0 (16+T_0)^{2.61}}{\left[1+0.12 \frac{T_0}{p_{a0}^{0.41}} (1-r)^{0.41}\right]^{1.51}} R a^{1.38} \kappa_{syn}^{0.79} B_t^{2.62} n_{e0}^{0.38} G(A) K\left(\alpha_n^{syn}, \alpha_T^{syn}, \beta_T^{syn}\right) \tag{2.118}$$

where

$$p_{a0} = 6.04 \times 10^3 \frac{a n_0}{B_t} \tag{2.119}$$

$$G(A) = 0.93 \left[1+0.85 \exp(-0.82A)\right] \tag{2.120}$$

$$K(\alpha_n, \alpha_T, \beta_T) = \frac{(1.98+\alpha_T)^{1.36}}{(\alpha_n+3.87\alpha_T+1.46)^{0.79}} \frac{\beta_T^{2.14}}{\left(\beta_T^{1.53}+1.87\alpha_T-0.16\right)^{1.33}} \tag{2.121}$$

and $C_{syn} = 3.84 \times 10^{-9.6}$, the elongation is defined as $\kappa_{syn} = V/2\pi^2 R_0 a^2$ and the profile coefficients are given by $\alpha_n^{syn} = c_n - 1$, $\alpha_T^{syn} = c_T - 1$, $\beta_T^{syn} = \beta_T$. $G(A)$ is a correction factor that considers different aspect ratios and $K\left(\alpha_n^{syn}, \alpha_T^{syn}, \beta_T^{syn}\right)$ is a profile correction factor. The reflection of radiation at the first wall can be taken into account by r_{syn}, the synchrotron reflection coefficient. The specific value of r_{syn} has to be assessed for metal walls foreseen in future devices. So far, $r_{syn} = 0.6 - 0.7$ is assumed [49].

Bremsstrahlung Radiation With respect to Maxwell's equations, the acceleration of charged particles leads to an emission of electromagnetic radiation, the bremsstrahlung. In a narrower sense, only accelerated motion based on the existence of matter is called bremsstrahlung (see the distinction of synchrotron radiation, for instance). In hot plasmas, charged particles are permanently accelerated as a result of Coulomb collisions with other particles. Allowing for the mass difference of ions and electrons, this effect is stronger for electrons leading to a significantly higher radiation. Thus, only electrons are considered in the following. Impurities enhance the emission of bremsstrahlung with respect to higher charge numbers. In general, bremsstrahlung radiation in the plasma can be estimated with [19],

$$P_{brem} = \int_{V_c} C_B Z_{\mathrm{eff}} (n_e(\rho))^2 (T_e(\rho))^{1/2} \, \mathrm{d}V = C_B Z_{\mathrm{eff}} \langle n_e \rangle^2 \langle T_e \rangle^{1/2} V_c f_{brem} \tag{2.122}$$

where $C_B = 5.355 \times 10^{-3}$ and the profile shape function for bremsstrahlung radiation is

$$f_{brem} = \frac{1}{\langle n_e \rangle^2 \langle T_e \rangle^{1/2} V_c} \int_{V_c} (n_e(\rho))^2 (T_e(\rho))^{1/2} \, \mathrm{d}V \tag{2.123}$$

Applying the definition for the effective ion charge by Equation 2.163, the emission of a specific amount of bremsstrahlung can be assigned to the existence of particular ion species. The total bremsstrahlung radiation is then simply the sum, i.e.

$$P_{brem} = \sum_j C_B f_j Z_j^2 \langle n_e \rangle^2 \langle T_e \rangle^{1/2} V_c f_{brem} \tag{2.124}$$

This approach is helpful for the evaluation of "pure" line radiation as explained below. Since bremsstrahlung losses are small in the mantle region due to significantly lower temperatures, these are only considered in the core volume (V_c). In the mantle region, the small contributions are included implicitly in the line radiation power losses.

Line Radiation Due to atomic processes like excitation and de-excitation, the plasma emits line radiation named with respect to the following observation. A particular species of atoms emits a characteristic electromagnetic spectrum based on a discrete structure of the energy levels for bound electrons. The radiated power density of a species with charge number Z is given by

$$\frac{\mathrm{d}P_{line,Z}}{\mathrm{d}V} = n_e n_Z L_Z(T) \tag{2.125}$$

where $L_Z(T)$ is the radiative power loss function. Figure 2.8 shows $L_Z(T)$ for some elements including tungsten, argon, helium, deuterium and tritium. That is a characteristic mix of elements supposed to be present in plasmas for future reactors. In addition to the data used by TREND [84, 85], values calculated with work of Post / Jensen [86] are given for comparison. In general, $L_Z(T)$ consists of contributions from different atomic processes including bremsstrahlung, for instance. Hence, bremsstrahlung has to be subtracted in case of general radiative power loss functions in order to avoid twofold consideration. For increasing temperatures, the atoms get more and more ionized until they are fully stripped. Thus, only bremsstrahlung is remaining at some point. That can also be seen in Figure 2.8 where radiative power loss functions for bremsstrahlung corresponding to Equation 2.122 are plotted in addition with dashed lines. The elements involved in fusion reactions, deuterium, tritium and helium, are fully stripped in plasmas for reactor conditions and do not contribute to the corrected line radiation. Hence, only seeded high-Z impurities and sputtered wall materials are responsible for line radiation in the plasma core.

The total line radiation power for core and mantle is given by the integration over the particular volume, V_C and V_M, and the sum over the existing elements j with concentrations f_j. As mentioned before, line radiation is corrected for bremsstrahlung in the core, whereas in the mantle, only line radiation is considered due to the smallness of bremsstrahlung in that region, i.e.

$$P_{lineCore} = \sum_j \left[f_j \langle n_e \rangle^2 L_{Z_j}^{*C} V_C - C_B f_j Z_j^2 \langle n_e \rangle^2 \langle T_e \rangle^{1/2} f_{brem} V_C \right] \tag{2.126}$$

$$P_{lineMantle} = \sum_j f_{jM} \langle n_e \rangle^2 L_{Z_j}^{*M} V_M \tag{2.127}$$

where

$$L_{Z_j}^{*C/M} = \frac{1}{\langle n_e \rangle^2 V_{C/M}} \int_{V_{C/M}} (n_e(\rho))^2 L_{Z_j}(T(\rho))\, \mathrm{d}V \tag{2.128}$$

are profile averaged radiative power loss functions. For simple calculations, $L_{Z_j}^{*C/M}$ as well as f_{brem} could be parametrized with respect to temperature and density profiles. Therefore, the amount of core and mantle radiation can be controlled by the impurity concentrations, f_j and f_{jM}, with the burden of an influence on the fuel concentration (see Equation 2.162).

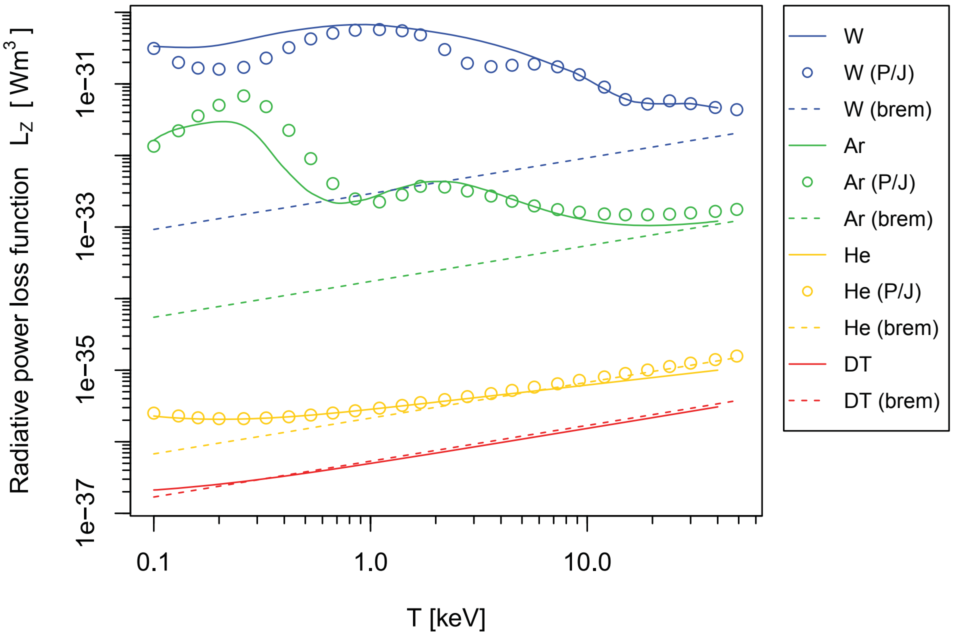

Figure 2.8.: Radiative power loss function based on corona equilibrium for some elements that could be present in plasmas of fusion devices: Tungsten (W), Argon (Ar), Helium (He), Deuterium and Tritium (DT). Ref: for TREND [84, 85], for Post / Jensen [86], the equivalent for bremsstrahlung is calculated based on Equation 2.122.

Technically speaking, the values for $L_Z(T)$ given in Figure 2.8 have been calculated for the specific case of corona equilibrium. A physical system is in thermal equilibrium, if each process is balanced by its reverse process. For fusion plasmas with low densities, the dominant processes for excitation are collisions and for de-excitation radiation recombination. The reverse counterparts, collision de-excitation and photo ionization play just minor roles. Hence, emitted photons leave the plasma, i.e. the plasma is optically thin. Moreover, the preconditions for thermal equilibrium are not fulfilled. Therefore, the “corona-ionization-equilibrium” model or simply the corona equilibrium was developed, since these specific conditions are also valid in the corona of the sun. In case that the density increases, the collision rate also increases limiting the validation of this model. That is important especially at the edge plasma and the divertor region. Thus, the radiative power loss functions should be updated with respect to different dwell times for the particles [87]. One idea would be to define $L_Z(T)$ in sections depending on particular temperature ranges, since each region has a characteristic temperature profile and distinguishes from adjacent regions.

Matthews et al. [88] developed a simple scaling relating the total line radiation to the effective ion charge number Z_{eff} that measures the impurity content,

$$P_{lineTot} = \frac{(Z_{\mathrm{eff}} - 1) S^{0.94} \overline{n}_e^{1.89}}{4.5 Z_s^{0.12}} \tag{2.129}$$

where Z_s is the atomic number of a seed impurity element, argon, for instance. This scaling is also implemented in TREND for comparison.

Profiles for Temperature, Density and Pressure

As explained before, a systems code has essentially a 0-dimensional structure. But some quantities of the physics module benefit from specific shapes of profiles for temperature and density. That includes the fusion power and radiation losses, for instance. Thus, simple parabolic type profiles for temperature and density are commonly implemented in systems codes. These are parametrized by

$$x(\rho) = x_0 \left(1 - \rho^2\right)^{\alpha_x} \tag{2.130}$$

with the normalized radial coordinate ρ defined in Chapter 2.2.1 and the profile coefficient α_x. An advantage of this simple type of profiles is the possibility to derive analytical descriptions for several parameters to avoid numerical integrations. However, the qualification of these profiles to model the specific shape of temperature and density especially in high confinement mode (H-mode) is rather poor. As explained in Chapter 2.3.7, H-mode is a plasma regime with reduced transport in the edge region leading to steep edge gradients. Hence, profiles that include the possibility to account for a pedestal at the edge are more suitable, i.e.

$$x(\rho) = \begin{cases} x_{ped} + \left(x_0 - x_{ped}\right) \left(1 - \left(\frac{\rho}{\rho_{ped}}\right)^{\beta_x}\right)^{\alpha_x}, & \text{for } 0 \leq \rho \leq \rho_{ped} \\ x_{sep} + \left(x_{ped} - x_{sep}\right) \frac{1-\rho}{1-\rho_{ped}}, & \text{for } \rho_{ped} < \rho \leq 1 \end{cases} \tag{2.131}$$

This profile modelling proposed by Johner [19] considers values for the pedestal top x_{ped} and the separatrix x_{sep} with a linear decrease in between. Inside the plasma core ($\rho \leq \rho_{ped}$), it still relies on the structure of simple parabolic shapes. It is obvious that the simple parabolic profile shape is a special case of the advanced one with $\rho_{ped} = 1$, $x_{ped} = 0$, $x_{sep} = 0$ and $\beta_x = 2$ [19]. Just recently, the application of these more advanced profiles was supported by a 1-dimensional analysis for the EU DEMO concepts [89]. This study suggests that the values at the pedestal are higher and the profile in the core is flatter than assumed by the simple scaling. That leads to lower fusion power yields for a given energy content deteriorating the overall power balance of the device. In TREND, both modellings are implemented and can be selected optionally. A comparison of simple and advanced profile shapes for the plasma temperature is presented in Figure 2.9.

Based on Equation 2.25, the volume-averaged values for temperature, density and pressure are defined by

$$\langle x \rangle = \frac{1}{V} \int x(\rho) \, \mathrm{d}V \tag{2.132}$$

For the simple profile shapes, also analytic descriptions are implemented in TREND allowing faster calculations. In addition to the volume-averaged quantities, also the line-averaged density $\overline{n}_e$ and the density normalized average temperature $\langle T \rangle_n$ are of importance for systems codes. These are defined by

$$\overline{n}_e = \frac{1}{a}\int_0^a n_e(r)\,\mathrm{d}r = \int_0^1 n_e(\rho)\,\mathrm{d}\rho \tag{2.133}$$

and

$$\langle T \rangle_n = \int n_e(\rho)\cdot T(\rho)\,\mathrm{d}V \Big/ \int n_e(\rho)\,\mathrm{d}V = \frac{\langle p_e \rangle}{\langle n_e \rangle} = \frac{c_n}{c_p} T_0 \tag{2.134}$$

where

$$c_x = \frac{x_0}{\langle x \rangle} \tag{2.135}$$

is the volume average peaking parameter of the profile shape for temperature c_T, density c_n and pressure c_p. Analogue to this definition, peaking parameters for pedestal and separatrix, $c_{xPed} = x_0/x_{ped}$ and $c_{xSep} = x_0/x_{sep}$ can be defined adapting the particular reference point in the denominator.

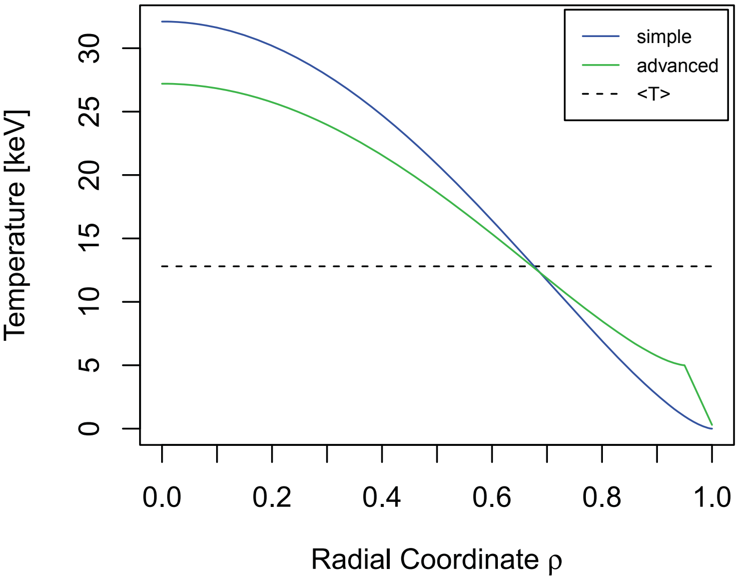

Figure 2.9.: Comparison of different profile modellings for the plasma temperature. The simple one is based on Equation 2.130 with the parameters for DEMO 1. The advanced is described by Equation 2.131. The location of the pedestal is set to $\rho_{ped} = 0.95$. The coefficients α_T and β_T are identical for both. The other profile parameters are assumed to be $T_{ped} = 5\,\mathrm{keV}$, $T_{sep} = 0.3\,\mathrm{keV}$ and the peaking was adjusted in such way that the volume average temperature is the same, $\langle T \rangle = 12.8\,\mathrm{keV}$, also marked in the plot by a dashed line. As a consequence, the peak temperature is reduced by about 15 % from 32.1 keV to 27.2 keV.

The consistency of the profiles for temperature and density with transport and stability calculations is often not considered inside the systems codes, since the profile parameters are often set externally. In the following, some suggestions are presented that could be a starting point in order to increase the self-consistency of the profiles in systems codes. These are implemented in TREND, at least for a subsequent consistency check. Starting from the edge, one of the basic advantages of divertor configurations is the fact that the temperature gradient from the separatrix to the first wall is significantly higher compared to limiter configurations. Since the temperature at the target is limited to about $T < 10\,\mathrm{eV} - 15\,\mathrm{eV}$ with respect to sputtering yields, the divertor configuration opens up the possibility for substantially higher temperatures at the separatrix. This temperature can be estimated based on a simple 2-point model [42] with one point at the divertor target T_{div} and the other at the so-called upstream location T_{sep} in the torus midplane. One of the main assumptions behind this model is the fact that conduction is the dominant process for heat transport. Other processes and losses are neglected. Hence, the parallel heat flux is given by $\vec{q}_{\|} = -\kappa \nabla T_e$, where $\kappa = \kappa_0\, T_e^{5/2}$ and the electron parallel conductivity coefficient is $\kappa_0 = 3.1 \times 10^4 \,/\, Z_{\mathrm{eff}} \, \ln\Lambda$ [90]. An integration along the field lines in the SOL yields

$$T_{sep} = \left(T_{div}^{7/2} + \frac{7}{2} \frac{L_{con} q_{sep}}{\kappa_0} \right)^{2/7} \tag{2.136}$$

where $L_{con} = \pi R_0 q_{95}$ [91] is the connection length and q_{sep} is the parallel power flux density leaving the plasma at the separatrix in $[\mathrm{W\,m^{-2}}]$, i.e.

$$q_{sep} = \frac{P_{sep}}{A_{q\|}} \tag{2.137}$$

with the surface area for the parallel power flux $A_{q\|} = 4\pi R_0 \lambda_q B_p/B_t$. The radial power decay length λ_q in [m] is based on the scaling of Eich et al. (see Equation 2.182). Assuming a circular cylindrical configuration, B_p/B_t at the separatrix can be replaced by q_{cyl}, giving $A_{q\|} \approx 2\lambda_q L/q_{cyl}$. The temperature at the divertor plate T_{div} can be neglected due to its smallness compared to T_{sep} and the corresponding exponent. More information on the 2-point model and its assumptions, as well as proposed extensions is given in Stangeby [42].

The situation at the pedestal top turns out to be the following. In the past, scalings have mainly been developed to evaluate the thermal pedestal pressure for a given configuration. Hence, the assumptions on temperature and density could only be assessed in combination based on

$$p_{ped} = (1+f_i)\, n_{ePed} T_{ped} \cdot e \tag{2.138}$$

with the electron charge e, the temperature T_{ped} given in [eV] and the electron density n_{ePed} in $[\mathrm{m^{-3}}]$. The following scalings for the pedestal pressure are implemented in TREND [92, 47],

$$p_{pedS1} = 2.41 \times 10^3 M^{0.33} n_{ePed}^{-0.33} \frac{R_0^{1.33}}{a^4 A^{2.94}} I_p^2 \frac{\kappa_X^{3.62} \left(1+\delta_X\right)^{3.2}}{\left(0.5\left(1+\kappa_X^2\right)\right)^{2.33}} \left(\frac{P_{heat}}{P_{LH}}\right)^{0.06} \tag{2.139}$$

and

$$p_{pedS2} = 3.35 \times 10^3 \left(1+f_i\right) \left\langle B_p \right\rangle_l^{0.87} \left(\frac{q_{95}}{q_{cyl}}\right)^{1.65} P_{heat}^{0.54} \tag{2.140}$$

The application of the second scaling was recommended by Schneider [93]. The original scaling is multiplied by $(1+f_i)$, since it was derived for the electron pressure. Unfortunately, both scalings exhibit large uncertainties.

Furthermore, the equilibration of ion and electron temperatures is often implicitly assumed in systems codes, i.e. $T_i \approx T_e$. In this case, the general definition of the mean temperature,

$$T = \frac{T_i + T_e}{2} \tag{2.141}$$

simplifies to $T = T_i = T_e$. In DEMO and future reactors, fast alpha particles created by fusion reactions and external heating systems will predominantly heat the electrons. Thus, an efficient heat exchange by collisions is the requirement for temperature equilibration of both species. In case that this is not provided, the performance of the plant can degrade, since less fusion reactions take place for the same plasma beta due to lower ion temperatures. Therefore, a discussion with experts [49] revealed that the option for different ion and electron temperatures should be implemented in systems codes in the future. In order to assess the accuracy of the assumption of equilibrated temperatures, the ratio of the energy confinement time τ_E to the characteristic time-scale for heat exchange τ_{ei}^E between electrons and ions is proposed as a starting point. According to Wesson [38], the latter is defined by

$$\frac{\mathrm{d}T_k}{\mathrm{d}t} = \frac{T_l - T_k}{\tau_{ei}^E} \tag{2.142}$$

where $k \in \{\text{electrons, ions}\}$ and l represents the other species. For a plasma consisting of electrons and single charged ions with charge Z, $\tau_{ei}^E = \tau_{ie}^E = \frac{m_i}{2m_e}\tau_e$ with the electron collision time,

$$\tau_e = 1.09 \times 10^{-4} \frac{T_e^{3/2}}{n_i Z^2 \ln \Lambda} \tag{2.143}$$

There seems to be some evidence that the average temperatures for ions and electrons can be regarded as equilibrated for $\tau_E / \tau_{ei}^E > 5$ [49]. In order to evaluate this criterion in more detail, we set up a simple 1-dimensional transport simulation that consists of the following set of equations for both species,

$$\nabla q_{e,i} = p_{e,i}^{heat} \pm p_{ei} \tag{2.144}$$

$$q_{e,i} = -\kappa_{e,i} \nabla T_{e,i} \tag{2.145}$$

where $\kappa_{e,i}$ is the electron / ion heat conductivity, $q_{e,i}$ is the electron / ion heat flux density, $p_{e,i}^{heat}$ is the electron / ion heating power density and p_{ei} is the heat exchange term,

$$p_{ei} = 3 \frac{m_e}{m_i} \frac{n_e}{\tau_e} (T_e - T_i) \tag{2.146}$$

that is derived with respect to Equation 2.142. This work is still in progress and implications based on different models for $\kappa_{e,i}$ are being analysed. Further insights in the justification of the temperature equilibration are also expected from transport studies with detailed transport codes in the framework of the European DEMO conceptual design.

2.3.5. Pressure Balance

Based on the equation of state for ideal gases, the thermal plasma pressure is given by the product of density and temperature, i.e.

$$p_{th}(\rho) = \left[n_e T_e \cdot e + \sum n_j T_j \cdot e\right](\rho) = \left[(1+f_i) n_e T \cdot e\right](\rho) \tag{2.147}$$

where $e = 1.602 \times 10^{-19}\,\mathrm{C}$ is the absolute value of the electron charge, the index j indicates different ion species, f_i is the total ion concentration (see Equation 2.159) and the units for electron density n_e and temperature T are $[\mathrm{m}^{-3}]$ and [eV], respectively. Hence, the volume-averaged thermal pressure is defined with respect to Equation 2.132 by

$$\langle p_{th}\rangle = (1+f_i)\langle n_e\rangle \langle T\rangle_n \tag{2.148}$$

A parameter of high importance for confined plasmas is the plasma beta β, since it characterizes the “efficiency of confinement of plasma pressure by magnetic field” [38]. In general, it is defined as the ratio of gas to magnetic pressure. Hence, the total thermal plasma beta with respect to the thermal gas pressure is

$$\beta_{th} = \frac{\langle p_{th}\rangle}{B_{tot}^2/(2\mu_0)} \tag{2.149}$$

The denominator constitutes an expression for a magnetic pressure due to the total magnetic field that is derived using force and pressure balance in steady state plasmas. Thus, the total plasma beta results from the consideration of additional contributions to the gas pressure based on non-thermalized fast particles, i.e.

$$\beta = \left(1+\gamma_{fast}\right)\beta_{th} \tag{2.150}$$

These contributions are quantified by $\gamma_{fast} = \beta_{fast}/\beta_{th}$, the fast particles fraction, that can be subdivided with respect to different sources, i.e.

$$\gamma_{fast} = \gamma_{f\alpha} + \gamma_{beam} \tag{2.151}$$

The fraction of fast beam particles γ_{beam} injected by external heating systems can be specified in the input file of TREND. The enhancement of the gas pressure due to fast alpha particles is estimated in TREND by a modified scaling that is given in the ITER Physics Design Guidelines [33],

$$\gamma_{f\alpha} = \begin{cases} 0.029 f_{DT}^2\left(\langle T\rangle_n - 3.7\right), & \text{for } \langle T\rangle_n \leq 20\,\mathrm{keV} \\ 0.473 f_{DT}^2, & \text{for } \langle T\rangle_n > 20\,\mathrm{keV} \end{cases} \tag{2.152}$$

This modification supposes that the original scaling on the fuel concentration is also valid for temperatures above $\langle T\rangle_n = 20\,\mathrm{keV}$ without further temperature dependencies [28]. More general, the fast alpha particles fraction is the ratio of the contribution to the total plasma beta that arises from the pressure increase due to the existence of these particles compared to the thermal plasma beta. Hence, the following proportionality can be derived based on some simple considerations,

$$\gamma_{f\alpha} = \frac{\beta_{f\alpha}}{\beta_{th}} \propto \frac{W_{f\alpha}}{W_{th}} \propto \frac{P_{fus}\tau_{sd}}{\langle n_e \rangle \langle T \rangle_n} \propto f_{DT}^2 \langle T \rangle_n^{1.5-2.5} \tag{2.153}$$

where $\tau_{sd} \propto \langle T \rangle_n^{3/2} / \langle n_e \rangle$ is the slowing down time for the thermalization of fast particles. The fusion power is assumed to scale like $P_{fus} \propto f_{DT}^2 \langle n_e \rangle^2 \langle T \rangle_n^{1-2}$ in line with the discussions above. Hence, the accuracy of the ITER scaling concerning the linear temperature dependence should be assessed.

The total plasma beta β in Equation 2.150 and the thermal plasma beta β_{th} in Equation 2.149 are explicitly defined with respect to the total magnetic field given by Equation 2.57. But also further definitions exist that provide a relation of the gas to the magnetic pressure based on the individual components of B_{tot}, the toroidal and poloidal magnetic field. Hence, the so-called toroidal and poloidal plasma beta with respect to the total, as well as the thermal gas pressure are,

$$\beta_t = \beta \left(\frac{B_{tot}}{B_t} \right)^2 \tag{2.154}$$

$$\beta_{t,th} = \beta_{th} \left(\frac{B_{tot}}{B_t} \right)^2 \tag{2.155}$$

$$\beta_p = \beta \left(\frac{B_{tot}}{\langle B_p \rangle_l} \right)^2 \tag{2.156}$$

$$\beta_{p,th} = \beta_{th} \left(\frac{B_{tot}}{\langle B_p \rangle_l} \right)^2 \tag{2.157}$$

2.3.6. Particle Balance

The plasma particles including electrons, fuel and impurity ions, as well as the individual charge states and transport processes are modelled rather simplistically in systems codes. It is implicitly assumed that ions and impurities have profile shapes similar to the electrons, since their concentration is simply modelled by a global fraction without spatial dependencies, i.e.

$$f_j = \frac{\langle n_j \rangle}{\langle n_e \rangle} \tag{2.158}$$

where $\langle n_j \rangle$ is the density of species j. For instance, the total ion concentration is

$$f_i = \frac{\langle n_i \rangle}{\langle n_e \rangle} = \frac{1}{\langle n_e \rangle} \sum_j \langle n_j \rangle = f_D + f_T + f_{He} + \sum_{\text{imp}} f_j \tag{2.159}$$

The last addend summarizes all the remaining ion fractions that are not directly involved in fusion reactions. These are referred to as the “impurities”. The total ion density fraction is in general not equal to unity, at least in case of plasmas with ion species that are more than single charged. That is based on the quasi-neutrality of the plasma, i.e.

$$\frac{\langle n_e \rangle - \sum_j \langle n_j \rangle Z_j}{\langle n_e \rangle} << 1 \qquad \Leftrightarrow \qquad \langle n_e \rangle \approx \sum_j \langle n_j \rangle Z_j \tag{2.160}$$

where Z_j is the charge number of ion species j. That is the first particle balance considered in TREND. Thus, the fuel concentration is given by

$$f_{DT} = \frac{\langle n_{DT} \rangle}{\langle n_e \rangle} = 1 - 2f_{He} - \sum_{\text{imp}} f_j Z_j \tag{2.161}$$

where the fuel density $\langle n_{DT} \rangle$ is defined as the sum of the deuterium and the tritium density. In the following, an optimal mixture of equal parts of deuterium and tritium is considered, i.e.

$$\langle n_{DT} \rangle = \langle n_D \rangle + \langle n_T \rangle = 2 \langle n_D \rangle = 2 \langle n_T \rangle \tag{2.162}$$

The evaluation of Equation 2.161 indicates that the fuel for fusion reactions is diluted by helium as a fusion product and additional impurities. A parameter that measures the dilution of the plasma compared to pure hydrogen plasmas is the effective ion charge number,

$$Z_{\text{eff}} = \sum \langle n_j \rangle Z_j^2 \Big/ \sum \langle n_j \rangle Z_j = 1 + 2f_{He} + \sum_{\text{imp}} f_j \left(Z_j^2 - Z_j \right) \tag{2.163}$$

Hence, for pure hydrogen plasmas, the effective ion charge number is equal to unity. Due to the simplification of constant ion species fractions without spatial distributions, the profile of Z_{eff} is also flat. Recently, in discussions at an experts workshop [49], it was proposed to implement at least different impurity fractions in the plasma core and mantle region, f_j and f_{jM}, respectively. That would allow to analyse enhanced mantle radiation due to increased impurity concentrations based on external seeding by gas puffing. The corresponding effective ion charge number of the mantle region is

$$Z_{\text{effM}} = 1 + 2f_{HeM} + \sum_{\text{imp}} f_{jM} \left(Z_j^2 - Z_j \right) \tag{2.164}$$

The second particle balance implemented in TREND is a rate equation for the helium density. In steady state,

$$\frac{\mathrm{d} \langle n_{He} \rangle}{\mathrm{d}t} = 0 = \frac{P_{fus}}{E_{fus} V} - \frac{\langle n_{He} \rangle}{\tau_p^*} \tag{2.165}$$

where the unit of $\langle n_{He} \rangle$ is [m^{-3}] and E_{fus} is given in [MW s]. The first term represents the source rate for helium due to fusion reactions, the second characterizes the loss rate. Moreover, it is implicitly assumed that the global confinement time for helium ions is similar to the global particle confinement time, i.e. $\tau_{He}^* \approx \tau_p^*$. The latter not only considers particle losses due to transport in the plasma, it also takes into account finite pumping. In case of ideal pumping systems, all particles that leave the plasma are instantaneously removed out of the plasma vessel. Hence, just a certain fraction is removed for finite pumping, the remaining particles can move back into the plasma leading to higher effective confinement times. Based on the observed relation between the thermal diffusivity and the particle diffusion coefficient [19], it can be assumed that the particle confinement time is proportional to the energy confinement time, i.e.

$$f_{P2E} = \frac{\tau_p^*}{\tau_E} = \text{const} \tag{2.166}$$

where $f_{P2E} \lesssim 5$ seems to be a reasonable limit [49]. At the lower end, the slowing down time for the thermalization of fast particles constitutes a criterion for the particle confinement [49]. In contrary to this approach, the ITER Physics Design Guidelines [33] specify a constant helium fraction of $f_{He} \approx 10\,\%$ with no dependency on the particular particle confinement.

2.3.7. Operational Limits

The operation point of tokamak plasmas cannot be chosen arbitrarily. There are several limits restricting the operation space. These constraints can be classified into soft and hard limits [94]. Soft limits are combined with a degradation of the energy confinement leading to a decrease of the plasma energy. That is linked with reductions of the fusion power. In case that hard limits are crossed, the plasma eventually disrupts. During the so-called "energy quench" of a plasma disruption, the temperature drops on small time-scales and the plasma energy is released to the first wall. The following phase is the "current quench", where the plasma current deceases rapidly. Hence, disruptions lead to high heat fluxes that can provoke the destruction of the first wall by erosion and melting. Moreover, large forces on the mechanical structure are induced. Therefore, disruptions have to be avoided in order to secure the availability and the lifetime of power plants. There are several means to manage this. First of all, sufficient safety margins to the operation limits should be considered. Moreover, disruptions can be stabilized by the strategic application of heating systems. Finally, there are ideas to mitigate disruptions by strong gas puffs or pellet injection spreading the plasma energy by radiation [94]. Figure 2.10 shows a so-called Plasma Operation Contour (POpCon) plot where several operational limits are included that restrict the potential operation space. These limits are discussed in more detail in the following. According to Koslowski [94], the operational limits can be subsumed into two general groups: "excessive radiation from the plasma, and violation of global as well as local MHD stability boundaries".

Plasma Shaping

The shape of plasmas in terms of elongation and triangularity is determined by the configuration of the PFCs. In studies with systems codes, both parameters are often specified as inputs. But systems codes should at least consider the limits on stability and controllability for a given set of PFCs. Therefore, the following scalings for the maximum controllable elongation and triangularity are proposed [31, 32],

$$\kappa_{Max} = 1.46 + \frac{0.5}{A-1} \tag{2.167}$$

$$\delta_{Max} = 0.6\left(\kappa_{Max} - 1\right) \tag{2.168}$$

Both are imposed on the particular values at the 95 % flux surface, κ_{95} and δ_{95}, respectively (see Chapter 2.3.1). The scaling for the maximum elongation was obtained by Zohm [32, 95]. The cylindrical limit of the “natural elongation” was adjusted with respect to the values of the ITER 15 MA ELMy H-mode configuration (see Figure 2.11). In general, $\kappa_{95} < 2.0$ seems to be a feasible value for a total upper limit [31]. High elongations imply higher risks for vertical displacement events (VDEs), these are instabilities based on vertical motion of the plasma [94]. The scaling for the maximum triangularity is proposed by Sauter [96]. Both scalings can be assessed and improved as soon as first equilibria for DEMO configurations are available.

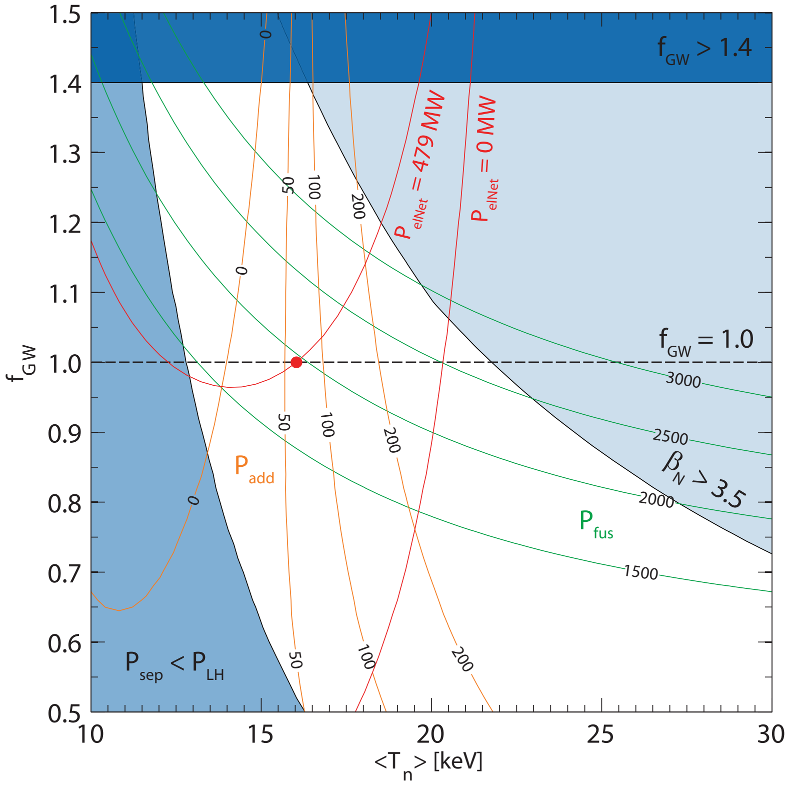

Figure 2.10.: Plasma Operation Contour (POpCon) plot based on a former configuration for DEMO 1 (see Hartmann et al. [97]). In addition to the reference operation point marked by a red dot, several operational limits are included: density limit, beta limit and H-mode threshold power.

Current Limit

In case that the flux surface labelled with $q = 2$ lies outside of the plasma, an ideal magneto-hydro-dynamic (MHD) mode becomes unstable, the $m = 2$, $n = 1$ external kink mode. This mode inevitably causes a disruption of the plasma [94]. Hence, it constitutes a hard limit for the edge safety factor, i.e.

$$q_{95} > 2.0 \tag{2.169}$$

and explains the nomenclature of this parameter. A discussion with experts [49] revealed that $q_{95} > 3.0$ includes an adequate safety margin for power plant designs and $2.3 < q_{95} < 3.0$ can be seen as a transition range for safety reasons (see Figure 2.12). Based on Equations 2.28 and 2.44, this lower limit for the safety factor represents an upper limit for the plasma current for a given toroidal magnetic field combined with a specific size and shaping of the plasma.

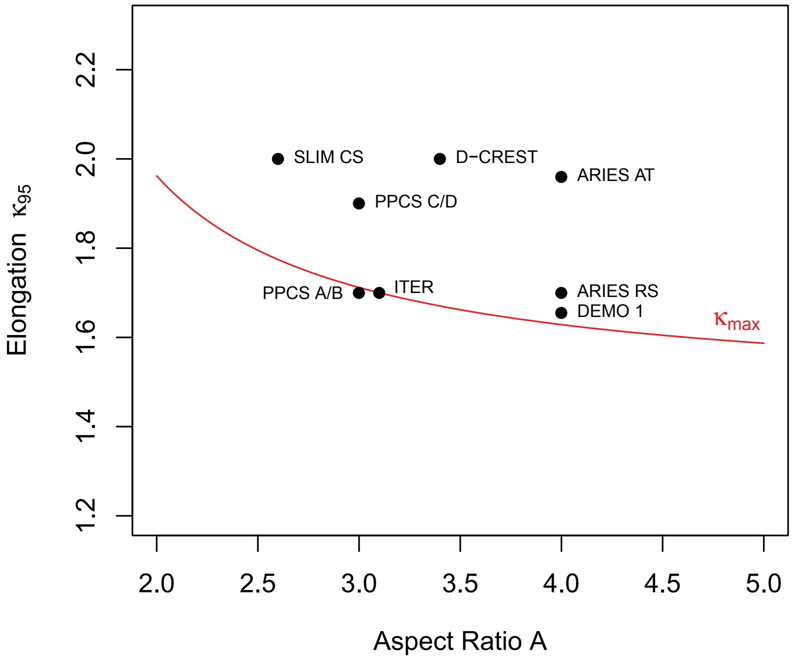

Figure 2.11.: Plasma elongation and aspect ratio of different conceptual fusion devices (except ITER). The red line is calculated with respect to Equation 2.167. The points well above the red line are "advanced physics" devices. Ref: [53, 98, 99, 100, 101, 102, 103, 104]

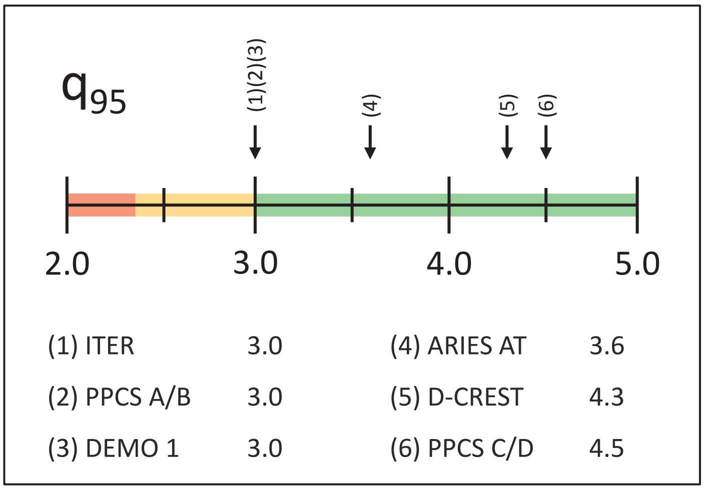

(1) ITER	3.0	(4) ARIES AT	3.6
(2) PPCS A/B	3.0	(5) D-CREST	4.3
(3) DEMO 1	3.0	(6) PPCS C/D	4.5

Figure 2.12.: Operation range for the edge safety factor. Ref: [49, 53, 98, 99, 100, 104]

Density Limit

Since bremsstrahlung and line radiation scale with n_e^2 (see Equations 2.122 and 2.127), a local increase of the electron density comes along with a strong increase of radiation leading to a temperature drop, especially in edge regions where fusion power plays only a minor role. This temperature drop can result in an enhancement of radiation due to negative derivatives of the radiative power loss functions for certain temperature ranges (see Figure 2.8). Hence, the plasma is locally cooled down further. This self-amplified process is the basic principle for thermal instabilities of the plasma like multifaceted asymmetric radiation from the edge (MARFE). The onset of these instabilities is sequentially connected with the detachment of the divertor, a degradation of confinement, changes in edge-localized mode (ELM) activity, the transition from high confinement mode (H-mode) to low confinement mode (L-mode), increased MHD activity and can finally cause major disruptions [105]. Thus, the electron density is limited in tokamaks based on these thermal instabilities. It was experimentally observed that these density limits follow a specific pattern. This can be described by the so-called Greenwald density that is empirically derived by Greenwald et al. [106] considering the minimum of the Murakami, Hugill, Granetz and fuelling limits,

$$n_{GW} = \frac{I_p}{\pi a^2} \tag{2.170}$$

Originally, it was assumed based on experimental observations that the Greenwald density constitutes an upper limit for the line-averaged electron density. That is a standard parameter for measurements with diagnostics. Thus, the corresponding Greenwald density fraction,

$$f_{GW} = \frac{\overline{n}_e}{n_{GW}} \tag{2.171}$$

seemed to be suited for an evaluation of the plasma density. But in the meantime, discharges with peaked density profiles based on central fuelling by pellets or modified particle transport at low collisionality showed that this empirical limit can be exceeded routinely without causing instabilities (see Figure A.5). Hence, the hypothesis was developed that the density limit is not a global phenomenon that can be described by global quantities like $\overline{n}_e$ [105, 107, 108]. It seems to be based on physical processes that are rather located at the plasma edge. Therefore, it is proposed that the Greenwald density is compared to the electron density at the pedestal top [31, 32]. The corresponding fraction is defined by

$$f_{GWped} = \frac{n_{ePed}}{n_{GW}} \tag{2.172}$$

A workshop with experts [49] yielded that the limits for the pedestal electron density could be characterized by $f_{GWped} < 0.9$ with a transition range of $0.9 < f_{GWped} < 1.0$ for safety reasons. Moreover, the results of transport modellings and data analysis allow for the assumption that the density profiles in fusion reactors are peaked substantially due to low collisionality [109, 110]. Hence, the original Greenwald limit can be exceeded significantly reaching values of up to $f_{GW} \approx 1.5$ [32, 107]. The impacts of increased densities on a reference design for DEMO 1 are analysed in Chapter 4.4.

Beta Limit

As mentioned before, an efficient use of the magnetic field is connected with high values for the plasma beta relating the confined gas pressure to the magnetic pressure. Based on Equation 2.106 in combination with assumptions on the temperature dependence of the thermonuclear reaction rate, it can be shown that an increase of the plasma beta is directly connected with higher fusion power yields. But MHD theory predicts that there is an upper limit for the plasma beta due to MHD instabilities. This limit has later on also been observed experimentally confirming the theoretical predictions. Troyon et al. [111] and others showed that the maximal plasma beta scales with I_p/aB_t (see Figure A.6). This semi-empirical scaling takes into account ideal MHD instabilities, ballooning modes and the Mercier criterion [94, 112]. Hence, a so-called normalized plasma beta can be defined in order to quantify this limit,

$$\beta_N = \beta_t \bigg/ \left(\frac{I_p}{aB_t}\right) \tag{2.173}$$

where the total toroidal plasma beta is used explicitly to account for the additional contribution of fast particles to the gas pressure (see Equation 2.154). This assumption seems to be valid at least for the contribution of the fast alpha particles due to their isotropic distribution [32]. For comparison, the thermal normalized plasma beta is given by

$$\beta_{N,th} = \beta_{t,th} \bigg/ \left(\frac{I_p}{aB_t}\right) \tag{2.174}$$

Based on Equation 2.150, both are simply connected by $\beta_N = \left(1+\gamma_{fast}\right)\beta_{N,th}$. Moreover, with respect to the original definition, one notices that $\left\langle B_t^2 \right\rangle \approx B_t^2$ is implicitly assumed. In case of tight aspect ratios, this assumption should be re-evaluated [96]. For monotonic q-profiles, theoretical and experimental observations give rise to the assumption that the limit on the total normalized plasma beta seems to scale linear with the internal inductance including a characteristic proportionality constant [113],

$$\beta_{N,max} = 4l_i \tag{2.175}$$

In addition, it was found that the maximum achievable plasma pressure drops, if the pressure profile exceeds a certain peaking [96]. Unfortunately, this dependency is not directly covered by the above scaling. However, this beta limit is also known as the ideal MHD limit, since it is connected with the appearance of ideal MHD instabilities. These would even exist in perfectly conducting plasmas. But there are also resistive instabilities or resistive MHD modes that can only be destabilized in plasmas with finite conductivity [94]. That includes tearing modes and neo-classical tearing modes (NTMs), for instance. These instabilities can constrain the plasma beta to even lower values compared to the ideal MHD limit [32, 94, 113]. Unfortunately, no simple criteria exist at present for these phenomena that can be included in systems codes. Moreover, there are diverse measures to stabilize MHD modes. Even for the ideal limit, a conducting wall can help to access higher plasma performance in terms of the plasma beta. But due to finite resistivity of the wall, resistive wall modes (RWMs) can then be destabilized [32]. For the time being, the ideal beta limit is included in TREND as a rule of thumb for MHD stability. As soon as further stability criteria are available, these should be implemented in order to improve self-consistency of the solutions.

H-mode Threshold

In the 1980s, a regime with increased confinement for energy and particles was observed in ASDEX [114]. It is called the high confinement mode (H-mode), compared to the standard regime with lower confinement, the L-mode. The H-mode is a plasma state with a transport barrier at the plasma edge based on reduced turbulence in this region leading to steep edge gradients in temperature, density and pressure. This edge transport barrier is violated quasi-periodically by so-called edge-localized modes (ELMs). These are instabilities that lead to cyclic relaxations of the profile gradients and expel particles and energy from the core plasma into the SOL. However, the confinement in H-mode in terms of confinement times is about twice as high as in L-mode. Therefore, the H-mode is currently the favoured scenario for fusion devices, at least for conventional configurations. When the applied heating power to magnetically confined plasmas exceeds a certain level, it is experimentally observed that the plasma undergoes a transition from L-mode to H-mode. Since the physical processes that are in charge for the existence of the edge transport barrier are not yet fully understood, only scalings on crucial machine parameters exist for this so-called L-mode to H-mode threshold power. The current scaling for ITER is given by Martin et al. [115],

$$P_{LH} = 0.0976 M^{-1} \overline{n}_e^{0.717} B_t^{0.803} S^{0.941} \tag{2.176}$$

where an inverse proportionality on the ion mass number M is included in order to consider the fact that the original scaling was developed mainly with data from deuterium discharges [19, 98, 115]. In present day experiments, the total heating power is compared to P_{LH}. But the working hypothesis, supported by experimental observations, is that the power transported across the separatrix is the figure of merit that has to be higher than the threshold power [98]. For present day experiments, there is often hardly any difference between P_{add} and P_{sep} based on the smallness of internal power gains and radiation losses. Hence, the state of the plasma with respect to the quality of confinement can be evaluated by

$$f_{LH} = \frac{P_{sep}}{P_{LH}} \tag{2.177}$$

where $f_{LH} > 1.0$ characterizes the requirement for H-mode. The opinions among experts [49] differ about the precise value and the limits for f_{LH}. On the one side, if H-mode is reached once, a hysteresis is observed in present day experiments, i.e. the back-transition to L-mode occurs at lower heating powers than characterized by P_{LH}. On the other side, the uncertainties for the determination of the threshold power are significantly large. Moreover, good confinement is often observed only for heating powers well above P_{LH}. Thus, operations points with $f_{LH} > 1.3$ are recommended for DEMO including a transition range of $1.0 < f_{LH} < 1.3$ [32, 49].

Power Exhaust in the Core Plasma

The reduction of impurities in the plasma core in order to get preferably "pure" plasmas seems to be helpful to limit the heat losses, especially by radiation. Moreover, plasmas with low fuel dilution promise high performance with respect to fusion power. But operation points with comparable low impurity content also pass major parts of the total heating power by means of energy and particles to the SOL and divertor region. Considering the severe constraints imposed by the technical specifications of the divertor plates (see next section), each measure reducing the power that enters this region is gladly accepted. Therefore, one idea is to modify the split of the total heating power into transport and radiation losses by seeding impurities with high radiation potentials such as noble gases (see Chapter 2.3.4 and Figure 2.8). Radiation distributes the heating power over a much wider effective area, the complete first wall, compared to the wetted area of the divertor plates that is in charge of the transport losses. However, radiation in the core and mantle regions cannot be increased arbitrarily to reduce the power transported across the separatrix [116]. In case that H-mode is the selected operation regime, the transport losses are limited by the H-mode threshold power, as mentioned above. Moreover, high radiation in the confined plasma, measured in terms of the radiation fraction, can lead to degradation of the confinement and radiation instabilities. In summary, f_{LH} and f_{rad} seem to be key indicators for systems codes in order to assess the power exhaust in plasma core and mantle regions.

2.4. Divertor Module

The divertor is a power plant component of high importance, since it provides a major interface between the core plasma and the surrounding wall. The material properties of the latter impose an upper limit for the peak power flux hitting the divertor plates. At present, a steady-state value of 5 MW/m^2 is under discussion for DEMO [32]. As mentioned before, that also limits the power flux entering the divertor region from the core plasma. Hence, a divertor module should at least allow to link the transport losses of the confined plasma to the power loads on the target plates. In addition, it should also provide the plasma conditions for this region and consider material erosion enabling an assessment of the divertor lifetime including maintenance needs. The modellings of the divertor as implemented in PROCESS and HELIOS have recently been reviewed to assess the reliability of their results. It seems that their predictive capability is limited and that no near-term improvement is available [23]. Due to the high importance of this component for systems code studies, I decided to implement at least a simple divertor module in TREND until reliable modellings are available. This module is based on the US systems code ASC [21, 117] and allows a rule of thumb estimate for the peak power flux on the target plates for single-null configurations. The basic idea is to classify the total power flux into radiative and conductive loss channels and to bring them into relation with approximations for the effective target areas.

As mentioned above, the power that has to be handled by the divertor is P_{sep}, the power crossing the separatrix in terms of energy and charged particles. It is assumed that major parts of P_{sep} leave the plasma at the low-field-side midplane region. After escaping the confined plasma region due to cross-field transport, these particles are still tied to the magnetic field lines guiding them in a thin layer directly to the target plates. In principle, these are split up into one part flowing to the inboard and one to the outboard divertor plates. That is quantified by the geometrical factor $f_{outboard}$ usually assumed to be about 66 %, i.e. a power distribution of 2:1 in favour of the outboard plates. On the way to the target, the particles can lose energy by radiation. The precise calculation of the achievable amount of radiation is challenging, especially with simplified models. Therefore, the so-called radiated power fraction f_{divRad} is defined that allows to distinguish between radiated and conducted power to the divertor, i.e.

$$P_{divRad} = f_{divRad} \cdot P_{sep} \tag{2.178}$$

$$P_{divCon} = (1 - f_{divRad}) \cdot P_{sep} \tag{2.179}$$

In general, high levels of impurity concentration based on additional seeding are attended by high radiation fractions. But the achievable levels are limited by thermal instabilities and the influences on the core plasma are still part of current research [23, 118].

The next step is the approximation of the effective areas over which the particular power is spread. These areas are modelled by skin surfaces of a straight cylinder. As indicated in Figure A.7, the radial location of the outboard divertor plates is assumed to be $r_{outb} \approx R_0 - a/2$ and that of the inboard plates $r_{inb} \approx R_0 - a$. Hence, the total surface area of the outboard and inboard divertor can be calculated by

$$A_{rad}^{outb} = 2\pi (R_0 - a/2) \cdot 2 \cdot a/2 \tag{2.180}$$

$$A_{rad}^{inb} = 2\pi (R_0 - a) \cdot 2 \cdot a/4 \tag{2.181}$$

where a factor of two accounts for two divertor legs each. The length of these legs is simply estimated by $l_{outb} \approx a/2$ and $l_{inb} \approx a/4$ for the outboard and inboard side, respectively. It is assumed that the radiative part of P_{sep} is spread uniformly over the whole surface area in the outboard and inboard divertor regions. The remaining part of P_{sep} is conducted inevitably in a thin layer to the divertor plates. The thickness of this layer is characterized by the power decay length. For this parameter different definitions exist. First, the power decay length at the outboard midplane is called λ_q and can be calculated with a recent scaling by Eich et al. [119],

$$\lambda_q = 0.73 B_t^{-0.78} q_{cyl}^{1.20} P_{sep}^{0.10} R_0^{0.02} \tag{2.182}$$

The specific value of λ_q reflects the competition between parallel and perpendicular heat transport. It is assumed in TREND that λ_q is similar for the outboard and inboard side, even if the scaling was obtained by analysing measurements of heat flux profiles on the outboard divertor plates detected with infrared thermography [119]. More important for the calculation of the peak heat load on the divertor plates is the so-called integral power decay length, λ_{int}, since it relates the peak heat load to the deposited power. Eich et al. [119] derived a linear scaling as follows,

$$\lambda_{int} = \left(1.3\lambda_q + 1.4\right) \tag{2.183}$$

In order to draw conclusions on the values of λ_{int} at the midplane from target measurements, the expansion of the magnetic flux has to be considered [119]. For conventional divertors, the magnetic flux expansion can be a factor of about 5 [32]. Moreover, the above scalings for λ_{int} and λ_q were obtained with data of H-mode discharges with low density, minimal gas puffing and for attached divertor conditions [119]. But for DEMO and future power plants, there is some evidence that these devices will operate at high density, with controlled impurity seeding leading to (partial) detachment of the plasma at the target plates. This will amplify the widening of the power decay length with respect to the original scaling by a factor of about 2-3 due to additional radial transport [32, 120]. Hence, a total expansion factor of $f_{exp} \approx 10 - 15$ can be assumed for the power decay length of DEMO and beyond taking into account both effects, the magnetic flux expansion and the widening based on enhanced radial transport. The optimization of the inclination of the plates could contribute additionally. However, this discussion corresponds to conventional divertor designs. In case that newly developed divertor concepts like snowflake [121] or super-X [122] are considered, the total expansion factor has to be adjusted. The effective or "wetted" areas for transport losses are consequently given by

$$A_{con}^{outb} = 2\pi\,(R_0 - a/2)\, f_{exp}\lambda_{int}\,[\mathrm{m}] \tag{2.184}$$

$$A_{con}^{inb} = 2\pi\,(R_0 - a)\, f_{exp}\lambda_{int}\,[\mathrm{m}] \tag{2.185}$$

For comparison, Table 2.7 lists values for the different effective areas obtained for the conditions of a reference parameter set for DEMO 1. It can be seen that the areas corresponding to conduction and radiation differ substantially indicating the advantage of transformations of conductive into radiative power.

Parameter	Unit	TREND
A_{con}^{inb}	[m^2]	1.7
A_{con}^{outb}	[m^2]	1.9
A_{rad}^{inb}	[m^2]	47.7
A_{rad}^{outb}	[m^2]	111.3

Table 2.7.: Comparison of effective areas on outboard and inboard side for conductive and radiative power flows in the divertor region.

The peak power loads on the target plates can finally be estimated by summing up the conductive and radiative contributions in terms of power divided by the corresponding effective area. This means for outboard and inboard side,

$$q_{peak}^{outb} = f_{outboard}\left(\frac{1 - f_{divRad}}{A_{con}^{outb}} + \frac{f_{divRad}}{A_{rad}^{outb}}\right) P_{sep} \tag{2.186}$$

$$q_{peak}^{inb} = (1 - f_{outboard})\left(\frac{1 - f_{divRad}}{A_{con}^{inb}} + \frac{f_{divRad}}{A_{rad}^{inb}}\right) P_{sep} \tag{2.187}$$

The dependence of the peak power load on the outboard divertor plates with respect to the radiation in the divertor region is visualized in Figure 2.13. In this case study, the radiative and conductive contributions are shown for different radiation fractions beginning with 80 % based on a reference operation point for DEMO 1 with a fixed power entering the divertor region. Clearly, the contribution by radiation only slightly increases for higher radiation fractions. Whereas a strong dependency can be determined for the transport contribution. Thus, high radiation fractions are necessary in DEMO requiring additional impurity seeding, since the radiated power scales linearly with the impurity concentration (see Equation 2.127). Recently, a procedure called double radiative feedback was developed and successfully proved in ASDEX Upgrade optimizing the power exhaust of the whole device [118]. The core radiation is controlled by seeded argon and the radiation in divertor region by seeded nitrogen. Hence, each impurity can contribute with its superiority concerning the radiative capability in regions with corresponding temperature levels. This procedure should be developed further considering particularly DEMO-relevant diagnostics [13]. Upper limits for radiation in the divertor are given by the risk of thermal instabilities able to cause disruptions. Moreover, the impact of extensive seeding on the core plasma performance should be assessed comprehensively.

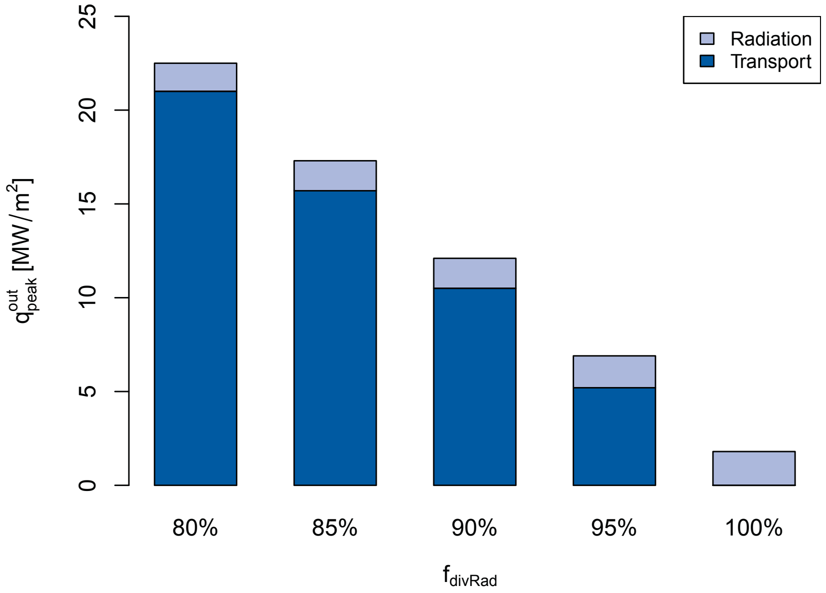

Figure 2.13.: Contributions to the peak power load on the outboard divertor plates based on radiation and transport for different radiation fractions with respect to a reference operation point for DEMO 1.

Finally, further work on a proper module for the divertor is seen to be absolutely necessary, since the limit of the peak power load on the divertor plates imposed by technology and material properties is a key driver for the design of DEMO or future power plants. Therefore, a reliable modelling in systems codes is crucial. In the current module of TREND, the specific design of the divertor and the foreseen operation conditions are represented basically by two parameters, the expansion factor f_{exp} and the divertor radiation fraction f_{divRad}. Both constitute in conjunction with the key indicators for the power exhaust of the plasma core and mantle, f_{rad} and f_{LH}, an exclusive set characterizing the whole power exhaust of the plasma.

Based on Equation 2.186 and the discussion above, the power crossing the separatrix P_{sep} can be seen as a key parameter for the power exhaust. The corresponding effective area scales in first order linearly with the machine size in terms of the major radius R_0, since no significant size scaling of the power decay length was observed in a recent study by Eich et al. [119]. Hence, the evaluation of P_{sep}/R_0 constitutes a 0-dimensional criterion for the assessment of the power loads that must be handled by the divertor [123]. Due to the current uncertainties of more sophisticated divertor modellings, this quotient can be seen as a key indicator for present studies. The value of the current reference design of DEMO 1, $P_{sep}/R_0 \approx 34\,\mathrm{MW/m}$, is far more than what is presently achieved in ASDEX Upgrade with $P_{sep}/R_0 \approx 7\,\mathrm{MW/m}$ [118]. But it is assumed that after upgrades of the heating systems even higher values can be demonstrated up to ITER values of $P_{sep}/R_0 \approx 15\,\mathrm{MW/m}$ and beyond [118]. Moreover, the core and mantle radiation of the present operation point for DEMO 1 is not yet optimized, $f_{LH} = 2.16$ and $f_{rad} = 0.34$. Hence, there seems to be some space for reductions of the power crossing the separatrix. In line with this discussion, there are generally two ways to facilitate the problems for the divertor.

The first is to increase the size of the machine. The second is to reduce the transport losses by increasing core and mantle radiation for a given heating power while keeping the L-H threshold power in mind (see Equation 2.176).

2.5. Power Flow Module

The power flows through different components of the power plant is described by the power flow module. Hence, it provides a connection of the plasma performance to the net electric power output to the grid. The latter is often defined as a target parameter for conceptual plant designs. For earlier DEMO concepts, about 1 GW of net electric power was chosen [9]. Figure 2.14 gives a schematic overview on the power flow module of TREND. The development of this module is based on Zohm [9] with improvements taking into account the modelling of PROCESS [26], HELIOS [19] and ASC [21], as well as recommendations of a recent concept study, HCLL-DEMO-2007 [124], and the preliminary version of the DEMO Technology Design Guidelines [24].

In general, three different regions can be distinguished, the plasma, the power conversion cycle and the power requirements and consumptions of the reactor itself. All plasma parameters are provided by the physics module (see Chapter 2.3) including the fusion power P_{fus} as one of the key parameters for the power flow. The energy due to fusion reactions is released in terms of kinetic energy of the reaction products with respect to the inverse mass ratio reflecting the energy and momentum conservation. The neutrons ($P_{neutron}$), not trapped by the magnetic field, leave the plasma and deposit their energy on the surrounding structures, i.e. first wall, blanket and shielding. The alpha particles (P_{α}) heat the plasma in combination with external heating systems (P_{add}). This total heating power, P_{heat}, is also transmitted to the surrounding structures via two major loss channels, radiation and transport (see Chapter 2.3.4).

The interface of the plasma to the power conversion cycle is constituted of blanket and divertor. Here, the term “blanket” includes also first wall, shielding and support structures. Hence, the power originating from the plasma and being deposited on the blanket P_{blkt} is composed of a certain fraction of the neutron power and the power of the radiation loss channel. This fraction, characterized by $f_{geoBlkt}$, incorporates geometrical assumptions on the surface area covered by the blanket and spatial distributions of the sources, i.e.

$$P_{blkt} = f_{geoBlkt} \left(f_{nMult} P_{neutron} + P_{rad} \right) \tag{2.188}$$

The blanket contains materials for tritium breeding and neutron multiplication, designed with the objective to reach a tritium breeding ratio (TBR) of more than one. This is an inevitable requirement for the tritium self-sufficiency of fusion reactors, since a certain amount of tritium losses has to be compensated. As a consequence, the source neutron power deposited in the blanket is increased due to nuclear heat of the involved reactions by a specific factor, f_{nMult}, that depends on the particular design of the blanket.

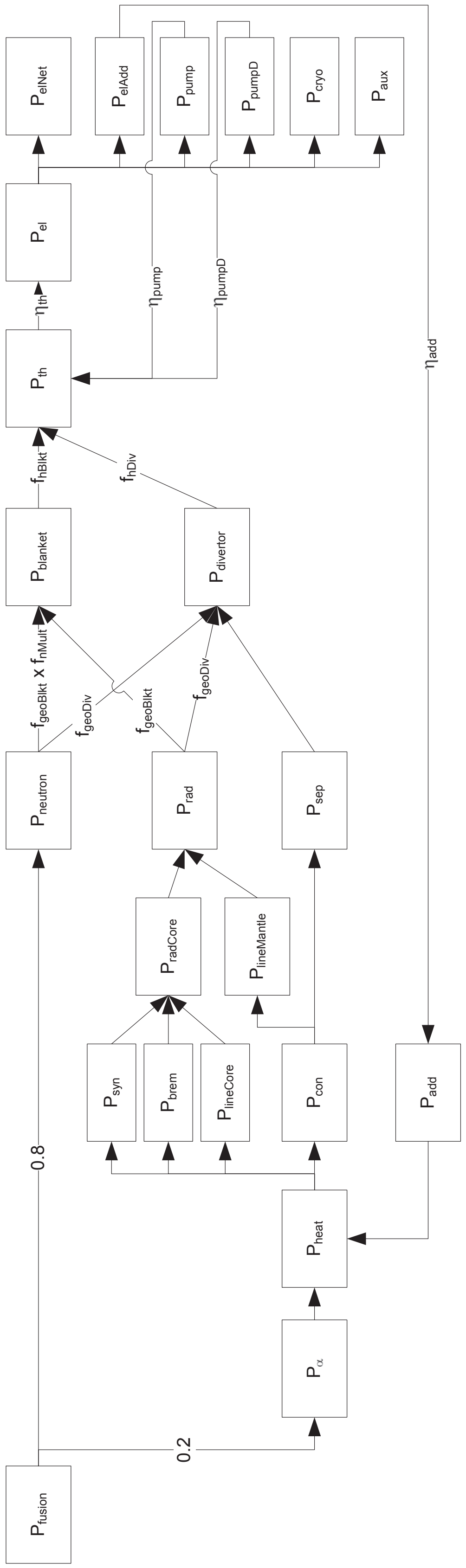

Figure 2.14.: Scheme of the power flow module of TREND.

Similar considerations are engaged for the power deposited on the divertor P_{div} by neutrons and radiation with respect to a geometrical factor f_{geoDiv}. In contrast to the modelling of other systems code, TREND does not assume that the neutron power entering the divertor is increased similar to the blanket, since no material for tritium breeding and neutron multiplication will be integrated. It seems that the requirements due to high localized heat loads are challenging enough for this component. These heat loads base on transport losses across the separatrix in terms of energy and charged particles. Those are subsequently directed along the magnetic field lines to the divertor plates. On the way, parts of the energy can be spread over the whole divertor area by radiation (see Chapter 2.4). Hence, the power deposited on the divertor P_{div} is given by

$$P_{div} = P_{sep} + f_{geoDiv} \left(P_{neutron} + P_{rad} \right) \tag{2.189}$$

The geometrical fractions for blanket and divertor, $f_{geoBlkt}$ and f_{geoDiv}, respectively, do not necessarily add up to unity. That arises from the fact that not all of the surface area is covered by blanket and divertor due to the requirements of diagnostics and H&CD systems. Obviously, this fraction should be minimized as far as possible to maximize the power output and the TBR. Hence, just a small fraction of available diagnostic systems used to control these days experiments can be integrated in DEMO or fusion power plants [125]. Moreover, the number of available diagnostic systems also reduces considering the high heat and neutron fluxes under reactor relevant conditions [13].

The thermal power P_{th} that can be converted into electric power is called high-grade or primary heat. The power originating from the plasma heats components like blanket and divertor. These are passed through by coolants that are heated up to high temperatures. Additionally, the power to pump the coolants through the particular circuit can also contribute to the high-grade heat of the whole system, i.e. P_{pump} for the blanket and P_{pumpD} for the divertor. The losses in the cooling loops are taken into account by corresponding efficiencies. Thus, the total high-grade thermal power is given by

$$P_{th} = f_{hBlkt} P_{blkt} + f_{hDiv} P_{div} + \eta_{pump} P_{pump} + \eta_{pumpD} P_{pumpD} \tag{2.190}$$

The factors f_{hBlkt} and f_{hDiv} allow for the fact that not all of the power deposited in the blanket or the divertor can be used as high-grade heat due to losses in structures being cooled at lower temperatures or not connected to the heat conversion cycle. This includes low-temperature shields or support structures, for instance. The corresponding power is called low-grade heat or secondary heat. That is not treated explicitly by TREND, since a direct conversion to electricity is not reasonable. But it seems that low-grade heat can be used to increase the conversion efficiency of the plant [24]. The distinction in separate pumping powers for the blanket and the divertor with individual efficiencies, as well as the application of the separate factors for high-grade heat for each, f_{hBlkt} and f_{hDiv}, allows to design cooling concepts with different fluids. Consequently, it is possible to consider reactor designs with helium cooling at high temperatures for the blanket and water cooling at low temperatures for the divertor.

The conversion of high-grade thermal power into electric power is modelled by just one parameter, the thermodynamic efficiency η_{th}. Hence, the gross electric power can be estimated by

$$P_{el} = \eta_{th} P_{th} \tag{2.191}$$

At present, the dependency of η_{th} on the particular design of the conversion cycle including heat-exchangers, turbines, condensers and pumps, the cooling fluids and corresponding temperature and pressure levels is assessed outside the systems codes. But there is work in progress in collaboration with different experts on this field to improve the modelling of the power conversion. The idea of this activity is to develop a sophisticated simulation for the power conversion of fusion power plants with established software tools like the energy-balance-model ENBIPRO that is widely applied to simulate conventional and renewable power plants (see [126, 127, 128, 129, 130, 131] and references therein). The results of such analyses can then be parametrized and implemented in the power flow modules of systems codes.

Since fusion reactors demand a substantial amount of electricity for the operation, the value of the electric power delivered to the grid is obtained by subtracting this recirculating electric power P_{elRec} from the generated gross electricity P_{el}. Therefore, the so-called net electric power P_{elNet} of the reactor is

$$P_{elNet} = P_{el} - P_{elRec} \tag{2.192}$$

Hence, the total efficiency of the power plant is usually defined by relating the net electric power to the fusion power,

$$\eta_{tot} = \frac{P_{elNet}}{P_{fus}} \tag{2.193}$$

summarizing several parameters of informative value for the reactor like the thermal efficiency. That includes also the so-called recirculating power fraction that is given by

$$f_{rec} = \frac{P_{elRec}}{P_{el}} \tag{2.194}$$

This parameter describes the electricity demand of the power plant itself compared to the gross electricity generation. The former consists of all requirements on electricity for several systems, i.e.

$$P_{elRec} = P_{elAdd} + P_{pump} + P_{pumpD} + P_{cryo} + P_{aux} \tag{2.195}$$

Accordingly, TREND discriminates electric power for the additional H&CD systems P_{elAdd}, for the coolant pumps of blanket P_{pump} and divertor P_{pumpD}, as well as for the cryo system P_{cryo}. Other demands for electricity are consolidated as auxiliary electric power P_{aux} including the power supply for the magnets or the diagnostics, for instance. Except for the needs of the plasma heating systems, it is assumed for simplicity that the electric power consumption of the other systems scale in first order with the total thermal power and consequently with the gross electric power of the plant (see [19]),

$$P_{pump} = f_{pump} P_{el} \tag{2.196}$$

$$P_{pumpD} = f_{pumpD} P_{el} \tag{2.197}$$

$$P_{cryo} = f_{cryo} P_{el} \tag{2.198}$$

$$P_{aux} = f_{aux} P_{el} \tag{2.199}$$

The requirements on electric power for the additional H&CD systems are related to the heating power P_{add} that is injected in the plasma via

$$P_{add} = \eta_{add} P_{elAdd} \tag{2.200}$$

where η_{add} is the so-called wall plug efficiency describing quantitatively the conversion of electricity into useful heating power. As mentioned before, that should be one of the fundamental outputs of comprehensive H&CD modules. For more information on H&CD systems, the reader is referred to page 33 and the following.

Recent reactor studies in the EU resulted in a concept called HCLL-DEMO-2007 with respect to the helium cooled lithium lead (HCLL) breeding blanket concept [124]. That is one of the promising concepts for European DEMO reactors. Based on this study, input parameters for the power flow module of TREND are calculated (see Table 2.8).

Parameter	Value
f_{nMult}	1.18
$f_{geoBlkt}$	0.91
f_{geoDiv}	0.06
f_{hBlkt}	0.95
f_{hDiv}	1.00
η_{th}	0.44
η_{add}	0.60

Parameter	Value
f_{pump}	0.185
f_{pumpD}	0.028
f_{cryo}	0.017
f_{aux}	0.007
η_{pump}	0.91
η_{pumpD}	0.91

Table 2.8.: Parameters for the power flow module of TREND based on the HCLL-DEMO-2007 reactor as shown in Figure A.8. Ref: [124]

The present version of the power flow module is just able to consider the power flows through the reactor without any time dependence. Therefore, only analysis of power flows during the so-called "burn" phase is possible (see Figure 2.15 for the definition of dynamic phases). It is desirable to implement similar approaches also for the other phases by one evaluation point per phase. This would allow for instance to assess the power plant needs on electricity in the current-ramp, heating and burn termination, as well as pump and recharge phases. Moreover, it seems to be promising to analyse the integration of heat storages in the heat conversion system with the objective to equalize the dynamic supply and needs of the plant on electricity to and from the grid. Here, work done for solar thermal power plants that use salt or concrete storages for exactly that purpose could be considered. In addition, the dynamic heat loads on the different materials and structures should be assessed for life-time approximations. There is work in progress in collaboration with the Technical University of Munich on these particular topics. It is hoped that these efforts lead to improvements of the power flow modelling in TREND.

2.6. Technology Module

The technology module summarizes different modellings of technological power plant systems that are not described by individual modules. That includes the description of the dynamical phases in terms of particular time-scales, the magnet systems and the life-time of the first wall.

Dynamical phases

Figure 2.15 shows schematically the distinction in different phases of the power plant operation. In principle, that is valid for pulsed as well as for steady state devices, since for the latter also phases without power production have to be considered, for instance due to maintenance. The difference of both concepts concerning this framework is the length of the so-called burn phase that is the actual operation mode for power production. For steady-state devices, there is no inherent limitation due to the fact that no current-drive by inductive means is applied in this phase. Whereas for pulsed machines, the burn time depends strongly on the design of the inductive current-drive system. At present, time-scales between about two and ten hours are under discussion for pulsed DEMO concepts [15, 132]. For fusion power plants, rather ten or more hours of operation are targeted. In the following, the discussion of the dynamical phases is oriented mainly on pulsed concepts.

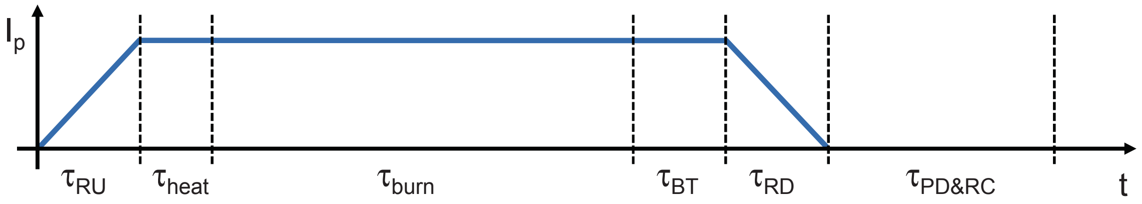

Figure 2.15.: Scheme of the dynamical phases of pulsed devices. For a description of the particular phases see Table 2.9.

Since the operation of fusion reactors is generally periodical, the starting point for one pulse can be selected arbitrarily. The modelling of TREND is schematically shown in Figure 2.15. In the first period of one pulse, the plasma current is ramped up to its target value of the operation point. The assigned time-scale τ_{RU} is calculated in the physics module (see Equation 2.87).

Parameter	Description
τ_{RU}	Plasma current ramp-up
τ_{heat}	Initial plasma heating
τ_{burn}	Burn phase (generation of power)
τ_{BT}	Burn termination
τ_{RD}	Plasma current ramp-down
$\tau_{PD\&RC}$	Pump-down and recharge of the CS

Table 2.9.: Dynamical phases of pulsed devices.

After that, the plasma is heated to establish the operation conditions foreseen for power generation including the build-up of the thermal plasma energy W_{th}. It is assumed that major drivers for the assigned processes are similar to those responsible for the reverse operation, the decrease of the stored plasma energy. Due to the lack of detailed understanding of the physical processes, the global energy confinement time τ_E was introduced to describe the decrease of W_{th} with respect to transport losses as discussed in the corresponding paragraph of Chapter 2.3.4. Hence, the time-span to build up the particular amount of stored energy by heating the plasma is assumed to scale linearly with the confinement time, i.e.

$$\tau_{heat} \propto \tau_E \qquad \Rightarrow \qquad \tau_{heat} = c_{heat} \cdot \tau_E \tag{2.201}$$

where values of $c_{heat} \approx 5$ seem to be a reasonable starting point for the proportionality constant [49]. When the conditions corresponding to the target operation point are established, the so-called burn phase starts. That is technically dedicated to produce (net) electricity based on fusion reactions. This phase is simply characterized by the timespan for the current flat-top τ_{flat} that calculated in the physics module (see Equation 2.78) reduced by requirements on time for initial plasma heating and burn termination,

$$\tau_{burn} = \tau_{flat} - \tau_{heat} - \tau_{BT} \tag{2.202}$$

During the burn termination phase, the plasma is prepared to allow a safe and controlled ramp-down of the plasma current without severe events like disruptions. That includes a decrease of the plasma density, for instance. Hence, a key driver for the assigned time-scale is assumed to be the global particle confinement time, analogue to the discussion above on the energy confinement time for the heating phase. Thus,

$$\tau_{BT} \propto \tau_p^* \qquad \Rightarrow \qquad \tau_{BT} = c_{BT} \cdot \tau_p^* \tag{2.203}$$

$$\Rightarrow \qquad \tau_{BT} = f_{P2E} \cdot \tau_{heat} \tag{2.204}$$

where $c_{BT} \approx c_{heat}$ is assumed. The ratio of the global particle to energy confinement time, f_{P2E}, is defined in Equation 2.166 of the physics module. The time-scale for the following ramp-down of the plasma current is assumed to be similar to the time requirements in the current ramp-up phase, i.e.

$$\tau_{RD} \approx \tau_{RU} \tag{2.205}$$

Subsequently, there is a period where the power plant is reinitialized for the next pulse. That includes the recharge of the central solenoid (CS), for instance. The time-scale for this process is defined by two times the stored energy of the CS divided by the power applied for the recharge in [W],

$$\tau_{RC} = \frac{2E_{CS}}{P_{RC}} \tag{2.206}$$

The factor two results from the dynamic operation of the CS as shown in Figure 2.16. As mentioned before, TREND assumes that one cycle starts with the ramp-up of the plasma current. This implies that the CS is pre-magnetized at that point in time, i.e. a certain amount of current is flowing through the coils. That shall be called the “maximum” current with respect to the specific direction. The current is then decreased resulting in a reduction of the magnetic field and consequently a change of the magnetic flux. Based on the Maxwell-Faraday equation, that causes an electric field in a specific direction leading to an inductively driven current in the conducting plasma (see Chapter 2.3.2). After crossing the zero point, this process is maintained until a “minimum” point for the current in the CS coils is reached. In principle, that could be the starting point for the next plasma pulse, but the induced electric field and consequently the plasma current would have the opposite direction. Unfortunately, the tilt angle of the divertor plates can only be optimized for one current direction. Hence, this precludes the productive use of the second part of the CS cycle unless other concepts are considered. Examples could be tilting divertor plates or a second divertor at the top that is optimized for the other current direction. These concepts are attended by major engineering challenges and are therefore not promising for the future.

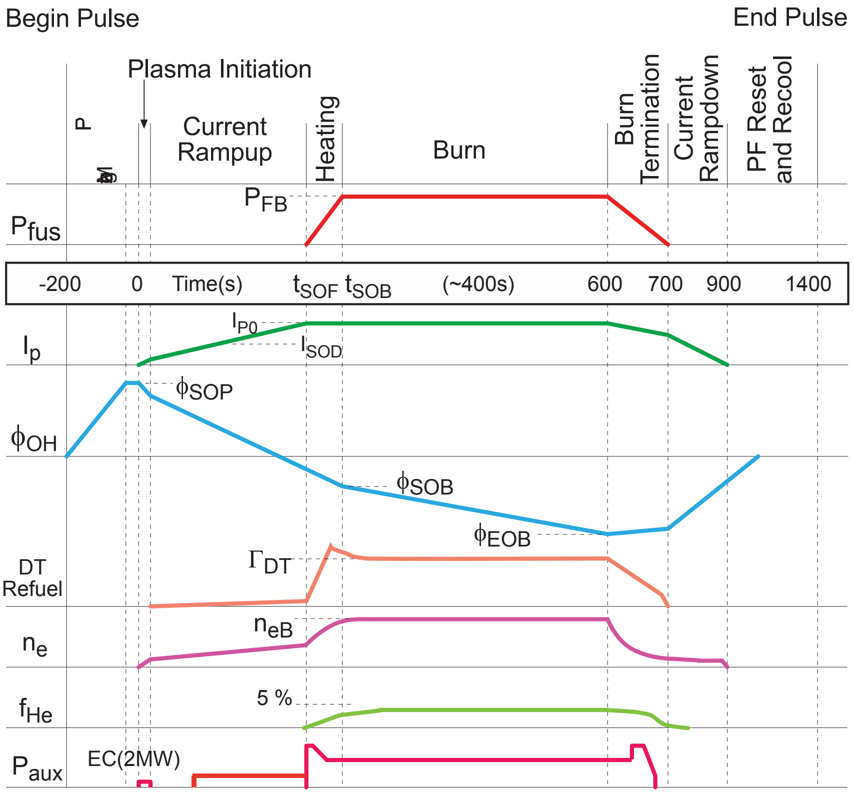

Figure 2.16.: Schematic of the ITER 15 MA inductive scenario. The corresponding time-scales are: 70 s-100 s for current ramp-up, $\approx$ 50 s for heating, 300 s-500 s for burn phase, 200 s-300 s for shutdown. A typical time-scale for pulse repetition is $\approx$ 1800 s. Ref: [133]

Assuming that the level of the "maximum" and "minimum" current points are similar, two times the corresponding energy has to be supplied to reach the initial pre-magnetized position again. This energy can be estimated by

$$E_{CS} = \int \frac{B^2_{CSmax}}{2\mu_0}\,\mathrm{d}V \approx \frac{B^2_{CSmax}}{\mu_0}\pi R^2_{CSe}\kappa_X a \tag{2.207}$$

where the volume of the CS is assumed to be $\pi R^2_{CSe} \cdot 2\kappa_X a$. The corresponding time-scale for this phase, τ_{RC}, cannot be chosen arbitrarily. It is limited by the available amount of electric power P_{RC} and the maximum for the induced loop voltage to prevent a plasma break-down in this period [132]. Therefore, high vacuum conditions are mandatory during the recharge. This can be achieved by pumping the remaining fuel, the fusion ash and other particles out of the plasma vessel. The assigned time-scale for a complete pump-down is estimated to be about [132],

$$\tau_{pump} \approx 20\,\text{min} \tag{2.208}$$

Unfortunately, no dependencies on the volume of the plasma vessel, the particle content at the beginning of the conditioning or the characteristics of the available pumping systems are included at present. There are ideas to overlap the pump-down and the recharge phases to minimize economically unattractive intervals. These ideas are supported by the application of magnetic fields to prevent a break-down [134]. In order to take an overlap into account, the requirements on time of each process is calculated individually in TREND. The time-scale for the whole process, $\tau_{PD\&RC}$, can then be estimated by a comparison of both contributions. Nonetheless, certain vacuum conditions should exist for safety reasons, before the recharge of the CS could be started [134]. Hence, about 25 % of the pump-down time requirements are reserved and not available for a potential overlap, i.e.

$$\tau_{PD\&RC} = 0.25\tau_{PD} + \max\left(0.75\tau_{PD}, \tau_{RC}\right) \tag{2.209}$$

Thus, the down time, defined as that interval where no significant fusion reactions are recorded, is given by the sum of the following “unproductive” but necessary phases,

$$\tau_{down} = \tau_{RU} + \tau_{heat} + \tau_{BT} + \tau_{RD} + \tau_{PD\&RC} \tag{2.210}$$

Therefore, the time-scale for one complete cycle can be estimated by

$$\tau_{cycle} = \tau_{burn} + \tau_{down} \tag{2.211}$$

Finally, the so-called “duty-cycle” reflecting the comparison of productive time-scales to the duration of the complete cycle is defined in TREND by

$$f_{DC} = \frac{\tau_{burn}}{\tau_{cycle}} \tag{2.212}$$

In general, this parameter is evaluated with respect to the total availability of the device and not just based on the down time between two pulses excluding maintenance intervals, for instance. Since the total availability is not modelled in TREND, the definition of the duty cycle should be updated after implementing specific modules.

Magnet systems

A comprehensive systems code should incorporate modules for all crucial magnet systems, the toroidal field coils (TFCs) and the poloidal field coils (PFCs) including the coils of the central solenoid (CS), since these systems have high impacts on the technological and economic performance of power plants [24, 135, 136, 137]. These modules should ideally combine information on the engineering design, coil currents and current densities, peak magnetic fields, stored energy, inductance and stresses [46]. For DEMO and fusion power plants, all crucial magnet systems are considered to base on superconducting technology. The design of the individual coils depends strongly on the choice of the specific superconducting material and the operation conditions. From physics point of view, an assessment of the maximum achievable magnetic field strength at the conductors is important (see calculation of B_t in Equation 2.56). In general, this limit is imposed for fusion applications rather by mechanical stress considerations than by the properties of the superconductor [138]. Therefore, the development of high temperature superconducting (HTS) materials is promising in that the operation conditions in terms of temperature levels will not differ significantly allowing nitrogen instead of helium cooling. But the selection of HTS materials operated at low temperatures provides the opportunity of more space for structural material leading to higher maximum field strength due to less space requirements of the conductor [138].

At present, no individual magnet modules are implemented in TREND. Only a relation of the maximum magnetic field B_{CSmax} of the CS to the average current density j_{CS} in $\left[\mathrm{A/m^2}\right]$ is considered based on Ampère's law [19],

$$B_{CSmax} = \mu_0 j_{CS} d_{CS} \tag{2.213}$$

where the radial thickness d_{CS} of the CS is provided by the geometry module (see Equation 2.6). This simple model is useful for the calculation of the available flux swing provided by the CS (see Equation 2.81). As major contributor to the flux balance, the CS coils have a high impact on the "productive" time-scales of pulsed plants, but also on the down time due to recharge requirements as discussed above. It is commonly assumed that the maximum magnetic field of the CS coils is similar to that of the TFCs with about $B_{CSmax} \approx B_{tMax} \approx 13\,\mathrm{T}$.

First wall life-time

The technology module also includes a simple model for the lift-time estimation of the first wall (FW) due to neutron irradiation. The caused damage is measured in displacement per atom (dpa) and can be calculated for each material by neutronic analysis where detailed information on damage cross sections as function of the neutron energy are used. For instance, the damage for a fusion spectrum in steel as structural material is calculated to be about 1 dpa for a fluence of $0.1\,\mathrm{MW\,a/m^2}$ and scales linearly for other fluencies [139]. This relation is used in TREND as a first approximation for the neutron damage per full-power year ND_a [dpa/a] caused by a certain neutron wall load q_{NWL}, i.e.

$$\mathrm{ND}_a = \frac{q_{NWL}}{\mathrm{ND}_{rate}} \tag{2.214}$$

where $\mathrm{ND}_{rate} \approx 0.1\,\mathrm{MW\,a/(m^2\,dpa)}$ [139]. For EUROFER, considered as a potential structural material of DEMO, the maximum acceptable neutron damage is assumed to be about $\mathrm{ND}_{max} \approx 60\,\mathrm{dpa}$ [24]. Hence, the life-time of the FW can then be estimated by

$$\tau_{FWLT} = \frac{\mathrm{ND}_{max}}{\mathrm{ND}_a} \tag{2.215}$$

Clearly, the neutron wall load is an essential driver of this simple model. It is defined by

$$q_{NWL} = \frac{P_{neutron}}{S_{FW}} \tag{2.216}$$

where the FW area, S_{FW}, can be evaluated based on Equation 2.23. In line with this definition, the heat wall load on the FW is given by

$$q_{HWL} = \frac{P_{heat}}{S_{FW}} \tag{2.217}$$

The presented modelling is basically valid for the main chamber. The life-time for the divertor is rather limited by erosion than by neutron irradiation. Hence, an individual assessment would be beneficial as soon as comprehensive divertor modules providing the plasma conditions are available. Moreover, maintenance schemes with reasonable intervals are discussed. That includes, for instance, an optimization of blanket designs with respect to neutron irradiation in combination with divertor designs with respect to erosion such that the divertor life-time is ideally half of the blanket life-time.

2.7. Costing Module

Comprehensive systems codes include assessments of the economic performance of fusion devices corresponding to specific operation points. In this context, the calculation of the so-called levelized costs of electricity (COE) is widely implemented. That is a transparent tool frequently used also outside the fusion community to compare the particular costs for power generation of different technologies [140] (see Figure A.9). The COE are generally defined by the “equality between the present value of the sum of discounted revenues and the present value of the sum of discounted costs” [140]. That leads to

$$\mathrm{COE} = \frac{\sum_t \left[\left(\mathrm{Inv}_t + \mathrm{O\&M}_t + \mathrm{Fuel}_t + \mathrm{Carbon}_t + \mathrm{Decom}_t \right) (1+r)^{-t} \right]}{\sum_t \left[\mathrm{Elec}_t \, (1+r)^{-t} \right]} \tag{2.218}$$

where Inv_t = investment costs, $\mathrm{O\&M}_t$ = operations and maintenance costs, Fuel_t = fuel costs, Carbon_t = carbon costs, Decom_t = decommissioning costs and Elec_t is the amount of electricity produced in year “t”. $(1+r)^{-t}$ is the discount factor with a constant interest rate “r” [140]. At present, no detailed costing module is implemented in TREND. But two simple scaling laws are available that allow at least a highly simplified evaluation of the economic performance. These can be used to assess different operation points by comparison to a given base case, for instance. The first scaling was developed by Ward et al. [141] with the costing module of PROCESS,

$$\mathrm{COE} \propto \eta_{th}^{-0.5} P_{elNet}^{-0.4} \beta_N^{-0.4} f_{GW}^{-0.3} \tag{2.219}$$

where parameters that are not available in TREND are neglected. The second is proposed by Biel [142] as a rule of thumb for power plant costs,

$$\mathrm{COE} \propto \frac{V}{P_{elNet}} \tag{2.220}$$

More information on the economics of fusion power plants and costing modules for systems codes is given in the following reference selection: [21, 137, 143, 144, 145, 146, 147, 148, 149, 150, 151, 152, 153].

3. Validation: Benchmarks with other Systems Codes

The development process of each computational code simulating a physical or technical system should include verification and validation procedures. That is part of the quality management to ensure that the code satisfies the requirements and specifications. This can be done by comparing the calculated results with the properties of the specific system. But all existing fusion devices are still experiments. These do not consist of all crucial systems for fusion power plants including breeding blankets or heat conversion cycles, for instance. Hence, it is not possible to verify the complete set of modules with existing systems. Even the verification of individual modules is questionable. Due to the lack of detailed understanding of involved processes, most of the modules consist of simple scaling laws. These were developed with the objective to make extrapolations to operation regimes of power plants (see Chapter 2). Thus, the comparison of the interaction of these scaling laws with experimental data is less promising. But it can help to assess the limitations of the applied modellings.

Therefore, benchmarks with other systems codes like PROCESS, HELIOS and TPC were conducted. The intention of this activity was to validate the results of TREND with results of similar systems codes. But it should be kept in mind that these results can possibly be far away from reality. Nevertheless, this procedure appeared to be helpful to debug the source code efficiently. In addition, modelling shortages of TREND could be identified and updated subsequently with more sophisticated models. The benchmarks with each code base on a selection of different parameter sets (see Table A.2). In order to report the particular results, one exemplary parameter set is selected for each systems code, since most of the discovered differences base on the use of different models or assumptions. More information on the involved systems codes is given in the corresponding chapters. For the sake of visibility, the values in the following tables are rounded. But the calculations in TREND were done with higher accuracy. Thus, small inconsistencies can occur due to rounding effects. The relative deviation is calculated with the following formula using the non-rounded values,

$$\text{Deviation} = \frac{|a-b|}{|a+b|/2} \tag{3.1}$$

where a represents the reference value and b the corresponding value of TREND. Deviations of less than 1 % are not reported. The benchmark of PROCESS, HELIOS and TREND was also part of the EFDA workprogramme of 2011 within the PPPT department [48]. The objective of this task was to identify improvement needs concerning the EU systems codes.

3.1. Benchmark with PROCESS

The systems code PROCESS is hosted and maintained by the Culham Centre for Fusion Energy (CCFE). Its name is an acronym for “Power Reactor Optimisation Code for Environmental and Safety Studies”. The original version was developed at the Oak Ridge National Laboratory with contributions from other U.S. laboratories. It is based on the STAR (Spherical Tokamak Analysis and Reactor) code [154] and even more on its origin, the TETRA (Tokamak Engineering Test Reactor Analysis) code [155]. PROCESS is written in FORTRAN and has a modular structure including modules for the following systems: plasma, blanket, shield, vessel, magnets, heat and power systems, site and buildings, costs. The first manual was written in 1996 by Knight [25]. Currently, a new documentation is in progress for some of the implemented modules [26]. PROCESS was widely used in the last decades for EU fusion reactor studies, especially for the Power Plant Conceptual Study (PPCS) [99, 156, 157] and DEMO design studies [75, 158, 159]. Besides its physical and technological comprehensiveness, a strength of PROCESS is its optimization mode. The output is a single set of parameters for a fusion reactor design that satisfies the specified boundary conditions and constraints. The solution can be optimized with respect to a selected figure of merit. That includes the cost of electricity, the major radius or the pulse length, for instance.

The parameter set selected to report the benchmark of PROCESS and TREND was obtained by PROCESS during the design work for DEMO 1 in the EFDA work programme of 2011 [15, 16]. In addition to the design targets for this concept (see Table 1.1), the heating power was constrained to at least 50 MW and the operation point was optimized with respect to the pulse length. Unfortunately, the operation point was changed slightly for the final report due to further iterations. Since some work for this thesis was already done using the former parameter set, I decided to keep this set for consistency. Same of the parameters listed below are not explicitly given in the PROCESS output. These have been calculated outside of PROCESS using the implemented modelling.

Plasma Geometry and Radial Build Parameters

Table 3.1 lists the parameters of the plasma geometry and the radial build including the particular values obtained by PROCESS and TREND. Since most of the parameters that describe the radial build like the major radius R_0, the aspect ratio A or the radial thickness of different components (δ_{int}, δ_{TFC}, δ_{CS}) are input values for TREND, no deviations are expected. But also the calculated values like the plasma volume V or the plasma surface area S are in good agreement. The small deviations of less than 1 % are caused by the difference in the elongation at the X-point, κ_X. That is based on the fact that not identical relations for κ_X to κ_{95} are implemented. TREND uses Equation 2.29 as recommended by the ITER Physics Design Guidelines [33]. Whereas PROCESS uses a sightly modified equation. Unfortunately, the reasons for this modification could not be figured out. If the PROCESS value for κ_X is used by TREND, the values for the plasma volume and the surface area are identical up to the given accuracy. Nevertheless, I decided to keep the same values for κ_{95} and not for κ_X in the following, since the former is relevant for more scaling laws that are implemented in TREND.

Parameter	Unit	PROCESS	TREND	Deviation
R_0	[m]	9.0	9.0	
a	[m]	2.25	2.25	
A		4.0	4.0	
κ_X		1.86	1.85	
κ_{95}		1.66	1.66	
δ_X		0.50	0.50	
δ_{95}		0.33	0.33	
d_{SOL}	[m]	0.15	0.15	
d_{int}	[m]	1.60	1.60	
d_{TFC}	[m]	1.60	1.60	
d_{CS}	[m]	0.99	0.99	
V	[m^3]	1527	1523	
S	[m^2]	1127	1124	
S_p	[m^2]		27.4	
L	[m]		20.3	

Table 3.1.: Parameters for plasma geometry and radial build as calculated by PROCESS and TREND for the parameter set “DEMO 1” including the relative deviation. Deviations of less than 1 % are not reported. Ref: [15, 16]

Plasma Current and Magnetic Fields

Most of the parameters of Table 3.2 are in good agreement. But a deviation of 64 % is determined for the internal inductance l_i. In PROCESS, a default value of $l_i = 0.65$ is used. Hence, the connection between the peaking of the current profile and the internal inductance is not considered explicitly. By contrast, TREND calculates l_i with respect to the particular current density profile according to Equation 2.52. As mentioned before, the calculated value of $l_i = 1.27$ for DEMO 1 seems to be high compared to ITER values and work on improved modellings is in progress (see Chapter 2.3.1). The small difference in the average poloidal field $\langle B_P \rangle_l$ is based on different modellings. That has also impacts on the vertical magnetic field B_V by means of the poloidal plasma beta in addition to the deviation in l_i (see Equation 2.58).

Profiles for Temperature and Density

Since temperature and density profile parameters are set as input values in TREND and the same profile modelling is implemented in both codes, no differences are observed (see Table 3.3). Due to the use of simple parabolic profile shapes, no values for the pedestal and the separatrix are calculated.

Parameter	Unit	PROCESS	TREND	Deviation
I_p	[MA]	16.0	16.0	
q_{95}		3.0	3.0	
q_{cyl}		2.62	2.62	
q_0		1.0	1.0	
c_j			3.1	
l_i		0.65	1.27	64 %
B_{tot}	[T]	7.13	7.13	
B_t	[T]	7.06	7.06	
B_{tMax}	[T]	12.34	12.34	
$\left\langle B_p \right\rangle_l$	[T]	0.987	0.991	
B_V	[T]	0.641	0.690	7 %

Table 3.2.: Parameters for plasma current and magnetic field as calculated by PROCESS and TREND for the parameter set "DEMO 1" including the relative deviation. Deviations of less than 1 % are not reported. Ref: [15, 16]

Parameter	Unit	PROCESS	TREND	Deviation
$\langle T \rangle$	[keV]	12.8	12.8	
$\langle T \rangle_n$	[keV]	16.0	16.0	
T_0	[keV]	32.1	32.1	
c_T		2.5	2.5	
$\langle n \rangle$	[10^{20}/m^3]	0.856	0.856	
$\overline{n}_e$	[10^{20}/m^3]	1.01	1.01	
n_0	[10^{20}/m^3]	1.28	1.28	
c_n		1.5	1.5	
n_{GW}	[10^{20}/m^3]	1.01	1.01	
f_{GW}		1.0	1.0	

Table 3.3.: Parameters for temperature and density profiles as calculated by PROCESS and TREND for the parameter set "DEMO 1" including the relative deviation. Deviations of less than 1 % are not reported. Ref: [15, 16]

Fuel and Impurities

Table 3.4 shows the parameters that describe the fuel content and the impurity concentrations in the plasma. The fuel concentration f_{DT} is not in total agreement, even if the impurity species and concentrations are the identical. The small difference could be traced back to the additional consideration of beam ions in PROCESS.

Parameter	Unit	PROCESS	TREND	Deviation
D:T		50:50	50:50	
M		2.5	2.5	
Z_{eff}		1.98	1.98	
Z_1		6	6	
Z_2		8	8	
Z_3		26	26	
f_i		0.870	0.870	
f_{DT}		0.764	0.769	
f_{He}		0.1	0.1	
f_{Z1}		0	0	
f_{Z2}		0	0	
f_{Z3}		0.0012	0.0012	
τ_p^*/τ_E		6.3	6.3	

Table 3.4.: Parameters describing the fuel content and impurities in the plasma as calculated by PROCESS and TREND for the parameter set “DEMO 1” including the relative deviation. Deviations of less than 1 % are not reported. Ref: [15, 16]

Plasma Pressure and Beta

Since the profiles for temperature and density are in perfect agreement, the same is also expected for the plasma pressure as well as the thermal plasma beta (see Table 3.5). Hence, the thermal normalized plasma beta $\beta_{N,th}$ should technically be the same. But PROCESS applies for its calculation the total thermal plasma beta that is defined with respect to the total magnetic field. Whereas TREND uses the toroidal thermal plasma beta according to Equation 2.173 as recommended by physics guidelines for DEMO [31].

Parameter	Unit	PROCESS	TREND	Deviation
β_N		2.39	2.49	4 %
$\beta_{N,th}$		2.01	2.05	2 %
γ_{fast}		0.187	0.211	12 %
β	[%]	2.41	2.46	2 %
β_{th}	[%]	2.03	2.03	
β_t	[%]	2.46	2.51	2 %
β_p	[%]	126	128	1 %
$\langle p_{th} \rangle$	[bar]	4.11	4.11	
p_0	[bar]	12.3	12.3	
c_p		3.0	3.0	

Table 3.5.: Parameters for the plasma pressure profile and different plasma betas as calculated by PROCESS and TREND for the parameter set “DEMO 1” including the relative deviation. Deviations of less than 1 % are not reported. Ref: [15, 16]

Moreover, different modellings of the fast particles fraction including the additional consideration of beam particles in PROCESS lead to a deviation of $\gamma_{fast} = 12\,\%$. That is also reflected in the values for β, β_t and β_p, as well as for β_N in addition to the different definitions of the thermal component.

Plasma Power Balance

The major differences of PROCESS and TREND concerning the plasma power balance arise from different modelling of radiation (see Table 3.6). The values for synchrotron radiation are the same based on an update of PROCESS to the most recent scaling also used in TREND (see Equation 2.118). Hence, the deviations in the total core radiation $P_{radCore}$ and the radiation fraction f_{rad} are caused by the modelling of bremsstrahlung and line radiation. In PROCESS, the total amount of line radiation and bremsstrahlung is calculated with undocumented scalings based on transport simulations [26]. PROCESS then assigns a certain fraction for each impurity to the plasma inside the separatrix. That is listed as P_{brem} in the PROCESS output, here 73 MW. The remaining, here 80 MW, represents radiation in the SOL used to calculate the power to the divertor. Thus, PROCES does not distinguish between line radiation and bremsstrahlung in the plasma core. Therefore, 73 MW of PROCESS should be compared to 94 MW as calculated by TREND giving still a relative deviation of 25 %.

Recently, the Bosch / Hale fit [76, 77] for the D-T reaction rate was implemented in PROCESS and HELIOS. That reduced the differences in fusion power P_{fus} to less than 1 %. The remaining deviation is due to different fuel content (see “Fuel and Impurities” above). The requirements on additional heating power result in both codes from the balance of power gains and losses in the plasma. Thus, the observed difference in core radiation is the main driver for the deviation 23 % in P_{add}. That is also the main reason for the unequal fusion gains showing the sensitivity of this parameter. For the ohmic heating power P_{OH}, a small deviation in the non-rounded values of 1 % is observed arising from different values for the loop voltage (see below).

The parameters describing the transport losses in the plasma core like τ_E, H, W_{th} and P_{con} are in good agreement. The difference in the power crossing the separatrix P_{sep} is based on additional mantle radiation that is considered in TREND. A mantle region is not implemented in PROCESS. That also explains the varying values for the H-mode power threshold fraction f_{LH}, although the threshold power P_{LH} is equal.

Auxiliary Current-Drive

The operation point used for this benchmark was constrained to hardly any external current-drive by non-inductive means (see small value of f_{CD} in Table 3.7). Hence, a large fraction of P_{add} is exclusively used for plasma heating and not for supportive current-drive. Hence, the discussions on P_{add} of the preceding paragraph are in charge for the deviations in P_{nCD}. Moreover, the deviation of f_{ind} is directly explained by unequal values for f_{BS}. These are based on different modellings, PROCESS applied the modelling of Nevins [59] and TREND that of Wilson [60] (see Chapter 2.3.2). The reason for the differing values of P_{CD} could not be identified, since most of the influencing parameters are in quite good agreement.

Parameter	Unit	PROCESS	TREND	Deviation
P_{fus}	[MW]	1943	1952	
P_{add}	[MW]	50	63	23 %
P_{OH}	[MW]	0.7	0.7	1 %
Q		38.7	30.4	24 %
P_{con}	[MW]	313	313	
P_{sep}	[MW]	313	304	3 %
W_{th}	[MW s]	942	939	
τ_E	[s]	3.01	3.00	
H		1.0	1.0	
ρ_{core}		1.0	0.9	11 %
$P_{radCore}$	[MW]	127	146	15 %
P_{syn}	[MW]	53	53	
r_{syn}		0.6	0.6	
P_{brem}	[MW]		55	
$P_{lineCore}$	[MW]		39	
$P_{lineMantle}$	[MW]		9	
f_{rad}		0.29	0.34	16 %
P_{LH}	[MW]	140	140	
f_{LH}		2.24	2.16	3 %

Table 3.6.: Parameters for the plasma power balance as calculated by PROCESS and TREND for the parameter set “DEMO 1” including the relative deviation. Deviations of less than 1 % are not reported. Ref: [15, 16]

Parameter	Unit	PROCESS	TREND	Deviation
CD System		NBI	NBI	
P_{CD}	[MW]	0.2	0.4	54 %
P_{nCD}	[MW]	50	63	23 %
$\langle \gamma_{CD} \rangle$	$[10^{20} \mathrm{A/Wm^2}]$	0.31	0.31	
η_{add}		0.40	0.40	
f_{CD}		0.001	0.001	
f_{BS}		0.360	0.352	2 %
f_{ind}		0.639	0.647	1 %

Table 3.7.: Parameters describing the auxiliary current-drive as calculated by PROCESS and TREND for the parameter set “DEMO 1” including the relative deviation. Deviations of less than 1 % are not reported. Ref: [15, 16]

Inductive Current-Drive and Flux Balance

Most of the observed discrepancies concerning the inductive current-drive and the flux balance base on two points (see Table 3.8). The first is the modelling of the current profile, particularly the connection to the internal inductance l_i as discussed above. Despite the significant deviation in l_i, quite similar values for the total plasma inductance L_p are observed. That could be traced back to the fact that PROCESS increases the sum of the internal and external plasma inductance by 25 % without stating the reasons for this rise. That also affects the inductive flux consumption Φ_{ind} during the plasma current ramp-up. The deviation in the resistive flux consumption Φ_{res} is based on different values for the Ejima coefficient. In PROCESS, c_{Ejima} is set as an input, whereas TREND applies a recently developed modelling with $c_{RU} = 10$ (see Equation 2.92).

The second point reflects different modelling of the flux swing provision by the CS and the other PFCs. PROCESS calculates the flux swing with respect to mutual inductances of the poloidal coil system and the plasma multiplied by specific coil currents. The approach of TREND and other systems codes is given by Equations 2.81 and 2.82 neglecting effects due to the finite length of the CS coils and their distance to the plasma. There is work in progress in order to improve the implemented modellings. Both points influence the available flux swing for the current flat-top Φ_{flat} and the corresponding time-scale τ_{flat}. The small difference in the loop voltage U_{loop} is mainly due to unequal inductive current-drive fractions based on different bootstrap models as discussed above.

Parameter	Unit	PROCESS	TREND	Deviation
τ_{flat}	[min]	147	186	24 %
U_{loop}	[V]	0.044	0.044	1 %
R_p	[Ω]	4.28×10^{-9}	4.28×10^{-9}	
L_p	[H]	1.98×10^{-5}	2.00×10^{-5}	1 %
c_{Ejima}		0.40	0.36	10 %
Φ_{tot}	[V s]	776	884	13 %
Φ_{CS}	[V s]	400	735	59 %
Φ_{PF}	[V s]	412	148	94 %
Φ_{RU}	[V s]	390	387	1 %
Φ_{res}	[V s]	73	66	10 %
Φ_{ind}	[V s]	318	321	1 %
Φ_{PI}	[V s]		0	
Φ_{flat}	[V s]	386	497	25 %
B_{CSmax}	[T]	12.43	12.43	
j_{CS}	[A/mm^2]	10.4	10.0	4 %

Table 3.8.: Parameters for inductive current-drive and the flux balance as calculated by PROCESS and TREND for the parameter set “DEMO 1” including the relative deviation. Deviations of less than 1 % are not reported. Ref: [15, 16]

Dynamical Phases

Table 3.9 comprises time-scales that characterize the different phases of pulsed devices. Substantial deviations are observed for some parameters indicating strong differences in the modelling of both systems codes. PROCESS often uses specified default values [26]. But a time-scale of $\tau_{RU} = 30\,\mathrm{s}$ to ramp up the plasma current to 16 MA implies a ramp rate of 0.53 MA/s. That seems to be rather unrealistic compared to calculations for ITER (see Chapter 2.3.3). The assumed time-scale to recharge the central solenoid of $\tau_{RC} = 30\,\mathrm{s}$ would suggest a recharging power of about $P_{RC} = 1340\,\mathrm{MW}$ as calculated by the simple modelling used in TREND (see Equation 2.206). Hence, the modelling of TREND helps to improve the plausibility of the time-scales for the different dynamical phases. But further work on this specific topic is strongly recommended.

Parameter	Unit	PROCESS	TREND	Deviation
τ_{cycle}	[min]	150	217	36 %
τ_{burn}	[min]	147	185	23 %
τ_{down}	[min]	3	32	164 %
f_{DC}		0.98	0.85	14 %
τ_{RU}	[min]	0.5	5.2	165 %
τ_{heat}	[min]	0.2	0.3	40 %
τ_{BT}	[min]		1.6	
τ_{RD}	[min]	0.5	5.2	165 %
τ_{pump}	[min]	1.7	20.0	169 %
τ_{RC}	[min]	0.5	6.8	172 %
P_{RC}	[MW]		100	

Table 3.9.: Parameters describing the dynamical phases as calculated by PROCESS and TREND for the parameter set “DEMO 1” including the relative deviation. Deviations of less than 1 % are not reported. Ref: [15, 16]

Power Flow

The heat recoveries in the blanket P_{blkt} and the divertor P_{div} as calculated by PROCESS and TREND are slightly different based on the particular power flow scheme (see Figure 2.14). Nevertheless, the total thermal power P_{th} is in good agreement (see Table 3.10). That leads to similar gross electric power P_{el}, since identical values for the thermal efficiency are used. Due to higher requirements on electricity for the H&CD systems as a result of the plasma power balance (see Table 3.6), the recirculating power P_{elRec} and the corresponding fraction f_{rec} are also higher for TREND. That causes slightly less net electric power output P_{elNet}. For this benchmark case, no explicit distinction between pumping power for blanket and divertor is considered in TREND.

Parameter	Unit	PROCESS	TREND	Deviation
f_{nMult}		1.18	1.18	
$f_{geoBlkt}$			0.909	
f_{geoDiv}			0.062	
f_{hBlkt}		0.96	0.96	
f_{hDiv}		0.99	0.99	
P_{blkt}	[MW]	1742	1812	4 %
P_{div}	[MW]	439	410	7 %
P_{th}	[MW]	2227	2194	1 %
η_{th}		0.33	0.33	
P_{el}	[MW]	735	724	1 %
P_{elNet}	[MW]	500	458	9 %
P_{elRec}	[MW]	235	266	12 %
f_{rec}		0.32	0.37	14 %
P_{elAdd}	[MW]	126	159	23 %
P_{pump}	[MW]	50	49	2 %
f_{pump}		0.068	0.068	
η_{pump}		1.0	1.0	
P_{cryo}	[MW]	31	30	2 %
f_{cryo}		0.042	0.042	
P_{aux}	[MW]	28	28	3 %
f_{aux}		0.038	0.038	
η_{tot}		0.26	0.24	9 %

Table 3.10.: Parameters describing the power flow through the power plant as calculated by PROCESS and TREND for the parameter set "DEMO 1" including the relative deviation. Deviations of less than 1 % are not reported. Ref: [15, 16]

Divertor and Power Exhaust

The peak power flux on the outboard divertor plates q_{peak}^{out}, shows a significant deviation indicating that the implemented modellings are completely different (see Table 3.11). Moreover, the width of the power decay length at the separatrix λ_q differs up to one order of magnitude. That is in agreement with recent work by Eich et al. [119] leading to a new scaling that is implemented in TREND. The small difference in P_{sep}/R_0 is based on the fact that TREND considers additional radiation in the mantle region that reduces the transport losses of the plasma core.

Neutron and Heat Load

The calculated neutron wall load q_{NWL} and the first wall area S_{FW} are quite similar (see Table 3.12). PROCESS uses a fixed factor of 1.09 to scale the plasma surface area [26]. Whereas TREND calculates this factor with respect to assumptions on the thickness of the SOL (see Equation 2.23). The reasons for the differences in the life-time of the first wall could not be figured out. PROCESS gives a value of 3.4 years for the divertor and 15.8 years for the blanket.

Parameter	Unit	PROCESS	TREND	Deviation
P_{sep}/R_0	[MW/m]	34.8	33.7	3 %
q_{peak}^{out}	[MW/m^2]	7.9	12.1	42 %
q_{peak}^{in}	[MW/m^2]		7.9	
q_{sep}	[GW/m^2]		30.1	
λ_q	[mm]	13.2	0.9	174 %
λ_{int}	[mm]		2.6	
f_{exp}			15	
f_{divRad}			0.90	
$f_{outboard}$			0.67	
A_{con}^{outb}	[m^2]		1.9	

Table 3.11.: Parameters describing the divertor conditions and the power exhaust as calculated by PROCESS and TREND for the parameter set “DEMO 1” including the relative deviation. Deviations of less than 1 % are not reported. Ref: [15, 16]

Parameter	Unit	PROCESS	TREND	Deviation
S_{FW}	[m^2]	1225	1199	2 %
q_{NWL}	[MW/m^2]	1.27	1.30	2 %
q_{HWL}	[MW/m^2]		0.38	
ND_{rate}	$[\frac{\text{MW}}{\text{m}^2}\frac{\text{a}}{\text{dpa}}]$		0.1	
ND_a	[dpa/a]		13.0	
ND_{max}	[dpa]		60	
τ_{FWLT}	[a]	3.4 / 15.8	4.6	109 %

Table 3.12.: Parameters describing the neutron and heat load as calculated by PROCESS and TREND for the parameter set “DEMO 1” including the relative deviation. Deviations of less than 1 % are not reported. Ref: [15, 16]

3.2. Benchmark with HELIOS

The systems code HELIOS is developed at the Commissariat à l’énergie atomique et aux énergies alternatives (CEA). The focus of HELIOS is especially on the plasma and power flows including the following features [19]: (I) sophisticated description of the plasma poloidal shape by means of four arcs using two elongations, two triangularities and four angles (see advanced geometry module of TREND, Chapter 2.2.2 and Figure 2.3), (II) exact analytical expressions for geometrical parameters (V, S, S_p and L) as well as proper surface and volume integration for arbitrary aspect ratio (see geometry modules of TREND, Chapters 2.2.1 and 2.2.2), (III) sophisticated profile shapes for density and temperature including finite values for pedestal and separatrix (see advanced profiles of TREND, Equation 2.131) and (IV) sophisticated calculation of the loop voltage in the current flat-top phase taking into account local dependencies of the equilibrium electric field and the plasma resistivity.

HELIOS is written in Fortran 77. A detailed documentation of version 1.0 including a demonstration of its application was published in 2011 by Johner [19]. The current version is 1.1 where updates mainly for the synchrotron radiation in terms of profile shapes for temperature and density were implemented [27]. A new activity started in 2011 at the CEA, where HELIOS is planned to be included as plasma module in a more comprehensive systems code called SYCOMORE (SYstem COde for MOdelling REactors). That is designed with a flexible and modular code architecture comprising additional modules for divertor, magnets, breeding blanket and shields [160].

Several parameter sets were used to benchmark HELIOS and TREND (see Table A.2). The so-called 3PT-SYS11-ACT5-B2 is selected to report the results, since it is the parameter set with most available information compared to other HELIOS runs. In addition, HELIOS used the Sadler / van Belle fit [161] for the reaction rates in former studies. That implied significant differences in terms of the fusion power. Since that is a crucial parameter for the overall design, the operation points were hardly comparable. The benchmark of HELIOS and TREND was also part of activity 5 of the EFDA PPPT work programme for 2011 [48]. Compared to the standard configuration of TREND, the advanced geometry module (see Chapter 2.2.2), the advanced profile shapes with pedestals for density and temperature (see Equation 2.131) and the Hoang et al. scaling for the bootstrap current (see Equation 2.72) were applied.

Plasma Geometry and Radial Build Parameters

An elliptical plasma cross-section was used for this parameter set, since that was the default geometry parametrization of TREND at that time. Others were implemented later (see Chapters 2.2.1 and 2.2.2). An elliptical cross-section implies $\kappa_X^1 = \kappa_X^2 = \kappa_X$, $\delta_X^1 = \delta_X^2 = \delta_X = 0$ and $\psi^{-(1)} = \psi^{-(2)} = \psi^{+(1)} = \psi^{+(2)} = 0$. Moreover, it was assumed in the HELIOS run that $\kappa_{95} = \kappa_X$ and $\delta_{95} = 0.33$. Hence, Equations 2.29 and 2.30 are skipped in TREND to match these assumptions. Using this modification, the parameters describing the plasma geometry and the radial build are in perfect agreement up to the given accuracy (see Table 3.13).

Plasma Current and Magnetic Fields

Good agreement is also observed for most parameters that describe the plasma current and magnetic fields (see Table 3.14). Only a deviation of 2 % in the internal inductance l_i and of 16 % in the vertical magnetic field B_V is determined. The former is due to the fact that l_i is considered as an input in HELIOS and no relation to the current profile peaking is implemented. That also affects the calculation of the vertical magnetic field. In addition, HELIOS applies the thermal poloidal beta instead of the total poloidal beta and implements an explicit dependency on elongation [19]. Moreover, the current profile peaking c_j was specified in TREND to be identical to the value of HELIOS. This assumption leads to a comparable high safety factor on axis of $q_0 = 1.69$, at least for conventional scenarios. I assume that the value for c_j was selected without considering the relation to the safety factor profile, since this link is not included in HELIOS.

Parameter	Unit	HELIOS	TREND	Deviation
R_0	[m]	8.5	8.5	
a	[m]	2.833	2.833	
A		3.0	3.0	
κ_X		1.66	1.66	
κ_{95}		1.66	1.66	
δ_X		0	0	
δ_{95}		0.33	0.33	
d_{SOL}	[m]		0.15	
d_{int}	[m]	1.9	1.9	
d_{TFC}	[m]	1.2	1.2	
d_{CS}	[m]	0.647	0.647	
V	[m^3]	2236	2236	
S	[m^2]	1284	1284	
S_p	[m^2]	41.9	41.9	
L	[m]	24.0	24.0	

Table 3.13.: Parameters for plasma geometry and radial build as calculated by HELIOS and TREND for the parameter set “3PT-SYS11-ACT5-B2” including the relative deviation. Deviations of less than 1 % are not reported. Note: Equations 2.29 and 2.30 are skipped in TREND to have the same values for κ_X and κ_{95} as assumed in the HELIOS run. Ref: [48, 162]

Parameter	Unit	HELIOS	TREND	Deviation
I_p	[MA]	23.1	23.1	
q_{95}		3.0	3.0	
q_{cyl}			2.49	
q_0			1.69	
c_j		1.81	1.81	
l_i		0.85	0.86	2 %
B_{tot}	[T]		5.87	
B_t	[T]	5.74	5.74	
B_{tMax}	[T]	13.0	13.0	
$\langle B_p \rangle_l$	[T]		1.21	
B_V	[T]	0.78	0.91	16 %

Table 3.14.: Parameters for plasma current and magnetic field as calculated by HELIOS and TREND for the parameter set “3PT-SYS11-ACT5-B2” including the relative deviation. Deviations of less than 1 % are not reported. Ref: [48, 162]

Profiles for Temperature and Density

As mentioned before, advanced profile parametrizations with pedestals for temperature and density were applied in both codes leading to equal values as expected (see Table 3.15).

Parameter	Unit	HELIOS	TREND	Deviation
$\langle T \rangle$	[keV]	20.6	20.6	
$\langle T \rangle_n$	[keV]		22.0	
T_0	[keV]	51.8	51.8	
T_{ped}	[keV]	3.33	3.33	
T_{sep}	[keV]	0.10	0.10	
c_T		2.52	2.52	
$\langle n \rangle$	[10^{20}/m^3]	0.910	0.910	
$\overline{n}_e$	[10^{20}/m^3]		0.947	
n_0	[10^{20}/m^3]	1.002	1.002	
n_{ped}	[10^{20}/m^3]	0.911	0.911	
n_{sep}	[10^{20}/m^3]	0.360	0.360	
c_n		1.10	1.10	
ρ_{ped}		0.925	0.925	
n_{GW}	[10^{20}/m^3]		0.916	
f_{GW}			1.03	

Table 3.15.: Parameters for temperature and density profiles as calculated by HELIOS and TREND for the parameter set “3PT-SYS11-ACT5-B2” including the relative deviation. Deviations of less than 1 % are not reported. Ref: [48, 162]

Fuel and Impurities

As far as information on fuel and impurities is available for HELIOS, similar values are observed in most cases (see Table 3.16). The difference in the ratio of the global particle to energy confinement time is mainly due to a deviation in the energy confinement time as discussed in the paragraph “Plasma Power Balance” below.

Plasma Pressure and Beta

Good agreement for the plasma pressure and the different thermal plasma betas can be determined (see Table 3.17). But different modelling of the fast particles fraction leads to a deviation of about 48 % that causes different values for the total plasma betas.

Parameter	Unit	HELIOS	TREND	Deviation
D:T		50:50	50:50	
M		2.5	2.5	
Z_{eff}		2.57	2.57	
Z_1		18	18	
Z_2		0	0	
Z_3		0	0	
f_i			0.824	
f_{DT}			0.719	
f_{He}		0.1	0.1	
f_{Z1}		4.48×10^{-3}	4.48×10^{-3}	
f_{Z2}		0	0	
f_{Z3}		0	0	
τ_p^*/τ_E		4.84	5.16	6 %

Table 3.16.: Parameters describing the fuel content and impurities in the plasma as calculated by HELIOS and TREND for the parameter set “3PT-SYS11-ACT5-B2” including the relative deviation. Deviations of less than 1 % are not reported. Ref: [48, 162]

Parameter	Unit	HELIOS	TREND	Deviation
β_N		3.61	3.90	8 %
$\beta_{N,th}$		3.14	3.14	
γ_{fast}		0.15	0.25	48 %
β	[%]		5.31	
β_{th}	[%]		4.27	
β_t	[%]	5.13	5.55	8 %
$\beta_{t,th}$	[%]	4.46	4.45	
β_p	[%]	116	125	8 %
$\beta_{p,th}$	[%]	101	101	
$\langle p_{th} \rangle$	[bar]	5.85	5.84	
p_0	[bar]		15.2	
c_p			2.60	

Table 3.17.: Parameters for the plasma pressure profile and different plasma betas as calculated by HELIOS and TREND for the parameter set “3PT-SYS11-ACT5-B2” including the relative deviation. Deviations of less than 1 % are not reported. Ref: [48, 162]

Plasma Power Balance

After the Bosch / Hale fit [76, 77] for the D-T reaction rate was implemented in HELIOS replacing the fit of Sadler / van Belle [161], similar values for the fusion power P_{fus} are observed for both codes (see Table 3.18). The additional heating power P_{add} is specified as an input in HELIOS. The chosen value of 201 MW leads to the fact that the particular operation point is not at thermal equilibrium. As mentioned, this parameter set was developed during a benchmark exercise of the EU systems codes and originated from a PROCESS run. Differences for radiation and the choice of the same amount of heating power as PROCESS pushed the operation point of HELIOS out of equilibrium. For the calculation with TREND, the constraint of an equilibrated power balance is maintained explaining the deviation in P_{add}. That also causes the variation of the fusion gain Q. Since the plasma current is identical, the difference in the non-rounded values of the ohmic heating power P_{OH} indicates unequal values for the loop voltage (see below).

Parameter	Unit	HELIOS	TREND	Deviation
P_{fus}	[MW]	3005	3004	
P_{add}	[MW]	201	218	8 %
P_{OH}	[MW]	0.1	0.1	19 %
Q		14.9	13.8	8 %
P_{con}	[MW]	497	529	6 %
P_{sep}	[MW]	475	514	8 %
W_{th}	[MW s]	1958	1958	
τ_E	[s]	3.94	3.70	6 %
H		1.3	1.3	
ρ_{core}		0.95	0.95	
$P_{radCore}$	[MW]	326	298	9 %
P_{syn}	[MW]	131	131	
r_{syn}		0.7	0.7	
P_{brem}	[MW]	116	115	1 %
$P_{lineCore}$	[MW]	79	52	42 %
$P_{lineMantle}$	[MW]	21	15	36 %
f_{rad}		0.43	0.38	13 %
P_{LH}	[MW]	129	129	
f_{LH}		3.85	4.00	4 %

Table 3.18.: Parameters for the plasma power balance as calculated by HELIOS and TREND for the parameter set “3PT-SYS11-ACT5-B2” including the relative deviation. Deviations of less than 1 % are not reported. Ref: [48, 162]

Given the identical modelling of temperature and density profiles in combination with the application of the same scaling law for the energy confinement (see Equation 2.113), good agreement is generally expected concerning the transport losses. But that just holds for the thermal energy of the plasma W_{th} reflecting the conformity of the profile modelling. Again the violation of the thermal equilibrium causes the observed deviation in the transport loss power P_{con} and the energy confinement time τ_E. HELIOS defines a so-called “net” power delivered to the plasma as the difference of the total heating power and the radiation losses in the core, $P_{net} = P_{heat} - P_{radCore}$. At thermal equilibrium, P_{net} is equal to P_{con}. But HELIOS reports a value of $P_{net} = 483\,\text{MW}$ that is used for the calculation of the transport losses in the plasma core. The observed difference increases further in the mantle region from 6 % to 8 % based on varying mantle radiation as discussed below. That also explains the deviation concerning the H-mode power threshold fraction f_{LH}, since both codes report identical values for the threshold power P_{LH}.

The values for synchrotron and bremsstrahlung radiation are quite similar. But line radiation in the plasma core $P_{lineCore}$ and the mantle region $P_{lineMantle}$ differs significantly. I assume that this is due to the application of different line radiation power loss functions (see Figure 2.8), since the impurity concentrations and the profiles are identical. That also causes differences in the total core radiation $P_{radCore}$ and the radiation fraction f_{rad}. The latter is influenced additionally by the discussed variations of P_{add}.

Auxiliary Current-Drive

The parameters describing the auxiliary current-drive are identical to the given accuracy (see Table 3.19). But HELIOS does not report any "pure" heating power P_{nCD}, since it is assumed that the entire heating power is also used for current-drive. In TREND, a non-current-drive heating power is implemented intentionally in order to satisfy the current-drive and the power balance at the same time maintaining thermal equilibrium without having to adjust the H-factor or radiation by means of the impurity concentrations.

Parameter	Unit	HELIOS	TREND	Deviation
P_{CD}	[MW]	201	201	
P_{nCD}	[MW]		17	
$\langle\gamma_{CD}\rangle$	[10^{20}A/Wm^2]	0.5	0.5	
η_{add}		0.60	0.60	
f_{CD}		0.563	0.563	
f_{BS}		0.348	0.348	
f_{ind}		0.089	0.089	

Table 3.19.: Parameters describing the auxiliary current-drive as calculated by HELIOS and TREND for the parameter set "3PT-SYS11-ACT5-B2" including the relative deviation. Deviations of less than 1 % are not reported. Ref: [48, 162]

Inductive Current-Drive and Flux Balance

A substantial disagreement is observed for the inductive current-drive and the flux balance (see Table 3.20). That can be traced back to the modelling of four parameters, the plasma inductance L_p together with its internal part l_i, the Ejima coefficient c_{Ejima}, the plasma conductivity σ and the vertical magnetic field B_V. The latter is discussed in the paragraph "Plasma Current and Magnetic Fields" causing the deviating flux swing of the poloidal field coils Φ_{PF}. That also explains the unequal values for the total available flux swing Φ_{tot}, since the flux swing provided by the CS coils is similar. That is based on identical modelling and similar assumptions for the magnetic field B_{CSmax} and the current density j_{CS}. The plasma inductance L_p is evaluated in HELIOS and TREND with different scaling laws. That is also the reason for the deviation in the inductive flux consumption Φ_{ind} (see Equation 2.93). The unequal values for the resistive flux consumption Φ_{res} are caused by the fact that the Ejima coefficient c_{Ejima} is an input for

HELIOS, whereas TREND applies a recently developed modelling (see Equation 2.84 and the following). Hence, the modellings of L_p and c_{Ejima} are responsible for different total current ramp-up flux consumption Φ_{RU}. Hence, the significant deviation on the available flux swing in the current flat-top phase Φ_{flat} results from a combination of different modellings for B_V, L_p and c_{Ejima}. But that is just one part of the large difference observed for the time-scale of the current flat-top τ_{flat}, even if it is the major driver (see Equation 2.78). The variation of the plasma resistance R_p and the loop voltage U_{loop} is based on a different modelling of the plasma conductivity σ. TREND still uses the global description as recommended in the ITER Physics Design Guidelines [33] (see Equation 2.61), whereas HELIOS utilizes a local approach. Currently, there is work in progress to develop a proper modelling of the plasma conductivity based on work of Sauter et al. [54, 55].

Parameter	Unit	HELIOS	TREND	Deviation
τ_{flat}	[min]	132	523	119 %
U_{loop}	[V]	4.62×10^{-3}	5.58×10^{-3}	19 %
R_p	[Ω]	2.25×10^{-9}	2.71×10^{-9}	19 %
L_p	[H]	1.70×10^{-5}	1.36×10^{-5}	22 %
c_{Ejima}		0.45	0.38	18 %
Φ_{tot}	[V s]	574	603	5 %
Φ_{CS}	[V s]	414	414	
Φ_{PF}	[V s]	160	189	16 %
Φ_{RU}	[V s]	503	407	21 %
Φ_{res}	[V s]	111	93	18 %
Φ_{ind}	[V s]	392	315	22 %
Φ_{PI}	[V s]	20	20	
Φ_{flat}	[V s]	51	175	110 %
B_{CSmax}	[T]	13	13	
j_{CS}	[A/mm^2]	16	16	

Table 3.20.: Parameters for inductive current-drive and the flux balance as calculated by HELIOS and TREND for the parameter set “3PT-SYS11-ACT5-B2” including the relative deviation. Deviations of less than 1 % are not reported. Ref: [48, 162]

Power Flow

In general, a reasonable agreement of the power flow modelling can be observed for both codes (see Table 3.21). The occurring deviations mainly base on different additional heating powers P_{add} as discussed above. Both codes calculate auxiliary requirements on electric power by means of specific fractions of the gross electric power (see Equations 2.196 to 2.199). Since P_{el} is similar, no significant differences are expected, even if the breakdown of TREND is more detailed. The characteristics of the power conversion system in terms of coefficients, efficiencies and auxiliary power fractions originate from the HCLL-DEMO-2007 concept (see Table 2.8). The comparable high fraction for the total pumping power in addition to the high thermodynamic efficiency of indicate that helium cooling is utilized.

Parameter	Unit	HELIOS	TREND	Deviation
f_{nMult}		1.18	1.18	
$f_{geoBlkt}$			0.91	
f_{geoDiv}			0.06	
f_{hBlkt}			0.95	
f_{hDiv}			1.00	
P_{blkt}	[MW]		2857	
P_{div}	[MW]		677	
P_{th}	[MW]	3723	3707	
η_{th}		0.44	0.44	
P_{el}	[MW]	1638	1631	
P_{elNet}	[MW]	913	881	4 %
P_{elRec}	[MW]	725	751	3 %
f_{rec}		0.44	0.46	4 %
P_{elAdd}	[MW]	335	364	8 %
P_{pump} (B+D)	[MW]	351	302 + 46	1 %
f_{pump} (B+D)		0.214	0.185 + 0.028	
η_{pump}		0.91	0.91	
P_{aux} (P_{cryo})	[MW]	39	39 (28)	
f_{aux} (f_{cryo})		0.024	0.007 (0.017)	
η_{tot}		0.27	0.29	10 %

Table 3.21.: Parameters describing the power flow through the power plant as calculated by HELIOS and TREND for the parameter set "3PT-SYS11-ACT5-B2" including the relative deviation. Deviations of less than 1 % are not reported. Ref: [48, 162]

Other Parameters

HELIOS does not contain a modelling for the dynamical phases of pulsed power plants. In addition, the information about divertor and power exhaust, as well as neutron and heat load is quite limited. Thus, the discussion of the few reported parameters is summarized in this paragraph. The corresponding tables can be found in the appendix (see Tables A.3, A.4 and A.5). The peak power flux to the outboard divertor plates is calculated in HELIOS by a simplified model. A value of $q^{out}_{peak} = 84.7\,\mathrm{MW/m^2}$ is reported for this operation point. The substantial deviation of 121 % compared to TREND indicates that the current modellings for the divertor include large uncertainties and the calculated values should be regarded with certain suspicion. Concerning the surface area of the first wall S_{FW}, HELIOS assumes that it is equal to the surface area of the plasma. But TREND considers in addition the distance between the separatrix and the first wall (see Equation 2.23). Thus, S_{FW} is enlarged up to about 5 % in this case explaining different neutron wall loads.

3.3. Benchmark with TPC

The systems code TPC (Tokamak Plasma Power Balance Calculation Code) is developed at the Japan Atomic Energy Agency (JAEA). TPC is a physics code that is based on the ITER Physics Design Guidelines [33]. The first versions consisted of plasma routines from TRESCODE (1987) [29]. The operation manual is written in Japanese by Fujieda et al. [28]. Amongst others, TPC was used for early analysis of ITER operation points (see [163], for instance). In 2002, the development of the systems code TOPPER was started at the JAEA as an extension of TPC, especially for the design of devices with low aspect ratios [22]. TOPPER applies TPC for the plasma physics and has additional engineering and economic assessment modules [29]. For instance, there is a module for the design of the TFCs and one for the calculation of individual components weights.

For the benchmark reported below, TPC and not TOPPER was used, since the available parameter sets were provided in the framework of benchmarks between TPC and PROCESS focusing in particular on the plasma physics modules [22]. These were conducted in 2011 as part of the contribution to the Broader Approach Agreement with Japan in the DEMO Design Activity [23] of the International Fusion Energy Research Centre (IFERC). The selected parameter set, named “DEMO 1-TPC”, is similar to the EU concept with the same name. It is also a large, pulsed device with conservative physics assumptions that produces about 500 MW of net electricity [23]. Based on the fact that TPC is just a physics code, no information is available on dynamical phases, power flow, divertor and power exhaust, as well as neutron and heat load. Hence, the corresponding tables with the values of TREND are presented for completeness in the appendix (see Tables A.6, A.7, A.8 and A.9).

Plasma Geometry and Radial Build Parameters

Good agreement is observed for the parameters of the plasma geometry and the radial build (see Table 3.22). TPC models a single-null configuration for the plasma volume and parametrizes the upper half of the cross-section by an ellipse and the lower half by two arcs [22]. Moreover, the plasma surface area is calculated with respect to a full elliptic cross-section explaining the observed deviation of 5 %.

Plasma Current and Magnetic Fields

Hardly any differences for the plasma current and magnetic fields can be identified as far as values for TPC are available (see Table 3.23). Again a substantial deviation is observed for the internal inductance. Similar to PROCESS and HELIOS, l_i is set as an input in TPC, i.e. no relation to the current profile peaking is implemented. In addition, neither a current nor a safety factor profile is considered explicitly. The comparable high value for l_i as calculated by TREND indicates that an assessment of the implemented modelling is advised (see Chapter 2.3.1).

Parameter	Unit	TPC	TREND	Deviation
R_0	[m]	10.0	10.0	
a	[m]	2.5	2.5	
A		4.0	4.0	
κ_X		1.85	1.85	
κ_{95}		1.66	1.66	
δ_X		0.50	0.50	
δ_{95}		0.33	0.33	
d_{SOL}	[m]		0.15	
d_{int}	[m]	1.602	1.602	
d_{TFC}	[m]	1.517	1.517	
d_{CS}	[m]		0.647	
V	[m^3]	2087	2090	
S	[m^2]	1316	1389	5 %
S_p	[m^2]		33.8	
L	[m]		22.6	

Table 3.22.: Parameters for plasma geometry and radial build as calculated by TPC and TREND for the parameter set “DEMO 1-TPC” including the relative deviation. Deviations of less than 1 % are not reported. Ref: [164]

Parameter	Unit	TPC	TREND	Deviation
I_p	[MA]	17.4	17.4	
q_{95}		3.0	3.0	
q_{cyl}			2.62	
q_0			1.0	
c_j			3.13	
l_i		0.65	1.27	64 %
B_{tot}	[T]		6.97	
B_t	[T]	6.90	6.90	
B_{tMax}	[T]	11.7	11.7	
$\langle B_p \rangle_l$	[T]		0.968	
B_V	[T]		0.655	

Table 3.23.: Parameters for plasma current and magnetic field as calculated by TPC and TREND for the parameter set “DEMO 1-TPC” including the relative deviation. Deviations of less than 1 % are not reported. Ref: [164]

Profiles for Temperature and Density

Simple parabolic profiles for temperature and density are applied in both codes leading to good conformity of all values (see Table 3.24).

Parameter	Unit	TPC	TREND	Deviation
$\langle T\rangle$	[keV]	13.2	13.2	
$\langle T\rangle_n$	[keV]	14.0	14.0	
T_0	[keV]	33.0	33.0	
c_T		2.5	2.5	
$\langle n\rangle$	[10^{20}/m^3]	0.859	0.859	
$\overline{n}_e$	[10^{20}/m^3]	0.892	0.892	
n_0	[10^{20}/m^3]	0.945	0.945	
c_n		1.1	1.1	
ρ_{ped}		1.0	1.0	
n_{GW}	[10^{20}/m^3]	0.887	0.887	
f_{GW}		1.0	1.0	

Table 3.24.: Parameters for temperature and density profiles as calculated by TPC and TREND for the parameter set “DEMO 1-TPC” including the relative deviation. Deviations of less than 1 % are not reported. Ref: [164]

Fuel and Impurities

Likewise, good agreement is observed for the impurity content of the plasma as far as information for TPC is available (see Table 3.25). Since this parameter set was originally developed for a benchmark of TPC and PROCESS, also iron was used in the impurity mix.

Parameter	Unit	TPC	TREND	Deviation
D:T			50:50	
M			2.5	
Z_{eff}		1.33	1.33	
Z_1		6	6	
Z_2		8	8	
Z_3		26	26	
f_i			0.895	
f_{DT}			0.795	
f_{He}		0.1	0.1	
f_{Z1}		0	0	
f_{Z2}		0	0	
f_{Z3}		0.0002	0.0002	
τ_p^*/τ_E			6.6	

Table 3.25.: Parameters describing the fuel content and impurities in the plasma as calculated by TPC and TREND for the parameter set “DEMO 1-TPC” including the relative deviation. Deviations of less than 1 % are not reported. Ref: [164]

Plasma Pressure and Beta

Table 3.26 summarizes parameters that describe the plasma pressure and beta. The modelling of the fast particles fraction γ_{fast} is similar, but an additional beam contribution of 0.07 % assumed by TPC leads to the observed small deviation. The difference in the normalized plasma beta β_N and its thermal component could be traced back to the particular definition. TPC uses the total plasma beta β and TREND the toroidal plasma beta β_t as reference (see Equation 2.173). But it was not possible to figure out the reasons for the variation in the poloidal plasma beta. I assume that this is based on different modelling of the poloidal magnetic field. Unfortunately, no values are reported for the latter that could help to investigate the backgrounds (see Table 3.23).

Parameter	Unit	TPC	TREND	Deviation
β_N		2.21	2.26	2 %
$\beta_{N,th}$		1.86	1.90	2 %
γ_{fast}		0.189	0.188	
β	[%]	2.23	2.24	
β_{th}	[%]	1.88	1.89	
β_t	[%]		2.28	
β_p	[%]	113	116	3 %
$\langle p_{th} \rangle$	[bar]		3.64	
p_0	[bar]		9.47	
c_p			2.6	

Table 3.26.: Parameters for the plasma pressure profile and different plasma betas as calculated by TPC and TREND for the parameter set “DEMO 1-TPC” including the relative deviation. Deviations of less than 1 % are not reported. Ref: [164]

Plasma Power Balance

A small difference is observed for the fusion power (see Table 3.27), even if the Bosch / Hale fit [76, 77] for the fusion reactivity is applied in both systems codes, the temperature and density profiles are identical, the impurity content is the same and the plasma volume is quite similar. Unfortunately, no values for the fuel content of TPC are available to compare the calculation of the fuel dilution. Another reason could be the fact that TPC allows a non-vanishing Shafranov shift. That could move the plasma outwards enlarging the highest power density regions. The operation point calculated by TREND was optimized in this case such that all of the heating power is also used for current-drive. Since identical current-drive fractions f_{CD} are assumed, the additional heating power P_{add} is equal for both codes. The optimization was done by adjusting the H-factor causing a small deviation of 1 %. The other transport loss parameters, i.e. P_{con}, τ_E and W_{th}, are still in good agreement. The deviation of the ohmic heating power P_{OH} is based on varying values for the loop voltage U_{loop} as discussed below.

The total radiation P_{rad} and the total radiation fraction f_{rad} are quite similar, but the particular contributions and the assumptions on accounting are different in both codes. Concerning the synchrotron radiation P_{syn}, TPC uses an outdated model of Trubnikov [165], whereas TREND applies the state-of-the-art model developed by Albajar et al. (see Equation 2.118). The line radiation P_{line} is calculated in TPC with averaged radiation power loss functions $\langle L_z \rangle$ based on Post et al. [86] and averaged values for temperature and density. TREND takes into account updated power loss functions and integrates along the profiles (see Chapter 2.3.4). In general, line radiation is assumed to be located predominantly at the plasma edge having reduced impact on the power balance of the plasma core. TREND accounts for this by implementing a radiating mantle region inside the separatrix (see $\rho_{core} = 0.9$). Whereas TPC simply considers only about 30 % of the calculated line radiation in the core power balance [22]. That is similar to the assumptions used in the US systems code ASC [21]. For the calculation of bremsstrahlung, TPC also uses just the averaged values for temperature and density without considering corrections to account for profile effects. Similar values of TPC and TREND indicate that the correction factor seems to be close to unity for this specific case.

Parameter	Unit	TPC	TREND	Deviation
P_{fus}	[MW]	1926	1955	1 %
P_{add}	[MW]	1.9	1.9	
P_{OH}	[MW]	0.7	0.7	1 %
Q		758	766	1 %
P_{con}	[MW]	289	289	
P_{sep}	[MW]		275	
W_{th}	[MW s]	1141	1142	
τ_E	[s]	3.94	3.95	
H		1.00	0.99	1 %
ρ_{core}		1.0	0.9	11 %
P_{rad}	[MW]	123	123	
$P_{radCore}$	[MW]	99	109	10 %
$P_{radMantle}$	[MW]	24	14	56 %
P_{syn}	[MW]	50	63	24 %
r_{syn}		0.6	0.6	
P_{brem}	[MW]	37	38	2 %
P_{line}	[MW]	36	22	50 %
$P_{lineCore}$	[MW]	12	8	38 %
$P_{lineMantle}$	[MW]	24	14	56 %
f_{rad}		0.32	0.31	3 %
P_{LH}	[MW]		154	
f_{LH}			1.79	

Table 3.27.: Parameters for the plasma power balance as calculated by TPC and TREND for the parameter set “DEMO 1-TPC” including the relative deviation. Deviations of less than 1 % are not reported. Ref: [164]

Auxiliary Current-Drive

As shown in Table 3.28 hardly any external current-drive power is applied. The significant deviation of the bootstrap current fraction f_{BS} is based on the application of different models, Nevins [59] in case of TPC and Wilson [60] for TREND. According to the plasma current balance (see Equation 2.59), that also leads to a difference of 4 % for the inductive current-drive fraction.

Parameter	Unit	TPC	TREND	Deviation
P_{CD}	[MW]	1.9	1.9	
P_{nCD}	[MW]		0.0	
$\langle\gamma_{CD}\rangle$	[10^{20}A/Wm^2]	0.30	0.30	
η_{add}			0.40	
f_{CD}		0.004	0.004	
f_{BS}		0.264	0.291	10 %
f_{ind}		0.732	0.705	4 %

Table 3.28.: Parameters describing the auxiliary current-drive as calculated by TPC and TREND for the parameter set “DEMO 1-TPC” including the relative deviation. Deviations of less than 1 % are not reported. Ref: [164]

Inductive Current-Drive and Flux Balance

Table 3.29 lists the parameters for inductive current-drive and the flux balance. The small difference in the loop voltage U_{loop} is assumed to base mainly on the deviation in the inductive current-drive fraction. Unfortunately, the contribution of the plasma resistance R_p could not be figured out, since no information on this parameter is available for TPC. Compared to TREND or HELIOS, TPC applies simplified modellings for the contribution of the central solenoid and the poloidal field coils to the total available flux swing Φ_{tot}. For instance, TPC assumes that the coils of the CS are infinitely thin implying that the current is conducted on an infinitely thin shell. Whereas the thickness of the CS used by TREND was optimized to get a current density of $j_{CS} = 16\,\text{A/mm}^2$ with respect to a maximum magnetic field of $B_{CSmax} = 13\,\text{T}$. In addition, TPC increases the calculated value for Φ_{CS} by 2 % and decreases that for Φ_{PF} by 50 % explaining the substantial differences. But the reasons for these adjustments is not reported. Moreover, it was not possible to trace back the deviation of the flux consumption for the current ramp-up Φ_{RU}, since TPC does not report the split in resistive and inductive parts. Considering the magnetic flux balance, these observations jointly cause a deviation of 15 % in the available flux swing for the current flat-top phase Φ_{flat} influencing also τ_{flat}, the corresponding time-scale of this phase.

Parameter	Unit	TPC	TREND	Deviation
τ_{flat}	[min]	519	438	17 %
U_{loop}	[V]	0.039	0.039	1 %
R_p	[Ω]		3.18×10^{-9}	
L_p	[H]		2.22×10^{-5}	
c_{Ejima}			0.36	
Φ_{tot}	[V s]	1688	1514	11 %
Φ_{CS}	[V s]	1599	1348	17 %
Φ_{PF}	[V s]	89	166	61 %
Φ_{RU}	[V s]	463	467	1 %
Φ_{res}	[V s]		79	
Φ_{ind}	[V s]		388	
Φ_{PI}	[V s]		20	
Φ_{flat}	[V s]	1205	1027	16 %
B_{CSmax}	[T]	13.0	13.0	
j_{CS}	[A/mm^2]		16.0	

Table 3.29.: Parameters for inductive current-drive and the flux balance as calculated by TPC and TREND for the parameter set “DEMO 1-TPC” including the relative deviation. Deviations of less than 1 % are not reported. Ref: [164]

4. Application: Parameter Studies on DEMO 1

Systems codes can in general be applied for a large variety of purposes. Based on the internal structure and the objectives guiding the development process, TREND has some advantages with respect to parameter studies. Hence, the results of some selected parameter studies are discussed in this chapter in order to show the application of TREND. The common idea of these studies is to analyse the implications of certain assumptions that manifest in particular values for key parameters of the power plant design. That includes the aspect ratio or the edge safety factor, for instance. These key parameters are often set a priori in conceptual design studies, but are expected to have major influence on the overall plant. Thus, the selected approach is to vary the values of these parameters individually in a reasonable range and to analyse the effects on a specific reference parameter set. In the following, an operation point for DEMO 1 was chosen as base case for the parameter studies. Detailed information about this parameter set can be found in Chapter 3.1 (see Tables 3.1 to 3.12). Moreover, a characteristic of all parameter studies is the fact that the plasma density is defined with respect to the Greenwald limit. Hence, the density scales with the plasma current according to Equations 2.170 and 2.171. That leads to different ways through the parameter space compared to initial studies where constant plasma beta was presumed.

As mentioned in the introduction, DEMO 1 is a concept for pulsed devices with conventional plasmas and mainly inductive current-drive combined with conventional technologies. The top level assumptions for DEMO 1 consist of a target for the net electric power output of about $P_{elNet} \approx 500\,\mathrm{MW}$ (see Table 1.1). That is combined in the following with a conservative constraint on the additional heating power, $P_{add} < 100\,\mathrm{MW}$. Considering the power flow scheme of TREND (see Figure 2.14), it can be shown that the net electric power is simply determined by the fusion power and the additional heating power,

$$P_{elNet} = c_1 P_{fus} - c_2 P_{add} \tag{4.1}$$

That is mainly based on the assumption that the powers for pumping, cryo and auxiliary systems scale essentially with the total thermal power. The coefficients c_1 and c_2 depend on the specific characteristics of the power flow describing the applied technologies. That includes the thermodynamic efficiency or the wall plug efficiency, for instance. For the reference design point of DEMO 1, $c_1 = 0.307$ and $c_2 = 2.22$. For comparison, the default values of TREND would imply that $c_1 = 0.389$ and $c_2 = 1.31$. The differences are basically due to the application of helium instead of water as cooling fluid and higher efficiencies for some of the involved processes. Figure 4.1 visualizes the relation of fusion power and additional heating power for fixed net electric power outputs. As a consequence of Equation 4.1, a specific value for the net electric power output is equivalent to a doublet for fusion and additional heating power in case of specified technologies, i.e.

$$P_{elNet} \equiv \left(P_{fus}, P_{add}\right) \tag{4.2}$$

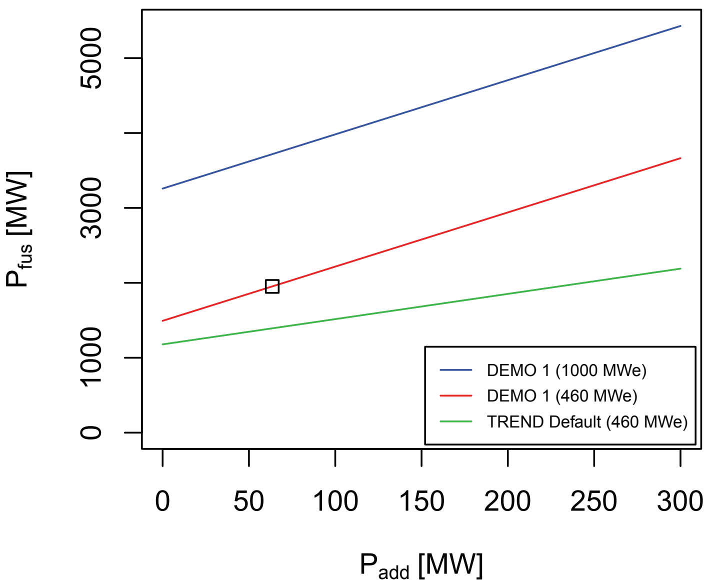

Figure 4.1.: Dependency of the required fusion power P_{fus} on the additional heating power P_{add} for a given net electric power output P_{elNet}. The black square marks the reference design point for DEMO 1. The red ($P_{elNet} = 460\,\mathrm{MW}$) and the blue ($P_{elNet} = 1000\,\mathrm{MW}$) line base on the reference parameters of DEMO 1. For the green line ($P_{elNet} = 460\,\mathrm{MW}$), the default power flow parameters of TREND are applied.

For instance, $460\,\mathrm{MW} \equiv (1950\,\mathrm{MW}, 60\,\mathrm{MW})$ for the reference parameter set of DEMO 1. Hence, the target for the net electric power output in combination with the restrictions on the additional heating power determines the requirements on fusion power. The latter is given with respect to Equation 2.106 by

$$P_{fus} \propto f_{DT}^2 \langle n_e \rangle^2 \langle \sigma v \rangle^* V \tag{4.3}$$

This formula can be transformed with the following assumptions based on Equations 2.9, 2.28, 2.44, 2.56, 2.107, 2.130, 2.133, 2.167, 2.168 and 2.170:

$$\begin{align} \langle n_e \rangle \propto n_0 \propto \overline{n}_e &\propto f_{GW} I_p A^2 / R_0^2 \tag{4.4} \\ \langle \sigma v \rangle^* &\propto \langle T \rangle_n^\alpha \qquad \text{with } \alpha > 0 \tag{4.5} \\ V &\propto \kappa_{95} R_0^3 / A^2 \tag{4.6} \\ I_p &\propto \frac{R_0 B_t}{q_{cyl} A^2} g\left(\kappa_{95}, \delta_{95}\right) \tag{4.7} \\ B_t &\propto B_{tMax} f_1\left(R_0, A\right) \tag{4.8} \\ q_{cyl} &\propto q_{95} / f_2\left(A\right) \tag{4.9} \end{align}$$

Hence, the following scaling for the electron density can be derived

$$\langle n_e \rangle \propto f_{GW} \frac{B_{tMax}}{q_{95}} \frac{f_1\left(R_0, A\right) f_2\left(A\right) g\left(\kappa_{95}, \delta_{95}\right)}{R_0} \tag{4.10}$$

leading to

$$P_{fus} \propto f_{DT}^2 f_{GW}^2 B_{tMax}^2 \frac{\langle T \rangle_n^{\alpha}}{q_{95}^2} f(R_0, A) \tag{4.11}$$

where

$$f(R_0, A) = \frac{R_0}{A^2} \left[f_1(R_0, A) \cdot f_2(A) \cdot f_3(\kappa_{95}(A), \delta_{95}(A)) \right]^2 \tag{4.12}$$

with

$$f_1(R_0, A) = 1 - \frac{1}{A} - \frac{d_{int}}{R_0} \tag{4.13}$$

$$f_2(A) = \frac{1.17 - 0.65A^{-1}}{(1 - A^{-2})^2} \tag{4.14}$$

$$f_3(\kappa_{95}, \delta_{95}) = \sqrt{\kappa_{95}} \cdot g(\kappa_{95}, \delta_{95}) \tag{4.15}$$

and

$$g(\kappa_{95}, \delta_{95}) = 1 + \kappa_{95}^2 \left(1 + 2\delta_{95}^2 - 1.2\delta_{95}^3\right) \tag{4.16}$$

$$\delta_{95}(A) = 0.5089 (\kappa_{95}(A) - 1) \tag{4.17}$$

$$\kappa_{95}(A) = 1.4883 + \frac{0.5}{A - 1} \tag{4.18}$$

Equations 4.17 and 4.18 correspond to Equations 2.167 and 2.168, but are adjusted such that both match to the values of DEMO 1 at $A = 4$. The exponent α for the temperature dependence of the profile averaged thermonuclear reaction rate $\langle \sigma v \rangle^*$ is positive, but even below one as can be seen in Figure 4.2 where the temperature profile in terms of the peak temperature was scanned based on the parameter set of DEMO 1. Other parameters including the electron density, the impurity concentrations and the machine dimensions are kept constant. This result is in line with previous work by Ward [75] and Bosch [166].

The above considerations were provoked by the following observation. During initial parameter studies, TREND often considered solutions with substantially increased fusion and heating powers as valid options, since these also satisfy the constraint on the net electric power output. But these operation points do not make an efficient use of the high amount of fusion yield, at least in terms of the recirculating power fraction. Hence, I decided to replace in the following studies the target on the net electric power output by the specific amount of fusion power in conjunction with the amount of external heating power of the DEMO 1 reference operation point (see Equation 4.2).

In addition to the power production, the corresponding time-scales are of high importance for pulsed devices. Therefore, the burn time τ_{burn} is selected as a figure of merit for the evaluation of the observed trends. The limits on the power exhaust are assessed in the following by P_{sep}/R_0 as a 0-dimensional criterion (see Chapter 2.4). The value of the reference design point for DEMO 1 is used as an upper limit keeping in mind that this value seems to be quite ambitious, at least compared to currently achieved values. But the aim of these parameter studies is not an

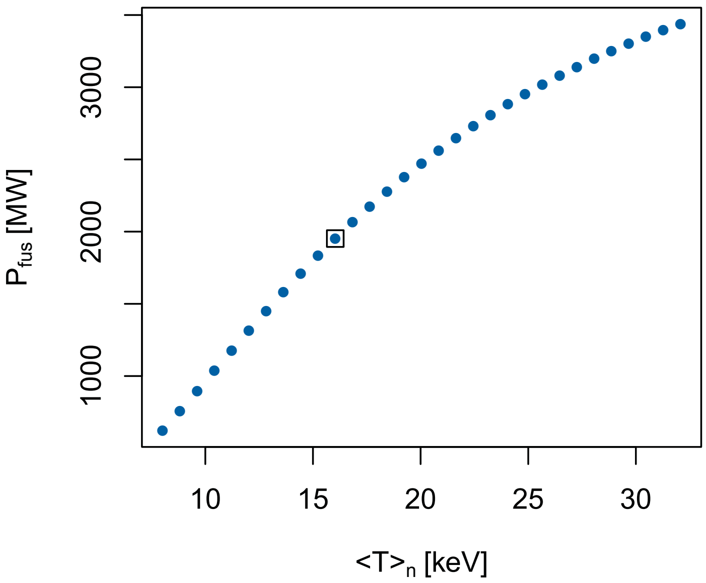

Figure 4.2.: Dependency of the fusion power P_{fus} on the density normalized plasma temperature $\langle T \rangle_n$ for DEMO 1 where only the temperature profile in terms of the core temperature was varied. The black square marks the reference design point for DEMO 1.

improvement of the current conceptual design for DEMO 1 with respect to the power exhaust conditions. These trend analyses should rather contribute to a validation of the assumptions on certain key parameters or suggest improvements for the next design iteration. Nevertheless, in order to reduce the value of P_{sep}/R_0 for the current design of DEMO 1, I would propose as first steps to change the impurity species from iron to tungsten and argon and to optimize the radiation fraction by adjusting the seeded impurity concentration, since the current operation point with $f_{LH} = 2.16$ is still well above the H-mode threshold.

4.1. Parametric Scans of the Aspect Ratio

The bending of the torus is generally characterized by the aspect ratio. In the limit of high aspect ratios, the corresponding device can locally be approximated by a cylinder. In former conceptual designs for power plants, the value of the aspect ratio is about 3 or about 4 (see Figure 2.11). That is also in line with the accumulation of experimental devices as shown in Figure 4.3. There, all ever existing tokamaks with a divertor configuration and a major radius of more than $R_0 \geq 0.5\,\mathrm{m}$ are included. The trend for aspect ratios between $A = 3-4$ comes even more obvious, if only those devices are considered that have been taken into account for the database dedicated to derive the energy confinement time scaling for ITER (see Equation 2.113). These experiments are marked in Figure 4.3 by cross-hatching. From physics point of view, there is no general limit for the aspect ratio, even if some differences are expected due to neoclassical effects [49]. The optimal aspect ratio should be an outcome of systems code analysis taking into account experimental data and technological limits.

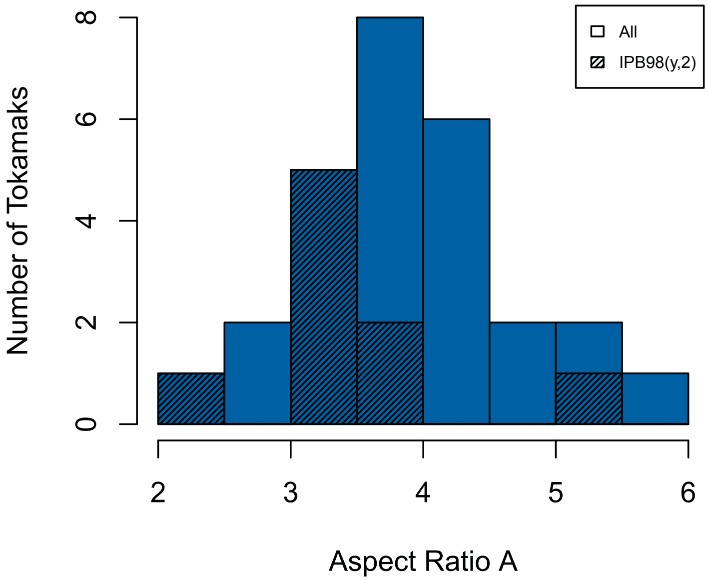

Figure 4.3.: Distribution of aspect ratios for conventional tokamaks all over the world. Only experiments with $R_0 > 0.5\,\mathrm{m}$ and a divertor configuration have been taken into account. The tokamaks that have been considered to derive the IPB(y,2) scaling law for the energy confinement time are marked by cross-hatching. Ref: [79, 80, 167]

The aspect ratio has multifaceted impact on the characteristics of the whole power plant. If only the aspect ratio is varied and all the other inputs of TREND are kept constant (i.e. R_0, d_{int}, B_{tMax}, q_{95}, H, $\langle T \rangle$, f_{GW} etc.), the following trends for increasing aspect ratios can be identified based on the reference configuration of DEMO 1 (see Figure 4.4). First of all, the size of the plasma decreases in terms of the minor radius, the plasma volume and the surface area. Based on Equation 4.18, also the elongation of the plasma cross-section declines. The toroidal magnetic field increases, since the plasma centre gets closer to the toroidal magnetic field coils. The plasma current decreases leading to lower poloidal magnetic fields and a degradation of the confinement that results in higher transport losses. Since the electron density scales with the current density due to constant Greenwald fraction, the electron density changes its trend and shows a minimum caused by similar trends for minor radius and plasma current. The aspect ratio also determines the fraction of the trapped particles in the plasma leading to an increase of the plasma conductivity. That is countered by the decrease of the cross-sectional area causing a turn of the trend for the plasma resistance. Even if the trapped particle fraction declines, the bootstrap current fraction increases due to higher poloidal plasma beta. The fact that less trapped electrons lead to lower current-drive efficiencies for NBI heating is not considered in TREND. For ECRH, it is the other way round.

Based on the discussion about the design targets for DEMO 1, the fusion power should remain more or less constant in case of variations of the operation point. A possibility to balance the effect of the aspect ratio on the fusion power (see Equation 4.11) would be to adjust the major radius. Therefore, the function $f(R_0, A)$ defined by Equation 4.12 can be evaluated, since it determines the dependency of the fusion power on the aspect ratio and the major radius. Figure 4.5

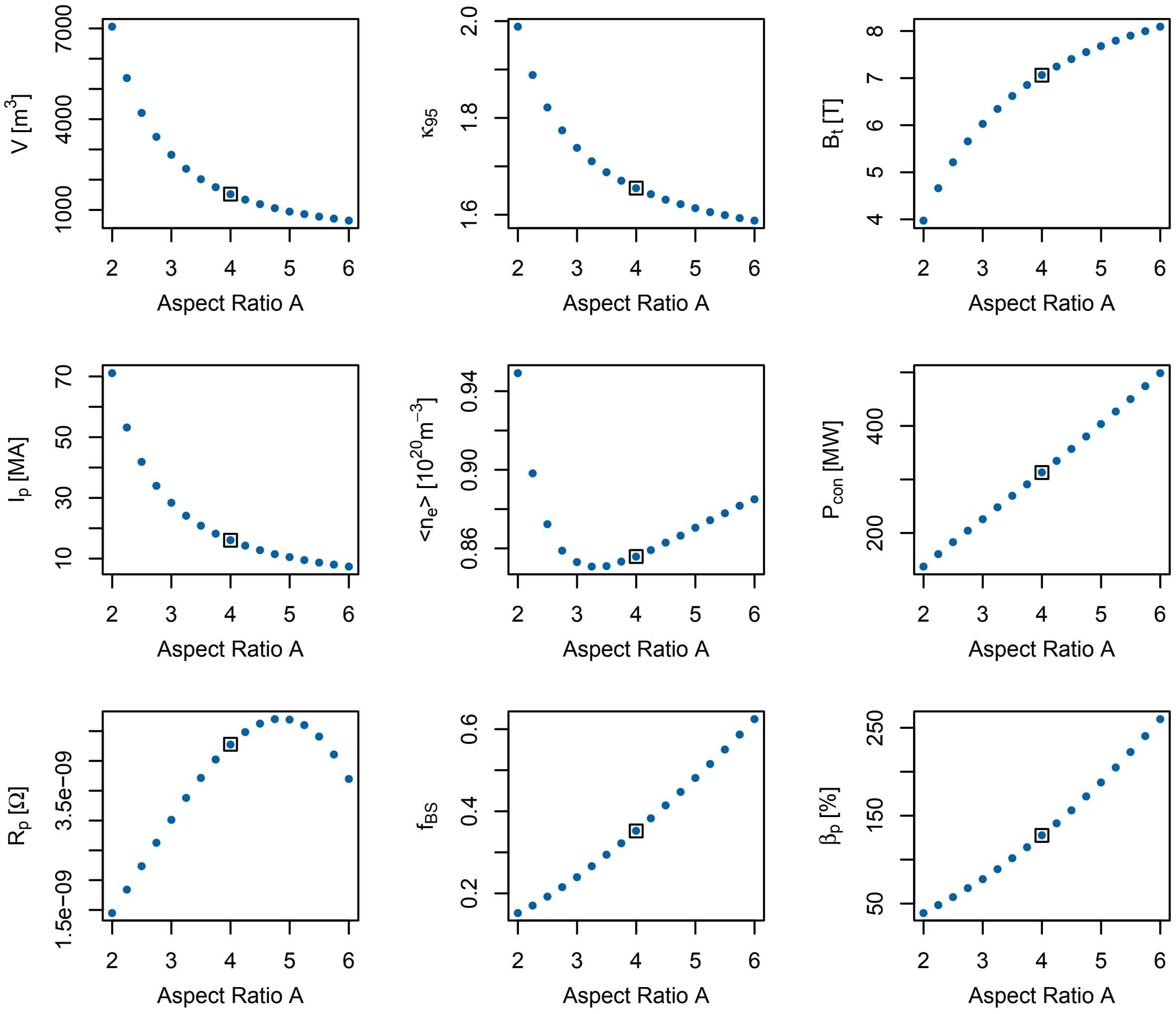

Figure 4.4.: Simple trends for variations of the aspect ratio based on a reference configuration for DEMO 1. The black square marks the DEMO 1 reference design point.

shows the results of some analytical calculations. These have been obtained by solving the equations implicitly and matching them to the DEMO 1 reference case. The red line corresponds to $f(R_0, A)$. Obviously, the trend is dominated by a scaling of $R_0 \propto A^2$ as shown by the green line. A certain smoothening results from considering the variation of the toroidal magnetic field as covered by $f_1(R_0, A)$ (see blue line and Equation 4.13).

Moreover, results of TREND are added for comparison (black circles). These are obtained by scanning the aspect ratio and the major radius. The other inputs are kept constant (i.e. d_{int}, B_{tMax}, q_{95}, H, $\langle T \rangle$, f_{GW} etc.). Then the fusion power was filtered to be conform within $\pm 50\,\mathrm{MW}$ to the reference value of DEMO 1. Other filters have been switched off. In general, quite good agreement of TREND and the analytical calculations is observed. The deviations are mainly due to the discreteness of the scan and the broadness of the filter for the fusion power. More precise scans in combination with smaller filters increased the accuracy, but caused also higher densities of points without providing any additional information. Remarkably, the curve for DEMO 1 is not far away from ITER values $(R_0 = 6.2\,\mathrm{m}; A = 3.1)$, but DEMO 1 has about four times higher fusion power. That is caused by the fact that the Greenwald density fraction and the plasma temperature are significantly lower in ITER leading also to lower values for the normalized plasma beta. In addition, the external radius of the CS for a DEMO concept with $R_0 = 6.2\,\mathrm{m}$ and $A = 2.8$ would be about $R_{CSe} \approx 0.8\,\mathrm{m}$. This calculation is based on a radial build with about $d_{int} = 1.6\,\mathrm{m}$ between the plasma and the inner leg of the TFCs and about the same distance, $d_{TFC} = 1.6\,\mathrm{m}$, for the TFCs itself. Assuming such a configuration, it is not possible to satisfy the magnetic flux balance. That also holds for some other constraints, since the corresponding filters have been switched off. Hence, some of the calculated operation points are not reliable. But the aim of this activity was only to prove, if the analytical trends can be reproduced by TREND without benefiting from additional ingredients included in systems codes.

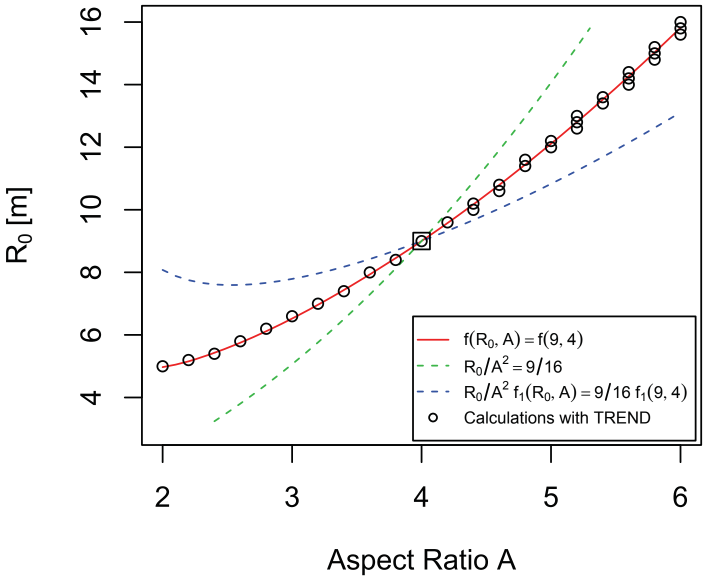

Figure 4.5.: Dependency of the major radius on the aspect ratio for constant fusion power based on Equation 4.11. The lines correspond to analytical solutions and the circles to calculations with TREND (see text). The black square marks the DEMO 1 reference design point.

In the following, TREND with all important constraints is used to analyse the impacts of variations of the aspect ratio on the machine size of DEMO 1 in terms of the major radius. The resulting operation points are evaluated with respect to the corresponding burn time. Table 4.1 lists the scanned parameters with the individual ranges and increments. Besides the aspect ratio and the major radius also other inputs are varied. That includes the helium concentration in order to consider constant particle to energy confinement ratios instead of constant helium inventory. Moreover, the temperature is varied together with the seeded iron concentration. These are methods to control the plasma power losses in terms of transport and radiation. That is mandatory due to the requirements imposed by a steady state power balance and the limits on the power exhaust. Table 4.2 contains some crucial input parameters that are kept constant. Other parameters are scaled based on the implemented scaling laws. That includes the plasma size (V, S_p, S, L), the plasma current and its peaking, the toroidal magnetic field on axis and the electron density, for instance. Moreover, the operation space is limited by filters (see Table 4.3). These are used for all parameter studies. The specific upper and lower boundaries for the fusion power, the additional heating power and the ratio of the particle to energy confinement time are chosen with respect to several viewpoints: the applied increments, the different impact of fusion and additional heating power on the net electric power output, reasonable number for different helium concentrations and the total amount of operations points that can reasonably be visualized.

Parameter	Unit	Range	Increment
A		3 – 5	0.1
R_0	[m]	7 – 14	0.2
$T_0/32.1$	[keV]	0.8 – 1.2	0.02
f_{He}		0.05 – 0.20	0.005
f_{Z3}		0 – 0.003	0.0002

Table 4.1.: Scanned parameters including individual ranges and increments for the analysis of the aspect ratio.

Parameter	Unit	Value
f_{GW}		1.0
c_n		1.5
c_T		2.5
H		1.0
q_{95}		3.0
q_0		1.0
B_{tMax}	[T]	12.34
d_{int}	[m]	1.60
d_{TFC}	[m]	1.60
f_{CD}		0.001
$\langle\gamma_{CD}\rangle$	[10^{20}A/Wm^2]	0.31

Table 4.2.: Selection of input parameters that are kept constant for the analysis of the aspect ratio.

Parameter	Filter
Φ_{flat}	$\Phi_{flat} \geq 0\,\mathrm{V\,s}$
τ_{burn}	$\tau_{burn} \geq 0\,\mathrm{s}$
P_{nCD}	$P_{nCD} \geq 0\,\mathrm{MW}$
f_{LH}	$f_{LH} \geq 1.3$
P_{fus}	$\left\|P_{fus} - 1952\,\mathrm{MW}\right\| \leq 40\,\mathrm{MW}$
P_{add}	$\left\|P_{add} - 63\,\mathrm{MW}\right\| \leq 10\,\mathrm{MW}$
τ_p^*/τ_E	$\left\|\tau_p^*/\tau_E - 6.3\right\| \leq 0.25$
P_{sep}/R_0	$P_{sep}/R_0 \leq 33.7\,\mathrm{MW/m}$

Table 4.3.: Filters that are applied for all parameter studies.

Figure 4.6 shows the results of this case study in terms of aspect ratio and major radius of the calculated operation points. The overall trend is similar to the former analytic discussion, higher aspect ratios imply larger devices with larger major radii. But the operation points do not agree properly with the analytic trend as given by the dashed black line. For small aspect ratios, the operation points have somewhat higher major radii. For high aspect ratios it is the other way round. Considering the derived scaling for the fusion power given by Equation 4.11, it seems to be promising to analyse the particular fuel content. Therefore, the operation points are coloured with respect to the individual fuel concentration. Unfortunately, the overlay of some points with different colours could not be prevented. Due to a precursory ordering of the database, always the colour that represents the highest fuel concentration is shown. This procedure is maintained also for the following analyses. Clearly, the varying fuel concentration is responsible for the observed deviations to the analytical solution. That is mainly based on a negative trend for the seeded iron concentration for increasing aspect ratios leading to a decrease of the effective ion charge (see Figure A.10). The variation of the helium concentration is less significant. Furthermore, an increase of the density normalized temperature can also be monitored that also contributes to the observed differences. Both, the variations of the plasma temperature and impurity content, are results of the combination of different constraints caused by an equalized power balance, as well as the limits on additional heating power, the power exhaust conditions and the H-mode threshold power.

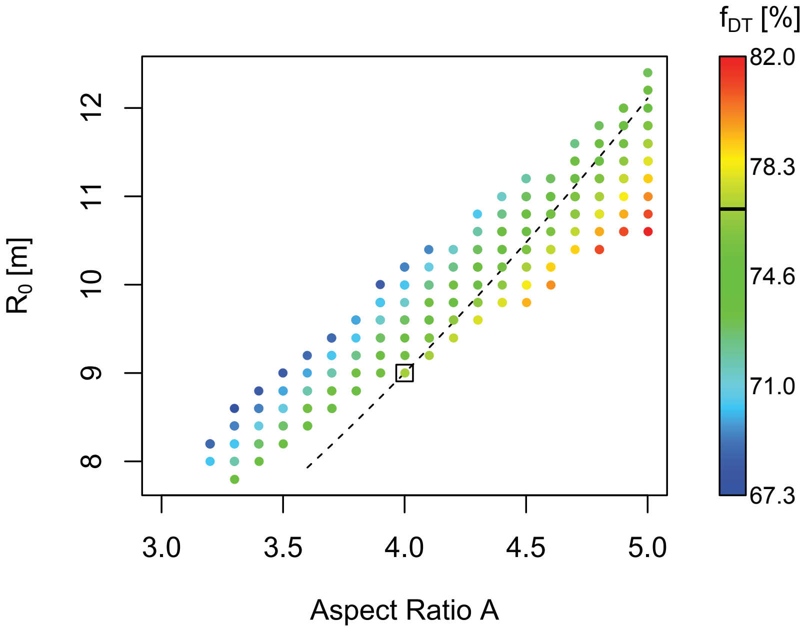

Figure 4.6.: Aspect ratio and major radius of calculated operation points with constant fusion power based on a reference configuration of DEMO 1. The operation points are coloured with respect to the individual fuel concentration. The dashed black line corresponds to an analytical analysis (see Figure 4.5 and Equation 4.12). The black square in the plot and the solid black line on the colour legend mark the DEMO 1 reference design point.

Based on the trend to larger major radii for increasing aspect ratios, one would expect that the conditions for the power exhaust in terms of P_{sep}/R_0 decrease, since the wetted area is getting larger. Therefore, the operation points are now coloured in Figure 4.7 with respect to

P_{sep}/R_0 showing that the power exhaust conditions do hardly change with increasing aspect ratios. The reason is that also the power crossing the separatrix observes a positive trend (see Figure A.11). That is mainly determined by the transport losses of the plasma core which scale like $P_{con} \propto (1+f_i)^{3.2} T_n^{3.2} h(R_0, A)$ for the prevailing circumstances (see Equation 4.19). This scaling shows the significant dependency of P_{con} on the density normalized temperature and the ion concentration. Both undergo an increase with higher aspect ratios. Fortunately, the spread of potential major radii for a fixed aspect ratio promises facilitation. Looking at one specific value for the aspect ratio, P_{sep}/R_0 decreases with increasing major radii, since the wetted area tends to get larger. But in addition, also P_{con} decreases. This evaluation of the power exhaust conditions reveals that the lowest achievable value for the analysed configurations is about $P_{sep}/R_0 \approx 21\,\mathrm{MW/m}$. That is due to the applied filter concerning the H-mode threshold power.

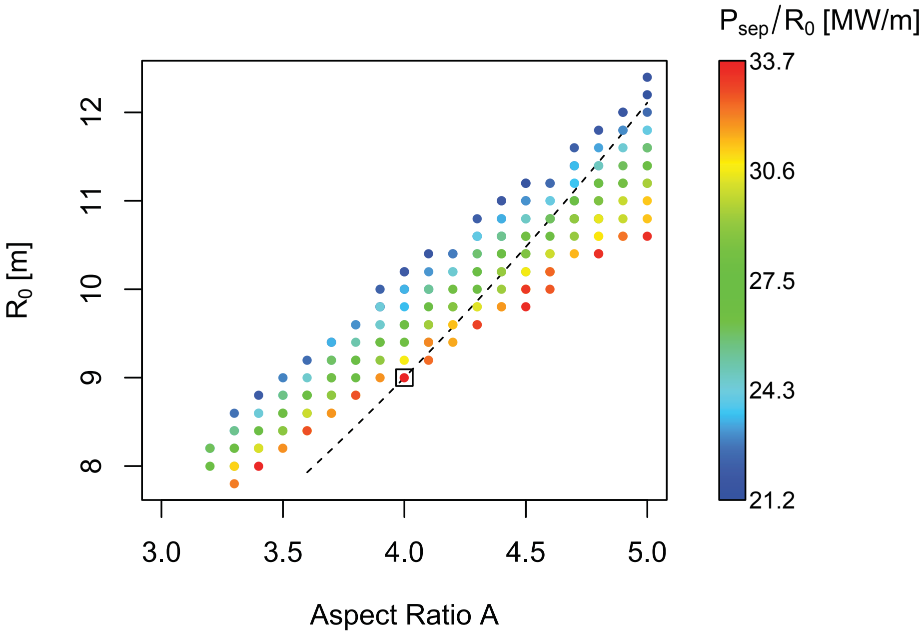

Figure 4.7.: Aspect ratio and major radius of calculated operation points with constant fusion power based on a reference configuration of DEMO 1. The operation points are coloured with respect to the individual value for P_{sep}/R_0. The dashed black line corresponds to an analytical analysis (see Figure 4.5 and Equation 4.12). The black square marks the DEMO 1 reference design point.

The observed trend for larger machine sizes allows the expectation of beneficial implications for the defined figure of merit, the burn time. The assumption of constant radial dimensions for blanket, shielding and the TFCs leads to a direct coupling of the CS dimensions to the size of the power plant. Thus, a larger device comes along with more space for the CS and consequently the provision of more magnetic flux swing. In Figure 4.8, the burn time is plotted against the aspect ratio. As expected, there is a substantial rise of the “productive” time-scale. But its magnitude leads to the assumption that the increase of the CS dimensions is not the only reason for this trend. Therefore, the operations points are coloured according to the individual loop voltage, since the burn time is determined by the time-scale for the current flat-top, $\tau_{flat} = \Phi_{flat}/U_{loop}$ (see Equation 2.78). Clearly, a significant variation of the loop voltage is observed. In order to identify the drivers for this trend, the plasma resistance and the inductively driven plasma current have to be analysed, since $U_{loop} = R_p f_{ind} I_p$ (see Equation 2.61). For this case study, all influencing parameters show clear trends supporting the development of the loop voltage for higher aspect ratios (see Figures A.10 and A.11). The plasma resistance decreases mainly due to higher temperatures, lower effective ion charge numbers and less trapped particles. The total plasma current decreases, but also the inductive current-drive fraction drops. That is due to an increase of the bootstrap current fraction based on higher poloidal beta in combination with the fact that the current driven by external heating systems is low and even kept constant. In summary, this twofold impact on the burn time leads to the result that the "productive" time-scale more than doubles for an aspect ratio of about $A = 4.3$ compared to the reference design point for DEMO 1. The "price" for this beneficial development would be an increase of the plant size to about 10 m in major radius.

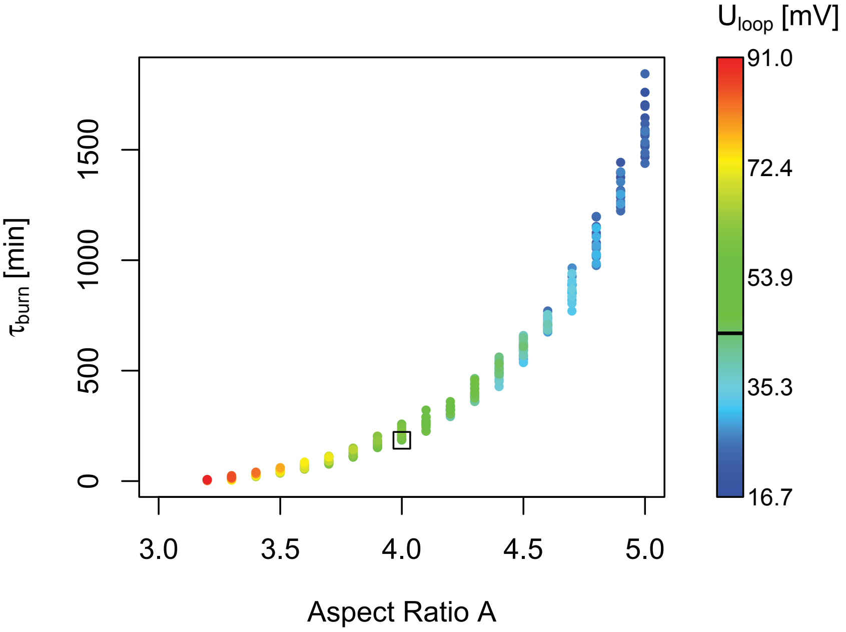

Figure 4.8.: Aspect ratio and burn time of calculated operation points with constant fusion power based on a reference configuration of DEMO 1. The operation points are coloured with respect to the individual loop voltage. The black square in the plot and the solid black line on the colour legend mark the DEMO 1 reference design point.

No operation points are observed for low aspect ratios with $A < 3.2$. The applied constraint on the fusion power force the design to small major radii for low aspect ratios. This trend is discovered in the analytical discussion, as well as in parameter scans with TREND. Hence, the diminishing space for the CS leads to the fact that at a certain point no magnetic flux swing is available for inductive current-drive in the flat-top phase. Thus, operation points with lower aspect ratios are rejected by the applied filters on the magnetic flux balance. This observation of a lower limit for the aspect ratio is only valid for machines with similar design targets, i.e. conservative assumptions about plasma performance and significant current-drive by inductive means in the flat-top phase.

In summary, low aspect ratio devices promise high plasma performances in terms of plasma current and plasma beta with all combined advantages [123, 168]. Moreover, there is also some evidence for an improvement of the economic performance with respect to the machine size.

However, one of the major concerns for low aspect ratio devices is the question of the power exhaust with respect to high plasma performance combined with small wetted areas [169]. Hence, a key driver for the design of such machines is the load on the divertor target plates. In contrary, conservative devices are rather characterized by moderate plasma performance including reasonable safety margins to the stability limits. That is often combined with pulsed operation based on the fact that the majority of the plasma current is driven inductively. Thus, a certain size for such devices in terms of the major radius seems to be mandatory, at least in case that reasonable time-scales for energy production are aspired. That implies automatically higher values for the aspect ratio in order to avoid extreme dimensions of the plasma volume causing either huge amounts of fusion power or an inefficient use of the magnetic field. This correlation of major radius and aspect ratio could be validated with TREND in the framework of this parameter study on DEMO 1. Taking into account the distribution of the existing experimental database for the development of scaling laws that are necessary for extrapolations, the choice of $A \approx 4$ for DEMO 1 seems to be wise. Nevertheless, this study showed that even small variations towards higher aspect ratios promise disproportional advantages in terms of time-scales for energy production. Doubtless, such a development could be connected with higher general investment costs. But a detailed evaluation of the economic performance seems to be promising considering the overall balance including investment costs, operation costs and the characteristics of the energy production of pulsed machines. However, the availability of reliable experimental data for this range of aspect ratios is necessary. In case that such conservative devices are envisaged, these parameter ranges should be explored by more experimental devices. Even if larger machines seem to be related to the attenuation of the power exhaust conditions due to the simple argument of increased wetted areas, it was not possible to identify significant improvements within this parameter study. Finally, the variation of the toroidal magnetic field ripple with the aspect ratio in combination with the expected losses is not implemented in TREND. Methods to balance increasing field ripples would be the adjustment of the coil thickness, the application of ferritic inserts or simply the adding of supplemental coils [169].

4.2. Parametric Scans of the Edge Safety Factor

The edge safety factor is one of the key parameters to evaluate the stability of operation points. In general, higher values come along with enhanced stability of the discharge. But there is a lower limit at $q_{95} = 2$ due to ideal MHD modes (see Chapters 2.3.1 and 2.3.7). Figure 2.12 summarizes the available operation range. For safety reasons, the lower limit was set to about $q_{95} \approx 2.3$ with a transition range up to about $q_{95} \approx 3.0$. Based on the inverse proportionality of the plasma current and the safety factor, $I_p \propto 1/q_{95}$, the plasma current can be maximized for a given magnetic field and geometric configuration by minimizing the safety factor (see Equation 2.44). Since the confinement scales basically linear with the plasma current, $q_{95} \approx 3.0$ is commonly considered for reactor studies. Even lower values would imply even higher plasma currents leading to enhanced confinement in combination with higher limits for the plasma density. By contrary, higher safety factors substantially reduce the likelihood or risk for disruptions and the corresponding disruption forces. Hence, the specific value for the edge safety factor is a trade-off between confinement and stability. In addition, lower plasma currents are expected to be attractive with respect to external current-drive requirements. Thus, the influence of the safety factor on the dynamical phases of pulsed devices is analysed in this section. Again, the configuration of DEMO 1 is selected as reference operation point.

The general impacts of the safety factor can be evaluated by a parameter scan with TREND keeping the other inputs constant (i.e. R_0, A, d_{int}, B_{tMax}, H, $\langle T \rangle$, f_{GW} etc.). Figure 4.9 shows some of the observed trends. As mentioned before, the main direct impact is on the plasma current characterized by the inverse proportionality. But that implies manifold subsequent effects, especially in case of constant Greenwald density fraction ($f_{GW} = 1.0$). Starting with the balances for current and magnetic flux, the decrease of the plasma current is accompanied by a reduction of the inductive current-drive fraction. That is mainly based on a rise of the bootstrap current fraction due to the linearity of the poloidal plasma beta with the safety factor for constant Greenwald density fraction. This trend is modulated by the dependency of the bootstrap coefficient on the increasing peaking of the current density profile for constant safety factor on axis. Thus, in combination with the decrease of the plasma current, the amount of inductively driven current diminishes. Since the requirements on flux swing in the ramp-up phase scale linear with the plasma current, more flux swing remains for the flat-top phase, even if the flux swing provided by the poloidal field coils decreases. Thus, the time-scale for the burn phase increases substantially as a consequence of both discussed trends. The main effects on the power balance are caused by the decline of the electron density based on the decrease of the Greenwald density limit with the plasma current. Hence, the fusion power as well as radiation losses fall by $1/q_{95}^2$. Furthermore, the decreasing plasma current leads to a degradation of the confinement that implies higher transport losses. These trends in combination cause serious consequences for the power exhaust as well as for the overall power balance, since an increasing amount of additional heating power is required for an equilibrated power balance. Therefore, the supply of net electric power to the grid drops to zero and even beyond.

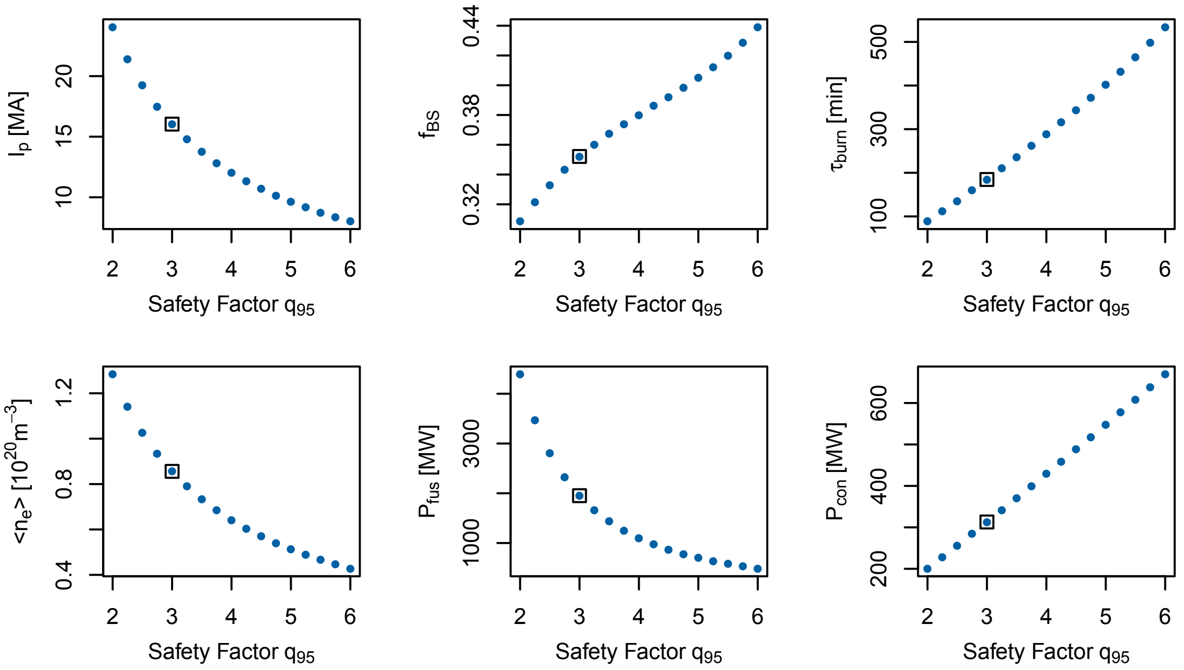

Figure 4.9.: Simple trends for variations of the edge safety factor based on a reference configuration for DEMO 1. The black square marks the DEMO 1 reference design point.

Aiming at the design targets for DEMO 1, suitable countermeasures should be applied in order to balance the discussed impacts on the fusion power. Based on Equation 4.11, one idea would be to use the plasma temperature as an adjustable screw. But also the transport and radiation losses have significant dependencies on the plasma temperature and these even exceed that of the fusion power (see Equation 4.19). It turned out in initial scoping studies that the constraints on the amount of additional heating power even force a decrease of the plasma temperature. Another idea would be to use the machine size in terms of the major radius instead. In the following, the implications of edge safety factor variations on the major radius are analysed taking into account the design objectives for DEMO 1. Similar as before, the plasma temperature, as well as the helium and the seeded impurity concentrations are also scanned for the discussed reasons. Table 4.4 lists all scanned input parameters with the individual ranges and increments. A selection of constant input parameters is given in Table 4.5. The applied filters are identical to those used before (see Table 4.3).

Parameter	Unit	Range	Increment
q_{95}		2 – 5	0.125
R_0	[m]	6 – 14	0.2
$T_0/32.1$	[keV]	0.8 – 1.2	0.02
f_{He}		0.05 – 0.15	0.005
f_{Z3}		0 – 0.003	0.0002

Table 4.4.: Scanned parameters including individual ranges and increments for the analysis of the edge safety factor.

Parameter	Unit	Value
A		4.0
f_{GW}		1.0
c_n		1.5
c_T		2.5
H		1.0
q_0		1.0
B_{tMax}	[T]	12.34
d_{int}	[m]	1.60
d_{TFC}	[m]	1.60
f_{CD}		0.001
$\langle\gamma_{CD}\rangle$	[10^{20}A/Wm^2]	0.31

Table 4.5.: Selection of input parameters that are kept constant for the analysis of the edge safety factor.

Figure 4.10 shows the results of this parameter study where the major radius is plotted against the safety factor. Based on Equation 4.11 and the preceding discussion, an increase in size for higher safety factors is expected in order to achieve fusion powers of about 1950 MW. This trend is confirmed by the calculated operation points, even if there is a certain range for each value of the safety factor. That is mainly based on different values for the helium concentration. Moreover, there are no operation points with $q_{95} > 4.125$. Considering the constraints on fusion power and additional heating, the total power losses in the plasma core by means of transport and radiation must be about 395 MW $(P_\alpha) + 63\,\mathrm{MW}\,(P_{add}) \approx 458\,\mathrm{MW}$ in order to equilibrate the power balance. In addition to the increase in size, also the temperature rises (see Figure A.12). That, in turn, causes higher transport losses, since $P_{con} \propto \langle T \rangle_n^{3.2} q_{95}^{1.1} h(R_0, A)$ according to Equation 4.19. The function $h(R_0, A)$ represents only a comparable small negative trend on the major radius. Hence, less radiation losses could be tolerated for increasing safety factors. That is confirmed by a negative trend of the seeded impurity concentration f_{Z3}. At $q_{95} = 4.125$, no further reduction is possible, since the seeded impurity concentration is already decreased down to zero (see Figure A.12). Thus, the need for lower radiation cannot be complied by less impurity content, i.e. there are no operation points beyond this point that satisfy the defined constraints. Moreover, similar trends on the safety factor for the transport losses and the major radius lead to the unfavourable expectation that the power exhaust conditions in terms of P_{sep}/R_0 remain steady, even if the size of the wetted area increases significantly. The operation points in Figure 4.10 are coloured with respect to the individual value of P_{sep}/R_0 approving the expected trend.

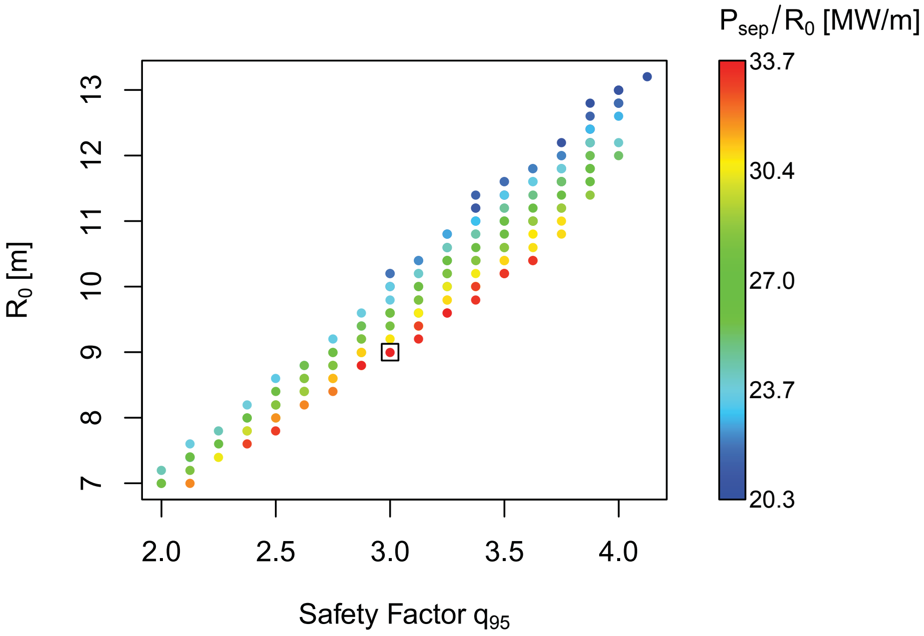

Figure 4.10.: Edge safety factor and major radius of calculated operation points with constant fusion power based on a reference configuration of DEMO 1. The operation points are coloured with respect to the individual value for P_{sep}/R_0. The black square marks the DEMO 1 reference design point.

As mentioned before, positive impacts on the dynamical phases are anticipated by higher edge safety factors in addition to higher stability of the operation point. The rationale behind this expectation is simply based on the inverse proportionality of the plasma current and the safety factor, as well as the assumption that the amount of inductively driven plasma current decreases likewise. The evaluation of the burn time is visualized in Figure 4.11. The calculated operation points are coloured with respect to the individual plasma current that is driven by inductive means. As expected, a substantial increase of the burn time with the safety factor is observed. But also a positive trend to higher absolute values for I_{ind} can be determined by the colour code. Hence, the rise of the burn time is not a consequence of the development of I_{ind}, it is even rather retarded. The background of this trend is mainly the increase of the inductive current fraction due to a drop of the bootstrap current fraction. That is supplemented by only small variations of the total plasma current, since its dependency on the safety factor is balanced by the variations of the major radius. Based on constant aspect ratios and only small trends to higher poloidal plasma betas, the decrease of the bootstrap current fraction is likely caused by the bootstrap coefficient. The latter depends in case of the applied Wilson modelling on the peaking factors for density, temperature, pressure and the current profile, as well as the aspect ratio and the effective ion charge number (see Equation 2.71). Except for c_j and Z_{eff}, the other parameters are constant. Furthermore, the current peaking even increases for higher edge safety factors, since the safety factor on axis is assumed to be fixed at $q_0 = 1.0$. Thus, the main driver for higher values of the inductive plasma current seems to be the reduction of the effective ion charge number. This trend is due to lower seeded impurity concentrations as forced by the limitations of the radiation losses.

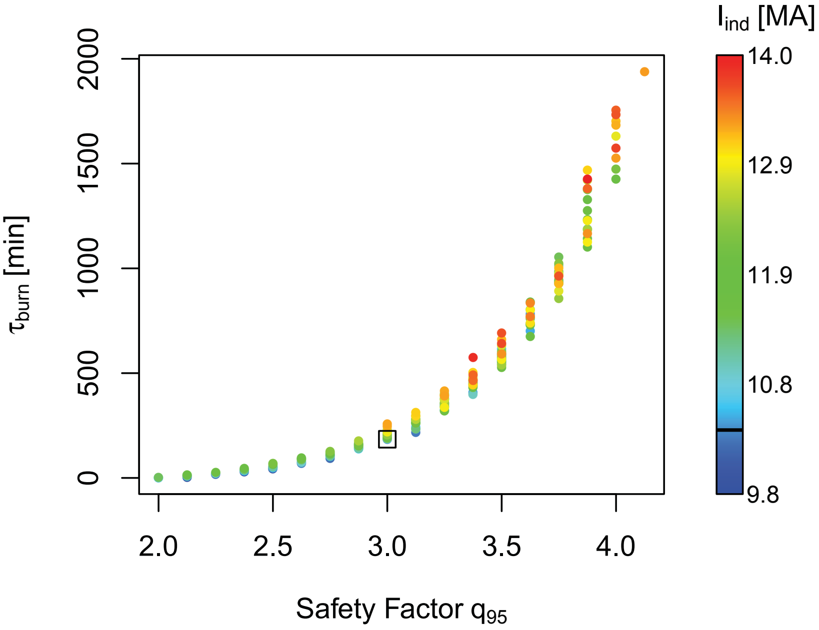

Figure 4.11.: Edge safety factor and burn time of calculated operation points with constant fusion power based on a reference configuration of DEMO 1. The operation points are coloured with respect to the individual amount of inductively driven plasma current. The black square in the plot and the solid black line on the colour legend mark the DEMO 1 reference design point.

Nevertheless, even if the inductive plasma current increases by trend, the loop voltage drops for higher safety factors (see Figure A.13). That is caused by a diminishing plasma resistance based on higher temperatures and lower effective ion charge numbers of the plasma (see Figure A.12). Furthermore, there is an increase of the available flux swing for the current flat-top phase. Considering the positive trend for the major radius, the main influencing factor is likely the amount of flux swing provided by the CS coils. This development is attenuated slightly by higher requirements on flux swing for the ramp-up phase, since both components, resistive and inductive, depend on the size of the plasma. Hence, the favourable trend of the burn time for higher safety factors can be traced back to the increase in machine size supported by a hotter and less contaminated plasma.

In summary, high edge safety factors are coupled to extensions of the productive time-scales in pulsed devices. But the variation of the operation point is dominated by negative impacts on the confinement and the density limit. Nevertheless, it could be shown that higher stability of the operation point in terms of higher values for the edge safety factor can be balanced by increasing the machine size. The other way round, low safety factors seem to support the development of compact devices. Thus, each step in the direction of higher safety factors as would be desirable considering the risks for disruptions is connected to a certain amount of money due to the observed increase in size. But that will balance to a certain extent with improved reliability and availability of the device, even if the potential disruption forces are taken into account. These are able to cause severe damages that could lead to extended downtimes for maintenance. Unfortunately, it is not possible to analyse this connection with TREND due to the lack of a sophisticated costing module and the detailed understanding of the likelihood of disruptions, as well as the connection to damage and maintenance requirements. Moreover, another positive consequence besides higher stability is the observed extension of the burn time. Productive time-scales of about 10 h seem to be realistic by simply increasing the safety factor to about $q_{95} = 3.5$. For such extended time-scales, the technical controllability of the current variation in the CS coils should be taken into account [132].

In the end, a general comment on the design of this parameter study is presented. The plasma density is set to the Greenwald limit by keeping $f_{GW} = 1.0$. This limit is proportional to the current density of the plasma (see Equation 2.170). That, in turn, depends on the total plasma current and the cross-sectional area. The latter is determined by the minor radius, at least for fixed aspect ratios. As mentioned before, it is observed that higher safety factors come along with increased major radii, i.e. increased minor radii for fixed aspect ratios. Considering the small variations of the total plasma current, the current density drops due to less cross-sectional area. Hence, a decline of the electron density is forced. That causes significant impacts on the contributors to the power balance, especially the fusion power. Therefore, in order to maintain the target value for the fusion power, the major radius must be increased. This correlation supports the trend to an increase in size of the device. Thus, the observed “explosion” of the machine dimensions could possibly be attenuated by trying to maintain the current density with adjustments of the plasma cross-section in terms of major radius and aspect ratio. That could be a specific topic for further parameter studies.

4.3. Parametric Scans of the H-factor (Energy Confinement)

The transport losses of the plasma are characterized by the energy confinement time. That is defined due to the lack of detailed understanding of the responsible physical processes as discussed in Chapter 2.3.4. For the conceptual design of ITER, several scaling laws have been developed. The so-called IPB98(y,2) scaling (see Equation 2.113) was recommended for the conceptual design of ITER [80]. The employed experimental data was selected explicitly with respect to operation scenarios for ITER. Since the operation conditions of DEMO presumably differ from those of ITER, Zohm et al. [32, 81] recently assessed the validity of the IPB98(y,2) scaling for DEMO and the following critical points have been identified. First, operation points with high plasma betas as assumed for DEMO have been excluded in the database. In addition, it is observed that the confinement in H-mode rather increases with higher plasma betas, whereas $\tau_{E,th}^{IPB98(y,2)} \propto \beta^{-0.9}$. Second, the database does hardly contain operation points above the Greenwald limit (see Figure A.4). But there is some evidence that DEMO can and consequently will operate at $\overline{n_e}/n_{GW} > 1.0$ (see Chapters 2.3.7 and 4.4). Moreover, in the vicinity of the Greenwald limit or even above, the confinement tends to deteriorate with higher densities. That is also not represented by the IPB98(y,2) scaling, since $\tau_{E,th}^{IPB98(y,2)} \propto \overline{n_e}^{0.41}$. Third, the database was explicitly restricted to operation points with limited core radiation. That is inconsistent with the assumption that DEMO will have to radiate a significant amount of the heating power in the core to attenuate the conditions in the divertor.

Therefore, the impacts of uncertainties concerning the energy confinement time are analysed in the following. A simple approach for this is the evaluation of the sensitivity of the operation points to variations of the H-factor, since the latter is also used as a figure of merit for confinement quality. In a strict sense, the H-factor directly affects just the transport losses in terms of the energy confinement time τ_E and the transport loss power P_{con}. That is shown in Figure 4.12, where just the H-factor is scanned with TREND and other input parameters are kept constant (i.e. R_0, A, d_{int}, B_{tMax}, q_{95}, $\langle T \rangle$, f_{GW} etc.). Similar to Equation 4.11 for the fusion power, the following scaling can be derived for the transport loss power in the plasma core,

$$P_{con} \propto H^{-3.2} \langle T \rangle_n^{3.2} f_{GW}^{1.9} q_{95}^{1.1} (1 + f_i)^{3.2} h(R_0, A) \tag{4.19}$$

where

$$h(R_0, A) = R_0^{-1.6} A^{1.4} \kappa_{95}^{0.7} \Big[f_1(R_0, A) \Big]^{-1.6} \Big[f_2(A) \cdot g(\kappa_{95}, \delta_{95}) \Big]^{-1.1} \tag{4.20}$$

and $f_1(R_0, A)$, $f_2(A)$, as well as $g(\kappa_{95}, \delta_{95})$ are defined in Equations 4.13, 4.14 and 4.16. Other parameters like the toroidal magnetic field at the inboard leg of the TFCs are neglected, since these are considered as constants. Based on the high exponent of the H-factor, the transport loss power changes significantly for small variations of $H = 1.0 \pm 25\,\%$. That, in turn, causes considerable effects on the operation point in terms of requirements on additional heating power, the margin to the H-mode threshold power and the power exhaust conditions.

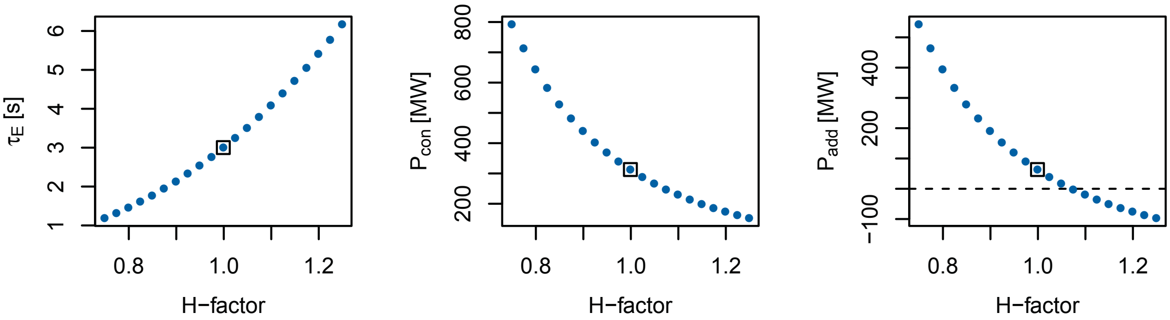

Figure 4.12.: Simple trends for variations of the H-factor based on a reference configuration for DEMO 1. The black square marks the DEMO 1 reference design point.

Thus, adequate counteractive measures have to be applied to stabilize the transport losses in order to satisfy the defined constraints and to achieve the design targets. An intuitive measure would be the adjustment of the plasma current by varying the edge safety factor. But initial scoping studies revealed that the stabilization of the transport losses is infeasible due to substantial differences in the corresponding exponents of both parameters based on a constant Greenwald density fraction (see Equation 4.19). In addition, the necessary changes of the safety factor would lead to substantial variations of the fusion power (see Equation 4.11). That would cause the elimination of most operation points by the corresponding filter on the fusion power. Hence, it is inevitable to consider a more comprehensive analysis including also the plasma temperature and the seeded impurities. Again, a reference design point of DEMO 1 is selected to analyse the impacts of over and underestimation of the energy confinement. Table 4.6 summarizes the scanned parameters. Several constant input parameters are given in Table 4.7, the applied filters again in Table 4.3.

Parameter	Unit	Range	Increment
H		0.75 – 1.25	0.025
q_{95}		2 – 4	0.05
$T_0/32.1$	[keV]	0.7 – 1.3	0.02
f_{He}		0.05 – 0.20	0.005
f_{Z3}		0 – 0.003	0.0002

Table 4.6.: Scanned parameters including individual ranges and increments for the analysis of the energy confinement.

Parameter	Unit	Value
R_0	[m]	9.0
A		4.0
f_{GW}		1.0
c_n		1.5
c_T		2.5
q_0		1.0
B_{tMax}	[T]	12.34
d_{int}	[m]	1.60
d_{TFC}	[m]	1.60
f_{CD}		0.001
$\langle\gamma_{CD}\rangle$	[10^{20}A/Wm^2]	0.31

Table 4.7.: Selection of input parameters that are kept constant for the analysis of the energy confinement.

In general, the transport losses are limited by two constraints that are represented by means of filters in TREND. The H-mode threshold power including the discussed safety margin imposes a limit for low values. On the other side, the power exhaust conditions characterized by P_{sep}/R_0 constitute an upper limit. Hence, the operation range for the plasma temperature as a major influencing factor is restricted, since the density is defined with respect to the Greenwald limit ($f_{GW} = 1.0$). A quite linear trend between the H-factor and the plasma temperature is observed within this parameter study (see Figure A.14). That seems to be reasonable considering the discussed limits for the transport losses and the fact that both parameters have the same exponent in the derived scaling for P_{con} (see Equation 4.19). Higher temperatures would lead to an enhancement of the fusion power. Thus, the edge safety factor can be raised in order to maintain the target value for the fusion power. This effect is attenuated by higher fuel dilution, since the particle confinement increases due to the assumed proportionality to the energy confinement resulting in higher helium concentrations. Therefore, the seeded impurity concentration can be lowered moderately keeping the effective ion charge number more or less constant. Moreover, the rise of the temperature also causes a positive trend for the normalized plasma beta, since the electron density is connected to the plasma current by a constant Greenwald fraction.

The burn time as figure of merit for the time-scale of energy production is plotted against the H-factor in Figure 4.13. Clearly, a rise of the burn time is observed for increasing confinement. One of the key drivers for this trend is certainly the loop voltage, since no major variations of the available flux swing are expected. Therefore, the individual value of the loop voltage is used to colour the calculated operations points. The observed drop for higher H-factors can be traced back to the increase of the plasma temperature and the decrease of the plasma current. The temperature directly affects the plasma resistance and both, temperature and plasma current, influence the poloidal plasma beta. That, in turn, causes an increase of the bootstrap current fraction leading in combination with lower plasma current to less inductively driven current. In addition, the magnetic flux swing that is available for the current flat-top phase slightly increases as well (see Figure A.15). That is based on the one hand on a diminution of the flux swing requirements for current ramp-up due to less plasma current. On the other hand, more of the CS flux swing can be used for the flat-top phase, since less flux swing of the CS coils is required in the ramp-up phase based on higher flux swing supply of the PFCs. The latter depends via vertical magnetic field on the plasma current and the poloidal plasma beta.

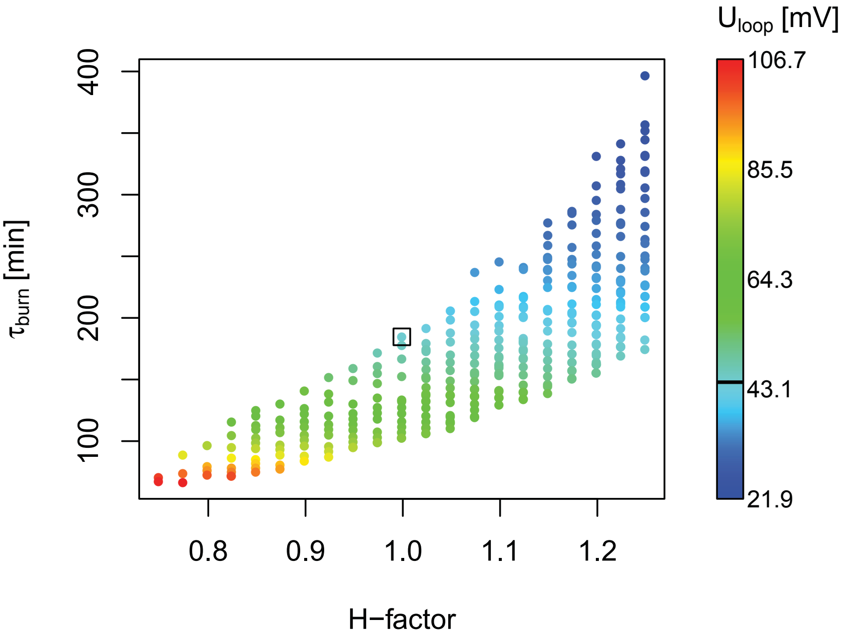

Figure 4.13.: H-factor and burn time of calculated operation points with constant fusion power based on a reference configuration of DEMO 1. The operation points are coloured with respect to the individual loop voltage. The black square in the plot and the solid black line on the colour legend mark the DEMO 1 reference design point.

The evaluation of the power exhaust conditions is presented in Figure 4.14 where the individual values for the edge safety factor are used for colouring. The operation points are basically spread over the whole parameter space. That is limited on the upper end by the applied filter on P_{sep}/R_0. Since no variation of the machine size is considered, the lower end represents the requirements on P_{sep} due to the H-mode threshold power. No distinctive dependency on the H-factor can be determined for the specific conditions of this parameter study. One of the reasons for this observation is the simultaneous variation of the H-factor and the plasma temperature. But considering a specific value of the H-factor, the power exhaust conditions can be modulated by small variations of the safety factor. Lower values for q_{95}, i.e. higher plasma current, lead to better confinement. That implies less transport losses and consequently lower P_{sep}/R_0, since the size of the device is not changed and the radiation in the mantle is marginal here. In the course of such an optimization of the operation point, the margin to the H-mode threshold power and the stability limits should also be considered.

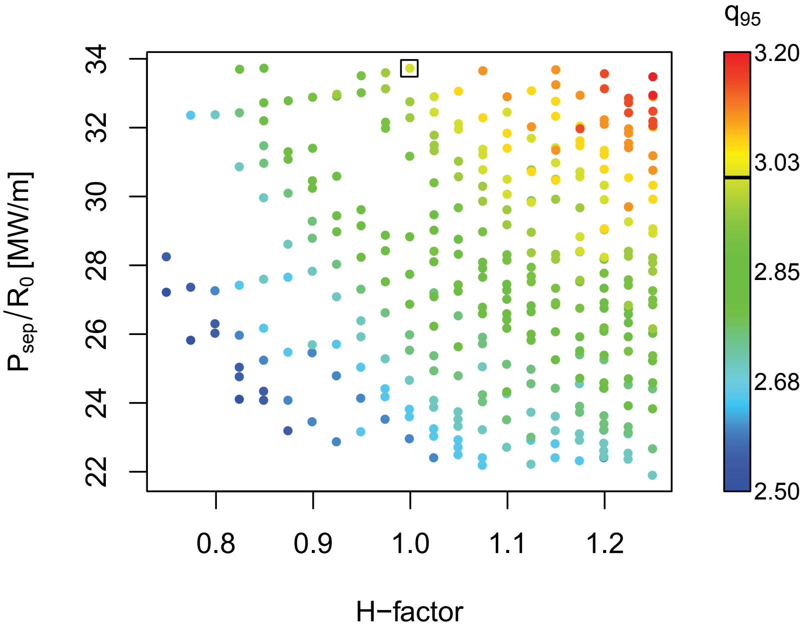

Figure 4.14.: H-factor and power exhaust conditions of calculated operation points with constant fusion power based on a reference configuration of DEMO 1. The operation points are coloured with respect to the individual value of the edge safety factor. The black square in the plot and the solid black line on the colour legend mark the DEMO 1 reference design point.

In summary, the underestimation of the energy confinement by current scaling laws as represented by higher values for the H-factor is observed to result in higher plasma temperatures and higher edge safety factors. That comes along with higher stability of the operation point and an extension of the pulse length leading to longer “productive” time-scales of the machine. Hence, better confinement would increase the reliability of the device without additional efforts or could help to save investment costs, since a reduction of the machine size could be contemplated. But in case of overestimation of the energy confinement, the edge safety factor has to be lowered in order to achieve the design objectives. Thus, the stability of the operation point could get a severe challenge. Moreover, the time-scale for energy production is reduced from about 3 h to just 2 h or even less. Hence, an increase in size could get necessary combined with a potential rise of investment costs. Therefore, further assessment of the confinement scaling laws seems to be beneficial in order to reduce the uncertainties for confinement predictions allowing more reliable designs of DEMO and beyond. Recently, some activities are started at the Max-Planck-Institute for Plasma Physics (IPP) where the specific characteristics of plasmas as foreseen in DEMO are analysed, i.e. higher radiation, higher Greenwald fraction and higher plasma beta compared to the ITER reference scenarios. The ultimate target of these activities is a comprehensive description of the transport losses in terms of DEMO-relevant scaling laws.

4.4. Parametric Scans of the Greenwald Fraction (Density Limit)

High plasma densities in fusion devices are beneficial for the plasma performance, since the fusion power is proportional to $\langle n_e \rangle^2$. But experimental observations show that the plasma density is limited in tokamaks by the Greenwald density (see Chapter 2.3.7 and Equation 2.170). Recent experiments with peaked density profiles lead to the assumption that this limit is rather an edge phenomenon limiting the pedestal density instead of the line-averaged density as a global parameter (see Figure A.5). Moreover, the density profiles in fusion reactors are assumed to be peaked substantially due to low collisionality [109, 110]. Thus, there seems to be some evidence that values up to $f_{GW} = \overline{n}_e / n_{GW} \approx 1.5$ can realistically be reached for permanent operation. The implications of such increases compared to the reference value of $f_{GW} = 1.0$ for DEMO 1 are analysed in the following.

First of all, the basic trends on the Greenwald density fraction for the configuration of DEMO 1 are evaluated with TREND without considering operational limits and the design targets. That is done by variations of f_{GW} while keeping other inputs constant (i.e. R_0, A, d_{int}, B_{tMax}, q_{95}, H, $\langle T \rangle$ etc.). As shown in Figure 4.15, the volume-averaged electron density increases linearly with increasing Greenwald fraction, since the profile shape in terms of the density peaking factor α_n is kept constant. That, in turn, implies various subsequent effects. Since the plasma temperature is kept constant, the plasma pressure and the plasma beta increase accordingly to the electron density. The same holds for the thermal energy content of the plasma causing higher transport losses. Moreover, the different processes contributing to the radiation losses of the plasma core like synchrotron, bremsstrahlung and line radiation obey all positive trends on the plasma density. These power losses are balanced somewhat by higher fusion power that scales quadratically with the electron density, as mentioned before. Hence, the additional heating power that has to be applied to maintain an equalized power balance remains within a small range. Due to an increase of the poloidal plasma beta, the bootstrap current fraction rises resulting in relaxed requirements on inductive current-drive. That is characterized by a drop of the loop voltage. Furthermore, higher poloidal plasma betas also require higher vertical magnetic fields. These, in turn, are in charge for increased magnetic flux swing by the PFCs. Both trends in combination involve an increase of the burn time. Finally, despite higher transport losses that may induce more serious conditions for the power exhaust, this simple analysis showed several advantageous trends that come along with higher plasma densities.

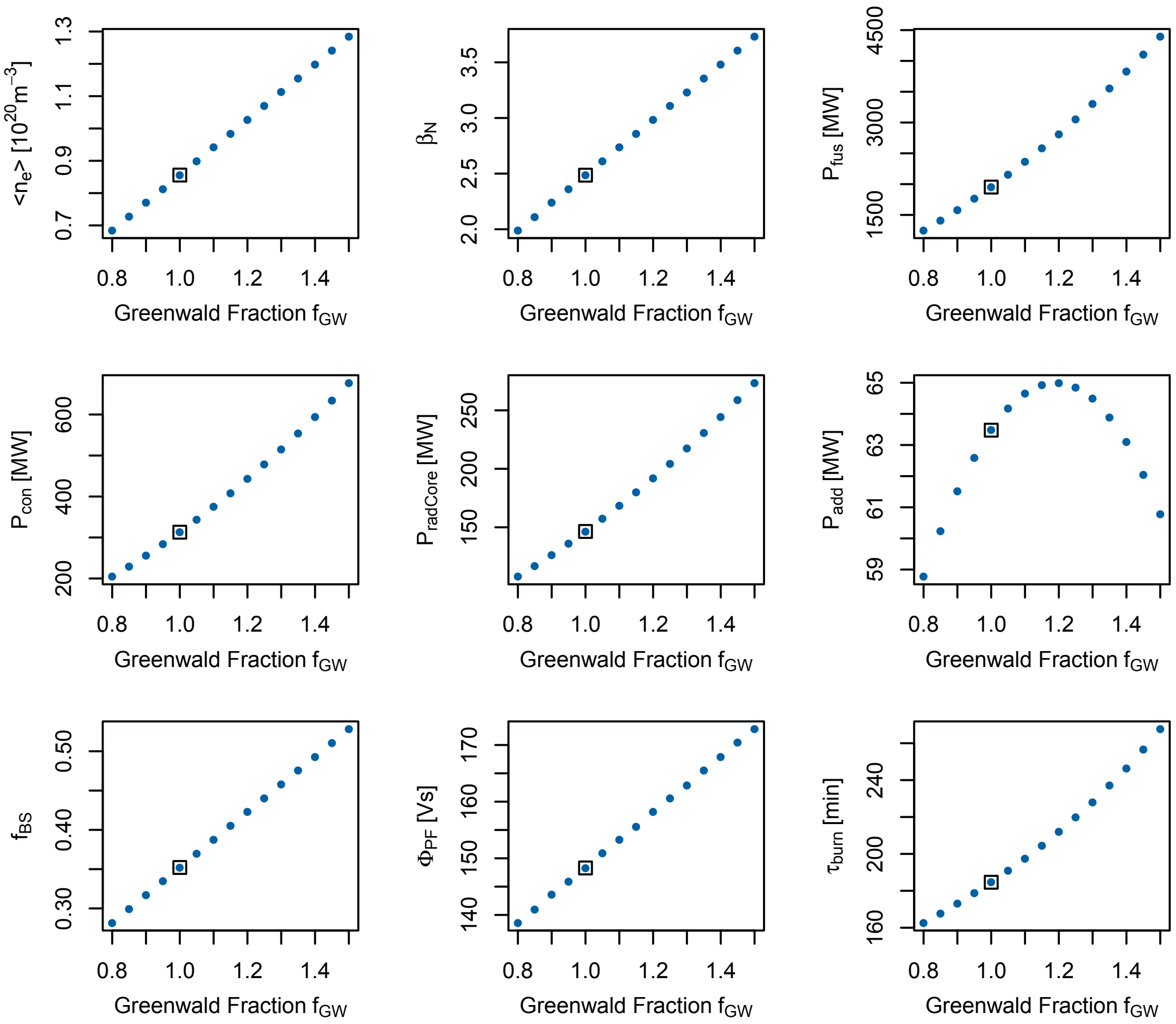

Figure 4.15.: Simple trends for variations of the Greenwald fraction based on a reference configuration for DEMO 1. The black square marks the DEMO 1 reference design point.

Considering the derived scaling for the fusion power (see Equation 4.11), there seem to be a few adjustable screws to counteract the increase in fusion power in order to maintain the design goals for DEMO 1. First, the plasma temperature would be an auspicious candidate, since the product of density and temperature determines the plasma beta for a given magnetic configuration. Hence, higher densities combined with disproportionate lower temperatures according to the exponents for constant fusion power would also imply higher MHD stability. But the operational window for the plasma temperature is generally dominated by the limits on the transport losses. The H-mode threshold power restricts the temperature at the lower end and the power exhaust conditions impose a limit for high temperatures, as discussed in the previous section. Therefore, the plasma temperature combined with the seeded impurity concentration is used to satisfy the constraints on the power balance and especially on the transport losses. Further promising candidates are the plasma current and the machine size in terms of the major radius. Thus, the first scenario to analyse the implications of increased plasma densities on the operation point is based on a fixed device that is defined by given values for major radius, aspect ratio, plasma shaping, etc. Besides the edge safety factor to vary the plasma current, the plasma temperature and the seeded impurities are scanned. The particular ranges and increments are listed in Table 4.8. Furthermore, Table 4.9 contains a selection of input parameters that are kept constant. The applied filters are identical to those used before (see Table 4.3).

Parameter	Unit	Range	Increment
f_{GW}		0.8 – 1.5	0.05
q_{95}		2 – 5	0.05
$T_0/32.1$	[keV]	0.5 – 1.5	0.02
f_{He}		0 – 0.25	0.005
f_{Z3}		0 – 0.003	0.0002

Table 4.8.: Scanned parameters including individual ranges and increments for the analysis of the density limit for scenario (S1).

Parameter	Unit	Value	Scenario
R_0	[m]	9.0	(S1)
A		4.0	
c_n		1.5	
c_T		2.5	
H		1.0	
q_{95}		3.0	(S2)
q_0		1.0	
B_{tMax}	[T]	12.34	
d_{int}	[m]	1.60	
d_{TFC}	[m]	1.60	
f_{CD}		0.001	
$\langle\gamma_{CD}\rangle$	[10^{20}A/Wm^2]	0.31	

Table 4.9.: Selection of input parameters that are kept constant for the analysis of the density limit. The major radius and the safety factor are constants just for one of the two scenarios (see Tables 4.8 and 4.10).

The main results of this scenario are basically lower plasma temperatures and higher edge safety factors for increasing Greenwald fractions (see Figure A.16). The operation range for the plasma temperature is rather small, whereas the safety factor and consequently the plasma current observe a wider distribution for a specific value of the Greenwald fraction. Based on the trend to disproportional lower plasma temperatures compared to the increase of the plasma density, the plasma beta decreases. But the normalized plasma beta observes rather a positive trend due to less plasma current. Furthermore, the helium concentration drops somewhat with respect to lower confinement. In combination with moderate variations of the seeded impurities, the fuel concentration increases more and more. Hence, the conditions for fusion reactions improve considering in addition the higher absolute densities. Therefore, more space for transformations towards higher stability given by lower plasma current becomes available. But these advantageous conditions do not penetrate directly to longer pulse length as may be expected. Higher poloidal plasma betas lead to higher bootstrap current fractions and in combination with the decrease of the total plasma current, the amount of inductively driven current is reduced (see

Figure A.17). Moreover, the requirements on magnetic flux swing for current ramp-up diminish due to less plasma current. That, in turn, allows an increase of the amount of available flux swing for the current flat-top phase. But the trend to lower plasma temperatures causes higher plasma resistance which dominates the trend for the loop voltage. Thus, the latter observes a moderate increase for higher Greenwald fractions with a significant spread due to the discussed counteracting effects. That also leads to a broad distribution of the burn time as can be seen in Figure 4.16 where the calculated operation points are coloured with respect to the individual loop voltage. The distribution narrows somewhat for higher Greenwald fractions resulting mainly from smaller ranges for the edge safety factor. Moreover, based on the fixed size of the machine, the power exhaust conditions are primarily constituted by the transport losses. For these, also no clear trend can be identified. Again a wide distribution is observed that is determined by the variation of the ion concentration and limited by the discussed constraints.

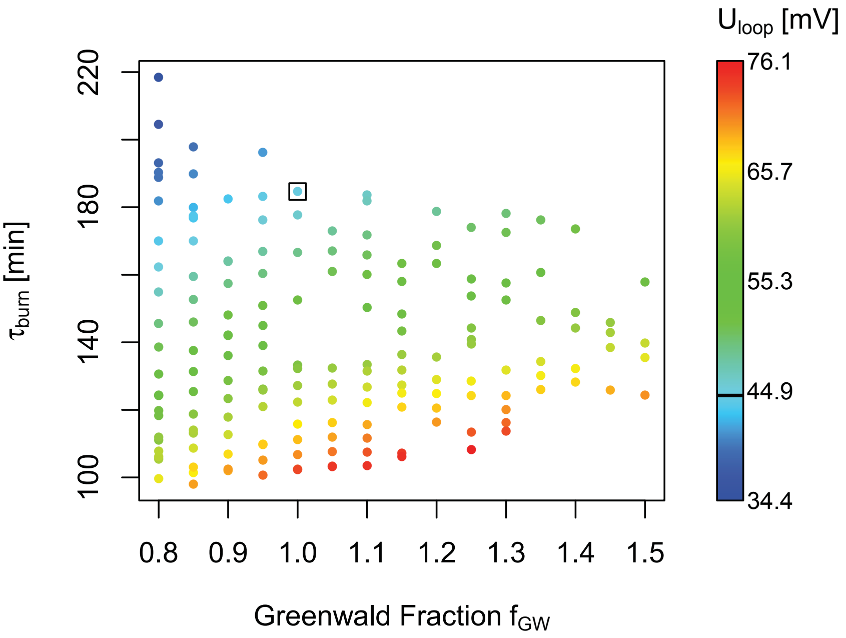

Figure 4.16.: Greenwald fraction and burn time of calculated operation points for scenario (S1) with constant fusion power based on a reference configuration of DEMO 1. The operation points are coloured with respect to the individual loop voltage. The black square in the plot and the solid black line on the colour legend mark the DEMO 1 reference design point.

The second scenario is dedicated to analyse the impacts of increased plasma density due to higher Greenwald fractions on the size of the machine. Table 4.10 shows the scanned parameters of this parameter study including the individual ranges and increments. Besides the Greenwald fraction and the major radius, again the plasma temperature, the seeded impurities and the helium concentration are varied in order to consider the constraints based on the power exhaust, as well as the power and the particle balance. Since this parameter study is quite similar to the preceding, the same selection of constant input parameters is used, just the safety factor is replaced by the major radius (see Table 4.9). Likewise, the applied filters can be found in Table 4.3.

As expected, the gains in absolute density based on higher Greenwald fractions allow a decrease of the machine size, since constant fusion power is claimed (see Figure A.18). Moreover, it can

Parameter	Unit	Range	Increment
f_{GW}		0.8 – 1.5	0.05
R_0		7 – 14	0.2
$T_0/32.1$	[keV]	0.5 – 1.5	0.02
f_{He}		0.05 – 0.20	0.005
f_{Z3}		0 – 0.003	0.0002

Table 4.10.: Scanned parameters including individual ranges and increments for the assessment of the density limit for scenario (S2).

be observed that the temperature decreases significantly. But this trend is not able to dominate the pressure balance, since the plasma beta still increases for higher Greenwald fractions. The decline in major radius results in a drop of the plasma current for otherwise fixed conditions. Hence, the normalized plasma beta increases, but stays still below the considered MHD limits. The same trend holds for the poloidal plasma beta leading to higher fractions of the bootstrap current. Less total plasma current and higher bootstrap current fractions combine to a drop of the inductively driven current. That, in turn, favours a decline of the loop voltage. But again, the plasma resistance increases significantly due to lower temperatures and dominates the development of the loop voltage such that it increases for higher Greenwald fractions (see Figure A.19). Furthermore, even if the requirements on magnetic flux swing for the current ramp-up reduce based on less total plasma current, the available flux swing for the current flat-top phase decreases. The main driver of this trend is the reduction of radial space for the CS coils due to smaller major radii. That combination causes a substantial decrease of the burn time for higher Greenwald fractions as shown in Figure 4.17. There, the operation points are coloured with respect to the external radius of the CS coils in order to visualize the discussed correlation. In addition, the weak trend towards lower transport losses for higher Greenwald fractions is attenuated by the fact that in smaller devices the wetted area diminishes. Thus, the power exhaust conditions do hardly benefit from the increase of the plasma density as would be expected, since the radiation losses scale about quadratically with the plasma density.

In summary, besides higher stability in terms of higher edge safety factors in the first scenario, no clear advantages could be identified in both studies. The second scenario even indicates that the gains in plasma performance by increased densities lead to an unfavourable decline of the burn time. Since DEMO 1 relies mainly on inductive current-drive, the space for the CS coils is of high importance. Hence, a major radius of about 9 m and even more seems to be inevitable depending on the details of the radial build. The other parameters should be selected by optimizing the design with respect to existing limits and the particular safety margins. In this context, a beneficial result of the first scenario is that the assumptions on the safety margins for the density and the safety factor seem to be antagonists. That means, higher edge safety factors can simply be realized by reducing the safety margin to the density limit and vice versa without affecting the power exhaust conditions and the time-scales for energy production in large scales. Therefore, the stability of the discharge with respect to both parameters can be balanced well for a given configuration of the machine. Finally, the advantages of increased densities for the power exhaust conditions as observed experimentally could not be validated within these parameter studies conducted with TREND. That is certainly based on the simple modelling of the divertor module. In particular, the radiation in the divertor region is modelled rather simplistic without considering the significant dependency on the plasma density. Hence, it is assumed that the analysis of operation points with high densities would benefit from improvements of the divertor module.

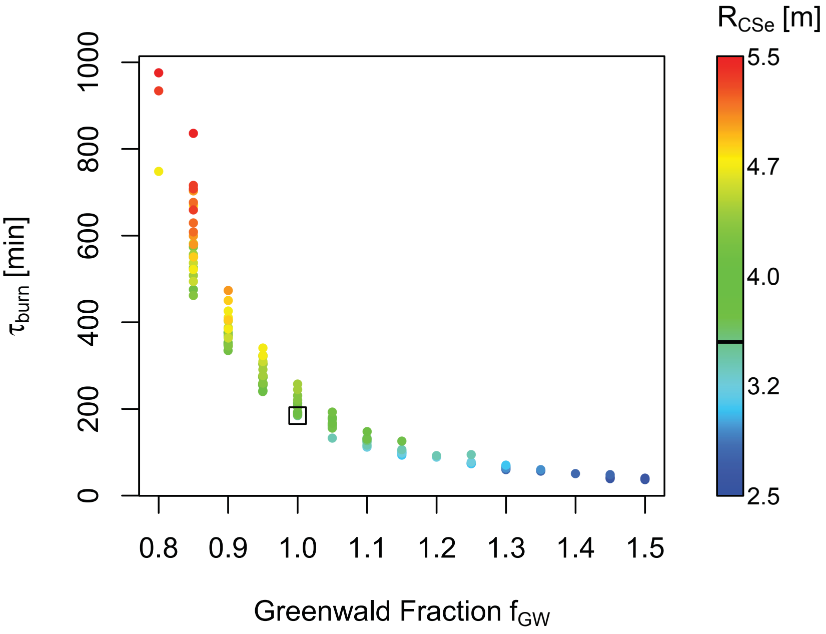

Figure 4.17.: Greenwald fraction and burn time of calculated operation points for scenario (S2) with constant fusion power based on a reference configuration of DEMO 1. The operation points are coloured with respect to the individual loop voltage. The black square in the plot and the solid black line on the colour legend mark the DEMO 1 reference design point.

5. Conclusions and Outlook

This thesis is about the development of the systems code TREND, its validation in terms of benchmarks with others systems codes and its application by means of four parameter studies based on a reference design for DEMO. Therefore, it is structured in three main chapters according to these three aspects. In the following, a summary of each chapter including conclusions and outlooks is presented.

Methodology: The Systems Code TREND

Chapter 2 covers the general structure of TREND and the implemented modellings of all existing modules. The key modellings are discussed in the following characterizing them in different categories: (I) state-of-the-art modelling, (II) proposals for updates, (IIIa) proposals for updates with proposals for simple modellings requiring further work and (IIIb) proposals for updates with proposals for advanced modellings (see also Tables A.10 and A.11). During the development of TREND, the available modellings of existing systems codes were assessed and compared to the scientific progress. As far as the modellings were consistent with state-of-the-art knowledge, these have been implemented in TREND. But for some of them, a need for improvement could be identified. In case that an updated modelling was available or a new modelling could be developed, the existing one was replaced. Otherwise, the hitherto existing modelling was implemented in TREND and work on improvements was initiated.

Concerning the general structure of systems codes, modular architectures are state-of-the-art and more and more systems codes apply this concept, including TREND. The present version of TREND consists of all basic modules for systems codes (see Table 2.1). Unfortunately, some modules are in a rather rudimentary status like the costing and the divertor module. Moreover, compared to the extent of comprehensive systems codes (see Table 2.2), TREND misses additional modules including those for magnets or maintenance, for instance. Since the development of TREND was focused so far on the core physics module, this module is one of the strengths compared to other systems codes. There are different reasons for the concentration on this specific module. First, TREND originates from a set of mainly physics equations derived and applied by Zohm [9]. Furthermore, I was part of a team that is working on physics guidelines for the conceptual design of DEMO [31, 32, 95]. Hence, the proposed guidelines could directly be verified for practical use by implementing them in TREND. In addition, the access to a wide network of experts on plasma physics within the Max-Planck-Institute for Plasma Physics (IPP) was advantageous during the development phase. Finally, the core physics module is also the core of comprehensive systems codes and most of the other modules rely on an accurate modelling.

One of the improvement needs that could be identified during the development of TREND is the lack of a relation between the current profile, the safety factor profile and the internal inductance including appropriate modellings. So far, this topic was mainly handled by setting input values for some parameters like the edge safety factor and the internal inductance. The equations presented in Chapter 2.3.1 can be seen as a first step in order to enhance the self-consistency in systems codes. But especially the proposed modelling for the internal inductance leads to comparable high values for elongated plasmas, since the applied scalings were developed assuming circular plasma shapes. Hence, more work on this topic seems to be necessary. In addition, Equation 2.44 is widely used to calculate the total plasma current. Since this equation was developed for ITER configurations, the validation for DEMO and beyond should be assessed in combination with accurate modellings for the current profile in order to extend the simple parabolic type profiles to more flexible shapes.

More detailed modelling of the plasma current profile would also be advantageous for the current balance, since some components of the total plasma current show strong radial dependencies. Thus, the modellings for the plasma conductivity including the neoclassical resistivity enhancement factor and the coulomb logarithm, as well as for the bootstrap current and the external current-drive in terms of current-drive efficiencies should be transformed from a global to a rather local approach. First ideas for that are presented in Chapter 2.3.2, but further work is necessary in order to develop modellings that can successfully be implemented in systems codes.

Moreover, two different modelling approaches for the calculation of the total magnetic flux swing exist. One uses the combination of magnetic fields and the particular geometry, the other relies on the coil currents in conjunction with the mutual inductances between the coils and the plasma. I decided to implement the former approach in TREND that is also applied by some other systems codes (see Chapter 2.3.3). Moreover, based on work by Fable [68], the modelling of the magnetic flux consumption during the current ramp-up phase could be linked to characteristic time-scales for this phase. That leads to a more accurate calculation of the available flux swing for the current flat-top phase that is crucial especially for pulsed devices.

Many modellings concerning the power balance of the core physics module are state-of-the-art. That includes the integration of a mantle region in order to consider the reduced impact of edge radiation on the core power balance and the confinement, the modelling of the fusion power by means of the Bosch / Hale fit [76, 77], the distinction and general modelling of synchrotron, bremsstrahlung and line radiation, as well as the modelling of the profile shapes for plasma temperature and density (see Chapter 2.3.4). But also some aspects could be identified that require improvement. A topic of high importance for systems codes is the modelling of the plasma transport losses. Besides the fact that the application of concepts that base on 0-dimensional energy confinement times is just a rather rough approximation for the underlying physical processes, the available scaling laws seem not to be adequate for DEMO and beyond. Moreover, significant improvement could also be realized by considering the consistency of the profiles for temperature and density with radiation, transport and stability calculations including the specific values at the separatrix and at the pedestal top, as well as the profile peaking. Finally, it seems to be worth assessing the synchrotron radiation reflection coefficient for tungsten walls that are foreseen in future devices. Some ideas for improvements connected to the plasma power balance are discussed in Chapter 2.3.4. That includes an extension of the radiative power loss functions for line radiation to non-corona equilibrium in the mantle and divertor region, as well as modellings for the temperature at the separatrix and the pedestal top. Also a simple criterion for the equilibration of ion and electron temperatures is discussed that would benefit from further refinement.

The modelling of the thermal part of the plasma pressure and the plasma beta is well-known and widely applied. But there are concerns on the modelling of the fast and beam particles contribution. That also holds for the impurity profiles and the concentrations of wall materials like tungsten. So far, profiles with the same shape as the electron density profile are assumed in systems codes leading to a flat profile for the effective ion charge number. This assumption does not sufficiently reflect the experimental observations. Thus, two different concentrations for the mantle and the core regions are implemented in TREND as a first step.

Furthermore, there seem to be a proper knowledge about the general limitations of the plasma operation space for DEMO and beyond. But often, the understanding of the underlying physical processes is still part of present research. Recently, some improvements could be achieved that are already considered in TREND. That includes the modelling of the density limit, for instance. Furthermore, an updated modelling of the limits for the plasma pressure in terms of the normalized plasma beta is implemented in TREND. But that does not explicitly consider effects due to the peaking of the pressure profile. Finally, the contribution of fast plasma particles could also be identified as a topic for future efforts.

Besides the module for the core plasma physics, modules for geometry, divertor, power flow, technology and costing are implemented in TREND. Two different modules for the power plant geometry currently exist and both are state-of-the-art concerning the modelling of the plasma geometry. But the geometrical modelling of other components like the toroidal field (TF) magnets or the blanket is rather rudimentary. The latter would certainly benefit from a proper module that includes estimations of the thickness for breeding and shielding zones with respect to neutron irradiation and the tritium breeding ratio (TBR).

One of the major concerns of systems codes is the modelling of the divertor, since the heat load on the divertor plates is a key driver for the conceptual design, especially of compact power plants. At present, a modelling also used in the ASC systems code is implemented in TREND with small improvements concerning the power decay length in the scrape-off layer (SOL). But this modelling is a rather rough estimation and no reliable modelling for the divertor radiation is currently available. Even the more sophisticated codes that are dedicated to simulate these effects are not able to reproduce the experimental observations for all regimes.

The structure and the modelling of the power flow in TREND is quite similar to other systems codes. But also some small improvements could be achieved. For instance, a correction factor for the effective surface of the blanket is implemented in order to consider ports for diagnostic or heating and current-drive (H&CD) systems. Moreover, the power that is deposited in the blanked and the divertor can be assigned individually to high and low-grade heat with respect to the heat quality. That allows to take into account different temperature levels of the coolants or losses in structures that are not connected to the heat conversion cycle. Furthermore, a distinction of individual powers for divertor and blanket pumping systems can be considered reflecting the application of different technologies. There is work in progress on assessing the efficiency of energy conversion systems as well as on the modelling of the requirements on electricity by the power plant itself.

The technology module combines different modellings that are not part of individual modules like the modelling of the dynamical phases. Just a few systems codes consider such a modelling at present and state-of-the-art is a rather simplistic approach. Therefore, an improved modelling was developed and included in TREND (see Chapter 2.6). But further work is necessary, particularly on the time-scales for the pump-down phase and the overlap with the recharging of the central solenoid (CS). The purpose of this activity is to get a proper understanding of the downtimes that affect the economic performance of the power plant. The same holds for the assessment of the first wall lifetime and a simple approach for this aspect is already implemented in TREND.

In summary, the current version of TREND includes the general structure and all basic modules for systems codes. Hence, it provides a fundamental framework for an extension to a more comprehensive systems code. During the development, several improvement needs with respect to the state-of-the-art modelling could be identified. Based on the high modularity and flexibility of TREND, some improvements could already be implemented and successfully assessed for an application in systems codes.

Validation: Benchmarks with other Systems Codes

Based on the approach of systems codes to extrapolate from existing devices to future machines like DEMO, it is not possible to validate the obtained results by comparison with the interaction of all systems in reality. Therefore, TREND was benchmarked to other systems codes including PROCESS, HELIOS and TPC in order to compare the obtained results at least with other calculations. This procedure appeared to be helpful during the development of TREND. Some of this work was also part of the EFDA PPPT work programme for 2011. It is expected that a benchmark with the ARIES systems code would also be advantageous for the future.

The benchmark of PROCESS and TREND is based on a reference design for DEMO 1 that is also used for parameter studies (see Chapter 4). The overall agreement of PROCESS and TREND is quite good. But TREND applied just the “standard” modellings for this case, i.e. standard geometry and standard profile shapes, for instance. These are quite similar to the modelling of PROCESS. Nevertheless, some differences could be identified. These are listed in Table 5.1. Moreover, I tried to evaluate the individual modellings with respect to the degree of deviation combined with the total impact on the design. That can be seen as a guideline in order to prioritize further work on the modellings. Since TREND consists just of basic modules, the benchmark with the other modules included in PROCESS is not conducted.

The parameter set named “3PT-SYS11-ACT5-B2” was selected to report the results of the benchmark of HELIOS and TREND. Compared to the standard configuration of TREND, the advanced profile shapes, the Hoang scaling for the bootstrap current and the advanced geometry module were applied. But due to an elliptical plasma shape, the full functionality of the advanced geometry module could not be assessed. That was done within another benchmark. In general, a quite good agreement of HELIOS and TREND could be determined. The observed differences are summarized in Table 5.2.

Modelling	Evaluation
Divertor	***
Dynamical phases	***
Bremsstrahlung and line radiation	***
Magnetic flux swing (CS and PFCs)	**
Fast particles	**
First wall life-time	**
Current profile	**
Internal plasma inductance	**
Normalized plasma beta	*
Ejima coefficient	*
Total plasma inductance	*
Elongation at 95 % flux	*
First wall area	*

Table 5.1.: Differences in modelling observed through the benchmark of PROCESS and TREND. The topics are rated with respect to the degree of deviation combined with the total impact: (*) small, (**) medium, (***) high.

Modelling	Evaluation
Divertor	***
Dynamical phases	***
Fast particles	**
Line radiation	**
First wall life-time	**
Plasma conductivity	**
Current profile	**
Internal plasma inductance	**
Total plasma inductance	**
Vertical magnetic field	*
Ejima coefficient	*
Plasma shaping at 95 % flux	*
First wall area	*

Table 5.2.: Differences in modelling observed through the benchmark of HELIOS and TREND. The topics are rated with respect to the degree of deviation combined with the total impact: (*) small, (**) medium, (***) high.

The benchmark of TPC and TREND is based on the parameter set “DEMO 1-TPC” that was developed within the Broader Approach Agreement with Japan in the DEMO Design Activity of the International Fusion Energy Research Centre (IFERC). Since TPC is mainly a physics code, no information about the dynamical phases, the power flow, the divertor and the power exhaust, as well as the neutron and heat load was available. Hence, the benchmark was limited to the geometry and the core physics module of TREND. Moreover, some values for important parameters are not reported. But as far as information was available, good conformity of TPC and the “standard” modelling of TREND is observed (see Table 5.3 for differences).

Modelling	Evaluation
Synchrotron radiation	**
Bremsstrahlung radiation	**
Line radiation	**
Magnetic flux swing (CS and PFCs)	**
Bootstrap current	**
Current profile	**
Safety factor profile	**
Internal plasma inductance	**
Plasma surface area	**
Normalized plasma beta	*

Table 5.3.: Differences in modelling observed through the benchmark of TPC and TREND. The topics are rated with respect to the degree of deviation combined with the total impact: (*) small, (**) medium, (***) high.

Application: Parameter Studies on DEMO 1

Four different parameter studies are discussed in Chapter 4 showing the application of TREND. The main results are recapitulated in the following. The fundamental approach of these studies is to scan a specific key parameter within a reasonable range based on a reference design for DEMO 1. The obtained operation points are analysed with respect to the burn time as figure of merit. The design targets for DEMO 1 are represented in TREND by means of constraints, i.e. constant fusion and constant additional heating power. Hence, specific ways through the multidimensional parameter space are analysed. These are in general rather complex and the consideration of all constraints imposed by the different systems can lead to surprising results when compared to simple models. This approach is similar to previous work by Zohm [9] and others. But due to significant improvements of the applied modellings, other ways through the parameter space are possible allowing a more differentiated analysis. Especially the consideration of additional limits for the plasma density and the power exhaust could be highlighted in this context. As a general result in case of fixed plasma densities, the potential range for the plasma temperature is observed to be clearly limited and determined by the H-mode threshold power on the one side and the power exhaust on the other side. That is based on a significant dependency of the power crossing the separatrix on the plasma temperature (see Equation 4.19).

The analysis of the aspect ratio within the first parameter study revealed a positive correlation with the machine size. As expected, small aspect ratios are combined with compact devices and vice versa. This simple trend could also be determined by analytical calculations that were done in parallel. But the advantages of a more comprehensive modelling became clearly visible. TREND considered also the development of the fuel concentration and the plasma temperature leading to a smoothening of the analytical trend. The enlargement of the machine size in terms of the major radius results in a substantial rise of the "productive" time-scales, since more and more space for the CS coils is available. But the magnitude of this rise is supported by a drop of the loop voltage that is driven by less resistivity, less total plasma current and higher bootstrap current fractions. Hence, a doubling of the burn time from about 3 h up to 6 h could be achieved for a device with ($R_0 \approx 10\,\mathrm{m}, A \approx 4.3$) compared to the reference design with ($R_0 = 9\,\mathrm{m}, A = 4.0$). Somehow counter-intuitive is the observation of hardly changing power exhaust conditions for increasing aspect ratios. Even if the machine size increases leading to larger wetted areas, the power crossing the separatrix also shows a positive trend due to higher temperatures and higher ion concentrations. The latter are based on reductions of the impurity content leading to less fuel dilution.

In general, high edge safety factors indicate higher stability of the operation points. Analyses of the edge safety factor with TREND show that the impacts of a design with higher plasma stability can possibly be balanced by increasing the major radius. Moreover, based on the inverse proportionality of the plasma current and the safety factor, a favourable trend for the burn time is expected and could also be confirmed within this parameter study. But it is observed that the amount of inductively driven plasma current counter-intuitively even increases for higher safety factors. This trend is counteracted by higher plasma temperatures and less contaminated plasmas resulting in a drop of the loop voltage. In addition, larger machines come along with more magnetic flux swing provided by the CS coils. Consequently, an increase of the edge safety factor from 3.0 to 3.5 would imply an enlargement of the burn time to about 10 h for the "price" of about 1.2 m more in major radius. Unfortunately, the increased size of the wetted area does not result in attenuated conditions for the power exhaust, since there is also a positive trend for the transport losses.

The state-of-the-art scalings laws for the energy confinement time have been developed explicitly for ITER operation scenarios. But these differ significantly to the operation scenarios of DEMO and beyond due to lower plasma density, lower plasma beta and lower radiation. Therefore, the impacts of over or underestimation of the energy confinement by the current scaling laws are analysed in the third parameter study by means of variations of the H-factor. It is discovered that exclusive adjustments of the plasma current in terms of the edge safety factor are not sufficient to compensate variations of the confinement in case that the design targets for DEMO 1 are considered additionally. But the combination with the plasma temperature appeared to be more expedient, since the transport losses show similar dependencies on the H-factor and the plasma temperature. Hence, the underestimation of the energy confinement requires higher plasma temperatures and higher edge safety factors in order to achieve the design targets. That fortunately leads to higher stability of the plasma and an extension of the burn time. In contrary, the overestimation can cause severe challenges with respect to the plasma stability. Moreover, the "productive" time-scale diminishes from about 3 h to about 2 h or even less. Furthermore, no clear trend for the power exhaust conditions could be identified. But considering a specific

H-factor, small variations of the safety factor can potentially be applied as an adjusting screw for the power exhaust without losing sight of the design targets.

Recent scientific achievements legitimate the assumption that the plasma density in DEMO could realistically be raised above the original Greenwald limit up to a factor of about 1.5, even for permanent operation. The impacts of higher densities are analysed with TREND for two scenarios. In the first scenario, increased densities are balanced by means of lower temperatures and less plasma current in terms of higher safety factors in order to still achieve the design targets for DEMO 1. But these advantageous conditions are hardly reflected in beneficial trends for the burn time and the power exhaust conditions as may be expected. Lower plasma temperatures lead to higher plasma resistance that is a key driver for an increase of the loop voltage. Thus, in combination with less plasma current and constant dimensions of the CS, the burn time stays within a rather small range. As already mentioned, the current modelling of the power exhaust is rather simplistic. Therefore, it is assumed that the implementation of a sophisticated modelling for the divertor would clearly show the experimentally observed optimization of the power exhaust conditions by higher densities. Hence, considering the observation that the burn time hardly changes, optimized operation points for DEMO will certainly be characterized by densities above the original Greenwald density limit. Furthermore, the first scenario revealed a correlation of the plasma density and the edge safety factor. That allows a proper optimization of the plasma stability with respect to the safety margins for both parameters without influencing significantly the power production and the corresponding time-scales. In the second scenario, the impacts of higher densities on the machine size in terms of the major radius are analysed. As expected, increased densities allow the design of smaller devices that could be operated at lower temperatures. But as an associated result, the burn time drops significantly due to less space for the CS coils in combination with higher plasma resistance. Moreover, the wetted area shrinks with a negative influence on the power exhaust conditions. But similar to the first scenario, an improvement of the divertor modelling is assumed to result in a more accurate estimation of the power exhaust. That is crucial for a precise assessment of the benefits expected from increased densities.

In summary, the application of TREND in terms of the discussed parameter studies show the advantages of systems codes that consider all requirements and constraints of each component of fusion power plants. Often, dependencies and trends seem to be obvious by intuition, but only one unconsidered constraint can lead to completely different ways through the parameter space. Moreover, considering the reference design for DEMO 1, the analyses conducted within this thesis revealed that there is some room for improvement of the current operation point. Further sensitivity studies that are planned this year within the PPPT department of EFDA and the iteration with more sophisticated and specialised codes will certainly improve the matureness of the conceptual design for DEMO.

A. Appendix

Introduction

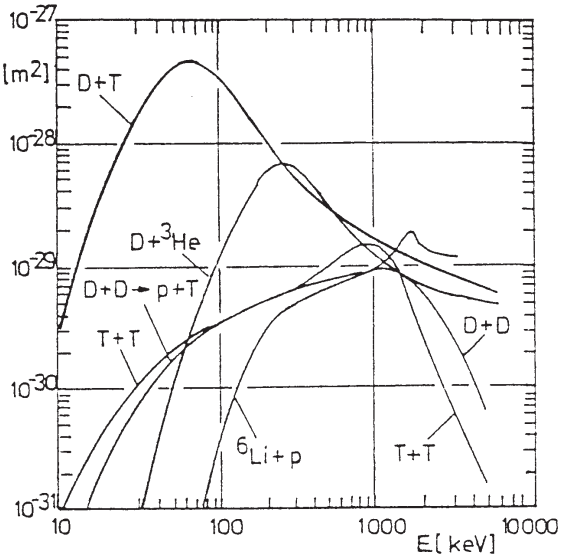

Figure A.1.: Cross sections for different fusion reactions plotted against the relative energy of the fusion reactants. Ref: [44]

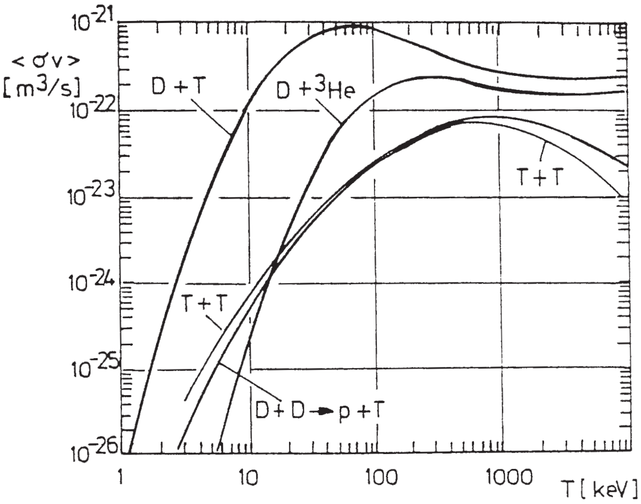

Figure A.2.: Reactivity of different fusion reactions for a thermal plasma with temperature T. The operation range for devices like DEMO is of the order of several 10s of keV. Ref: [44]

Physics Module

$$
\begin{array}{ll}
a_1 = 1.41\left(1-0.28\alpha_{jW}^{1/2}\right)\left(1+0.12Z_{eff}^{-1}\right) & b_1 = 1 \\
a_2 = 0.36\left(1-0.59\alpha_{jW}^{1/2}\right)\left(1+0.8Z_{eff}^{-1}\right) & b_2 = \alpha_{pW} \\
a_3 = -0.27\left(1-0.47\alpha_{jW}^{1/2}\right)\left(1+3Z_{eff}^{-1}\right) & b_3 = \alpha_{TW} \\
a_4 = 0.0053\left(1+5Z_{eff}^{-1}\right) & b_4 = \alpha_{pW}\alpha_{TW} \\
a_5 = -0.93\left(1-0.34\alpha_{jW}^{1/2}\right)\left(1+0.15Z_{eff}^{-1}\right) & b_5 = \varepsilon^{1/2} \\
a_6 = -0.26\left(1-0.57\alpha_{jW}^{1/2}\right)\left(1-0.27Z_{eff}\right) & b_6 = \alpha_{pW}\varepsilon^{1/2} \\
a_7 = 0.064\left(1-0.6\alpha_{jW}+0.15\alpha_{jW}^{2}\right)\left(1+7.6Z_{eff}^{-1}\right) & b_7 = \alpha_{TW}\varepsilon^{1/2} \\
a_8 = -0.0011\left(1+9Z_{eff}^{-1}\right) & b_8 = \alpha_{pW}\alpha_{TW}\varepsilon^{1/2} \\
a_9 = -0.33\left(1-\alpha_{jW}+0.33\alpha_{jW}^{2}\right) & b_9 = \varepsilon \\
a_{10} = -0.26\left(1-0.87\alpha_{jW}^{-1/2}-0.16\alpha_{jW}\right) & b_{10} = \alpha_{pW}\varepsilon \\
a_{11} = -0.14\left(1-1.14\alpha_{jW}^{-1/2}-0.45\alpha_{jW}^{1/2}\right) & b_{11} = \alpha_{TW}\varepsilon \\
a_{12} = -0.0069 & b_{12} = \alpha_{pW}\alpha_{TW}\varepsilon
\end{array}
$$

Table A.1.: Coefficients of the Wilson bootstrap scaling. Ref: [60]

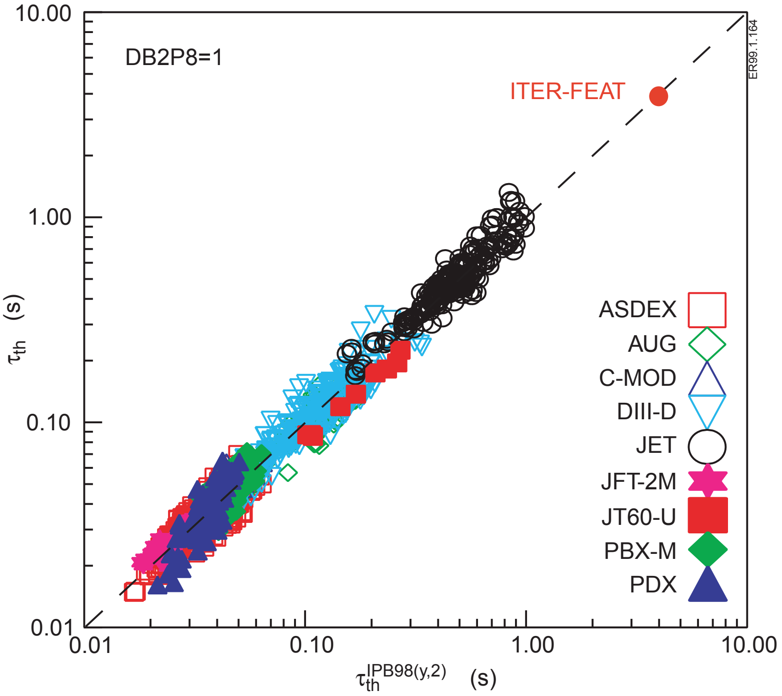

Figure A.3.: Comparison of ELMy H-mode thermal energy confinement times with the scaling expression IPB98(y,2) given by Equation 2.113 and the prediction for a ITER-FEAT discharge with $Q = 10$. Ref: [170]

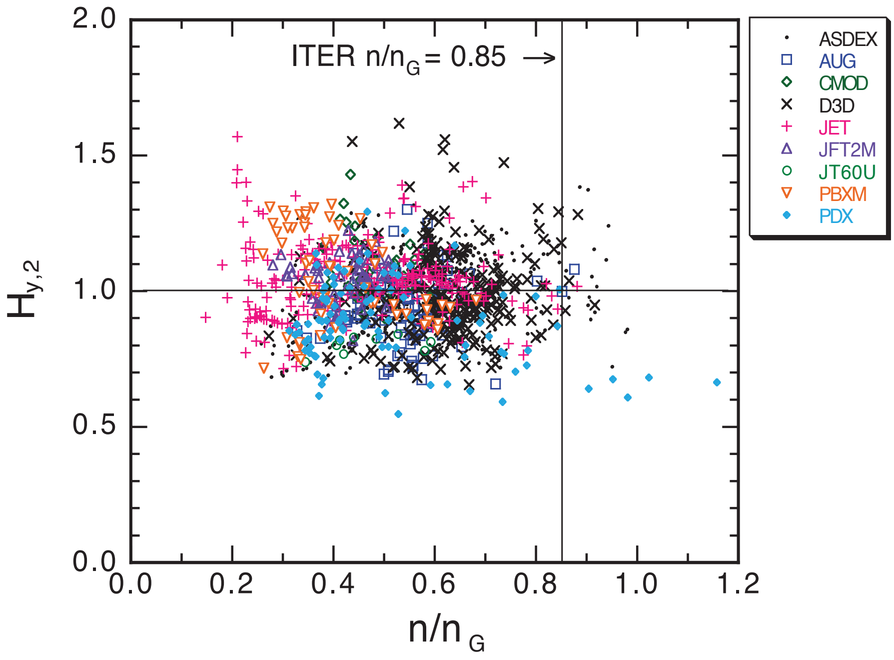

Figure A.4.: Experimental IPB98(y,2) H-factors for energy confinement and Greenwald density fractions of the dataset used to develop the IPB98(y,2) scaling. Ref: [171]

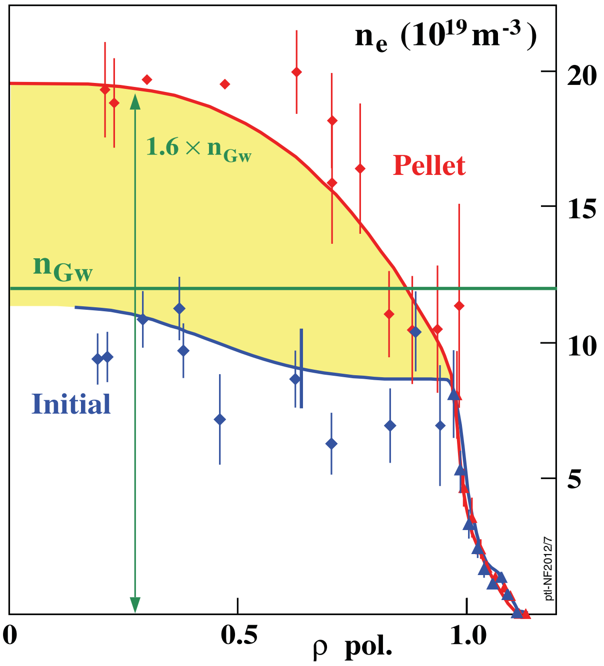

Figure A.5.: Profiles for electron density obtained in recent experiments at ASDEX Upgrade of an initial reference phase and a pellet phase where the Greenwald density limit is exceeded using optimized pellet fuelling while maintaining ELM mitigation by magnetic perturbation coils. Ref: [107]

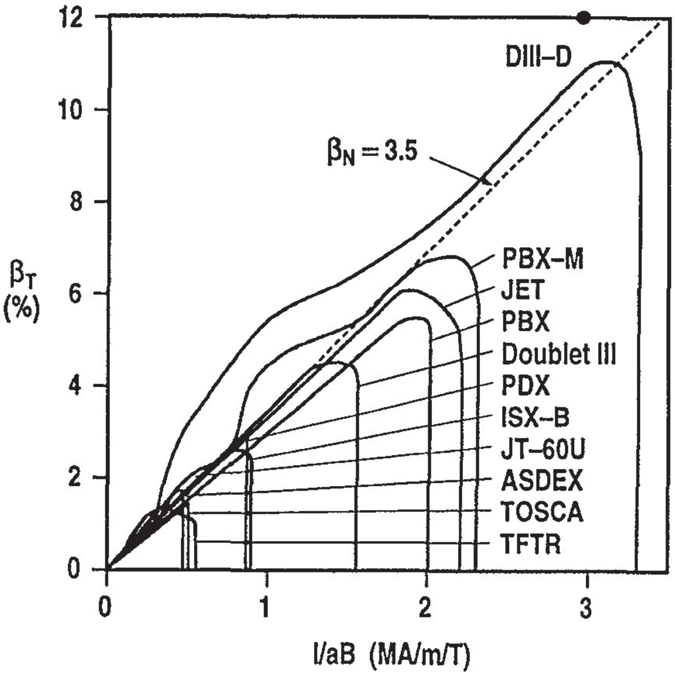

Figure A.6.: Comparison of the Troyon scaling with beta limits observed in different experiments. Ref: [112]

Divertor Module

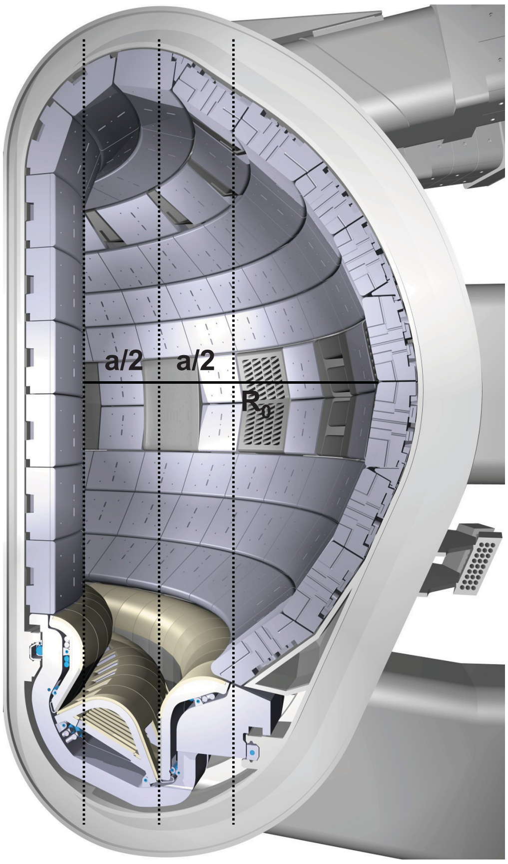

Figure A.7.: Poloidal cross-section of ITER for the determination of the radial location of the outboard and inboard divertor plates. Reference of the original image: [73]

Power Flow Module

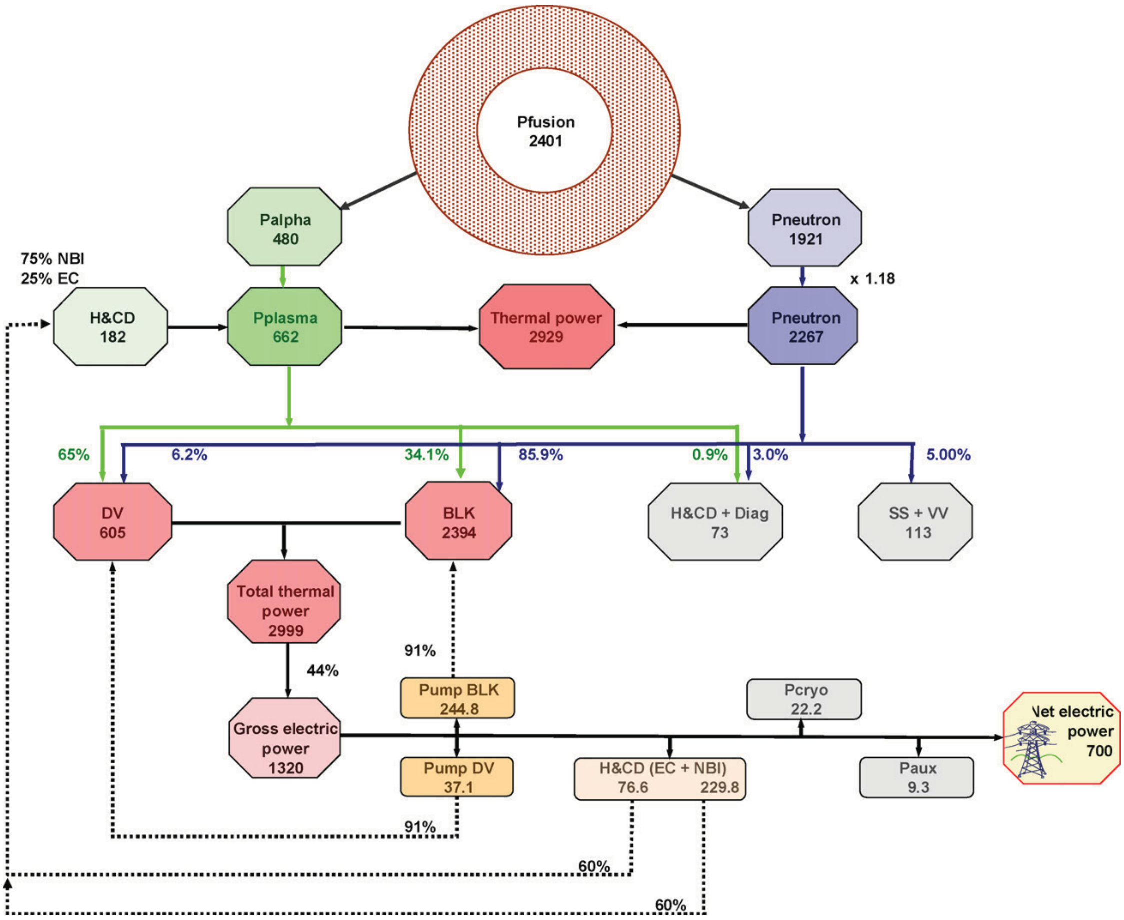

Figure A.8.: Power flow scheme of the HCLL-DEMO-2007 reactor with a HCLL breeding blanket. Ref: [124]

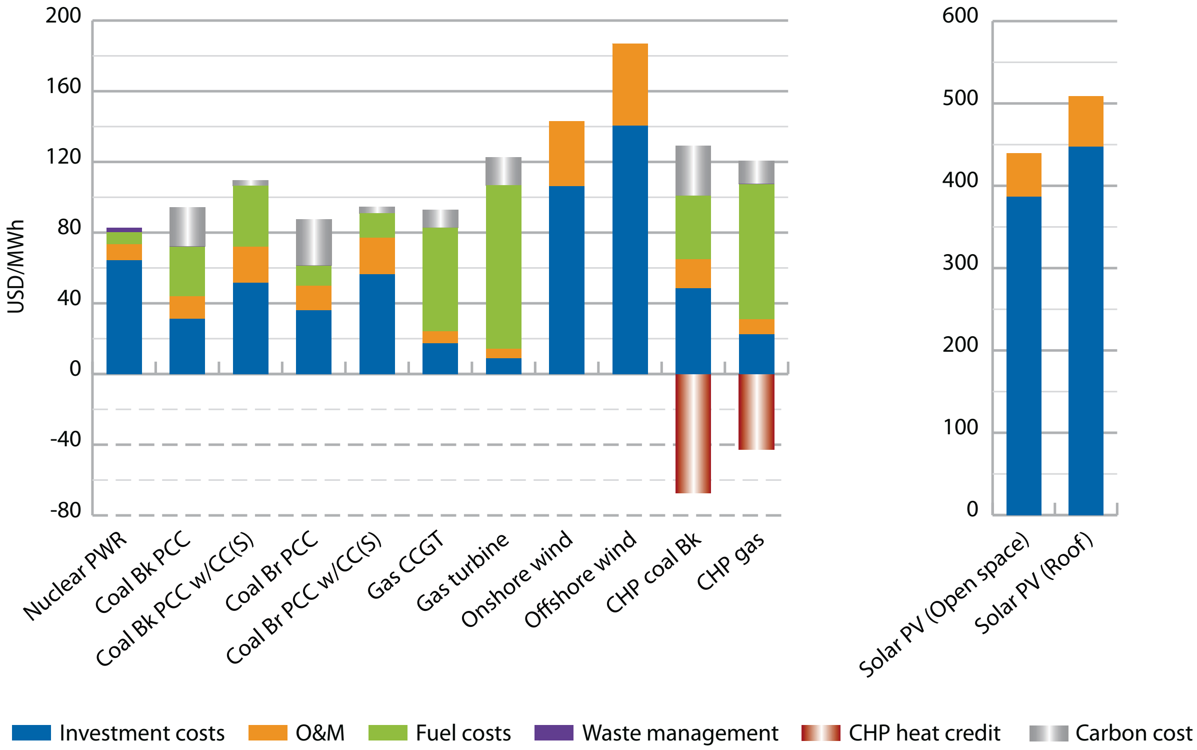

Figure A.9.: Levelized costs of electricity (COE) for different power plant technologies in Germany 2010 at 10 % discount rate. PWR = pressurised water reactor, Bk = black coal, Br = brown coal, PCC = pulverised coal combustion, CC(S) = carbon capture where currently no storage is included, CCGT = combined cycle gas turbine, CHP = combined heat and power, PV = photovoltaic. Ref: [140]

Benchmarks with other Systems Codes

Systems Code	Name of Parameter Set	References
PROCESS	DEMO 1*	[15, 16]
PROCESS	DEMO 2	[15, 16]
PROCESS	3PT-SYS11-ACT5-B1	[48]
PROCESS	PPCS A	[99, 156, 157]
PROCESS	PPCS AB	[157]
PROCESS	PPCS B	[99, 156, 157]
PROCESS	PPCS C	[99, 156, 157]
PROCESS	PPCS D	[99, 156, 157]
HELIOS	3PT-SYS11-ACT5-B2*	[48, 162]
HELIOS	ITER Scenario 2	[19]
HELIOS	DEMO PPCS-C	[19]
HELIOS	DEMO Inductive	[19]
TPC	DEMO 0-TPC	[164]
TPC	DEMO 1-TPC*	[164]
TPC	DEMO 2-TPC	[164]

Table A.2.: Overview on parameter sets used for benchmarks with PROCESS, HELIOS and TPC. Parameter sets marked with an asterisk were selected to report the results of the benchmarks within this thesis.

Benchmark with HELIOS

Parameter	Unit	HELIOS	TREND	Deviation
τ_{cycle}	[min]		550	
τ_{burn}	[min]		521	
τ_{down}	[min]		30	
f_{DC}			0.95	
τ_{RU}	[min]		3.9	
τ_{heat}	[min]		0.3	
τ_{BT}	[min]		1.6	
τ_{RD}	[min]		3.9	
τ_{pump}	[min]		20.0	
τ_{RC}	[min]		4.4	
P_{RC}	[MW]		100	

Table A.3.: Parameters describing the dynamical phases as calculated by HELIOS and TREND for the parameter set “3PT-SYS11-ACT5-B2” including the relative deviation. Deviations of less than 1 % are not reported. Ref: [48, 162]

Parameter	Unit	HELIOS	TREND	Deviation
P_{sep}/R_0	[MW/m]	55.9	60.5	8 %
q_{peak}^{out}	[MW/m^2]	84.7	20.8	121 %
q_{peak}^{in}	[MW/m^2]		14.3	
q_{sep}	[GW/m^2]		33.1	
λ_q	[mm]		1.1	
λ_{int}	[mm]		2.8	
f_{exp}			15	
f_{divRad}			0.90	
$f_{outboard}$			0.67	
A_{con}^{outb}	[m^2]		1.9	

Table A.4.: Parameters describing the divertor conditions and the power exhaust as calculated by HELIOS and TREND for the parameter set “3PT-SYS11-ACT5-B2” including the relative deviation. Deviations of less than 1 % are not reported. Ref: [48, 162]

Parameter	Unit	HELIOS	TREND	Deviation
S_{FW}	[m^2]	1284	1352	5 %
q_{NWL}	[MW/m^2]	1.87	1.77	5 %
q_{HWL}	[MW/m^2]		0.61	
ND_{rate}	$[\frac{\mathrm{MW}}{\mathrm{m}^2}\frac{\mathrm{a}}{\mathrm{dpa}}]$		0.1	
ND_a	[dpa/a]		17.7	
ND_{max}	[dpa]		60	
τ_{FWLT}	[a]		3.4	

Table A.5.: Parameters describing the neutron and heat load as calculated by HELIOS and TREND for the parameter set “3PT-SYS11-ACT5-B2” including the relative deviation. Deviations of less than 1 % are not reported. Ref: [48, 162]

Benchmark with TPC

Parameter	Unit	TPC	TREND	Deviation
τ_{cycle}	[min]		472	
τ_{burn}	[min]		435	
τ_{down}	[min]		37	
f_{DC}			0.92	
τ_{RU}	[min]		7.4	
τ_{heat}	[min]		0.3	
τ_{BT}	[min]		2.2	
τ_{RD}	[min]		7.4	
τ_{pump}	[min]		20.0	
τ_{RC}	[min]		12.5	
P_{RC}	[MW]		100	

Table A.6.: Parameters describing the dynamical phases as calculated by TPC and TREND for the parameter set “DEMO 1-TPC” including the relative deviation. Deviations of less than 1 % are not reported. Ref: [164]

Parameter	Unit	TPC	TREND	Deviation
P_{sep}/R_0	[MW/m]	28.9	27.5	5 %
q_{peak}^{out}	[MW/m^2]		9.7	
q_{peak}^{in}	[MW/m^2]		6.3	
q_{sep}	[GW/m^2]		24.3	
λ_q	[mm]		0.9	
λ_{int}	[mm]		2.6	
f_{exp}			15	
f_{divRad}			0.90	
$f_{outboard}$			0.67	
A_{con}^{outb}	[m^2]		2.2	

Table A.7.: Parameters describing the divertor conditions and the power exhaust as calculated by TPC and TREND for the parameter set “DEMO 1-TPC” including the relative deviation. Deviations of less than 1 % are not reported. Ref: [164]

Parameter	Unit	TPC	TREND	Deviation
f_{nMult}			1.18	
$f_{geoBlkt}$			0.909	
f_{geoDiv}			0.062	
f_{hBlkt}			0.95	
f_{hDiv}			1.0	
P_{blkt}	[MW]		1784	
P_{div}	[MW]		380	
P_{th}	[MW]		2268	
η_{th}			0.44	
P_{el}	[MW]		998	
P_{elNet}	[MW]		758	
P_{elRec}	[MW]		240	
f_{rec}			0.24	
P_{elAdd}	[MW]		3	
P_{pump} / P_{pumpD}	[MW]		185 / 28	
f_{pump} / f_{pumpD}			0.185 / 0.028	
η_{pump} / η_{pumpD}			0.91	
P_{cryo}	[MW]		17	
f_{cryo}			0.017	
P_{aux}	[MW]		7	
f_{aux}			0.007	
η_{tot}			0.39	

Table A.8.: Parameters describing the power flow through the power plant as calculated by TPC and TREND for the parameter set “DEMO 1-TPC” including the relative deviation. Deviations of less than 1 % are not reported. Ref: [164]

Parameter	Unit	TPC	TREND	Deviation
S_{FW}	[m^2]		1472	
q_{NWL}	[MW/m^2]		1.06	
q_{HWL}	[MW/m^2]		0.27	
ND_{rate}	$[\frac{\text{MW}}{\text{m}^2}\frac{\text{a}}{\text{dpa}}]$		0.1	
ND_a	[dpa/a]		10.6	
ND_{max}	[dpa]		60	
τ_{FWLT}	[a]		5.7	

Table A.9.: Parameters describing the neutron and heat load as calculated by TPC and TREND for the parameter set “DEMO 1-TPC” including the relative deviation. Deviations of less than 1 % are not reported. Ref: [164]

Parametric Scans of the Aspect Ratio

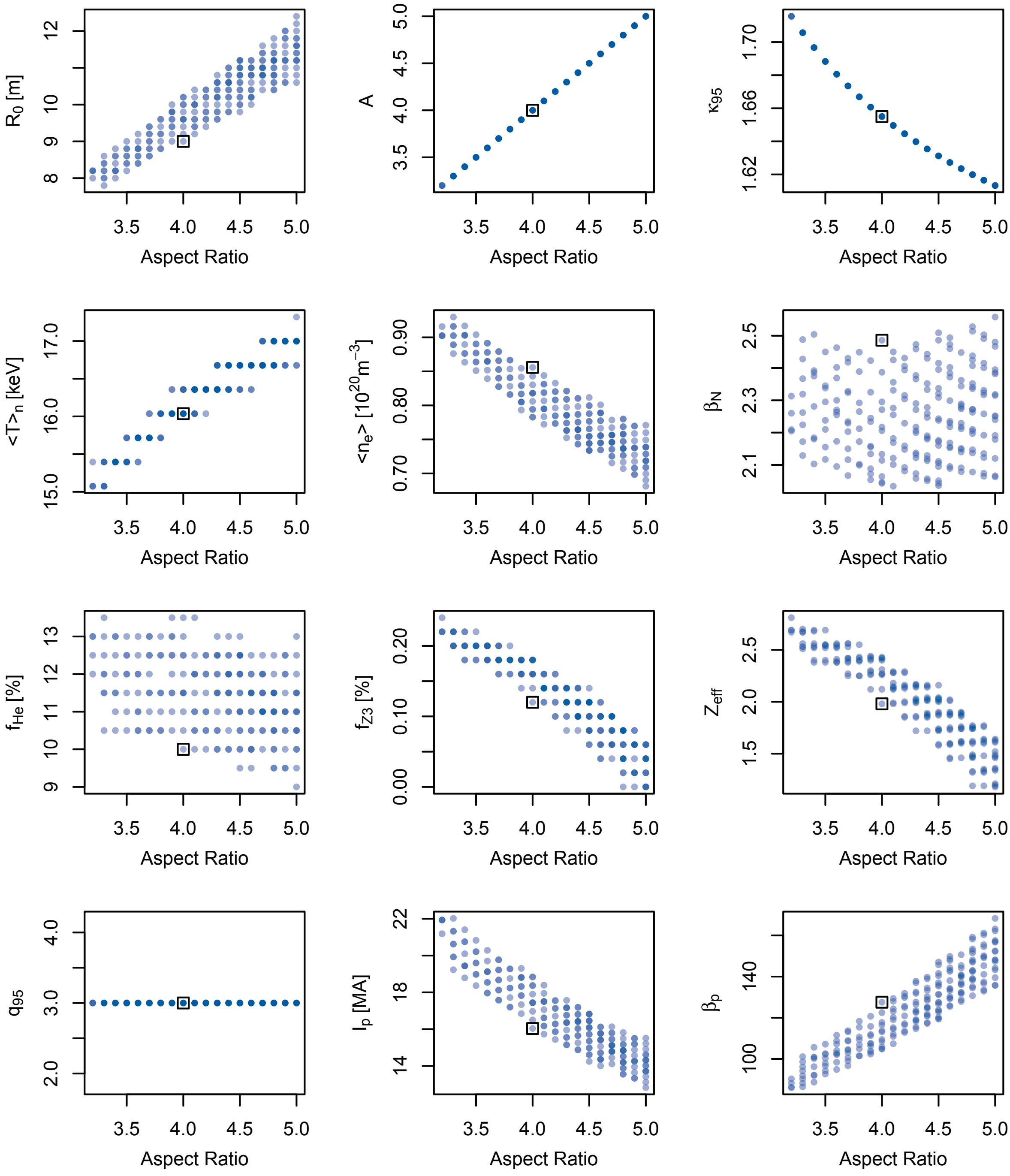

Figure A.10.: Trends for variations of the aspect ratio based on a reference configuration of DEMO 1. The black square marks the DEMO 1 reference design point. Transparency is applied in order to visualize overlaying operation points.

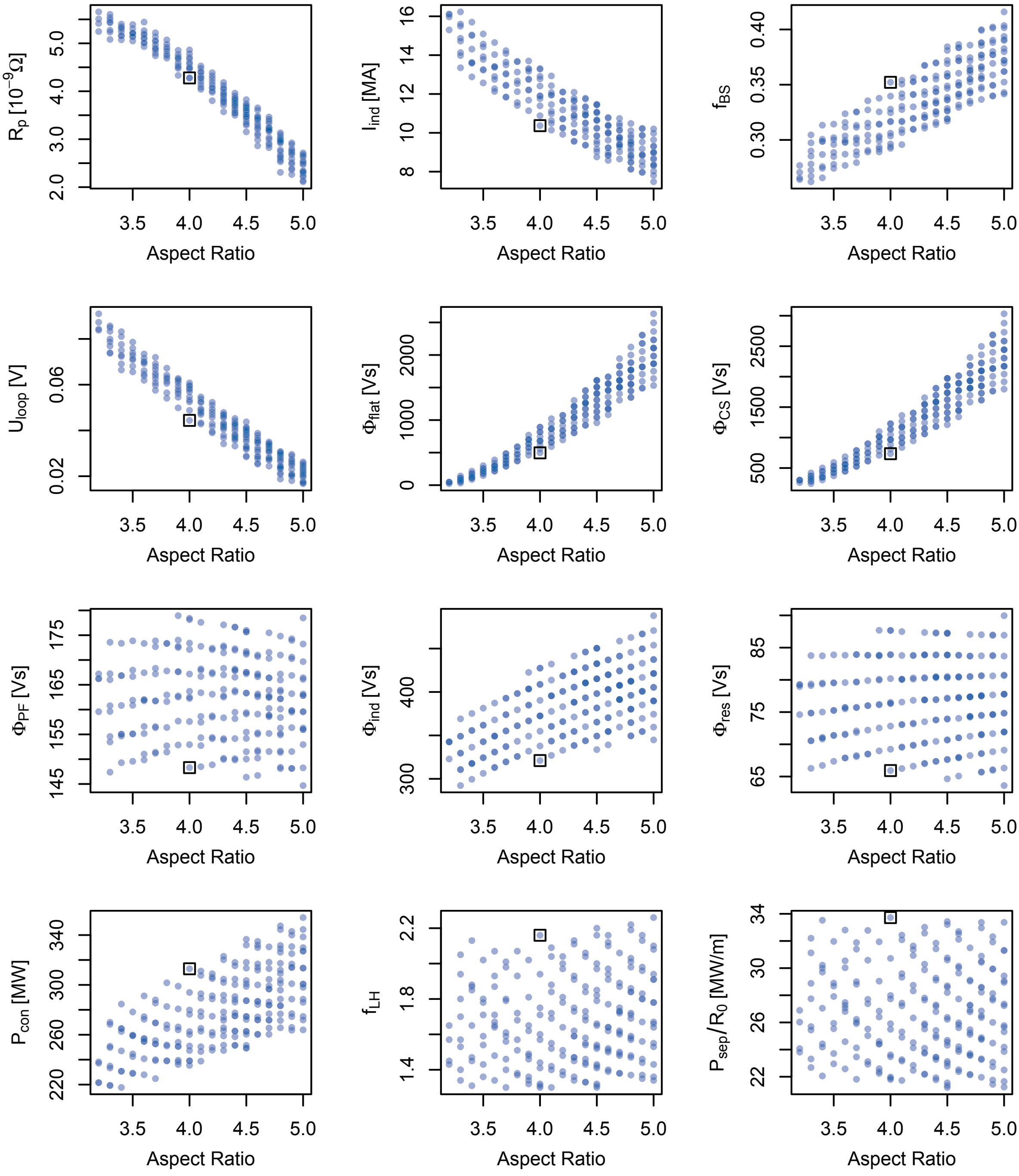

Figure A.11.: Trends for variations of the aspect ratio based on a reference configuration of DEMO 1. The black square marks the DEMO 1 reference design point. Transparency is applied in order to visualize overlaying operation points.

Parametric Scans of the Edge Safety Factor

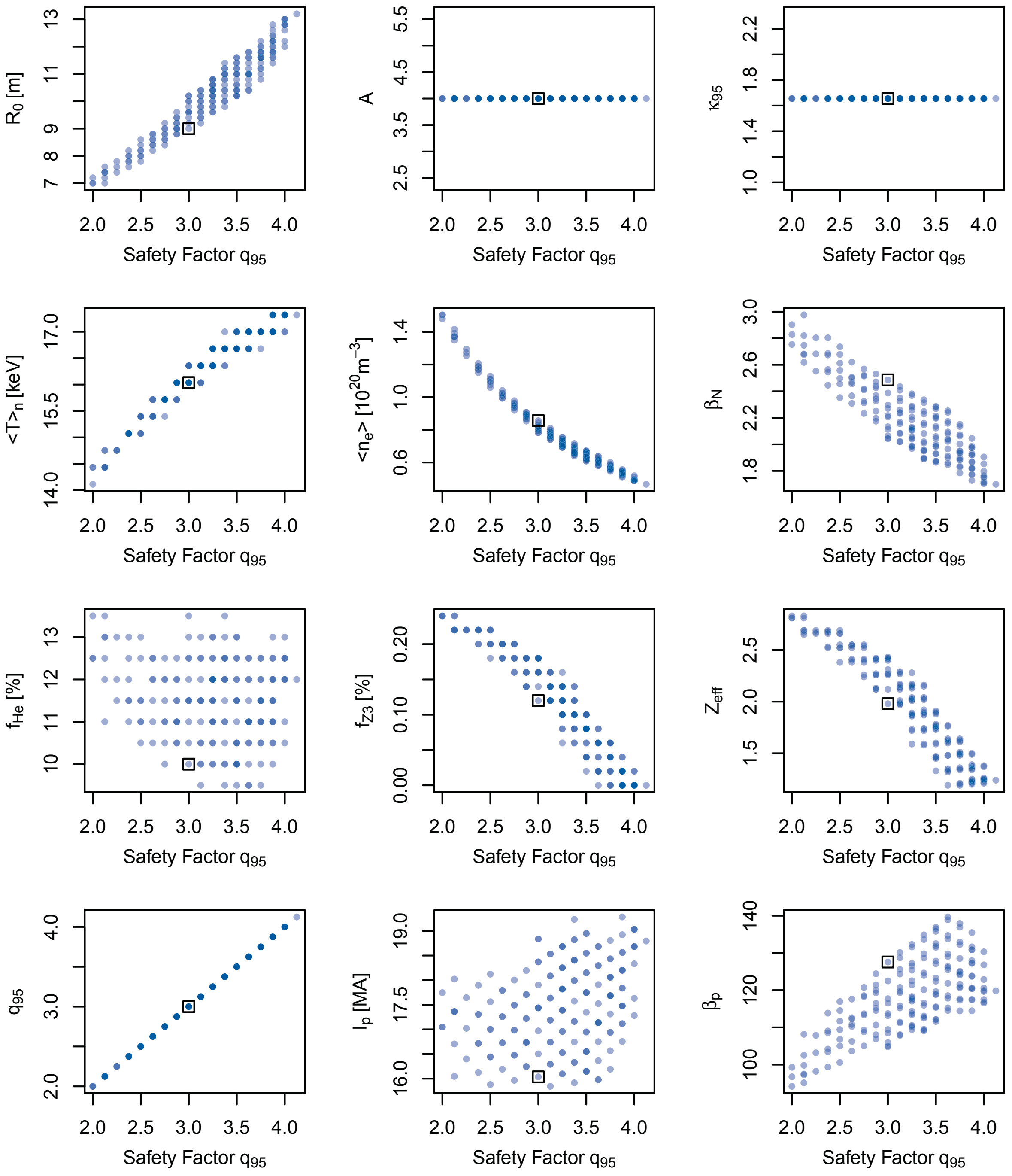

Figure A.12.: Trends for variations of the edge safety factor based on a reference configuration of DEMO 1. The black square marks the DEMO 1 reference design point. Transparency is applied in order to visualize overlaying operation points.

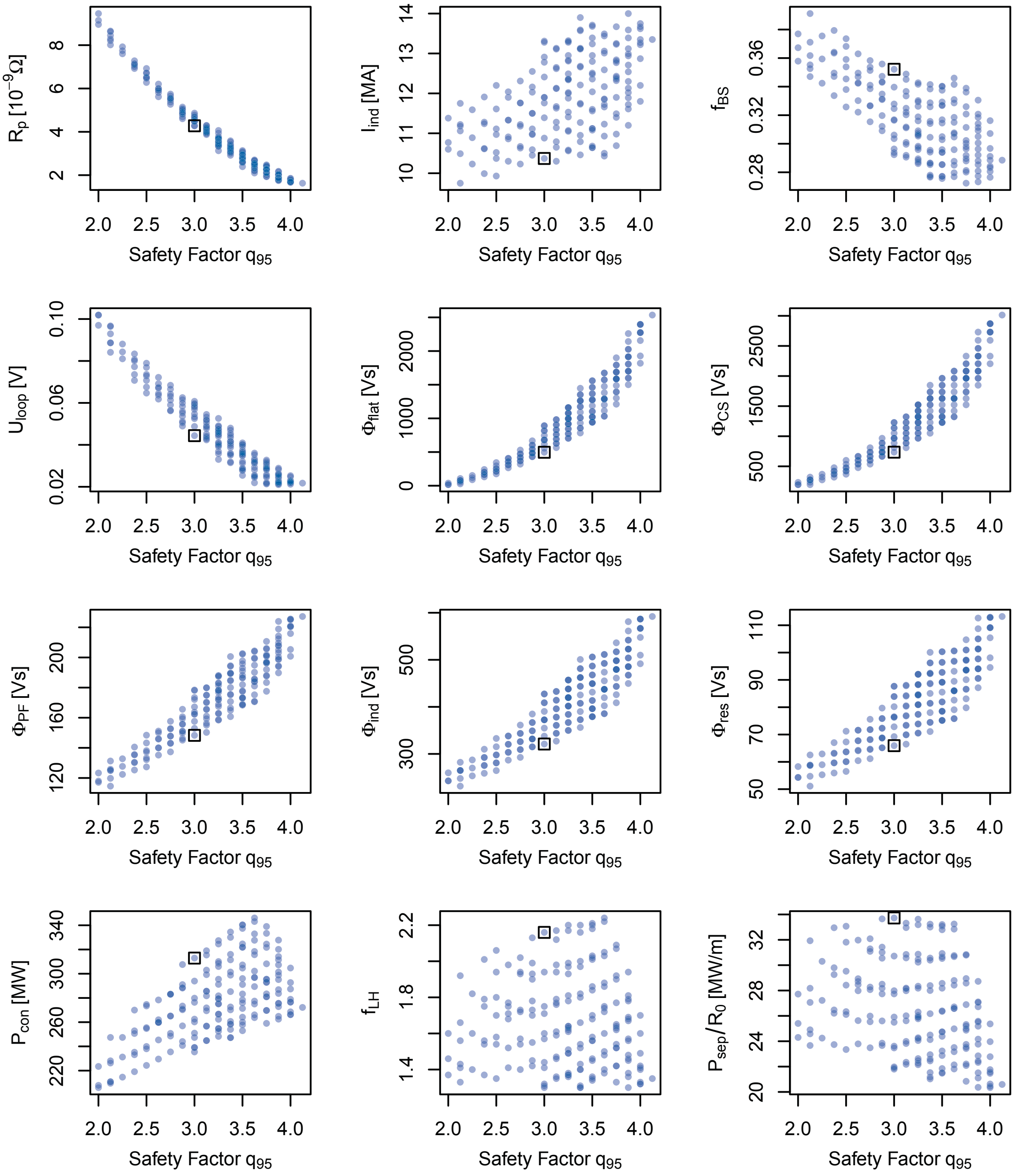

Figure A.13.: Trends for variations of the edge safety factor based on a reference configuration of DEMO 1. The black square marks the DEMO 1 reference design point. Transparency is applied in order to visualize overlaying operation points.

Parametric Scans of the H-factor (Energy Confinement)

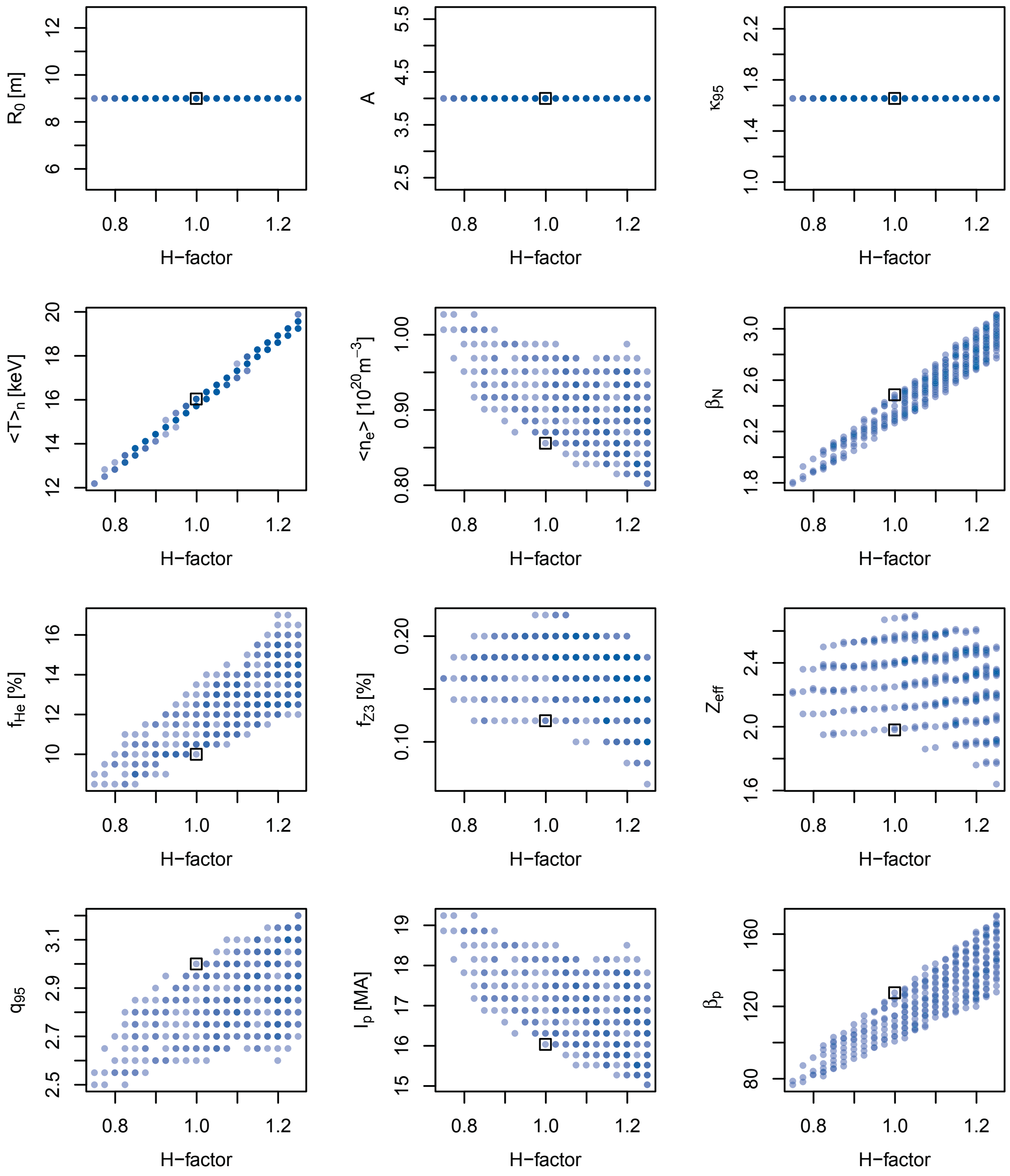

Figure A.14.: Trends for variations of the H-factor based on a reference configuration of DEMO 1. The black square marks the DEMO 1 reference design point. Transparency is applied in order to visualize overlaying operation points.

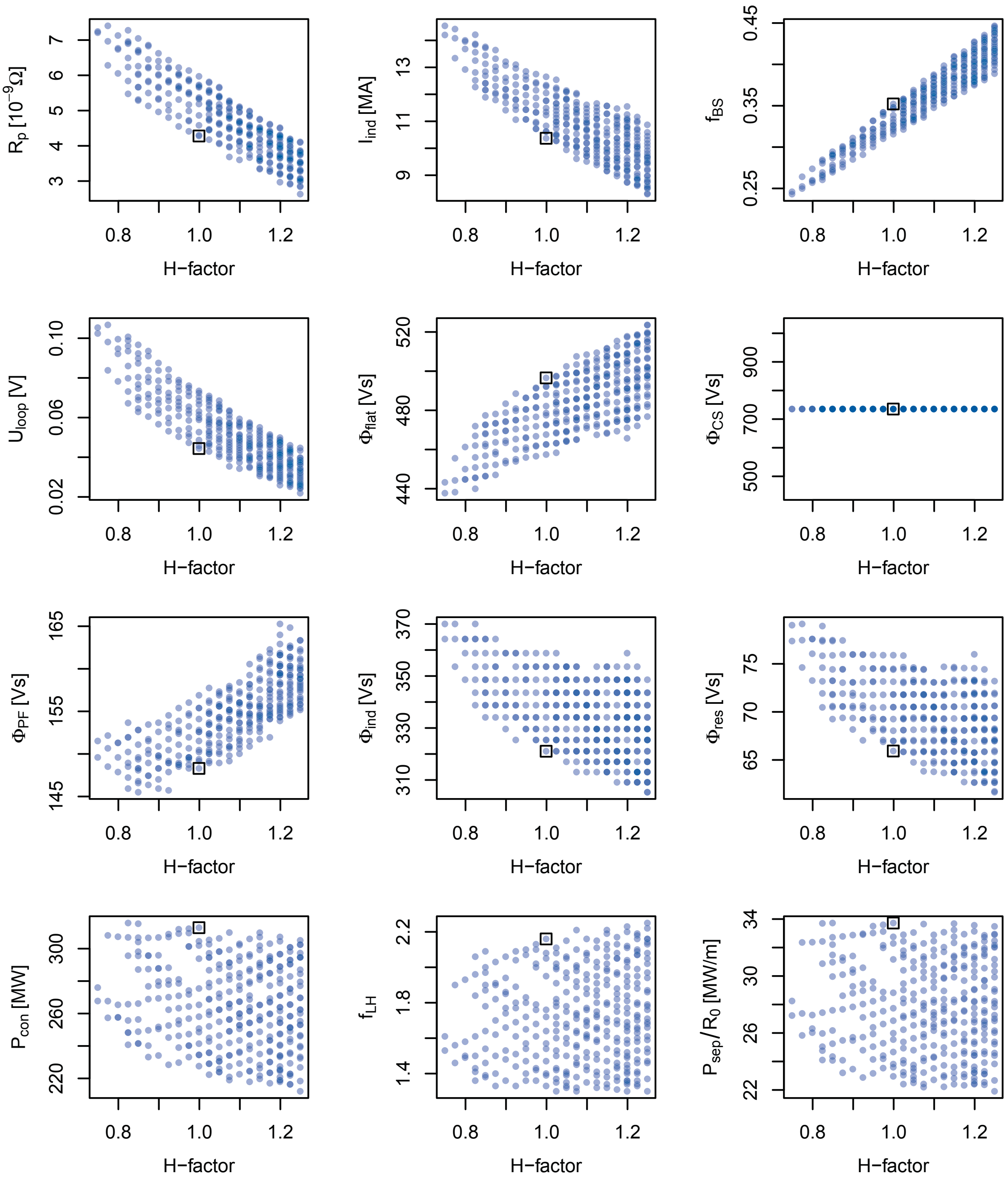

Figure A.15.: Trends for variations of the H-factor based on a reference configuration of DEMO 1. The black square marks the DEMO 1 reference design point. Transparency is applied in order to visualize overlaying operation points.

Parametric Scans of the Greenwald Fraction (Density Limit)

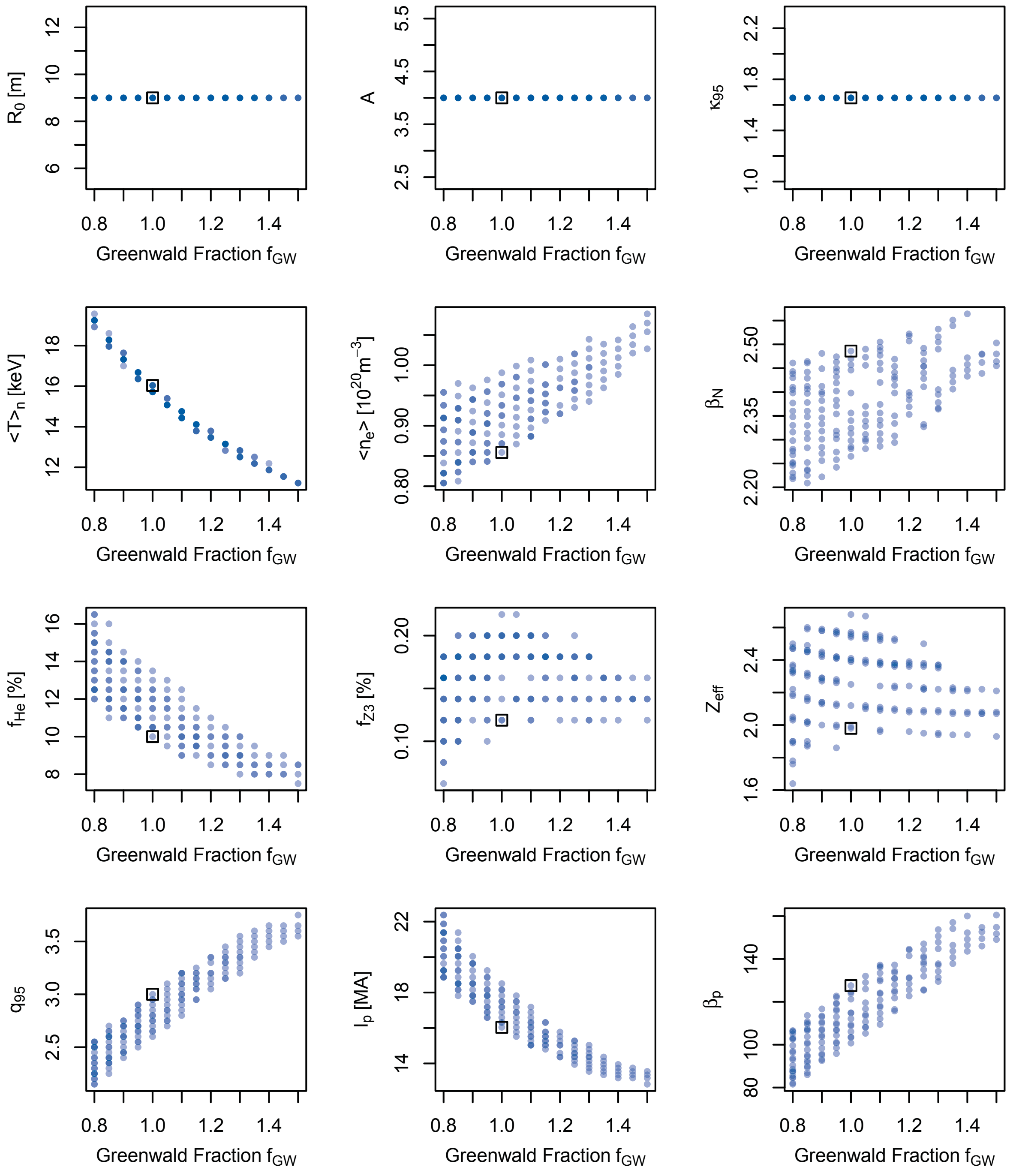

Figure A.16.: Trends for variations of the Greenwald fraction based on a reference configuration of DEMO 1 (scenario 1). The black square marks the DEMO 1 reference design point. Transparency is applied in order to visualize overlaying operation points.

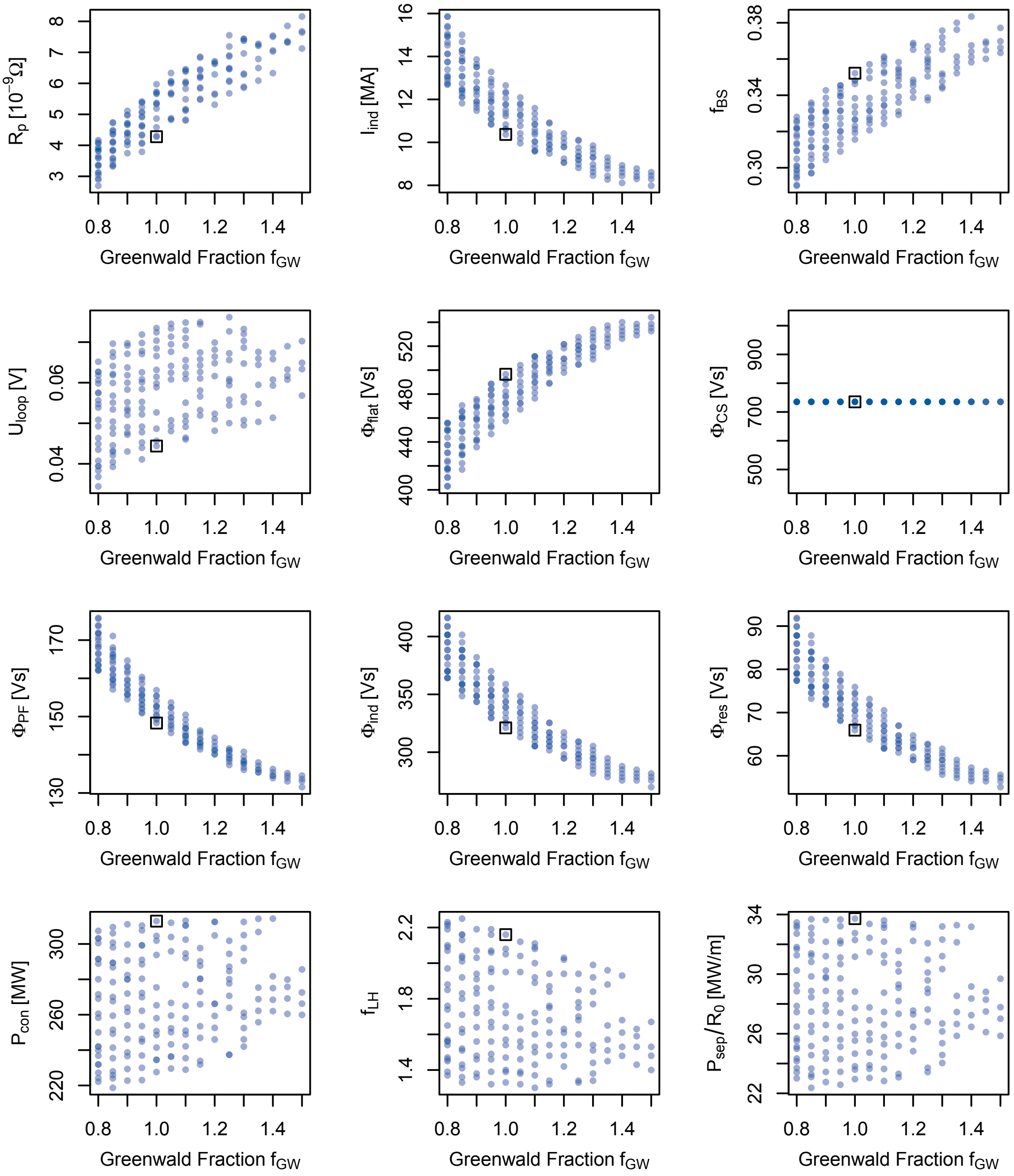

Figure A.17.: Trends for variations of the Greenwald fraction based on a reference configuration of DEMO 1 (scenario 1). The black square marks the DEMO 1 reference design point. Transparency is applied in order to visualize overlaying operation points.

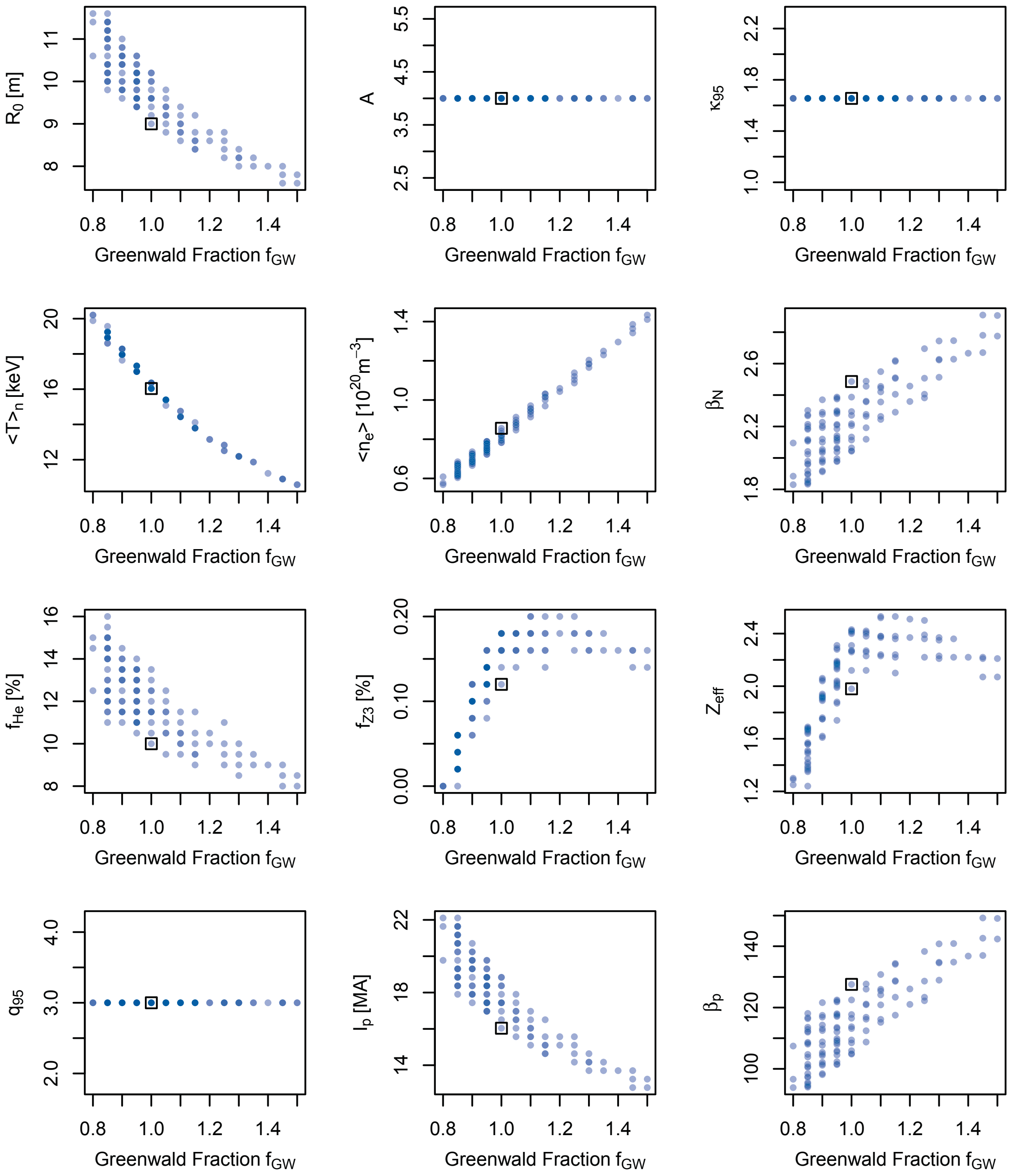

Figure A.18.: Trends for variations of the Greenwald fraction based on a reference configuration of DEMO 1 (scenario 2). The black square marks the DEMO 1 reference design point. Transparency is applied in order to visualize overlaying operation points.

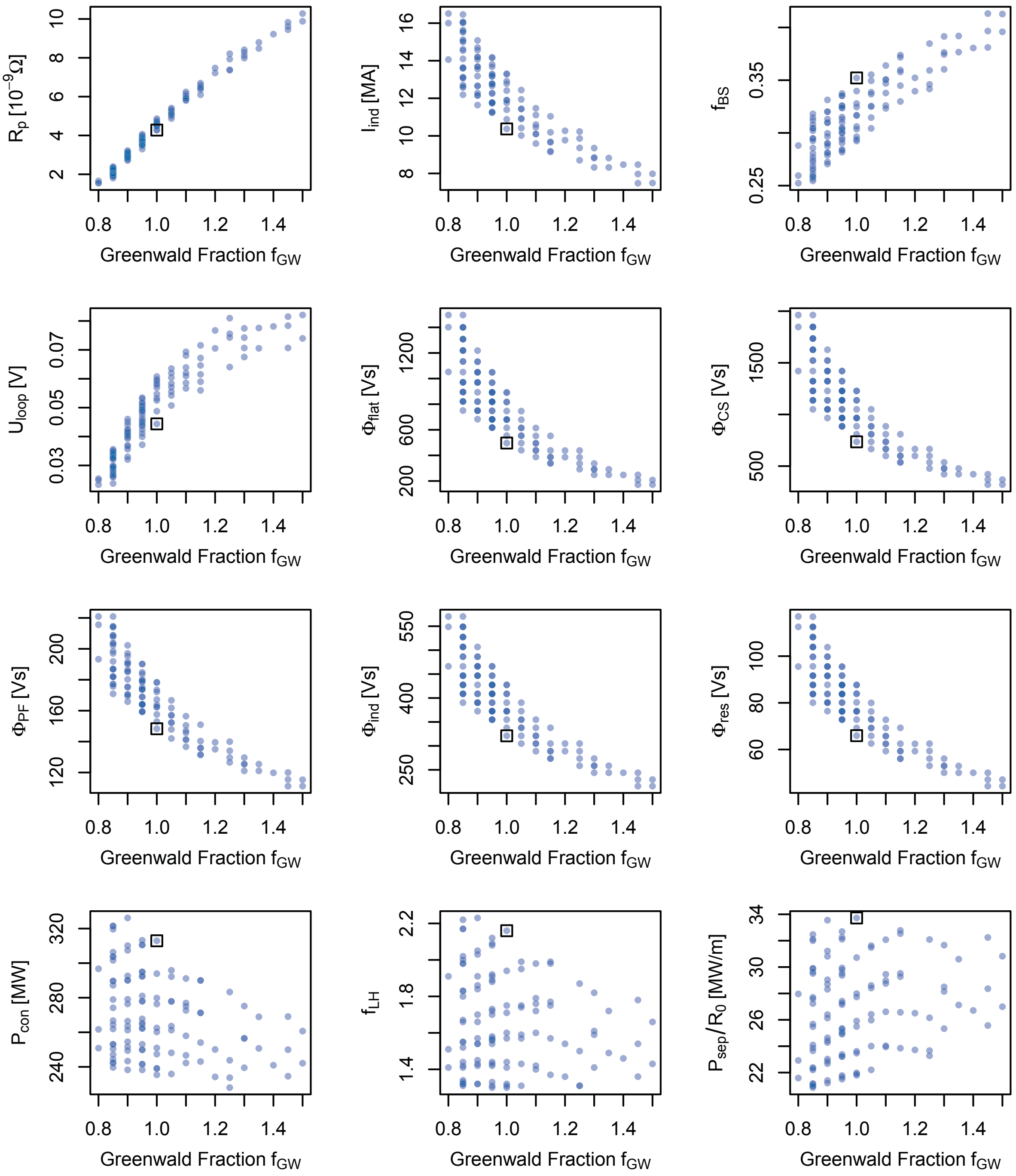

Figure A.19.: Trends for variations of the Greenwald fraction based on a reference configuration of DEMO 1 (scenario 2). The black square marks the DEMO 1 reference design point. Transparency is applied in order to visualize overlaying operation points.

Conclusions and Outlook

Chapter	Modelling	Category
2.1 General Structure	Modular architecture	(I)
2.2 Geometry Module	Radial build	(II)
	Plasma cross-section	(I)
	Plasma size	(I)
	FW area	(IIIa)
2.4 Divertor Module	Effective areas	(I)
	Power decay length	(IIIa)
	Divertor radiation	(II)
	Peak power load	(II)
2.5 Power Flow Module	General structure	(I)
	Effective surface corrections	(IIIb)
	Heat quality levels	(IIIa)
	Pumping power	(IIIa)
	Energy conversion	(II)
	Recirculating power contributions	(II)
2.6 Technology Module	Dynamical phases	(IIIa)
	First wall lifetime	(IIIa)
	Magnet systems	(II)
2.7 Costing Module	General structure	(II)

Table A.10.: Evaluation of implemented modellings without those of the core physics module. Categories: (I) state-of-the-art modelling, (II) proposals for updates, (IIIa) proposals for updates with proposals for simple modellings requiring further work and (IIIb) proposals for updates with proposals for advanced modellings.

Chapter (Core Physics Module)	Modelling	Category
2.3.1 Equilibrium Properties	Safety factor	(I)
	Plasma current and profile	(IIIa)
	Internal inductance	(IIIa)
	Consistency of equilibrium properties	(IIIa)
	Magnetic fields	(I)
2.3.2 Current Balance	Current balance	(II)
	Plasma conductivity	(II)
	Coulomb logarithm	(II)
	Bootstrap current	(II)
	Current-drive efficiencies	(II)
2.3.3 Magnetic Flux Balance	Sources for Magnetic Flux	(I)
	Flux consumption in ramp-up	(IIIb)
2.3.4 Power Balance	Plasma regions	(I)
	Fusion power	(I)
	Additional heating power	(IIIb)
	Transport losses	(II)
	Synchrotron and bremsstrahlung	(I)
	Line radiation	(IIIa)
	Profile shapes	(I)
	Profile peaking	(II)
	Profile consistency	(II)
	Temperature equilibration	(IIIa)
2.3.5 Pressure Balance	Thermal pressure	(I)
	Plasma betas	(I)
	Fast particles fraction	(II)
	Beam particles fraction	(II)
2.3.6 Particle Balance	Helium concentration	(I)
	Impurity profiles and concentrations	(IIIa)
2.3.7 Operational Limits	Plasma shaping	(IIIa)
	Current limit	(I)
	Density limit	(IIIa)
	Beta limit	(IIIa)
	Fast particles limit	(II)
	H-mode threshold	(I)

Table A.11.: Evaluation of implemented modellings for the core physics module. Categories: (I) state-of-the-art modelling, (II) proposals for updates, (IIIa) proposals for updates with proposals for simple modellings requiring further work and (IIIb) proposals for updates with proposals for advanced modellings.

References

[1] United Nations, Department of Economic and Social Affairs Population Division, World Urbanization Prospects: The 2011 Revision, New York, 2012.

[2] International Energy Agency (IEA), World Energy Outlook 2009, Paris, 2009.

[3] P. Muehlich and T. Hamacher, Fusion Engineering and Design **84**, 1361 (2009).

[4] H. Cabal et al., The possible role of fusion power in a future sustainable global energy system using the EFDA Times global energy model, Madrid, 2010.

[5] T. Eder, ETM Scenarios. Private Communication, 06.12.2012.

[6] R. Kleiber and R. Bilato, IPP Summer University for Plasma Physics, Greifswald, 2011.

[7] Max-Planck-Institute for Plasma Physics, Image Database, 2013.

[8] G. H. Neilson et al., Nuclear Fusion **52**, 047001 (2012).

[9] H. Zohm, Fusion Science and Technology **58**, 613 (2010).

[10] H. Zohm, 1st IAEA DEMO Programme Workshop, Los Angeles: Realistic Operational Scenarios for a DEMO Tokamak. Presentation, 15.10.2012.

[11] P. Batistoni et al., Report of the Ad hoc Group on DEMO Activities. CCE-FU 49/6.7, 2010.

[12] H. Zohm, General Atomics, San Diego: DEMO Physic Challenges. Presentation, 26.03.2012.

[13] R. Kemp, Comments on PhD Thesis. Private Communication, 11.03.2013.

[14] R. Kemp et al., DEMO design concepts from PPPT-SYS: EFDA PPPT WP11-SYS01-ACT5, 2012.

[15] R. Kemp, DEMO Design Summary: Draft-Version of 18/04/12. Private Communication, 18.04.2012.

[16] R. Kemp, PROCESS Output of DEMO 1 v18/04/12. Private Communication, 18.04.2012.

[17] D. J. Ward, System Studies. Presentation, 10.05.2011.

[18] D. J. Ward, EU Power Plant Systems Studies: The 8th Workshop on DEMO in the Broader Approach Activities. Presentation, 2011.

[19] J. Johner, Fusion Science and Technology **59**, 308 (2011).

[20] Z. Dragojlovic et al., Fusion Science and Technology **56**, 913 (2009).

[21] Z. Dragojlovic et al., Fusion Engineering and Design **85**, 243 (2010).

[22] M. Nakamura et al., Fusion Engineering and Design **87**, 864 (2012).

[23] G. Federici et al., Annual Report 2011: EU Contributions to the IFERC DEMO Design Activities (DDAs): IDM-BA-D-225U7A, 2012.

[24] F. Franza et al., Preliminary Version of the DEMO Technology Design Guidelines: EFDA PPPT WP11-SYS01-ACT2, 2012.

[25] P. J. Knight, A User's Guide to the PROCESS Systems Code: Edition 2.1.0, UKAEA, 1996.

[26] M. Kovari, R. Kemp, P. J. Knight, and D. J. Ward, The PROCESS fusion reactor systems code. PROCESS summary paper: DRAFT 22/08/2011, 2011.

[27] J. Johner, Draft HELIOS 1.1 description. Private Communication, 23.06.2011.

[28] H. Fujieda, Y. Murakami, and M. Sugihara, Tokamak Plasma Power Balance Calculation Code (TPC Code) Outline and Operation Manual: JAERI-M 92-178, 1992.

[29] H. Utoh and K. Tobita, Modeling of JAEA System Code and Results of the Benchmark Test Case in JA: The 8th Workshop on DEMO in the Broader Approach Activities, 2011.

[30] M. Nakamura, Results of the joint work on benchmarking the systems codes. Presentation, 01.02.2012.

[31] T. Hartmann et al., Towards a "Physics Design Guidelines for a DEMO Tokamak" Document. Report on EFDA Power Plant Physics and Technology Work Packages: EFDA PPPT WP11-SYS01-ACT3, 2012.

[32] H. Zohm et al., On the Physics Guidelines for a Tokamak DEMO. IAEA CN-197/FTP/3-3, 24th IAEA Fusion Energy Conference, San Diego, USA, 2012.

[33] N. A. Uckan and ITER Physics Group, ITER Physics Design Guidelines: 1989, ITER Documentation Series No. 10, IAEA, Vienna, 1990.

[34] W. Demtröder, *Experimentalphysik 1: Mechanik und Wärme*, Springer, Berlin and Heidelberg, 2008.

[35] W. Demtröder, *Experimentalphysik 2: Elektrizität und Optik*, Springer, Berlin and Heidelberg, 2009.

[36] W. Demtröder, *Experimentalphysik 3: Atome, Moleküle und Festkörper*, Springer, Berlin and Heidelberg, 2005.

[37] W. Demtröder, *Experimentalphysik 4: Kern-, Teilchen- und Astrophysik*, Springer, Berlin and Heidelberg, 2005.

[38] J. A. Wesson, *Tokamaks*, Clarendon Press, Oxford, 2008.

[39] J. P. Freidberg, *Plasma Physics and Fusion Energy*, Cambridge University Press, Cambridge, 2007.

[40] M. Kaufmann, *Plasmaphysik und Fusionsforschung*, Teubner, Stuttgart, 2003.

[41] A. Dinklage et al., *Plasma Physics: Confinement, Transport and Collective Effects*, Springer, Berlin, Heidelberg, New York, 2005.

[42] P. C. Stangeby, *The plasma boundary of magnetic fusion devices*, Institute of Physics Publishing, Bristol, 2000.

[43] J. Raeder, *Kontrollierte Kernfusion*, Teubner, Stuttgart, 1981.

[44] H. Zohm, Fusionsforschung. Lecture Notes, München, 2009.

[45] H. Zohm, Plasmaphysik. Lecture Notes, München, 2009.

[46] F. Franza, T. Hartmann, H. Zohm, and F. Warmer, Modules of a comprehensive systems code. Private Communication, 11.06.2012.

[47] P. A. Schneider, Characterization and scaling of the tokamak edge transport barrier. PhD-Thesis, LMU Munich, 2012.

[48] J. Johner, R. Kemp, T. Hartmann, and D. Ward, HELIOS / PROCESS / IPP Benchmarks: Draft-Version of 15/11/11. Private Communication, 15.11.2011.

[49] T. Hartmann, Workshop on Physics Assumptions for a Tokamak DEMO. Personal Notes, Garching, 14.03.2012.

[50] N. Pomphrey, Bootstrap dependence on plasma profile parameters: Princeton Plasma Physics Laboratory PPPL-2854, 1992.

[51] A. C. C. Sips et al., Nuclear Fusion **49**, 085015 (2009).

[52] C. E. Kessel et al., Nuclear Fusion **49**, 085034 (2009).

[53] S. C. Jardin et al., Fusion Engineering and Design **80**, 25 (2006).

[54] O. Sauter, C. Angioni, and Y. R. Lin-Liu, Physics of Plasmas **6**, 2834 (1999).

[55] O. Sauter, C. Angioni, and Y. R. Lin-Liu, Physics of Plasmas **9**, 5140 (2002).

[56] S. P. Hirshman, Physics of Fluids **31**, 3150 (1988).

[57] C. E. Kessel, Nuclear Fusion **34**, 1221 (1994).

[58] A. G. Peeters, Plasma Physics and Controlled Fusion **42**, B231 (2000).

[59] W. M. Nevins, Summary Report: ITER Specialists' Meeting on Heating and Current Drive: ITER-TN-PH-8-4, Garching, 1988.

[60] H. R. Wilson, Nuclear Fusion **32**, 257 (1992).

[61] G. T. Hoang et al., Bootstrap fraction in TFTR, Tore Supra and TEXTOR: Proc. 24th EPS Conference in Berchtesgarden: Vol. 21A Part III p. 965, 1997.

[62] M. C. R. Andrade and G. O. Ludwig, Plasma Physics and Controlled Fusion **50**, 065001 (2008).

[63] K. Tobita and Sub-Cluster for Fusion Energy Realization, Systems code of JAEA. Presentation, 07.10.2009.

[64] H. Zohm, German DEMO Working Group - Topic P1: Steady State Operation. Presentation, 02.05.2011.

[65] H. Zohm, German DEMO Working Group - Topic P1: Steady State Operation. Presentation, 17.11.2011.

[66] H. Zohm et al., Final report on PPP&T-WP12-DAS-HCD-PC: Physics Coordination, 2013.

[67] S. Ejima et al., Nuclear Fusion **22**, 1313 (1982).

[68] E. Fable, Notes on estimate of relevant current ramps parameters for tokamaks. Private Communication, 20.03.2012.

[69] S. Kim et al., Plasma Current Ramp-up Phase Simulation of ITER: 34th EPS Conference on Plasma Physics, Warsaw, P-5.142, 2007.

[70] E. Fable, ITER ramp rate. Private Communication, 13.03.2012.

[71] E. Fable, Flux consumption vs ramp rate. Private Communication, 27.03.2012.

[72] S. P. Hirshman and G. H. Neilson, Physics of Fluids **29**, 790 (1986).

[73] ITER Organization, ITER Image Galleries. http://www.iter.org/galleries, 20.03.2013.

[74] T. Hartmann, Systems Code Studies: Fusion Gain for DEMO. Presentation, 19.10.2010.

[75] D. J. Ward, Plasma Physics and Controlled Fusion **52**, 124033 (2010).

[76] H.-S. Bosch and G. M. Hale, Nuclear Fusion **32**, 611 (1992).

[77] H.-S. Bosch and G. M. Hale, Nuclear Fusion **33**, 1919 (1993).

[78] O. Kardaun, Discussion on the energy confinement time. Private Communication, 11.11.2010.

[79] F. W. Perkins et al., Nuclear Fusion **39**, 2137 (1999).

[80] M. Shimada et al., Nuclear Fusion **47**, S1 (2007).

[81] H. Zohm, Report on EFDA Power Plant Physics and Technology work packages: EFDA PPPT WP11-SYS01-ACT7, 2012.

[82] F. Albajar, J. Johner, and G. Granata, Nuclear Fusion **41**, 665 (2001).

[83] I. Fidone, G. Giruzzi, and G. Granata, Nuclear Fusion **41**, 1755 (2001).

[84] H. P. Summers, ADAS User manual 2.6: http://www.adas.ac.uk/manual.php, 2004.

[85] T. Pütterich et al., Nuclear Fusion **50**, 025012 (2010).

[86] D. E. Post et al., Atomic Data and Nuclear Data Tables **20**, 397 (1977).

[87] R. Dux, Radiation in fusion plasmas. Private Communication, 11.11.2010.

[88] G. F. Matthews et al., Nuclear Fusion **39**, 19 (1999).

[89] G. Giruzzi et al., EFDA PPPT SYS01 2012 Remote Meeting 2. First METIS simulations of DEMO1 scenario, 06.09.2012.

[90] D. Post et al., Physics of Plasmas **2**, 2328 (1995).

[91] A. Kallenbach et al., Journal of Nuclear Materials **337-339**, 381 (2005).

[92] E. J. Doyle et al., Nuclear Fusion **47**, S18 (2007).

[93] P. A. Schneider, Pedestal Pressure Scalings. Private Communication, 22.10.2012.

[94] H. R. Koslowski, Fusion Science and Technology **49**, 147 (2006).

[95] H. Zohm et al., Physics Guidelines for a Tokamak DEMO. Presentation, 24th IAEA Fusion Energy Conference, San Diego, USA, 12.10.2012.

[96] O. Sauter, DEMO Physics Guidelines. Private Communication, 17.01.2012.

[97] T. Hartmann, H. Zohm, and T. Hamacher, TREND: A Zero-Dimensional Systems Code for the Analysis of Next-Step Fusion Devices. Contribution to the 39th European Physical Society Conference on Plasma Physics, Stockholm, 2012.

[98] IAEA, Summary of the ITER final design point: ITER EDA Documentation Series No. 22, 2001.

[99] D. Maisonnier et al., Fusion Engineering and Design **75-79**, 1173 (2005).

[100] R. Hiwatari et al., Nuclear Fusion **45**, 96 (2005).

[101] K. Tobita et al., Nuclear Fusion **49**, 075029 (2009).

[102] F. Najmabadi et al., Fusion Engineering and Design **38**, 3 (1997).

[103] S. C. Jardin et al., Fusion Engineering and Design **38**, 27 (1997).

[104] F. Najmabadi et al., Fusion Engineering and Design **80**, 3 (2006).

[105] M. Greenwald, Plasma Physics and Controlled Fusion **44**, R27 (2002).

[106] M. Greenwald et al., Nuclear Fusion **28**, 2199 (1988).

[107] P. T. Lang et al., Nuclear Fusion **52**, 023017 (2012).

[108] T. H. Osborne et al., Physics of Plasmas **8**, 2017 (2001).

[109] G. V. Pereverzev et al., Nuclear Fusion **45**, 221 (2005).

[110] C. Angioni et al., Nuclear Fusion **47**, 1326 (2007).

[111] F. Troyon et al., Plasma Physics and Controlled Fusion **26**, 209 (1984).

[112] E. J. Strait, Physics of Plasmas **1**, 1415 (1994).

[113] O. Sauter et al., Physics of Plasmas **4**, 1654 (1997).

[114] F. Wagner et al., Phys. Rev. Lett. **49**, 1408 (1982).

[115] Y. R. Martin et al., Journal of Physics: Conference Series **123**, 012033 (2008).

[116] T. Hartmann and H. Zohm, Power Exhaust in Next-Step Fusion Devices. Contribution to the 38th European Physical Society Conference on Plasma Physics, Strasbourg, 2011.

[117] C. E. Kessel, Peak heat load on divertor. Private Communication, 03.02.2011.

[118] A. Kallenbach et al., Nuclear Fusion **52**, 122003 (2012).

[119] T. Eich et al., Physical Review Letters **107**, 215001 (2011).

[120] A. Kallenbach et al., Multi-machine comparisons of divertor heat flux mitigation by radiative cooling with nitrogen: IAEA CN-197/ITR/P1-28, 2012.

[121] D. D. Ryutov, Physics of Plasmas **14**, 064502 (2007).

[122] M. Kotschenreuther et al., Physics of Plasmas **14**, 072502 (2007).

[123] S. C. Jardin et al., Fusion Engineering and Design **48**, 281 (2000).

[124] A. Li-Puma et al., Fusion Engineering and Design **84**, 1197 (2009).

[125] W. Biel et al., German DEMO Working Group - Topic P5: Plasma Diagnostics and Integrated Control. Presentation, 26.04.2012.

[126] H. Zindler, Dynamische Kraftwerkssimulation: Kopplung von Finiten Volumenverfahren und Prädiktor-Korrektor-Verfahren durch Adjungiertenverfahren. PhD-Thesis, TU Braunschweig, Fakultät für Maschinenbau, 2007.

[127] A. Hauschke, Dynamische Simulation und Optimierung eines Abhitzedampferzeugers. Diploma-Thesis, TU Braunschweig, Institut für Wärme- und Brennstofftechnik, 2007.

[128] R. Leithner, A. Hauschke, H. Zindler, C. Schlitzberger, and B. Apascaritei, Stationäre und dynamische Simulation und Validierung von Kraftwerkskreisläufen, 2008.

[129] B. Epple, R. Leithner, W. Linzer, and H. Walter, *Simulation von Kraftwerken und wärmetechnischen Anlagen*, Springer, Wien, 2009.

[130] G.-N. Stamatelopoulos, *Berechnung und Optimierung von Kraftwerkskreisläufen. Fortschritt-Berichte VDI, Reihe 6, Energietechnik*, VDI-Verlag, Düsseldorf, 1996.

[131] IWBT, Institut für Wärme- und Brennstofftechnik, TU Braunschweig. http://www.wbt.ing.tu-bs.de, 07.01.2010.

[132] W. Biel, German DEMO Working Group - Action A5: Discuss downtime duration for pulsed scenarios. Presentation, 03.05.2011.

[133] G. Janeschitz, ITER Status and Prospects. Presentation: HEPP Colloquium, Greifswald 2012, 26.09.2012.

[134] H. Zohm, Discussion on dynamical phases of a pulsed power plant. Private Communication, 14.09.2011.

[135] J. L. Duchateau et al., Journal of Physics: Conference Series **97**, 012038 (2008).

[136] J. L. Duchateau et al., Applied Superconductivity **17**, 1342 (2007).

[137] P. Hertout, Algorithm for Cost Evaluation of Tokamaks with copper or superconducting magnets. Internal note AIM/NTT-2004.002, 2004.

[138] K.-P. Weiss et al., German DEMO Working Group - Topic T5: High Temperature Superconductors. Presentation, 26.04.2012.

[139] L. Boccaccini, Correlation of Fluence and Damage in Steel for Fusion Neutrons. Private Communication, 19.09.2011.

[140] International Energy Agency and OECD Nuclear Energy Agency, *Projected Costs of Generating Electricity 2010*, OECD Publishing and Nuclear Energy Agency, Paris, 2010.

[141] D. J. Ward, I. Cook, and P. J. Knight, The impact of physics assumptions on fusion economics. IAEA CN-77/FTP2/20, 18th IAEA Fusion Energy Conference, Sorrento, Italy, 2000.

[142] W. Biel, An approach towards different design options for DEMO: International MFE Roadmapping Workshop, Princeton, USA. Presentation, 09.09.2011.

[143] J. D. Galambos et al., Nuclear Fusion **35**, 551 (1995).

[144] T. C. Hender, P. J. Knight, and I. Cook, Fusion economics. Report UKAEA FUS-333: A note prepared for the 1996 European Fusion Programme Evaluation Board, 1996.

[145] T. C. Hender et al., Fusion Technology **30**, 1605 (1996).

[146] I. Cook, T. C. Hender, P. J. Knight, and D. J. Ward, Direct Cost of Electricity from Fusion Power Plants. 26th EPS Conference on Controlled Fusion and Plasma Physics, 1999.

[147] T. Hamacher et al., Fusion Engineering and Design **56-57**, 95 (2001).

[148] I. Cook et al., Fusion Engineering and Design **63-64**, 25 (2002).

[149] D. J. Ward et al., Fusion Engineering and Design **75-79**, 1221 (2005).

[150] S. P. Marburger, Analyse der Wirtschaftlichkeit von Kernfusionskraftwerken. Diploma-Thesis, TU Berlin, 2006.

[151] W. E. Han et al., Fusion Engineering and Design **84**, 895 (2009).

[152] G. Zollino et al., Fusion Engineering and Design **86**, 2787 (2011).

[153] T. Bläsche, Tokamak Economic Modelling. Diploma-Thesis, University of Ulm, 2012.

[154] J. D. Galambos, STAR Code: Spherical Tokamak Analysis and Reactor Code.

[155] R. L. Reid et al., ETR/ITER Systems Code. Oak Ridge Report ORNL/FEDC-87/7, 1988.

[156] D. Maisonnier et al., A conceptual study of commercial fusion power plants: Final Report of the European Fusion Power Plant Conceptual Study (PPCS), 2005.

[157] D. Maisonnier et al., Nuclear Fusion **47**, 1524 (2007).

[158] D. Maisonnier et al., Fusion Engineering and Design **81**, 1123 (2006).

[159] D. Maisonnier, Fusion Engineering and Design **83**, 858 (2008).

[160] F. Imbeaux et al., SYCOMORE: SYstem COde for MOdelling REactors, a flexible and modular system code architecture. Presentation, EFDA PPPT SYS Task Planning Meeting, 27.02.2012.

[161] G. J. Sadler and P. van Belle, An Improved Formulation of the D(t,n)4He Reaction Cross-Section: JET-IR(87)08, Joint European Torus, 1987.

[162] J. Johner, HELIOS / PROCESS / IPP Benchmarks. Private Communication, 21.10.2011.

[163] Y. Murakami et al., Journal of Plasma and Fusion Research **77**, 712 (2001).

[164] M. Nakamura, DEMO 0-2 parameters calculated by TPC. Private Communication, 22.03.2012.

[165] B. A. Trubnikov, Reviews of Plasma Physics **7**, 345 (1979).

[166] H.-S. Bosch, Die Physik der Alpha-Teilchen in einem Fusionsreaktor mit Deuterium-Tritium-Plasmen: IPP 1/325. Habilitation, Humboldt-Universität Berlin, 1999.

[167] N. Balshaw, All-the-World's Tokamaks. http://www.tokamak.info, 23.11.2012.

[168] Y. Wu, Fusion Engineering and Design **81**, 2713 (2006).

[169] Y. Murakami et al., Fusion Engineering and Design **48**, 347 (2000).

[170] IAEA, ITER-FEAT Outline Design Report: ITER EDA Documentation Series No. 18, 2001.

[171] M. Shimada et al., Physics Basis of ITER-FEAT: IAEA-CN-77/ITERP/05, 2000.

List of Tables

List of Figures

List of Acronyms

ARIES	Advanced Reactor Innovation and Evaluation Study
ASDEX	Axially Symmetric Divertor EXperiment
CCFE	Culham Centre for Fusion Energy
CD	current-drive
CEA	Commissariat à l'énergie atomique et aux énergies alternatives
COE	levelized costs of electricity
CS	central solenoid
DP	design point
dpa	displacement per atom
ECRH	electron-cyclotron resonance heating
EFDA	European Fusion Development Agreement
ELM	edge-localized mode
ETM	EFDA Times Model
FW	first wall
FWLT	first wall life-time
H-mode	high confinement mode
H&CD	heating and current-drive
HCLL	helium cooled lithium lead
HTS	high temperature superconducting
ICRH	ion-cyclotron resonance heating
IFERC	International Fusion Energy Research Centre
IPP	Max-Planck-Institute for Plasma Physics
JAEA	Japan Atomic Energy Agency
JET	Joint European Torus
L-mode	low confinement mode
LCMS	last closed magnetic surface
LHCD	lower hybrid current-drive
MARFE	multifaceted asymmetric radiation from the edge
MHD	magneto-hydro-dynamic

NBI	neutral beam injection
NTM	neo-classical tearing mode
O&M	operation and maintenance
OP	operation point
PE	power exhaust
PF	poloidal field
PFC	poloidal field coil
PI	plasma initiation
POpCon	Plasma Operation Contour
PPCS	Power Plant Conceptual Study
PPPT	Power Plant Physics and Technology
PWI	plasma wall interaction
RC	re-charge
RMSE	root-mean-square error
RWM	resistive wall mode
SOL	scrape-off layer
TBR	tritium breeding ratio
TF	toroidal field
TFC	toroidal field coil
VDE	vertical displacement event
VF	vertical field

List of Symbols

Symbol	Unit	Input	Description
A		**	Aspect ratio
A_{con}^{inb}	[m^2]		Inboard effective area (conduction)
A_{con}^{outb}	[m^2]		Outboard effective area (conduction)
A_{rad}^{inb}	[m^2]		Inboard effective area (radiation)
A_{rad}^{outb}	[m^2]		Outboard effective area (radiation)
a	[m]		Minor radius
B_{CSmax}	[T]	* (13)	Maximal magnetic field of the CS coils
$\langle B_p \rangle_l$	[T]		Poloidal magnetic field (surface-line-averaged)
B_t	[T]	*	Toroidal magnetic field on axis
B_{tMax}	[T]	* (13)	Toroidal magnetic field at inboard TF coils (max.)
B_{tot}	[T]		Total magnetic field
B_V	[T]		Vertical magnetic field
COE			Levelised costs of electricity (normalized)
c_{Ejima}		*	Ejima coefficient
c_{heat}		* (5)	Coefficient for the heating phase
c_j			Ratio of peak to surface-averaged current density
c_n			Ratio of peak to volume-averaged density
c_{nPed}		**	Ratio of peak to pedestal density
c_p			Ratio of peak to volume-averaged pressure
c_{RU}		* (10)	Coefficient for the plasma current ramp-up phase
c_{RUrate}	[MA/s]		Plasma current ramp-up rate
c_T			Ratio of peak to volume-averaged temperature
c_{Tped}		**	Ratio of peak to pedestal temperature
d_{CS}	[m]	* (1.0)	Radial width of the central solenoid
d_{int}	[m]	* (1.6)	Radial width of inboard SOL, blanket and shield
d_{SOL}	[m]	* (0.15)	Radial width of the inboard SOL
d_{TFC}	[m]	* (1.6)	Radial width of the inboard TF coils
f_{aux}		* (0.007)	Fraction of P_{el} for the auxiliary systems
f_{BS}			Bootstrap current fraction
f_{cryo}		* (0.017)	Fraction of P_{el} for the cryo system

Table A.13 – continued on next page

Table A.13 – continued from previous page

Symbol	Unit	Input	Description
f_{CD}		**	External current-drive fraction
f_{DC}			Duty cycle
f_{DT}			Fuel concentration (core)
f_{DTM}			Fuel concentration (mantle)
f_{divRad}		* (0.90)	Divertor radiation fraction
f_{exp}		* (15)	Expansion factor from midplane to target plate
f_{GW}		*	Greenwald density fraction
$f_{GW\,ped}$			Greenwald density fraction (pedestal)
$f_{geoBlkt}$		* (0.909)	Fraction of the blanket to the total surface area
f_{geoDiv}		* (0.062)	Fraction of the divertor to the total surface area
f_{He}		**	Helium concentration (core)
f_{HeM}		*	Helium concentration (mantle)
f_{hBlkt}		* (0.95)	High grade heat fraction of the blanket
f_{hDiv}		* (1.0)	High grade heat fraction of the divertor
f_i			Thermal ion concentration
f_{ind}		*	Inductive current fraction
f_{LH}			Ratio of transport loss to H-mode threshold power
f_{nMult}		* (1.18)	Neutron energy multiplication factor
$f_{outboard}$		* (0.67)	SOL power flux fraction to the outboard side
f_{P2E}			Ratio of particle to energy confinement time
f_{pump}		* (0.185)	Fraction of P_{el} for blanket pumps
f_{pumpD}		* (0.028)	Fraction of P_{el} for divertor pumps
f_{rad}			Fraction of radiated heating power
f_{rec}			Recirculating power fraction
f_{Z1}		**	Concentration of impurity 1 (core)
f_{Z1M}		*	Concentration of impurity 1 (mantle)
f_{Z2}		**	Concentration of impurity 2 (core)
f_{Z2M}		*	Concentration of impurity 2 (mantle)
f_{Z3}		**	Concentration of impurity 3 (core)
f_{Z3M}		*	Concentration of impurity 3 (mantle)
H		* (1.0)	Confinement enhancement factor
I_{BS}	[MA]		Plasma current (bootstrap effect)
I_{CD}	[MA]		Plasma current (external current-drive)
I_{ind}	[MA]		Plasma current (inductively driven)
I_p	[MA]		Plasma current
$\langle j \rangle_{S_p}$	[A/m^2]		Plasma current density (surface-averaged)
j_0	[A/m^2]		Plasma current density on axis

Table A.13 – continued on next page

Table A.13 – continued from previous page

Symbol	Unit	Input	Description
j_{CS}	[A/mm^2]		Average current density in the CS coil
L	[m]		Plasma poloidal perimeter at the separatrix
L_p	[H]		Plasma inductance
l_i		*	Plasma internal inductance
M	[AMU]	* (2.5)	Average mass number
ND_a	[dpa/a]		Annual neutron damage
ND_{max}	[dpa]	* (60)	Maximal neutron damage / FW lifetime limit
ND_{rate}	$[\frac{\text{MW}}{\text{m}^2}/\frac{\text{dpa}}{\text{a}}]$	** (0.1)	Neutron damage rate
$\langle n_{DT}\rangle$	[10^{20} m^{-3}]		Fuel density (volume-averaged)
$\langle n_e\rangle$	[10^{20} m^{-3}]		Electron density (volume-averaged)
$\overline{n}_e$	[10^{20} m^{-3}]		Electron density (line-averaged)
n_{e0}	[10^{20} m^{-3}]	**	Electron density on axis
n_{ePed}	[10^{20} m^{-3}]	**	Electron density at the pedestal top
n_{eSep}	[10^{20} m^{-3}]	* (0.3)	Electron density ate the separatrix
n_{GW}	[10^{20} m^{-3}]		Greenwald density
$\langle n_i\rangle$	[10^{20} m^{-3}]		Thermal ion density (volume-averaged)
P_{add}	[MW]		Additional heat & CD power
P_{aux}	[MW]		Electric power for auxiliary systems
P_α	[MW]		Alpha power
P_{blkt}	[MW]		Blanket thermal power
P_{brem}	[MW]		Bremsstrahlung radiation power
P_{CD}	[MW]		Current-drive power
P_{con}	[MW]		Transport loss power
P_{cryo}	[MW]		Electric power for cryo systems
P_{div}	[MW]		Divertor thermal power
P_{el}	[MW]		Gross electric power
P_{elAdd}	[MW]		Electric power for additional heating and CD
P_{elNet}	[MW]		Net electric power
P_{elRec}	[MW]		Recirculating electric power
P_{fus}	[MW]		Fusion power
P_{heat}	[MW]		Total plasma heating power
P_{LH}	[MW]		H-mode threshold power
P_{line}	[MW]		Line radiation power
$P_{lineCore}$	[MW]		Line radiation power (core)
$P_{lineMantle}$	[MW]		Line radiation power (mantle)

Table A.13 – continued on next page

Table A.13 – continued from previous page

Symbol	Unit	Input	Description
$P_{lineTot}$	[MW]		Total line radiation (Matthews)
P_{nCD}	[MW]		Pure heating power (no CD)
$P_{neutron}$	[MW]		Neutron power
P_{nonRad}	[MW]		Total non radiated power
P_{OH}	[MW]		Ohmic heating power
P_{pump}	[MW]		Electric power for blanket pumping system
P_{pumpD}	[MW]		Electric power for divertor pumping system
P_{RC}	[MW]	* (100)	Power to recharge the CS
P_{rad}	[MW]		Radiated power in plasma core and mantle
$P_{radCore}$	[MW]		Radiated power (core)
$P_{radMantle}$	[MW]		Radiated power (mantle)
P_{sep}	[MW]		Power crossing the separatrix
P_{syn}	[MW]		Synchrotron radiation power
P_{th}	[MW]		Total thermal power (high grade heat)
$\langle p_{th} \rangle$	[Pa]		Thermal plasma pressure (volume-averaged)
p_0	[Pa]		Thermal plasma pressure on axis
p_{ped}	[Pa]		Thermal plasma pressure at pedestal top
Q			Fusion gain
q_0		*	Safety factor on axis
q_{95}		**	Safety factor at 95% flux
q_{cyl}			Safety factor (cylindrical equivalent)
q_{HWL}	[MW/m^2]		Average surface heat flux
q_{NWL}	[MW/m^2]		Average neutron wall load
q_{peak}^{inb}	[MW/m^2]		Peak thermal load on inboard divertor plates
q_{peak}^{outb}	[MW/m^2]		Peak thermal load on outboard divertor plates
q_{sep}	[MW/m^2]		Parallel power flux density at the separatrix
R_0	[m]	**	Major radius
R_{CSe}	[m]		External radius of the CS coils
R_{CSi}	[m]		Internal radius of the CS coils
R_p	[Ω]		Plasma resistivity
r_{syn}		* (0.6)	Wall reflection coefficient for synchotron radiation
S	[m^2]		Plasma surface area
S_{FW}	[m^2]		First wall surface area
S_p	[m^2]		Plasma poloidal cross-sectional area
$\langle T \rangle$	[keV]		Plasma temperature (volume-averaged)

Table A.13 – continued on next page

Table A.13 – continued from previous page

Symbol	Unit	Input	Description
T_0	[keV]	**	Plasma temperature on axis
T_{div}	[keV]	* (0.015)	Plasma temperature on divertor plate
$\langle T \rangle_n$	[keV]		Plasma temperature (density-averaged)
T_{ped}	[keV]	**	Plasma temperature at pedestal top
T_{RU}	[keV]	* (0.6)	Average temperature after current camp up
T_{sep}	[keV]	* (0.1)	Plasma temperature at the separatrix
U_{loop}	[V]		Loop voltage
V	[m^3]		Plasma volume
W_{th}	[MW s]		Internal energy of the plasma
Z_1		**	Charge number of impurity 1
Z_2		**	Charge number of impurity 2
Z_3		**	Charge number of impurity 3
Z_{eff}			Effective ion charge (core)
Z_{effM}			Effective ion charge (mantle)

Table A.13.: List of Latin symbols used throughout this thesis. Required input parameters are marked with two asterisk. Optional ones are marked with one asterisk. In case that these are not specified in the input file, TREND uses implemented modellings or default values that are given in brackets.

Symbol	Unit	Input	Description
α_j		**	Coefficient of the current profile
α_n		**	Coefficient of the density profile
α_T		**	Coefficient of the temperature profile
β	[%]		Total plasma beta
β_N	[%]		Total normalized plasma beta
$\beta_{N,max}$	[%]		Maximal normalized plasma beta
$\beta_{N,th}$	[%]		Thermal normalized plasma beta
β_n		* (2.0)	Coefficient of the density profile
β_p	[%]		Total poloidal plasma beta
$\beta_{p,th}$	[%]		Thermal poloidal plasma beta
β_T		* (2.0)	Coefficient of the temperature profile
β_t			Total toroidal plasma beta
$\beta_{t,th}$			Thermal toroidal plasma beta
β_{th}	[%]		Thermal plasma beta
γ_{beam}		* (0)	Ratio of beam to thermal beta
$\langle\gamma_{CD}\rangle$	$[10^{20}\,\frac{\mathrm{A}}{\mathrm{W\,m^2}}]$	*	Normalized current-drive efficiency (global)
γ_{fast}			Ratio of fast particles to thermal beta
$\gamma_{f\alpha}$			Ratio of fast alpha to thermal beta
γ_{NC}			Neoclassical resistivity enhancement factor
δ_{95}		*	Plasma triangularity at 95% flux
δ_{max}			Plasma triangularity (maximum)
δ_X			Plasma triangularity at the X-point (mean)
δ_{X1}		*	Plasma triangularity at the X-point (top)
δ_{X2}		*	Plasma triangularity at the X-point (bottom)
ε			Inverse aspect ratio
η_{add}		* (0.60)	Wall plug efficiency of heat and CD systems
η_{pump}		* (0.91)	High-grade heat from blanket pumping power
η_{pumpD}		* (0.91)	High-grade heat from divertor pumping power
η_{th}		* (0.44)	Thermodynamic efficiency of the power conversion
η_{tot}			Total plant efficiency
Θ_L			Correction factor for plasma poloidal perimeter
Θ_S			Correction factor for plasma surface area
Θ_{S_p}			Correction factor for plasma cross-sectional area
Θ_V			Correction factor for plasma volume

Table A.14 – continued on next page

Table A.14 – continued from previous page

Symbol	Unit	Input	Description
κ_{95}		*	Plasma elongation at 95% flux
κ_a			Plasma elongation (average)
κ_{max}			Plasma elongation (maximum)
κ_X			Plasma elongation at the X-point (mean)
κ_{X1}		*	Plasma elongation at the X-point (top)
κ_{X2}		*	Plasma elongation at the X-point (bottom)
λ_{int}	[m]		Integral power decay length
λ_q	[m]		SOL power decay length
$\ln\Lambda$			Coulomb logarithm
ρ_{core}		* (0.90)	Normalized radial coordinate of the plasma core
ρ_{ped}		* (0.95)	Normalized radial coordinate of the pedestal top
$\langle\sigma\rangle_{S_p}$	$[\Omega^{-1}\text{m}^{-1}]$		Plasma conductivity (surface-averaged)
τ_{BT}	[s]		Time-scale of the burn-termination phase
τ_{burn}	[s]		Time-scale of the burn phase
τ_{cycle}	[s]		Time-scale of the total cycle
τ_{down}	[s]		Down / dwell time
τ_E	[s]		Energy confinement time
τ_{FWLT}	[a]		First wall lifetime
τ_{flat}	[s]		Time-scale of the flat-top phase
τ_{heat}	[s]		Time-scale of the heating phase
τ_{PD}	[s]		Time-scale of the pump-down phase
τ_p^*	[s]		Global particle residence time
τ_{RC}	[s]		Time-scale of the coils recharge phase
τ_{RD}	[s]		Time-scale of the current ramp-down phase
τ_{RU}	[s]		Time-scale of the current ramp-up phase
τ_{res}	[s]		Resistive time-scale in the current ramp-up phase
ψ_{M1}		*	Plasma shape angle inboard top
ψ_{M2}		*	Plasma shape angle inboard bottom
ψ_{P1}		*	Plasma shape angle outboard top
ψ_{P2}		*	Plasma shape angle outboard bottom
Φ_{CS}	[V s]		Magnetic flux of the CS coils
Φ_{flat}	[V s]		Magnetic flux for inductive CD in the flat-top phase
Φ_{ind}	[V s]		Inductive magnetic flux during current ramp-up
Φ_{PF}	[V s]		Magnetic flux of the PF coils

Table A.14 – continued on next page

Table A.14 – continued from previous page

Symbol	Unit	Input	Description
Φ_{PI}	[V s]	* (0)	Magnetic flux for plasma initiation
Φ_{RU}	[V s]		Magnetic flux needed to ramp up the plasma current
Φ_{res}	[V s]		Resistive magnetic flux during current ramp-up
Φ_{tot}	[V s]		Total magnetic flux of CS and PF coils

Table A.14.: List of Greek symbols used throughout this thesis. Required input parameters are marked with two asterisk. Optional ones are marked with one asterisk. In case that these are not specified in the input file, TREND uses implemented modellings or default values that are given in brackets. For the advanced geometry module, the specification of the elongation, the triangularity and the shape angles is necessary.

Acknowledgements

The scientific progress benefits from various collaborations of dedicated scientists. I am deeply grateful for the warm welcome in the fusion community and I want to express my sincere appreciation for all my colleagues from the Max-Planck-Institute for Plasma Physics, as well as from the other research institutes and universities. It was a great pleasure and honour to work and collaborate with all of you. Furthermore, I would like to thank the Max-Planck-Institute for Plasma Physics, the European Fusion Development Agreement, the International Helmholtz Graduate School for Plasma Physics, the TUM Graduate School and the Hanns Seidel Foundation for financial and ideational support of this PhD project. My very special thanks go to the following persons:

Prof. Dr. Thomas Hamacher for his attentive supervision, the initiation and the comprehensive freedom during the development of this PhD project. Moreover, I feel very honoured about his trust in me.

Prof. Dr. Hartmut Zohm for the acceptance of the scientific supervision, the introduction to the world of plasma physics, as well as his multiple and manifold suggestions, excellent ideas and extensive support during the development and the finalization of this thesis. I absolutely appreciated each minute that was granted for fruitful discussions with him. His unlimited motivation and positive attitude often helped me to keep my motivation high.

Prof. Dr. Sibylle Günter for her willingness to act as a referee in the board of examiners and her sympathetic ear for the problems of PhD students.

Dr. David Ward and Dr. Richard Kemp for giving me the possibility to work with them during my stays at the CCFE. I gladly enjoyed the great hospitality, the long walks after lunch and the fruitful discussions.

Prof. Dr. Armin Reller, Dr. Jens Söntgen and Dr. Simon Meissner for their kind support during my time at the University of Augsburg.

Dr. Richard Kemp, Felix Warmer, Peter Böhme, Tobias Eder and Robert Hartmann for carefully reading and commenting on this thesis.

Finally, I want to use this opportunity to express my deepest gratefulness to my parents Gitta and Alois Hartmann for their infinite and unconditional support from the first day in my life. Many thanks also go to my brothers Robert, Armin and David. Moreover, I would like to thank Julia Stefan for accompanying and encouraging me on my way for a long time.